An Investigation of the Structure, Pinning and Magnetoresistance of Domain Walls in Ni81Fe19 Planar Nanowires

BOGART, LARA,KATRINA

An Investigation of the Structure, Pinning and Magnetoresistance of Domain Walls in $Ni_{81}Fe_{19}$ Planar Nanowires

Lara Katrina Bogart

A thesis submitted in partial fulfilment of the requirements for the degree of Doctor of Philosophy

University of Durham

2010

“*Why is a raven like a writing desk?*”

The Hatter

Alice’s Adventures in Wonderland

Table of contents

Abstract

The research and development of $Ni_{81}Fe_{19}$ thin films and planar nanowire structures has attracted considerable interest in recent years; in terms of improving the fundamental understanding of the basic physical processes and also for the development of potential applications. Example applications include sensors and the data storage devices. The optimisation of such devices requires detailed knowledge of the thickness dependence and microstructural influences on the magnetic and magnetoresistance properties, along with a thorough understanding of the effect of geometrical confinement on domain wall (DW) structure and pinning behaviour in nanowire structures.

The out-of-plane structural properties of thermally evaporated $Ni_{81}Fe_{19}$ thin films on pre-oxidised silicon substrates have been investigated using x-ray scattering techniques and transmission electron microscopy (TEM). These techniques have been used to provide information on the out-of-plane lattice parameter, the presence and degree of texture and also to quantify the width of the $SiO_2/Ni_{81}Fe_{19}$ interface. Magneto-optical Kerr effect (MOKE) magnetometry, differential phase contrast TEM imaging, micromagnetic simulations and anisotropic magnetoresistance measurements (AMR) have been used to make a detailed study of the thickness dependence of the magnetic behaviour of both thin films and nanowire structures.

The resistivity of thin films produced in this study is found to exhibit a higher value and lower mean free path than has previously been reported in the literature, which is attributed to the presence of a microstructure characterised by a small crystallite grain structure. The AMR is strongly thickness dependent for $t < 10$ nm, and tends toward zero for $t < 7$ nm. It is suggested that this is due to strain at the $SiO_2/Ni_{81}Fe_{19}$ interface, which changes the magnetostriction and is related to the AMR by spin-orbit effects.

The structure and pinning behaviour of DWs has been systematically investigated as a function of nanowire width, thickness and notch geometry. Although the wall structure is sensitive to the nanowire cross-sectional area, the DW depinning behaviour is relatively insensitive to notch geometry and instead is highly sensitive to wall type and chirality. A detailed model has been developed to make predictions for the AMR of individual DWs in nanowires. The model incorporates experimentally derived thickness dependent resistivity parameters and detailed DW spin structures from micromagnetic simulations. The magnitude of DW resistance is sensitive to wire width and the AMR ratio, and is found to be extremely sensitive to the magnitude of the magnetoresistance.

Declaration

I hereby declare that the work contained in this thesis is my own and has not been submitted for examination for any other degree at any University. The work of collaborators is acknowledged as appropriate. High resolution transmission electron microscopy images of $Ni_{81}Fe_{19}$ thin films presented in chapter 5 were taken by Dr. Budhika Mendis and co-ordinated by the author. Vibrating sample magnetometry measurements presented in chapter 6 were made by Alexis Ridler at Rutherford Appleton Laboratories using samples fabricated by the author. Nanowire structures investigated by differential phase contrast transmission electron microscopy imaging in chapter 7 were fabricated by Kerry O'Shea in the University of Glasgow with experimental measurements co-ordinated by the author.

Acknowledgments

I would like to take this opportunity to thank the many people who have helped me over the past few years with advice, encouragement and friendship.

The work presented here would not have been possible without the supervision and guidance of Del Atkinson. I am extremely grateful for his friendship, honesty and patience throughout the entire PhD process. I am also very grateful to Brian Tanner for his advice on x-ray scattering techniques and for providing lots of advice for life in general.

I would like to thank people in room 12 for putting up with all my idiosyncrasies and for helping to make my PhD such fun. A big thank you to David Eastwood, Rachael Houchin, Miriana Vadala, Jenny King, Helen Armstrong, Alex Pym, Tom Hase, Erhan Arac and David Burn. I have had some great discussions with you all that have really helped develop my understanding of things, whether it's been to do with the latest Sky Showbiz news or about domain walls! Also thanks to John Dobson for endless jokes and for always knowing when I needed help with fixing equipment. I would also like to thank Lynne for keeping my spirits up with tea and yummy Double Decker bars.

This thesis could not have been done without the tremendous support of my family and Chris, all of whom deserve my heartfelt thanks. You have always had faith in me even when I have not. To my dear parents and Calum for all their love and support throughout this and everything beforehand that has helped me get here. To Leon - this isn't quite a discovery of the Bogart, but hopefully it is 'Johnny Scholar' enough to be a suitable equivalent. Most of all I would like to thank Chris for being a constant source of encouragement, banter and - most importantly - you have always believed I could do this. You kept me sane, always made me laugh and I really could not have done this without you.

List of publications

Controlling domain wall pinning in planar nanowires by selecting domain wall type and its application in a memory concept

Applied Physics Letters **92** (2008) 022510

D. Atkinson, D. S. Eastwood, and L. K Bogart

The effect of geometrical confinement and chirality on domain wall pinning behaviour in planar nanowires

Journal of Applied Physics **104** (2008) 033904

L. K. Bogart, D. S. Eastwood, and D. Atkinson

Domain wall anisotropic magnetoresistance in planar nanowires

Applied Physics Letters **94** (2009) 042511

L. K. Bogart and D. Atkinson

Dependence of domain wall pinning potential landscapes on domain wall chirality and pinning site geometry in planar nanowires

Physical Review B **79** (2009) 054414

L.K. Bogart, D. Atkinson, K. J. O'Shea, D. McGrouther, and S. McVitie

ChiralMEM: A novel concept for high density magnetic memory technology

Nanotech Conference and Exposition Vol 1 Technical Proceedings (2009) 623-635

J. A. King, D. S. Eastwood, L. K. Bogart, H. Armstrong, and D. Atkinson

List of symbols

The following is a list of frequently used symbols and their definitions used within this thesis.

α	Gilbert damping parameter
α_c	Critical angle
α_{in}	Grazing angle of the x-ray beam relative to the sample surface
$\alpha_{1,2,3}$	Direction cosines
β	Imaginary component of the deviation of *n* from unity; absorption coefficient
γ	Gyromagnetic ratio
δ	Real component of the deviation of *n* from unity; dispersion coefficient
δ_{DW}	Domain wall width parameter
$\delta\rho$	Anisotropic magnetoresistance
$\Delta(2\theta)$	Full width at half maximum
$\boldsymbol{\varepsilon}$	Dielectric permittivity tensor
θ	Rotation of the plane of polarisation of light, also angle of sample $\left(\frac{2\theta}{2}\right)$
2θ	Angle of the detector relative to the incident beam at the sample
κ	Constant related to lineshape of the diffraction peak
λ	Wavelength
λ_s	Magnetostriction constant
Λ	Micromagnetic exchange length
μ	Relative magnetic permeability
μ_B	Bohr magneton
μ_0	Permeability of free space
$\mu_m^{orbital}$	Orbital magnetic moment
μ_m^{spin}	Spin magnetic moment
μ_m	Total magnetic moment

ρ	Electron density
ρ_{ave}	Average resistivity
$\rho_{\|\|}$	Resistivity when the applied field and current are parallel
$\rho_{\perp}$	Resistivity when the applied field and current are perpendicular
σ	Magnetoelastic tensor
τ	Torque
φ_{total}	Total free energy density
φ_{A}	Exchange energy density
φ_{k}	Magnetocrystalline energy density
φ_{σ}	Magnetoelastic energy density
φ_{s}	Magnetostatic energy density
φ_{Zeeman}	Zeeman energy density
χ	Magnetic susceptibility
ω_{L}	Larmor frequency
a	Lattice parameter
$\mathbf{a}_1, \mathbf{a}_2$ and $\mathbf{a}_3$	Real space lattice vectors
$\mathbf{a}_1^*, \mathbf{a}_2^*$ and $\mathbf{a}_3^*$	Reciprocal space lattice vectors
A	Exchange stiffness parameter
$\mathbf{B}$, B	Magnetic field induction
C	Curie constant
d_{hkl}	Interplanar spacing
D	Crystallite grain size
$\mathbf{D}$	Electric displacement vector
e	Charge of the electron
$E_{\uparrow\downarrow}, E_{\downarrow\downarrow}$	Energy associated with antiparallel and parallel spin alignment
E_{DW}	Total domain wall energy
E_{F}	Fermi energy
E_{total}	Total free energy
$f_{\text{A}}^{'}, f_{\text{A}}^{''}$	Real and imaginary parts of the dispersion correction
$\mathbf{G}$	Reciprocal lattice vector
$\mathbf{H}$, H	Applied magnetic field

I	Applied current
J	Current density
$J_{exchange}$	Exchange integral
$\mathbf{J}$	Total angular momentum
k_B	Boltzmann constant
$\mathbf{k}$	Wavevector
K_1, K_2	Magnetocrystalline anisotropy constants
$\mathbf{L}$	Total orbital angular momentum
M_s	Saturation magnetisation
$\mathbf{M}$, M	Magnetisation
n	Index of refraction
$\mathbf{q}$	Scattering vector
Q_V	Voigt constant
$R_{average}$	Average resistance
$R_{\|\|}$	Resistance when the applied field and current are parallel
$R_{\perp}$	Resistance when the applied field and current are perpendicular
$\mathbf{S}$	Total spin angular momentum
t	Thin film or nanowire thickness
T	Temperature
T_c	Curie temperature
T_n	Néel temperature
V	Applied voltage or volume element
w	Nanowire width

Chapter 1. Introduction

1.1 Introduction

The recent surge in interest in the magnetic behaviour of small elements stems from a combination of three factors: firstly, the continuous development in the techniques for deposition of thin metal films which allows for the growth of high quality metal structures with controllable crystallinity; secondly, the wider availability of electron-beam lithography in the research centres; and thirdly, the development of highly sensitive magnetic characterisation techniques which are able to operate both on shorter timescales and with greater spatial resolution. The confluence of these trends has allowed for the rapid exploration of the magnetism of small magnetic structures, with the potential for device applications in memory and sensor devices a constant motivation throughout.

In particular, developments in lithography have made it possible to fabricate well-defined nanowire structures. Such advances have allowed for the study of domain walls in confined magnetic nanostructures with lateral dimensions as small as a few tens of nanometres. In magnetic materials with weak intrinsic anisotropies such as cobalt rich CoFe-based amorphous alloys or polycrystalline permalloy nanowires (with a nominal composition around $Ni_{80}Fe_{20}$), the magnetisation is largely constrained by magnetostatic energy considerations to lie along the long axis of the wire with spins parallel to the surfaces and edges. As a consequence, the magnetisation direction in magnetically soft nanowires is defined by the geometry of the nanowire and when structural features such as notches are patterned within the nanowire, the spin structure tends to follow the magnetostatics of these features.

In planar $Ni_{81}Fe_{19}$ nanowire devices, information can be encoded in the magnetisation direction of domains with the nucleation and propagation of domain walls in nanowires allowing for the input, manipulation and readout of stored information. Such devices require a high level of control of the domain wall propagation behaviour which may be achieved through local pinning centres that can provide defined stable locations which confine domain wall propagation. As a result, the magnetic configurations of such structures can be engineered by properly shaping them which thus allowing the pinning and propagation behaviour of a single magnetic domain wall to be studied. Understanding and controlling the field driven motion of domain walls in planar nanowire structures is

important for potential applications of nanowire structures and is also a preliminary step to studying their current-driven dynamics. Quantitative correlation between the depinning field and pinning site geometry is highly relevant to both field and spin-polarised current-induced domain wall behaviour and may ultimately lead to optimising the control and efficiency of these devices.

The aim of this thesis is to develop an understanding of key quasi-static properties of domain walls in planar nanowires; namely, the structural properties, pinning behaviour and magnetoresistance behaviour of magnetic domain walls in $Ni_{81}Fe_{19}$ nanowires. The physical background required to underpin the discussion of measurements presented here is provided in chapters 2 and 3, in which an understanding of the theory of ferromagnetism (with particular focus on the $Ni_{81}Fe_{19}$ alloy) is developed. The structural properties of $Ni_{81}Fe_{19}$ thin films have been investigated using x-ray scattering techniques and have been related to the magnetic behaviour through detailed magnetoresistance measurements. Insight into the micromagnetic structure of domain walls in planar nanowire structures has been developed through a combination of magneto-optical Kerr effect magnetometry, differential phase contrast transmission electron microscopy imaging and micromagnetic simulations. Knowledge of the magnetoresistance behaviour of $Ni_{81}Fe_{19}$ thin films, combined with the detailed understanding of the micromagnetic structure within the wall has resulted in the development of a detailed model that is based on anisotropic magnetoresistance and allows for the identification of both the presence and structure of domain walls in nanowires.

1.2 Thesis outline

Chapter 2 describes the electronic contribution to the total atomic magnetic moment and reviews the different types of magnetisation response a material can have to an applied field. This chapter establishes an understanding of the relationship between atomic magnetic moments and macroscopic magnetisation behaviour of ferromagnets.

In chapter 3, the free energy terms of a ferromagnet are introduced and the concept of micromagnetics is developed. The energetic contributions that lead to the formation of ferromagnetic domains are reviewed and an understanding of the relationship between the domain wall energy and the micromagnetic structure is developed.

Chapter 4 introduces the primary investigative techniques used within this thesis to characterise the microstructural features, the magnetic properties and the

magnetoresistance behaviour of $Ni_{81}Fe_{19}$ thin films and planar nanowires. This includes sample fabrication, grazing incidence x-ray reflectivity, x-ray diffraction, magneto-optical Kerr effect magnetometry, micromagnetic modelling and anisotropic magnetoresistance measurements. The physical principles behind each technique are discussed and the relevant experimental methods used here are described.

In chapter 5, a study of the structural properties of $Ni_{81}Fe_{19}$ thin films thermally evaporated onto pre-oxidised silicon substrates is presented. Characterisation of film thickness, substrate interface width, out-of-plane texture (preferred orientation) and crystallite grain size has been achieved through a combination of x-ray reflectivity and x-ray diffraction techniques as well as high resolution transmission electron microscopy imaging.

The investigation of the magnetic and magnetoresistance behaviours of $Ni_{81}Fe_{19}$ thin films is presented in chapter 6. MOKE hysteresis loops provide information on the coercivity and (indirectly) measure the magnetisation of the film, as well as on the nature of any magnetic anisotropy present within the films. Thin film resistivity is deduced from high resolution anisotropic magnetoresistance measurements. The structural properties of the thin films studied in chapter 5 are used to develop an explanation of the observed anisotropic magnetoresistance behaviour as a function of film thickness.

A study of quasi-static pinning behaviour of magnetic domain walls in 10 nm thick planar $Ni_{81}Fe_{19}$ nanowire structures is presented in chapter 7. The pinning behaviour of a domain wall pinned at the interface between a nucleation pad and a nanowire as a function of nanowire width is initially described. Following this, the pinning behaviour of domain walls pinned at triangular and rectangular notches is examined and detailed pinning potential landscapes deduced from micromagnetic simulations are presented. Micromagnetic simulations are combined with MOKE hysteresis measurements to provide an in-depth analysis of the domain wall pinning behaviour as a function of domain wall micromagnetic spin structure. This is used to develop a thorough understanding of the pinning potential landscape experienced by a specific domain wall within a nanowire.

Chapter 8 brings together the experimental measurements of thin film magnetoresistance presented in chapter 6, with knowledge of the domain wall structure obtained in chapter 7, to develop a model used to predict values of domain wall AMR based on micromagnetic simulations. It is shown how a detailed model is necessary to correctly identify both the presence and structure of domain walls using anisotropic

magnetoresistance, in which the importance of fully characterising the magnetoresistance behaviour thin films is highlighted. The thesis concludes with a summary of the key results obtained in this investigation.

1.3 Definitions and Units

1.3.1 Magnetic field induction vector

The magnetic induction vector (or flux density vector), **B**, is defined by:

$$\mathbf{B} = \mu_0(\mathbf{H} + \mathbf{M}) \tag{1:1}$$

Where μ_0 is the permeability of free space; equal to 4π x 10^{-7} henry/m in S.I units and **M** is the volume magnetisation within the sample. The magnetic response of a material to an applied field **H** causes $\mathbf{B}/\mu_0$ to differ from **H** inside the material. The magnetic induction vector **B** is a field that includes both the external field $\mu_0\mathbf{H}$ and the material response $\mu_0\mathbf{M}$; thus, **H** is the cause and **M** is the material effect. The **B** field is be used for the magnetic field when microscopic currents contribute to the flux density; specifically for situations in which the contribution of the magnetisation is important.

1.3.2 Magnetic susceptibility and permeability

The magnetic susceptibility and permeability present different ways of describing the response of a material to an applied magnetic field. It is empirically found that the volume magnetisation is related to the applied field according to the relation:

$$\mathbf{M} = \chi\mathbf{H} \tag{1:2}$$

Where χ is the magnetic susceptibility and in *S.I.* units is a dimensionless constant of proportionality. Magnetic susceptibilities are measured from magnetisation versus applied field, (**M** vs. **H**) curves. The magnetic permeability, μ is defined by:

$$\mu = \mu_r\mu_0 \tag{1:3}$$

Where μ_r is the relative permeability, given by:

$$\mu_r = 1 + \chi \tag{1:4}$$

It is usual to state values of permeability relative to the permeability in a vacuum which is 1 in *C.G.S.* units. The magnetic induction is related to both the reversible magnetisation and small applied field by the permeability and so the magnetic induction **B** may be expressed as:

$$\mathbf{B} = \mu_0(\mathbf{H} + \mathbf{M}) = \mu_0(\mathbf{H} + \chi\mathbf{H}) = \mu_0(1 + \chi)\mathbf{H} = \mu\mathbf{H} \qquad (1:5)$$

1.3.3 Principal units used in magnetism

All equations and relations presented within this thesis will be given in *S.I.* units, however, since the literature abounds with measurements in the *C.G.S.* system, so the relations between the two unit systems are considered here. The conversion factors between these unit systems are:

$$1 \text{ oersted} = (1000/4\pi) \text{ A/m} \approx 79.58 \text{ A/m}$$

$$1 \text{ gauss} = 10^{-4} \text{ tesla}$$

$$1 \text{ emu/cm}^3 = 1000 \text{ A/m}$$

$$1 \text{ emu} = 10^{-3} \text{ Am}^2$$

It follows that the *C.G.S* unit system offers a more sensible basis for presenting data on magnetic phenomena in chapters 5 to 8 inclusive; thus although equations and relations will be given in *S.I.* units, magnetic properties presented in chapters 5 to 8 will be stated in Oe. Units of key properties in both systems of measurements are presented in Table 1:1.

Quantity	Symbol	*S.I.*	*C.G.S.*
Field	H	A/m	oersteds
Magnetisation	M	A/m	emu/cm^3
Induction	B	tesla	gauss
Moment	μ_m	Am^2	emu
Pole strength	p	Am	emu/cm
Field equation	-	$B = \mu_0 (H + M)$	$B = H + 4\pi M$
Energy of moment	E_{mag}	$- \mu_0 \mu_m H$	$- \mu_m . H$
Torque on moment	τ	$\mu_0 \mu_m$ x H	μ_m x H

Table 1:1. Principal *S.I.* and *C. G. S.* units currently used in magnetism and within this thesis. Conversion factors between the two systems of measurements are stated within the text.

Chapter 2. Background and theory of ferromagnetism

2.1 Introduction

This chapter describes the relationship between atomic magnetic moments and the macroscopic magnetisation behaviour of materials and provides the physical background required to understand the discussion presented in subsequent chapters. To begin, the electronic contributions to the total atomic magnetic moment are described and the different types of magnetisation response a material can have to an applied field are presented. A discussion of paramagnetic behaviour is provided as a foundation for developing an understanding of ferromagnetic phenomena. An understanding of ferromagnetism is gained through a discussion of the exchange interaction which includes a description of the Curie-Weiss model, the Heisenberg theory and the Stoner band theory.

2.2 Atomic magnetic moments

Atomic theory has shown that the magnetic dipole moments observed in bulk matter arise from the angular momentum associated with the motion of electrons as shown in Figure 2:1. Whilst the nucleus also has a magnetic moment it is approximately three orders of magnitude smaller than the electronic contribution and can thus be neglected when considering the total atomic magnetic moment [1]. This section discusses the origin of both the orbital and spin magnetic moments associated with an electron, and describes how they combine to form the total magnetic moment of an atom. An understanding of atomic magnetic moments is crucial to understanding the different types of macroscopic magnetisation properties that are described in section 2.3.

The orbital motion of the electron about the nucleus is considered to be equivalent to an electric current flowing in a closed circular loop of wire with zero resistance. An electron with charge $-e$ and mass m_e orbiting about a nucleus with velocity v in a circular Bohr orbital of radius r gives rise to an equivalent magnetic moment, $\boldsymbol{\mu}_m^{orbital}$, which is orientated perpendicular to the plane of the orbit, as shown in Figure 2:1 (a). There is an orbital angular momentum, **L**, associated with this magnetic moment which points in the opposite direction to the orbital magnetic moment.

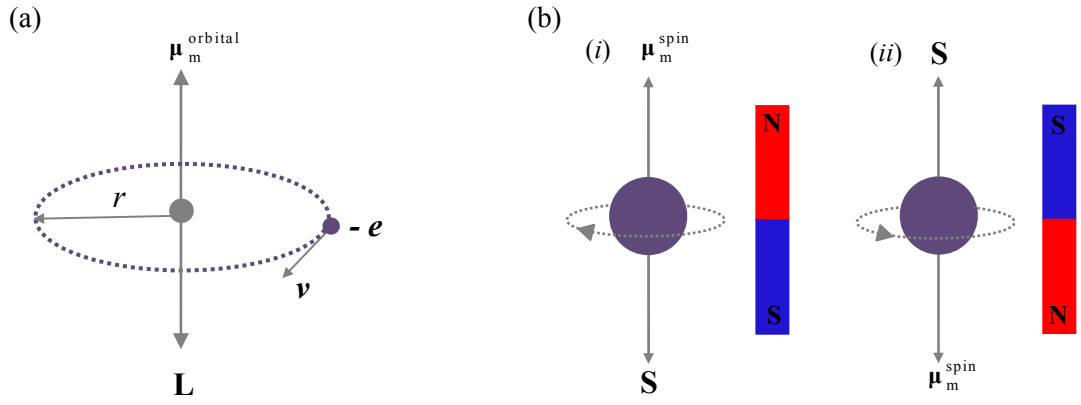

Figure 2:1. Schematic of the two kinds of magnetic moments associated with an electron in an atom: (a) orbital motion about the nucleus gives rise to an orbital magnetic moment with associated angular momentum, **L** (b) spin of the electron about its own axis resulting in a spin magnetic moment with associated angular momentum, **S**. The spin of the electron is limited to two directions only (*i*) clockwise and (*ii*) counter-clockwise allowing the electron can be visualised as a bar magnet.

The spin magnetic moment, $\boldsymbol{\mu}_m^{spin}$, is associated with the phenomenological rotation of the electron about its own axis. The concept of electron spin was proposed by Uhlenbeck and Goudsmit [2, 3 and 4] following the anomalous Zeeman effect which was famously observed by Stern and Gerlach in 1922 [5]. Although spin is a fundamental property of all electrons in all states of matter at all temperatures, it is a purely quantum mechanical concept with no classical analogy. As such, the directions about which the electron can spin are discretised which means that the electron can spin in one of two ways only, as shown in Figure 2:1 (b). As a result the corresponding magnetic moment can only orientate in one of two ways also, known as 'spin-up' and 'spin-down', accordingly. A classical understanding of electron spin can be achieved by considering the electron as a solid sphere. If it is assumed that the electronic charge lies along the surface of this sphere, then, by analogy to the orbital motion, rotation of the charge produces many tiny current loops, each of which has a magnetic moment directed along the rotation axis and which all sum together to yield the spin magnetic moment. There is a spin angular momentum, **S**, associated with this magnetic moment which points in the opposite direction to $\boldsymbol{\mu}_m^{spin}$.

The total magnetic moment of the electrons in an atom, $\boldsymbol{\mu}_m$, is given by the vector sum of the orbital and spins components and is expressed as:

$$\boldsymbol{\mu}_{\mathrm{m}} = -\frac{g\mu_{\mathrm{B}}}{\hbar}\mathbf{J} \tag{2:1}$$

Where **J** is the total angular momentum of the atom, given by Hund's rules [6], g is the dimensionless Landé g factor and μ_B is the Bohr magneton. The Bohr magneton corresponds to the magnitude of the magnetic dipole moment of an orbiting electron in the ground state and is defined in *S.I.* units as:

$$\mu_{\mathrm{B}} = \frac{e\hbar}{2m_{\mathrm{e}}} \tag{2:2}$$

Where e is the electronic charge of the electron, $\hbar$ is the reduced Planck constant and m_e is the electron mass. The Landé g factor relates angular momentum to the magnetic moment and for a free atom depends upon the relative proportions of the spin, **S**, and orbital, **L,** angular momenta via the relation:

$$g = 1 + \frac{\mathbf{J}(\mathbf{J}+1) + \mathbf{S}(\mathbf{S}+1) - \mathbf{L}(\mathbf{L}+1)}{2\mathbf{J}(\mathbf{J}+1)} \tag{2:3}$$

In general, the Landé g factor lies somewhere between 1 and 2 [7], and may be measured from either gyromagnetic or magnetic resonance experiments. For orbital motion alone, g is equal to 1 whilst for spin only g is equal to 2 [1]. The gyromagnetic ratio, γ, is the ratio of angular momentum to magnetic moment, and is given by:

$$\gamma = \frac{-eg}{2m_{\mathrm{e}}} = \frac{-g\mu_{\mathrm{B}}}{\hbar} \tag{2:4}$$

The gyromagnetic ratio describes the frequency of the orbital motion of the electron, and is equal to 1.76×10^{11} s^{-1} T^{-1} [8].

2.3 The magnetisation behaviour of materials

The presence of circulating currents that produce atomic magnetic dipole moments modifies the magnetic field produced by currents. All magnetic effects of matter can be understood on the basis of atomic magnetic dipoles. Materials may be classified as either dia-, para-, ferro- or antiferromagnetic according to the magnetisation response to an applied magnetic field. Both dia- and paramagnetic materials may be classed as weak magnetic materials and are typically described using their respective magnetic susceptibilities. Magnetically ordered materials (including ferro-, antiferro- and

ferrimagnetic materials) are characterised by the long range ordering of magnetic moments in the absence of an applied field. This section reviews the main types of magnetisation response in materials. For each classification, the magnetisation behaviour in an applied field is discussed, with examples of materials are provided and an explanation in terms of atomic magnetic moments is provided.

2.3.1 Diamagnetism

Figure 2:2 presents typical magnetisation and susceptibility curves of a diamagnetic material. Diamagnetic materials exhibit a negative magnetisation response to an applied magnetic field. This is characterised by a small, linear negative magnetic susceptibility, $\chi_{diamagnetic}$, of the order -10^{-6} [9] and a permeability $\mu_{diamagnetic}$ that is slightly less than one relative to the permeability of a vacuum. The diamagnetic response persists for as long as the field is applied and, in general, the diamagnetic susceptibility is largely temperature invariant. Examples of diamagnetic materials include bismuth, silver, carbon, the noble gases and almost all organic compounds. A type I superconducting material (and type II below the lower critical field H_{C1}) such as lead is considered to be a perfect diamagnetic material since it excludes all flux from its interior. Diamagnetism occurs in atoms and molecules with partially and completely filled orbitals and is unlike the types of magnetic response considered later in this section in that it does not result from the alignment of a pre-existing atomic moment [9].

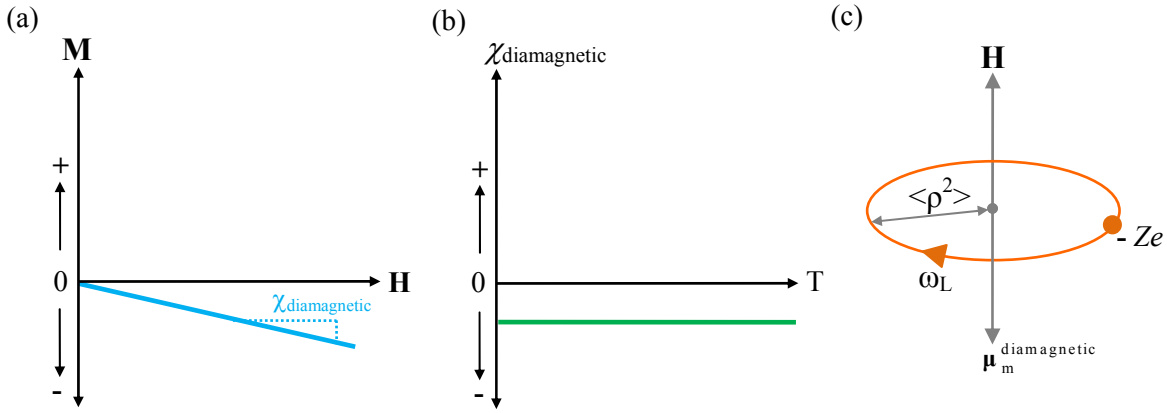

Figure 2:2. (a) Magnetisation curve of a typical diamagnetic material at room temperature (b) diamagnetic susceptibility as a function of applied temperature and (c) simplified schematic of the induced orbital motion with Larmor frequency ω_L. The Larmor precession gives rise to a diamagnetic magnetic moment and that opposes the applied field as shown in (c), where $<\rho^2>$ is the mean square of the perpendicular distance of the electron from the field axis through the nucleus.

All substances exhibit a diamagnetic response to an applied field, although the induced magnetic moment is often masked by the existence of a larger permanent magnetic dipole moment.

The theory of diamagnetism was developed by Langevin in 1905 [10]. Diamagnetism is essentially Lenz's law and can be understood as the tendency of electrical charges to partially shield the interior of a body (the nucleus) from an applied magnetic field. In the absence of an applied field, the average current around the nucleus is zero since the orbital and spin magnetic moments tend to orientate in such a way so as to cancel one another out. The application of a magnetic field causes a Larmor precession of the electrons; the Larmor precession of Z electrons is equivalent to an electric current around the nucleus. This is established in such a direction so as to produce a diamagnetic moment that opposes the change in applied field. The magnitude of the angular frequency of the Larmor precession in an applied field **B** is given by the Larmor frequency, ω_{L}, which is expressed as:

$$\omega_{\mathrm{L}} = \frac{g\mu_{\mathrm{B}}}{\hbar}\mathbf{B} \tag{2:5}$$

For a spherical and symmetrical distribution of electrons, the Langevin diamagnetic susceptibility per unit volume is given by:

$$\chi_{\mathrm{diamagnetic}} = -\frac{\mu_0 NZe^2}{6m_{\mathrm{e}}} r^2 \tag{2:6}$$

Where N is the number of atoms per unit volume, Z is the number of electrons, and r is the average of the orbital radii and is given by $\left\langle r^2 \right\rangle = \frac{3}{2}\left\langle \rho^2 \right\rangle$ where $\left\langle \rho^2 \right\rangle$ is the mean square of the perpendicular distance of the electron from the field axis through the nucleus. A quantum mechanical approach yields the same result [1] although it is not discussed here.

2.3.2 Paramagnetism

Figure 2:3 presents typical susceptibility and magnetisation curves of a paramagnetic material. The application of a small applied field induces a positive magnetisation in a paramagnetic material. When the applied field becomes sufficiently large, the paramagnetic magnetisation tails off toward saturation, the value of which is intrinsic to the specific material.

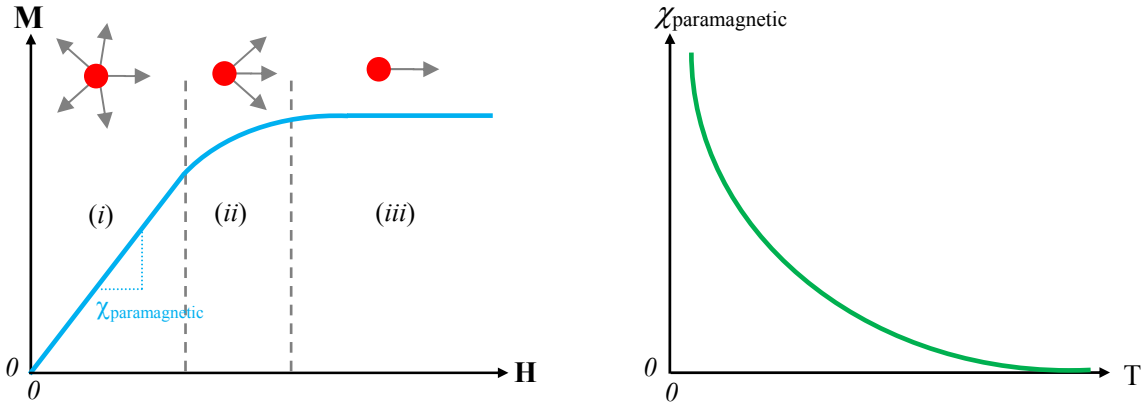

Figure 2:3. (left) Typical magnetisation curve of a paramagnetic material at room temperature indicating the corresponding alignment of the magnetic moments at (*i*) low applied field, (*ii*) approaching saturation and (*iii*) at high applied fields and (right) paramagnetic susceptibility as a function of temperature.

The paramagnetic susceptibility varies with the absolute temperature according to the Curie relation:

$$\chi_{\text{paramagnetic}} = \frac{C}{T} \tag{2:7}$$

Where C is the Curie constant, which is described by:

$$C = \frac{N\mu_0 \mu_B^2 g_j^2 J(J+1)}{3k_B} \tag{2:8}$$

Where N is the number of atoms per unit volume, J is the total angular momentum of the atom in its ground state and k_B is the Boltzmann constant. Many of the transition metal ions such as manganese form paramagnetic materials, as well as transition metal salts such as $CuSO_4$ and $NiSO_4$ [7, 9].

The first systematic measurements of the susceptibility of paramagnetic substances over a substantial temperature range were made by Curie in 1895. Paramagnetism is the alignment of pre-existing atomic magnetic moments which are the result of unfilled electronic orbitals. At room temperature, however, in the absence of an applied field paramagnetic materials exhibit no net magnetic moment since thermal energy results in randomisation of isolated atomic moments yielding a net zero magnetisation. For a given temperature, the application of a small applied field tends to align the dipole moments parallel to the field, as shown in Figure 2:3 (*i*), which results in a magnetisation that adds to the applied field, such that paramagnetic materials exhibit a positive susceptibility. As the applied field is increased, as shown in Figure 2:3 (*ii*), the number of magnetic moments

aligned approaches a saturation value in which all the magnetic moments are aligned parallel to the applied field, and is illustrated in Figure 2:3 (*iii*). The saturation value is intrinsic to the material and is determined by the number of unpaired magnetic dipole moments in atom or ion. An increase in temperature increases the randomising effect of thermal agitation, which works against the aligning effect of the applied magnetic field and subsequently decreases $\chi_{\text{paramagnetic}}$.

All free atoms with unfilled orbitals will display paramagnetic behaviour on the application of an applied magnetic field. Indeed, there is no difference between *free* paramagnetic and ferromagnetic atoms; it is only when atoms bond to form solids that it is possible to observe paramagnetic and ferromagnetic behaviour. In paramagnetic materials there are no strong magnetic interactions between the magnetic dipoles of adjacent atoms atoms/ions as the constituent atoms/ions are isolated. As a result, the spatial orientation of the magnetic dipole moments in paramagnetic atoms can be changed without changing the electronic configuration of the constituent atom. Spatial overlap of adjacent wavefunctions causes magnetic dipole moments on neighbouring atoms to interact due the quantum mechanical exchange interaction [6], and is responsible for strongly ordered magnetic systems such as ferromagnetism. The origin and nature of the exchange interaction is discussed in detail in section 2.4.

2.3.3 Ferromagnetism

Ferromagnetic materials can possess a large *spontaneous* magnetisation in the absence of an applied field, as shown in Figure 2:4. The spontaneous magnetisation is a maximum at $T = 0$ K and drops to zero at the Curie temperature, T_c. Above T_c ferromagnetic materials exhibit a paramagnetic response to an applied field where the susceptibility is described by the Curie-Weiss law:

$$\chi_{\text{ferromagnetic}}^{T>T_c} = \frac{C}{T - \theta_w} \tag{2:9}$$

Where C is the Curie constant, θ_w is the Curie-Weiss constant and T is the temperature. The magnetisation response of a ferromagnetic material to an applied field for temperatures below the Curie temperature is shown in Figure 2:5.

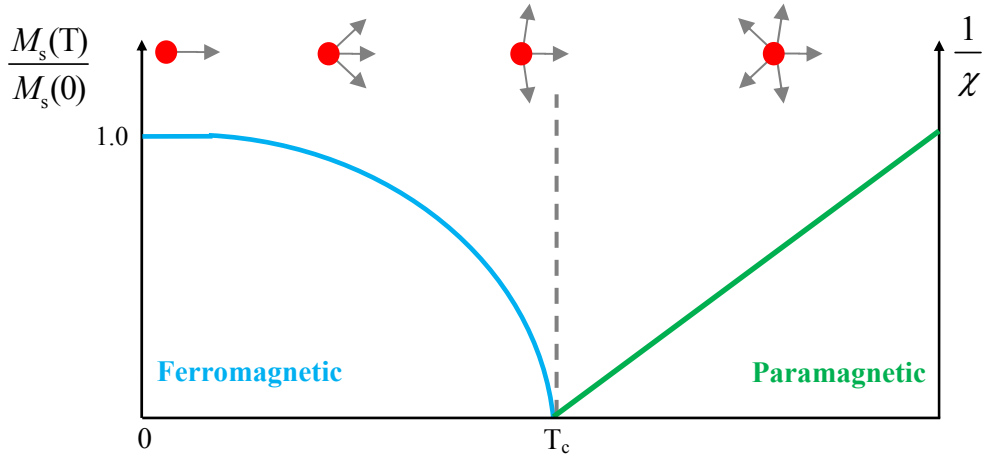

Figure 2:4. Magnetisation and susceptibility curves of a single ferromagnetic domain below and above the Curie temperature. The sketches indicate the distribution of spin direction within a single domain below and above the Curie temperature.

Ferromagnetic materials exhibit a non-linear response to an applied field, with the sample remaining magnetised on the removal of the applied magnetic field. The magnetic induction curve is also included in Figure 2:5 since ferromagnetic materials are useful in electromagnetic devices where the rate of change of induction is important in yielding a voltage [9].

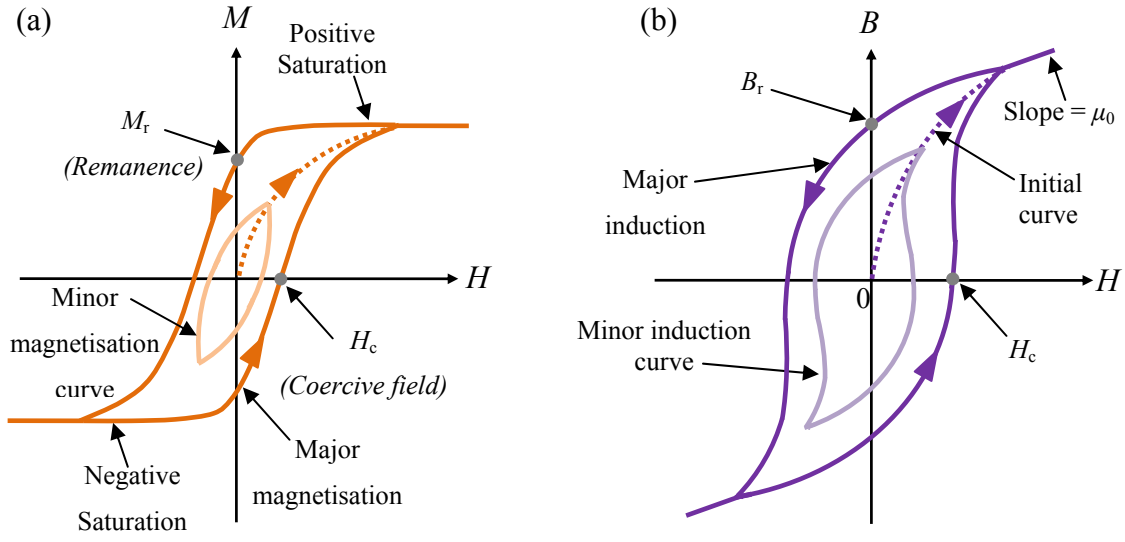

Figure 2:5. Schematic of a typical ferromagnetic response to an applied field; (a) example ferromagnetic magnetisation curve and (b) an induction curve. Each schematic also indicates the initial curve from the demagnetised state to positive saturation. The induction curve is larger than the magnetisation curve since it represents total magnetic induction i.e. $\mathbf{B} = \mu_0(\mathbf{M}+\mathbf{H})$.

Consequently, ferromagnetic permeability is often used in applications to describe the response of ferromagnetic materials. The relation between susceptibility and permeability was described in section 1.4.

The shape of the hysteresis loop presented in Figure 2:5 (a) is understood as follows. If it is assumed that the ferromagnetic material is initially in a demagnetised state, when a magnetic field is applied the magnetisation increases along the dotted line until the magnetisation increases no more and magnetisation saturation is achieved. By reducing the applied field to zero, increasing it in the reverse direction and finally decreasing it to zero once more, the magnetisation follows the solid line, tracing out a magnetic hysteresis loop which is symmetric about the origin and reproducible on successive field cycles. The coercivity, denoted by H_c, corresponds to the field required to reduce the magnetisation to zero from saturation. The remanence, denoted by M_r (B_r for induction), corresponds to the value of magnetisation retained by the material in the absence of an applied field. Materials with a low coercivity are termed magnetically soft materials; an example of which is $Ni_{81}Fe_{19}$ which is used in this study. Converesly, materials with a high coercivity are termed hard materials. Both the susceptibility and the permeability of ferromagnetic materials are large and positive, and are typically several of orders magnitude larger than paramagnetic materials.

There are very few ferromagnetic elements at room temperature; these include the 3*d* transition metals iron, cobalt and nickel as well as the rare earth gadolinium. Ferromagnetism may also be observed in the binary and ternary alloys of the ferromagnetic elements with other elements and in alloys which do not contain any ferromagnetic elements [7, 11]. Indeed, the onset of ferromagnetic behaviour is sensitive to the interatomic spacing of atoms: the formation of alloy systems can change the interatomic spacing and may lead to ferromagnetic behaviour. This is discussed further in section 2.4.

In ferromagnetic materials, like paramagnetic materials, the atoms have pre-existing atomic magnetic moments that are the result of unfilled electronic orbitals. However, in addition, there is a strong coupling between the unpaired atomic dipole moments known as the exchange interaction. This means that a *spontaneous* magnetic moment exists within the material in the absence of an applied field. A solid knowledge of the exchange interaction is required for a thorough understanding of the nature of domain

wall structure, propagation and pinning behaviour in nanowire structures presented in chapter 7, and is described in section 2.4.

At temperatures below the Curie temperature ferromagnetic materials can be composed of small regions called domains, within each of which the magnetisation is saturated to the spontaneous value. In a demagnetised sample, the directions of the domains are orientated to yield approximately zero resultant moment. An understanding of the energies leading to the formation of ferromagnetic domains and domain walls is developed in chapter 3.

2.3.4 Antiferromagnetism

Antiferromagnetic materials exhibit small positive susceptibilities at all temperatures as shown in Figure 2:6. The antiferromagnetic susceptibility is described by the Curie-Weiss law:

$$\chi_{\text{antiferromagnetic}}^{T>T_N} = \frac{C}{T-\theta_w} \tag{2:10}$$

Where the Curie-Weiss constant, θ_w, is negative. Antiferromagnetic materials display a paramagnetic response above the Néel temperature, T_N. The only antiferromagnetic elements are chromium and α-manganese, and examples of other antiferromagnetic substances tend to include ionic compounds such as MnO_2 and α-Fe_2O_3 [7, 9]. The theory of antiferromagnetism was chiefly developed by Néel in a series of papers beginning in 1932 [12].

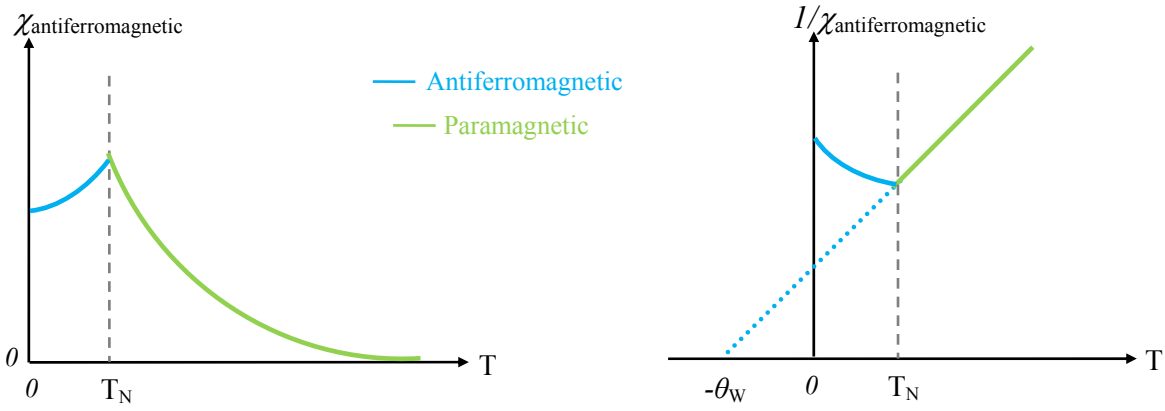

Figure 2:6. (*left*) Variation of antiferromagnetic susceptibility and (*right*) inverse susceptibility with temperature. Above the Néel temperature antiferromagnetic materials display a paramagnetic response.

In antiferromagnetic materials, the neighbouring magnetic moments point in opposite directions to yield an overall net magnetisation of zero in the absence of an applied field. Antiferromagnetism is usually related to the crystal structure of the material, and an antiferromagnetic crystal can be regarded as comprising of two interpenetrating sub-lattices on which the spins in each point in opposite directions.

2.3.5 Ferrimagnetism

Ferrimagnetic materials exhibit a substantial spontaneous magnetisation at room temperature and exhibit magnetic hysteresis behaviour similar to that observed for ferromagnetic materials. Above the Curie temperature, T_c, the spontaneous magnetisation within ferrimagnetic materials disappears and a paramagnetic response to an applied field is observed. Ferrimagnetism is exhibited in magnetite, Fe_3O_4, and magnetic iron garnets [11] and is particularly sensitive to the crystal structure. In ferrimagnetic materials, the magnetic moments of the different atoms are on different sub-lattice structures with an antiparallel arrangement [11]. However, the opposing moments are unequal and a spontaneous magnetisation remains. The spin alignment of ferrimagnetic materials is shown in Figure 2:7, in the nature of spin magnetic dipole moments alignment present in para-, ferro-, antiferro- and ferrimagnetic materials are compared.

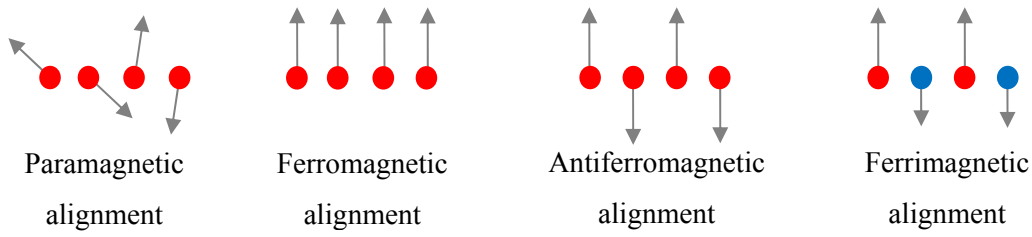

Figure 2:7. Schematic to show the spin alignment present in para-, ferro-, antiferro- and ferrimagnetic materials.

2.4 The exchange interaction in ferromagnetic materials

2.4.1 Introduction

Ferro-, antiferro- and ferrimagnetic phenomena differ from that of paramagnetic behaviour by the nature of the exchange interaction experienced by unpaired spin magnetic moments on neighbouring atoms. The exchange interaction governs the alignment of unpaired

electron spins both *within* an individual atom and *between neighbouring* atoms; and as such there is an energy associated with the alignment of spin magnetic moments. In an unfilled electron orbital, electron spins tend to align parallel so as to reduce the exchange energy within the atom, as dictated by the restrictions of the Pauli exclusion principle. In ferromagnetic materials, the exchange energy is also minimised when the spins on neighbouring atoms are aligned parallel.

In this section, an understanding of the origin of the exchange interaction in ferromagnetic materials is gained by discussing two models: the local moment theory developed by Heisenberg [13], and the band theory developed by Slater [14, 15, and 16] and Stoner [17, 18, and 19]. In the local moment theory, the electrons responsible for ferromagnetism are considered to be localised at each atom. Each atom has a finite magnetic moment that depends upon the number of electrons occupying incomplete electron orbitals in the ground state. In contrast, within the band theory model the electrons responsible for ferromagnetism are considered to be delocalised and thus belong to the crystal as a whole. There are also several band theories, for example the Friedel model [20], which is intermediate between the localised and band models although the discussion presented here is limited to the Stoner model only. The problem of treating transition metals in terms of the electronic structure is difficult since the 3*d* electrons in ferromagnetic metals are neither free electron-like or atom-like. Instead, it is the blend of these seemingly conflicting approaches that give the present understanding of ferromagnetic behaviour.

The exchange interaction and associated energy make a significant contribution to the behaviour of magnetic domain walls in soft nanowire structures (discussed in detail in section 3.5). Detailed knowledge of the exchange interaction is essential in the design of nanowire structures in which the ability to control the propagation behaviour of domain walls is critical for device applications. Such processes form the basis of the investigations presented in chapter 7.

2.4.2 Quenching of the orbital magnetic moment

In the ferromagnetic transition elements, the 3*d* electrons responsible for the magnetic moment are very strongly influenced by the crystal field that is created by the neighbouring atoms in the crystal. The presence of the crystal field effectively quenches the orbital angular momentum such that is reduced to zero [1]. Although the orbital

momentum is quenched as a result of the crystal lattice field, the spin-orbit interaction means that when the spin orientation is changed it may drag some orbital moment with it. Spin-orbit coupling results from the interaction of the electron spin with the magnetic field that the electron 'sees' as it moves about the nucleus. This interaction couples the magnetic moment of the electron with its motion. In non-magnetic materials, the spin-orbit interaction is not as strong as there are approximately an equal number of spin-up and spin-down electrons and so the effect cancels out. In ferromagnetic materials, however, the spin-orbit interaction is important because of the unbalanced populations of electron spins.

If the exchange interaction favours parallel orientation of the spin and orbital magnetic moments, then the total magnetic moment will be larger than for just spin along and so g will be greater than 2. Experimental values of the Landé g factor for the 3d ferromagnetic elements and permalloy ($Ni_{78}Fe_{22}$) are given in Table 2:1.

Material	g^*	$g^\dagger$
Iron	2.12 - 2.17	2.08
Cobalt	2.22	2.18
Nickel	2.2	2.09 - 2.19
$Ni_{78}Fe_{22}$	2.07 - 2.14	2.10

** measured from magnetic resonance experiments*

† calculated using values obtained from gyromagnetic experiments

Table 2:1. Values of the g factor for the 3d ferromagnetic elements (reproduced from data in [21]).

2.4.3 The Weiss theory

It is helpful to begin a discussion of the exchange interaction with a description of the molecular field theory introduced in 1906 by Weiss [22, 23]. The Weiss theory was the first attempt to develop an explanation for the existence of the spontaneous magnetisation. Although this theory is useful in terms of gaining an insight into the nature of the spontaneous magnetisation, the approach is incorrect and a proper treatment requires a quantum mechanical approach.

In the Weiss theory, unpaired atomic dipole spin moments align parallel in a ferromagnetic material due to the molecular field, $H_{\text{molecular}}$. The molecular field was thought to be an internal field that was strong enough to magnetise a substance to saturation in the absence of an applied field at temperatures below T_c. The orientating effect of this field was opposed by the thermal agitation associated with temperature. At the Curie temperature, T_c, the thermal energy is sufficient to destroy the spontaneous alignment of the magnetisation. An estimate of the magnitude of the molecular field can be obtained by equating the thermal energy to the energy of a magnetic dipole in an applied field. For atoms with a dipole moment of one Bohr magneton:

$$k_B T_c = \mu_B H_{\text{molecular}} \tag{2:11}$$

Where k_B is the Boltzmann constant, T_c is the Curie temperature, μ_B is the Bohr magneton and $H_{molecular}$ is the molecular field. Inserting a value of the order of $T_c = 1000$ K (a representative value for iron) for into this equation yields an internal molecular field of the order of 10^7 Oe, which is much larger than the magnetic fields that can be easily produced in the laboratory. Furthermore, it is significantly larger than that produced by the dipole-dipole interaction which would yield a molecular field of approximately 10^3 Oe. It was thus concluded that the spontaneous magnetisation could not be the result of dipole-dipole interactions, although the Weiss theory made no attempt to explain the origin of the molecular field.

To explain the existence of the demagnetised state, Weiss further postulated the existence of small regions now known as domains. It was proposed that the magnetisation was saturated within each domain and it was suggested that in order to obtain the demagnetised state the directions of the domains were randomly orientated to yield a net magnetisation of zero. The existence of domains was justified by Landau and Lifshitz in 1935 [24] and led to the development of micromagnetics which is reviewed in chapter 3.

2.4.4 The Heisenberg theory

In 1928, Heisenberg [13] proved that the quantum-mechanical exchange interaction plays a decisive role in ferromagnetism. Heisenberg demonstrated that under certain conditions the parallel alignment of spins on neighbouring atoms would have a lower energy that those with anti-parallel alignment, which would have similar effects to that of the Weiss molecular field. The exchange interaction cannot be introduced from any classical theories

and as such has no classical analogies. Only the main features of the theory are presented here; an in-depth analysis of the exchange interaction is given in references [9, 25 and 26]. Knowledge of the exchange interaction is developed in this section by the combination of a qualitative description, from which both semi-quantitative and quantitative understandings are developed.

Qualitative description of the exchange interaction

Consider two electrons in a hydrogen molecule: electron 1 moves about proton 1 and electron 2 about proton 2. There is an attractive force between electron 1 and proton 1 and likewise for electron 2 and proton 2. There is also a repulsive force between both electrons and both protons which is electrostatic in origin and can be understood classically by Coulomb's Law. It is because of this electron-electron repulsion that the electrons prefer to stay further apart. Quantum mechanics, however, demands that electrons are indistinguishable, hence the interaction of electron 1 with proton 2 and vice versa - the *exchange* of labels - must also be considered. This exchange of labels introduces an additional interaction, the exchange interaction. The strength of exchange interaction is determine by the relative orientation of the spins of the two respective electrons within the rules of the Pauli exclusion principle whilst the exchange energy is the difference in energy between parallel and antiparallel spin states, as shown in Figure 2:8.

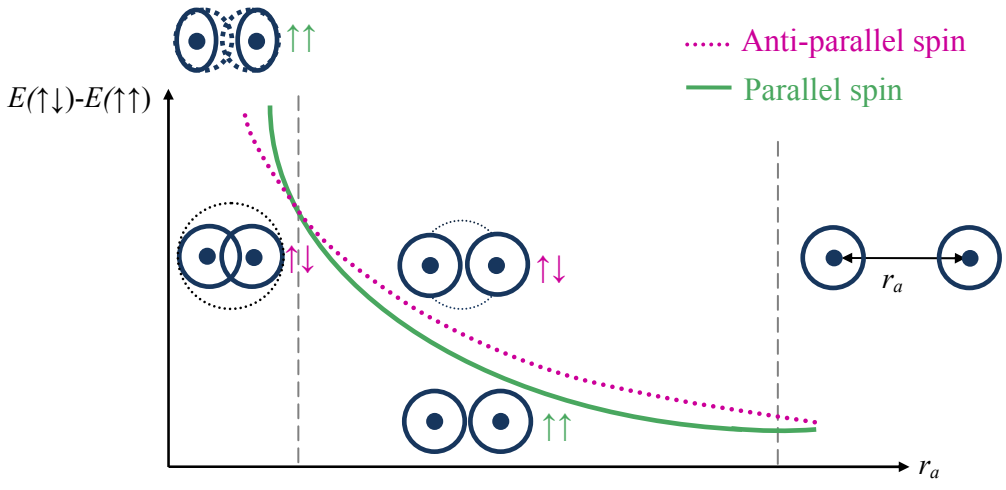

Figure 2:8. Schematic of the exchange energy for parallel (↑↑) and anti-parallel spin (↑↓) alignment as a function of interatomic separation, r_a. The relative spin orientation is determined by the nature of the spatial overlap of the orbitals, as illustrated in the corresponding sketches. As the overlap of the orbitals increases, the spins are forced to occupy the same spatial co-ordinates and thus the spins are forced to align anti-parallel in accordance with the Pauli exclusion principle. (After Figure 5.3 [9]).

Parallel alignment of spins is favoured in materials when electrons share the same wavefunction but are confined to separate regions of space, which is often referred to as anti-bonding. When the spacing between adjacent atoms decreases further the electron wavefunctions are forced to overlap spatially. As the Pauli exclusion principle forbids two electrons occupying the same spatial co-ordinates from sharing the same spin orientation, the spins are forced to align antiparallel and accept the higher cost of exchange energy.

As electrostatic interactions become negligible at large separations, the corresponding difference in energy between parallel and antiparallel spin arrangement becomes negligible as the exchange interaction between neighbouring atoms vanishes. Thus, although exchange is a purely quantum-mechanical interaction, it is essentially electrostatic in origin since the ordinary Coulomb interaction becomes fundamentally modified by the relative spin orientations.

Semi-quantitative description of the exchange interaction

The appearance of ferromagnetism may also be reasoned using the Bethe-Slater curve which is presented in Figure 2:9 and correctly separates the ferromagnetic elements iron, cobalt and nickel from antiferromagnetic manganese. Figure 2:9 shows the postulated variation of the difference in the exchange integral as a function of the ratio r_a/r_{3d} where r_a is the radius of an atom and r_{3d} is the radius of the 3*d* orbital. The exchange integral is the difference between the energy associated with antiparallel and parallel spin alignment, and is given by:

$$J_{\text{exchange}} = E_{\uparrow\downarrow} - E_{\uparrow\uparrow} \qquad (2:12)$$

Where $E_{\uparrow\downarrow}$ and $E_{\uparrow\uparrow}$ are the energies associated with antiparallel and parallel alignment of neighbouring spins.

The diameter of the atom is given by $2r_a$, which is also the centre to centre separation of two atom centres since the atoms within a solid are in close contact with one another. If two atoms of the same kind are brought increasingly closer together without any change in the radius of the 3*d* sub-shells the ratio r_a/r_{3d} will decrease from large to small values. Accordingly, the best conditions for a positive value of the exchange interaction is for the interatomic spacing to be large compared to the radii of the orbitals. The value of J_{exchange} for $Ni_{81}Fe_{19}$ is also shown in Figure 2:9 in order to illustrate its behaviour relative to the transition metal elements.

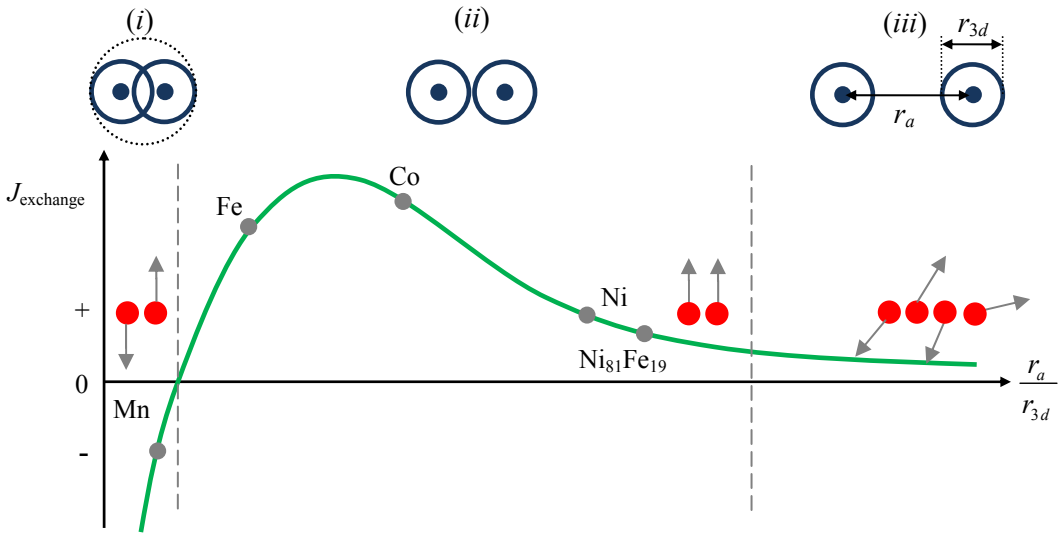

Figure 2:9. Schematic of the Bethe-Slater curve, illustrating the importance of the ratio of interatomic separation, r_a, to the radius of the 3*d* band, r_{3d}, on the sign and magnitude of the exchange interaction and sketches to illustrate to spatial overlap of the electronic wavefunctions. Antiferromagnetism, (*i*), is the result of a negative exchange interaction since due to considerable overlap of the orbitals, whilst in ferromagnetism (*ii*) there is a positive exchange and adjacent spins align parallel. In paramagnetism (*iii*) the atoms are spatially isolated and the magnetic moments have random orientation.

Figure 2:9 also explains why compounds of non-ferromagnetic material may become ferromagnetic. Indeed, whilst manganese and chromium are not ferromagnetic, some of their compounds are; for example MnAs and MnSb are both ferromagnetic with a lattice spacing of 2.85 Å and 2.89 Å respectively compared to the lattice spacing of pure manganese which is 2.58 Å [7]. Thus, small changes in the interatomic spacing may result in favourable conditions for a positive exchange interaction. Further decrease in the interatomic spacing, however, brings the 3*d* electrons close enough so that their spins are forced to become antiparallel. As a result antiferromagnetism ensues.

Quantitative description of the exchange interaction

A quantitative expression for exchange energy can be obtained by the following analysis. If two atoms *i* and *j* have spin angular momentum $\mathbf{S}_i$ and $\mathbf{S}_j$, where $\mathbf{S}_i = \sum \mathbf{s}_i$ and $\mathbf{S}_j = \sum \mathbf{s}_j$ are the total spin angular momentum of atoms *i* and *j* respectively, then the exchange energy experienced between them is given by the van Vleck formula [27]:

$$E_{\text{exchange}} = -2J_{\text{exchange}}\mathbf{S}_i \cdot \mathbf{S}_j = -2J_{\text{exchange}}S^2 \sum_{i>j} \cos\phi_{i,j} = -2J_{\text{exchange}}S_i S_j \cos\phi \qquad (2:13)$$

Where J_{exchange} is the exchange integral and ϕ is the angle between adjacent spins. For ferromagnetic materials, the exchange integral is positive and so the exchange energy is negative when the spins are parallel and positive when they are antiparallel. As the exchange interaction decreases rapidly with distance, this allows the summation to be restricted to nearest-neighbour pairs [11]. Furthermore, by assuming the angle between adjacent atoms to be small then the above expression may be reduced yet further to give an expression for the change in exchange energy associated with a change in angle between nearest neighbour spins. This is written as:

$$\Delta E_{\text{exchange}} = J_{\text{exchange}} S^2 \left(\Delta\phi\right)^2 \tag{2:14}$$

Where $\Delta\phi$ is the change in angle between neighbouring spins. This simplification is valid provided that all electrons have the same exchange integral J_{exchange}, and that the exchange energy between electrons of the same atom is constant and hence may be omitted from the summation. The first assumption is reasonable if the orbital angular momentum is quenched whereas the second is valid if spin angular momentum is not quenched. The exchange stiffness parameter, A, is defined as:

$$A = \frac{J_{\text{exchange}} S^2}{a} \tag{2:15}$$

Where a is the lattice parameter. The exchange stiffness parameter is a measure of the energy penalty incurred when nearest neighbour spins are not completely parallel. For iron, cobalt and nickel this is measured as 20.7×10^{-11} J/m, 30.2×10^{-11} J/m and 0.6×10^{-11} J/m, respectively, whilst for $Ni_{81}Fe_{19}$, it is measured as 1.3×10^{-11} J/m [28]. Equation (2:15) implies that exchange forces depend mainly on interatomic distances and not on any geometrical regularity of atom position; indeed crystallinity is *not* a requirement for ferromagnetism. The first reports of an amorphous ferromagnetic material was reported by Mader *et al.* in 1965 [29] for Co-Au alloys.

2.4.5 Band theory

The preceding discussions of the exchange interaction have been based upon the assumption that the 3*d* electrons are localised at the individual atoms. However, since the ferromagnetic transition elements are metallic this assumption is obviously not entirely valid. Band theory is a broad theory of the electronic structure of solids; when it is

specifically applied to magnetic problems it is often referred to as the collective-electron theory. The first applications of collective-electron theory were made in 1933-1936 by Slater [14, 15, and 16] and Stoner [17, 18, and 19] in an attempt to explain why the effective number of Bohr magnetons for the ferromagnetic transition elements are non-integer values. The effective number of Bohr magnetons, n_{eff}, provides information on the number of unpaired spins per atom and is deduced via:

$$n_{\text{eff}} = \frac{M_{\text{s}}(0)}{n\mu_{\text{B}}} \tag{2:16}$$

Where $M_{\text{s}}(0)$ is the saturation magnetisation at $T = 0$ K, n is the number of atoms per unit volume and μ_{B} is the Bohr magneton. For iron, cobalt and nickel the values of n_{eff} are 2.22, 1.72 and 0.60 Bohr magnetons per atom, respectively. These values quantify the number of electrons contributing to the magnetic moment of the solid atom. For nickel there are a total of 10 valence electrons, and so a value of 0.60 μ_{B} suggests that there are 9.40 electrons in the 3*d* band and 0.60 in the 4*s* band. In this section, an explanation for these significant experimental observations is developed.

Energy bands form when there is considerable spatial overlap of electron wavefunctions in atomic orbitals of neighbouring atoms. When n atoms come together to form a solid, each level of the free atom must split into n levels since the Pauli exclusion principle applies to the whole group of n atoms. As such, the energy levels within a band are spaced extremely closely so as to constitute a continuum of allowed energies. It is necessary to refer to the density of levels in the band, which is a function of the energy itself. The outermost electrons of the ferromagnetic transition elements occupy the 3*d* and 4*s* orbitals; when these elements bond to form solids it is these orbitals that are the first to overlap and form energy bands, as shown in Figure 2:10. A simplified form of the 3*d* band is used in this figure, which is of schematic significance only. In the rigid band model, described here, it is assumed that the shape of these bands does not change from one element to another. Whilst this is not physically accurate it is acceptable for the purposes of the discussion presented here.

The exchange interaction may be understood by considering the shapes of the energy bands in Figure 2:10. The 3*d* band is a narrow energy band, with a maximum occupancy of ten electrons per atom and subsequently has a high electron density. In the transition elements the 3*d* band is never completely full since it overlaps in energy of the 4*s* band.

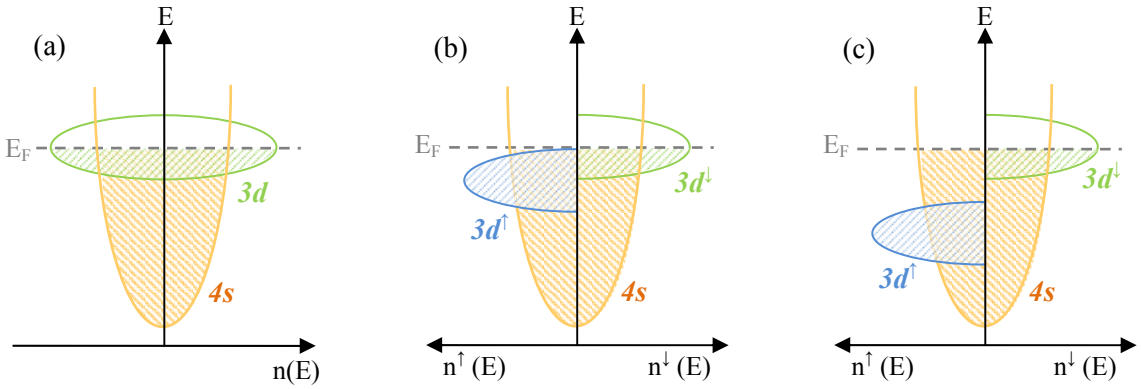

Figure 2:10. Schematic to illustrate the density of levels in the 3*d* and 4*s* bands for (a) no spin imbalance, (b) with exchange splitting in the 3*d* energy band and (c) with large exchange splitting in the 3*d* energy band. Exchange splitting means that spins will preferentially align parallel (↑) first before the antiparallel (↓) spin channel fills. The Fermi level, E_F, is defined as the highest occupied state in the valence band at 0 K and separates filled electronic states from vacant electronic states.

The 4*s* band penetrates closer to the nucleus than the 3*d* band and so is preferentially screened; as a result the 4*s* band is lower in energy than the 3*d* band and is filled first. The 4*s* band is a broad band with a maximum occupancy of two electrons per atom and so has a low electron density. The occupation of each band is shown by the dashed line, which corresponds to the Fermi energy. In the ferromagnetic transition elements the 3*d* band is exchange split as shown in Figure 2:10 (b). This means that 3*d* band is divided into two half-bands – parallel (↑) and antiparallel (↓) sub-bands - with a total capacity of five electrons each. As discussed in section 2.4.1, there is a lower energy associated with parallel spin alignment, and so the parallel band preferentially fills ahead of the antiparallel band. The valence electronic structure of iron, cobalt and nickel are $4s^2 3d^6$, $4s^2 3d^7$ and $4s^2 3d^8$ respectively. In each case, the spin-up band, $n^{\uparrow}(E)$, is full (and so exists below the Fermi level E_F as shown in Figure 2:10 (b) and (c)) , and as a result of the exchange split 3*d* band a spin imbalance is created which results in the creation of a net magnetic moment.

Non-integer values of the Bohr magneton can thus be understood as follows. If the total number of electrons per atom is represented by *t*, the total number of *s* electrons is represented by *s* and the number of *d* electrons is represented by *d*, then a simple bit of manipulation yields n_{eff}. The spin imbalance is expressed as:

$$n_{\text{eff}} = \left[5-\left(t-s-5\right)\right]\mu_B = \left[10-\left(t-s\right)\right]\mu_B \qquad (2:17)$$

Consider the electronic structure of nickel: there are five spin-up and three spin-down electrons, respectively. The measured value of n_{eff} is 0.60 μ_B which means that $s = 0.60$, which is proportional to the number of 4*s* electrons below the Fermi level in Figure 2:10 (c). From this, it is assumed that the number of 4*s* electrons is constant at 0.60 for elements near nickel. It follows that:

$$n_{\text{eff}} = \left[10.6 - t\right]\mu_B \tag{2:18}$$

Using the number of valence electron structures for iron, cobalt and nickel given on the previous page yields values of n_{eff} equal to 2.6 μ_B, 1.6 μ_B and 0.6 μ_B respectively. It is apparent that this approach is not rigorous since, if similar values are inserted for manganese then a value of $n_{\text{eff}} = 3.6$ μ_B is obtained, which should be zero. Nonetheless, it is useful for a qualitative understanding of the exchange interaction in ferromagnets. Once it is assumed that the 4*s* electrons do not contribute to the magnetic properties then non-integral values of the effective number of Bohr magnetons follow naturally from the band theory. More often than not, the division of an integral number of valence electrons (3*d* + 4*s*) between two bands leads to a non-integral number electrons occupying the 3*d* band.

Chapter 3. The theory of ferromagnetic domains and domain walls

3.1 Introduction

This chapter provides the foundation for a solid understanding of the physical origin of ferromagnetic domains and the associated domain walls. This begins with a discussion of the development of the modern understanding of domains and an empirical description of why a domain structure may be expected to form is provided. Quantitative expressions for the individual energetic contributions to the total energy of a ferromagnet are presented and the concept of a micromagnetic approach is introduced. Knowledge of the physical origin and the mathematical forms of each energy term is extremely useful when developing an understanding of magnetisation reversal behaviour in magnetically soft thin films and nanowires in which some of the energy terms may be reduced, negligible, or absent. The chapter concludes by considering the energy and structure of domain walls in bulk systems, thin films and nanowires during which the relationship between energy of domain wall and the micromagnetic structure is introduced.

3.2 Historical development of the domain concept

3.2.1 The domain concept

The ferromagnetic domain concept was introduced by Weiss [22, 23] in order to allow the molecular field theory to be reconciled with experimental observations of ferromagnetic materials. By postulating the existence of small regions, now known as ferromagnetic domains, Weiss was able to explain the existence of the demagnetised state. Within each individual domain, the magnetisation was magnetised to the saturation value of the material and it was suggested that the magnetisation directions of adjacent domains were randomly orientated such that the resultant magnetisation along any direction was zero. The domain concept proposed by Weiss was extremely primitive and made no attempt to explain the physical origin of *why* ferromagnetic domains would form and how they would contribute to the phenomenon of hysteresis.

3.2.2 Experimental investigation of ferromagnetic domains

The first experimental confirmation of the domain concept was provided in 1919 by Barkhausen [30]. Barkhausen discovered that the magnetisation process is often discontinuous, giving rise to a characteristic noise (later termed Barkhausen jumps) when made audible by an amplifier. These jumps had originally been interpreted as evidence for domain *switching*, although this is no longer considered to be the case [25]. Nonetheless, further pursuit of Barkhausen jumps led to the famous Sixtus and Tonks experiments [31]; investigation of the magnetisation reversal of stressed nickel wires showed that magnetisation reversal occurred by a single large jump from one saturated state to the opposite. The analysis of this processes and the Barkhausen noise led Langmuir to conclude that such jumps could only occur by a spatially inhomogeneous process; namely by the propagation of a boundary between domains of opposite magnetisation. This development led Bloch to provide a theoretical analysis of the transitions between adjacent domains [32]; this analysis was the first theoretical treatment of what are now known as domain walls. Indeed, from Bloch's treatment it was established that domain walls have a finite structure with a width that can extend up to several hundred lattice constants (for iron).

In parallel developments, many experimentalists in the 1930s were investigating the nature of magnetocrystalline anisotropies and magnetoelastic effects - in particular how internal stresses affected measured magnetisation curves. Of these, the most notable work was that by Honda [33], Becker [34] and Akulov [35], the latter of whom laid the foundations for the modern understanding of magnetisation curve theory. These experiments showed for the first time that the magnetic microstructure is related to the crystallographic structure of the material. In particular it was shown that the magnetisation vector preferentially aligns with the easy axes of a crystal, with the spontaneous deformation of the crystal related to the magnetisation direction. Both of these findings are material dependent properties that cannot be derived from the Weiss theory.

3.2.3 The development of a theoretical understanding

The effect of the crystallographic microstructure on the experimentally observed ferromagnetic magnetisation behaviour was first considered by Becker [36, 37]. In an attempt to qualitatively explain magnetisation properties of soft magnetic materials, Becker developed the rigid magnetisation model. This model suggested that magnetic domains are

primarily a consequence of inhomogeneous distribution of internal stress which caused the equilibrium direction of magnetisation to vary. Thus the domain structure would depend upon microscopic irregularities within the crystal structure. However, this model failed to explain the low field behaviour of soft magnetic material. Despite the inclusion of an inversion mechanism in an attempt to resolve this, there was a considerable doubt and argument surrounding the nature of the contribution of inversion to the magnetisation process and the rigid magnetisation model was not developed further.

In 1932, Bitter produced the first experimental images of the magnetic domains using a powder technique [38]. These images demonstrated several important features of domains that were, at this point, yet to be considered: domains were *static* and could be large, with regular and periodic appearance. By the mid 1930s some workers [39, 40] had begun to consider the importance of magnetostatic energy in the formation a domain structure. The first quantitative explanation for the existence of domains was provided by Landau and Lifshitz in 1935 [24], who showed that the sub-division of a ferromagnetic specimen into domains could result in a considerable reduction of the magnetostatic energy associated with a saturated condition.

This theory was developed and refined in numerous papers published by Stoner and Wohlfarth [41], Kittel [42] and Brown [43]. The modern theory of micromagnetism is based on seminal work published by Brown in 1940 and 1941 [44, 45, 46, and 47]. Brown provided a rigorous approach to the determination of a domain structure which led to the development of the micromagnetic equations. Micromagnetics provides information on the magnetic microstructure, which is obtained by searching for magnetisation distributions with the lowest total energy. In real systems, however, the observed domain structure may not be that of the lowest total energy due to the presence of grain boundaries and other similar defects within the microstructure of the crystal.

3.3 Description of the ferromagnetic domain structure

For temperatures below the Curie temperature a domain configuration is a natural consequence of the various contributions to the total energy of a ferromagnetic body. In general, the total energy of a ferromagnet includes contributions from exchange energy, magnetocrystalline anisotropy energy, magnetoelastic energy and magnetostatic energy, each of which is discussed in detail in section 3.4.

The large magnetostatic energy associated with a stray field may be decreased by introducing a domain structure. Indeed, a domain structure is to expected if it can reduce - if not completely remove - any uncompensated poles on the surface of the specimen. This section describes how magnetostatic energy leads to a domain structure, and how this is affected by sample size and shape.

3.3.1 Magnetostatic energy and shape anisotropy

There is a large magnetostatic energy, E_s associated with a stray field, given by:

$$E_s = \frac{\mu_0}{2} \int H_s^2 dV \qquad (3:1)$$

Where H_s is the stray field and dV is the volume element of space. The magnetostatic energy is due to the energy of interaction between magnetic dipoles, and the factor of one-half arises so that dipoles are not counted twice (once as a source and once as a magnet in the field). It is important to note that the magnetic dipole-dipole interaction is very much smaller than the strong exchange interaction which is very short range. However, Landau and Lifshitz showed that the magnetic dipole-dipole interaction is long range and so this interaction is important for magnetic moments that are separated by large distances. Indeed, the energy associated with uncompensated free poles is large enough to lead to the formation of a domain structure if it can reduce the magnetostatic energy.

The origin of domains can be understood by considering the structures presented in Figure 3:1.

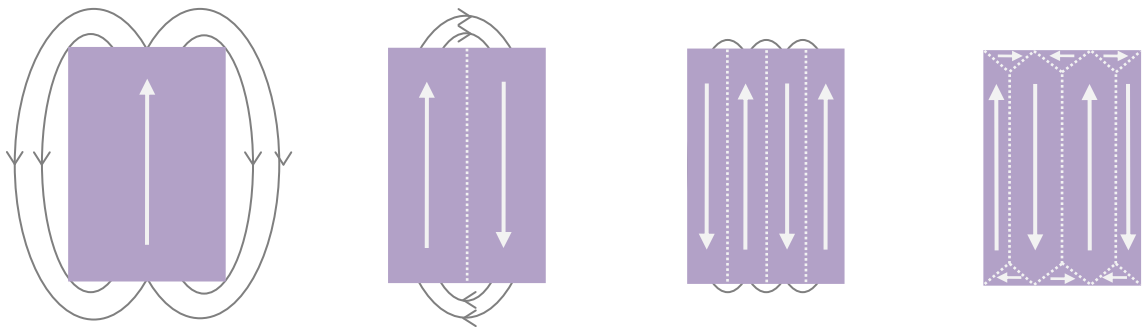

Figure 3:1. Schematic to show hypothetical domain configurations in a perfect single uniaxial crystal of ferromagnetic material. The domain structure has its origin in the possibility of lowering the magnetostatic energy of a system by going from a saturated condition shown in (a) with a large stray field to a flux closed system shown in (d) with considerable reduction in the stray field due to the lack of free poles on the sample surface.

In this figure, each sketch represents a cross section through a ferromagnetic single crystal and any uncompensated magnetic poles on the surfaces of the crystal act as the source of a large stray field. Figure 3:1 (a) shows a single domain configuration. In Figure 3:1 (b), the magnetostatic energy is reduced by approximately half since this configuration decreases the spatial extent of the stray field and a domain wall is created. Additional subdivision, as shown in Figure 3:1 (c), further reduces the magnetostatic energy to approximately a quarter of the value of the saturated condition. The formation of closure domains, such as in Figure 3:1 (d), completely removes the stray field. Further subdivision into an increasing number of domains may continue only until the energy required for the formation of each additional domain wall is greater than the consequent reduction in magnetostatic energy and, eventually, an equilibrium domain size will be attained. The characteristic properties of a domain wall, such as its width, structure and energy are described in section 3.5.

Domain structures are often more complicated than those considered in this example, however, it is important to understand that the domain structure has its origin in the *possibility* of lowering the energy of a system by going from a saturated configuration with high energy, governed by the magnetostatic energy, to a domain configuration with a lower energy.

3.3.2 Single domain particles

A ferromagnet will spontaneously sub-divide into domains in order to reduce the magnetostatic energy associated with a uniform magnetisation state. However, under certain circumstances, the lowest energy state corresponds to a uniformly magnetised, single domain state. Firstly, a ferromagnet will become uniformly magnetised to the saturation value on the application of a sufficiently large magnetic field. Secondly, a ferromagnet can exist in a uniformly magnetised single domain structure in the absence of an applied field provided that the size, and most importantly the *shape* of a specimen is less than a critical size for a given magnetic material.

Frenkel and Dorfman [39] were the first to show below a critical size a domain structure cannot exist. Thus, sufficiently small particles will exist in a uniformly magnetised state; the creation of domains does not result in a corresponding reduction in energy of the system. In addition, calculations by both Brown [44] and Kittel [48] have highlighted the importance of sample shape in determining the existence of a domain

structure. A sufficiently long cylinder, or a prolate spheroid, are both examples of sample shapes in which the lowest energy state is achieved by having a uniform magnetisation orientated along the long axis.

3.4 The energetic contributions to a ferromagnet

In order to understand the detailed domain structure that may be observed in some ferromagnetic materials it is necessary to examine them on an intermediate scale between that of individual atomic sites and its macroscopic properties. Such a scale is small enough to resolve the transitions between adjacent domains, yet large enough to permit the use of a continuous vector rather than individual magnetic moments. Micromagnetics is a phenomenological theory that is based on the study of the continuum theory of magnetic moments; the basic concept of this is a vector magnetisation, $\mathbf{M}(r)$, whose direction cosines vary continuously with position.

Micromagnetic calculations, such as those described in section 4.5, are used to determine the ideal micromagnetic structure of a ferromagnet. In practise, this is achieved by using a variational principle to search for the magnetisation distribution with the smallest total energy. This requires that the various energetic contributions to the ferromagnetic system are expressed in terms of the directions throughout the crystal. In this section, quantitative expressions for the energetic contributions to the ferromagnetic system are presented and the physical origin of each is described.

3.4.1 The total free energy of a ferromagnet

The first requirement to any micromagnetic calculation is to find an expression for the total free energy of the ferromagnetic system. The total free energy, E_{total}, of a ferromagnetic system in thermodynamic equilibrium is given by:

$$E_{\text{total}} = \int_V \phi_{\text{total}} dV = 0 \tag{3:2}$$

Where ϕ_{total} is the free energy density of the system and V is the sample volume. The total free energy density of a ferromagnet is comprised of five key terms:

$$\phi_{\text{total}} = \phi_{\text{A}} + \phi_{\text{k}} + \phi_{\sigma} + \phi_{\text{s}} + \phi_{\text{Zeeman}} \tag{3:3}$$

Where the individual components correspond to the exchange, magnetocrystalline anisotropy, magnetoelastic, magnetostatic and Zeeman energy densities, respectively. The relevant ferromagnetic energy densities are summarised here in the form of succinct mathematical expressions; rigorous and exhaustive derivations of the expressions of individual terms are given in the text by Hubert and Schäfer [25].

3.4.2 Exchange energy

The exchange energy density is written as:

$$\phi_{\mathrm{A}} = A \sum_{i=1}^{3} \left(\nabla \alpha_i (r)^2 \right) \tag{3:4}$$

Where A is the exchange stiffness parameter, defined in equation (2:12), and $\alpha_{1,\,2,\,3}$ are the direction cosines of the spin at lattice point r. This equation relates the exchange energy density to the magnitude of the angle between adjacent spins. As previously discussed in section 2.4, the exchange energy is very short range and is essentially a nearest neighbour interaction. Equation (3:4) shows that as the angle between two adjacent spins increases, the associated energy also increases.

3.4.3 Magnetocrystalline anisotropy energy

The magnetocrystalline anisotropy energy acts in such a way that the magnetisation tends to be directed along certain definite crystallographic axes, which are termed directions of *easy* axes of magnetisation. Conversely, the directions along which it is most difficult to align the magnetisation in the crystal are called *hard* axes. It has been found experimentally that the energy to magnetise a ferromagnetic crystal to saturation along a hard axis is often considerably more than the energy required to magnetise the same ferromagnetic crystal to saturation along an easy axis. The excess energy required to achieve saturation of the magnetisation along a hard axis is the magnetocrystalline anisotropy energy.

Magnetisation curves measured at room temperature along each of the principal crystallographic axes of iron, nickel and cobalt are shown in Figure 3:2. Iron and nickel are arranged in a body-centred cubic structure and face-centred cubic structure, respectively. In iron, it is seen that crystal can be magnetised to saturation along the [100] axes significantly easier when compared to the [111] directions.

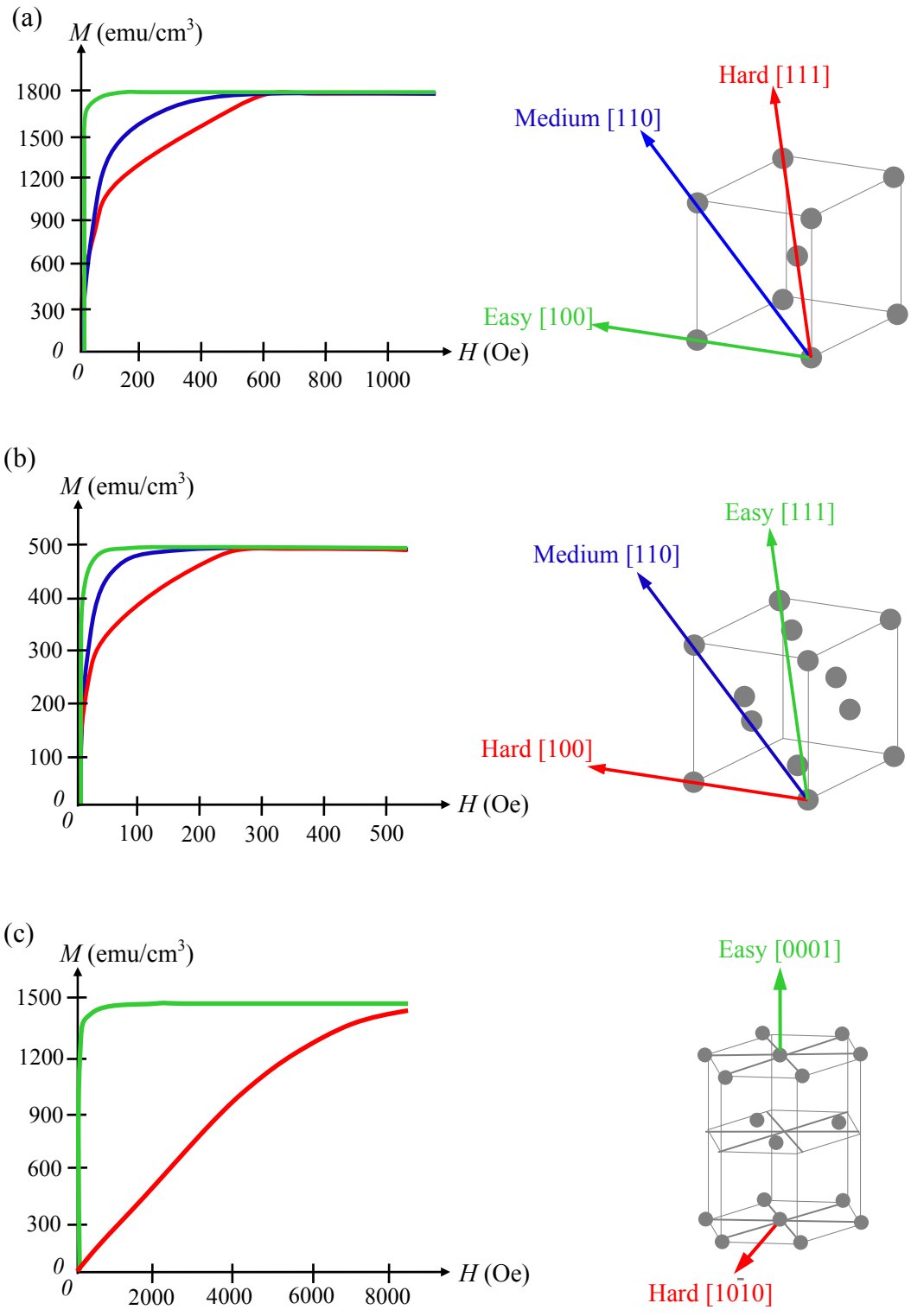

Figure 3:2. Magnetisation curves for the three principle axes of (a) single crystal iron [49] and (b) single crystal nickel [50] and (c) single crystal cobalt [51].

Thus, the [100] axes in iron are the easy magnetisation axes whilst the [111] axes correspond to hard axes of magnetisation. For nickel, magnetisation curves show that the [111] directions correspond to easy axes of magnetisation whilst the [100] directions are measured to be the hard axes of magnetisation. For cobalt, which has a hexagonal close-packed structure, it is the hexagonal *c* axis that is easy, and, within the accuracy of the measurements, all directions in the basal plane are found to be equally hard.

For cubic crystals (such as iron and nickel), the magnetocrystalline anisotropy energy density, ϕ_k , is expressed as:

$$\phi_k = K_1\left(\alpha_1^2\alpha_2^2 + \alpha_2^2\alpha_3^2 + \alpha_3^2\alpha_1^2\right) + K_2\left(\alpha_1^2\alpha_2^2\alpha_3^2\right) \tag{3:5}$$

Where, K_1 and K_2 are constants for a particular material and $\alpha_{1,2,3}$ are the direction cosines relative to the cube edges. For iron, values of K_1 and K_2 are 4.8 x 10^4 J/m^3 and -1.0 x 10^4 J/m^3 respectively. For nickel, K_1 and K_2 are measured to be -4.5 x 10^3J/m^3 and -2.5 x 10^3 J/m^3 respectively [28]. For uniaxial crystals, such as cobalt, the magnetocrystalline anisotropy energy density is given by:

$$\phi_k = K_1 \sin^2(\theta) + K_2 \sin^4(\theta) \tag{3:6}$$

Where K_1 and K_2 are 45.3 x 10^4 J/m^3 and 14.5 x 10^4 J/m^3, respectively [28] and θ is the angle between the easy axis and the magnetisation. It is experimentally observed that magnetocrystalline anisotropy constants almost always decrease as temperature increases and become essentially zero before the Curie temperature is reached. This was originally investigated by Bozorth in 1937 [52], and is due to the thermal expansion of the lattice parameter which causes the magnetocrystalline anisotropy to disappear. In addition, the magnetocrystalline anisotropy constants of alloy systems can vary markedly with chemical composition.

Whilst magnetocrystalline anisotropy plays an important part in the behaviour of nearly all ferromagnetic materials, its effects only appear in simple form in single-crystal specimens. For polycrystalline samples with a truly random orientation of crystallite grains the magnetocrystalline anisotropy will average out and the sample will exhibit no net magnetocrystalline anisotropy, although the local magnetisation distribution will be influenced by the local magnetocrystalline anisotropy. A truly random distribution of crystallite orientation is, however, very rare and the majority of polycrystalline samples have a preferred orientation, or texture, which can be enhanced by the preparation

technique. In this case, the strength of the magnetocrystalline anisotropy depends upon the degree of preferred orientation within the sample.

For binary nickel-iron alloys, which are of particular relevance here, the magnetocrystalline anisotropy depends sensitively upon the percentage nickel content as shown by Bozorth [53] and reproduced in Figure 3:3. The magnetocrystalline anisotropy constant, K_1, is seen to pass through zero for nickel compositions between 75 and 80% nickel. For the nickel-iron composition $Ni_{81}Fe_{19}$, K_1 is very small and slightly negative, which indicates that easy axes of magnetisation corresponds to the [111] set of directions.

The physical origin of magnetocrystalline anisotropy was first described by van Vleck [54], and it was thought to be due to the combination of the spin-orbit interaction and the partial quenching of the orbital angular momentum. The spin magnetic moment of the electron interacts with the orbital magnetic moment by means of the spin-orbit interaction. In turn, the orbital magnetic moment interacts with the crystal lattice and as the electron orbitals are strongly coupled to the crystal lattice this results in the orbital magnetic moment being almost entirely quenched.

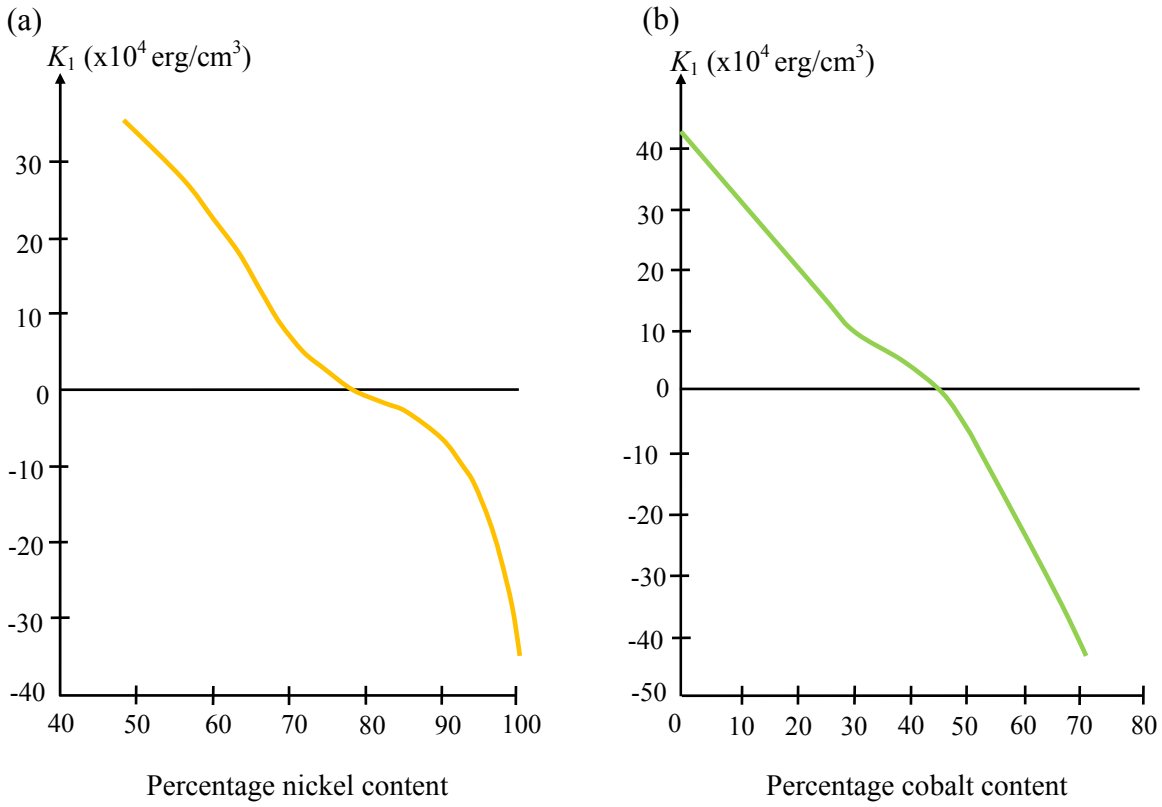

Figure 3:3. Variation of the magnetocrystalline anisotropy constant, K_1, with (a) percentage nickel content in iron, reproduced from data presented in [52] and (b) percentage cobalt content in iron, reproduced from data presented in [21].

As the orientations of the 3*d* orbitals are fixed very strongly to the crystal lattice, the application of very large applied magnetic fields cannot change the orientations. The magnetocrystalline anisotropy energy is then the energy required to overcome the spin-orbit coupling needed to re-orientate the magnetisation direction.

3.4.4 Magnetoelastic energy

The magnetoelastic energy arises from the interaction between the magnetisation and the mechanical strain of the crystal lattice. For an unstrained crystal lattice, the magnetoelastic energy is zero and the magnetisation behaviour in an applied field is determined by both the magnetocrystalline anisotropy and shape anisotropy energies.

This phenomenon was first described in 1842 by Joule, who noted that when a ferromagnetic substance is exposed to a magnetic field the sample either expands or contracts, and an overall change in the dimensions of the sample is observed. This is known as magnetostriction, although it is sometimes referred to as the Joule effect. The inverse effect is also true; the application of stress to a ferromagnetic sample can change the magnetisation state and easy axes, and this is known as the Villari effect.

Linear magnetostriction is the fractional change in length that results when a ferromagnetic sample is magnetised to saturation from the demagnetised state. For a cubic crystal this is defined as:

$$\begin{aligned}\frac{\Delta l}{l} &= \tfrac{3}{2}\lambda_{100}\left(\alpha_1^2\beta_1^2 + \alpha_2^2\beta_2^2 + \alpha_3^2\beta_3^2 - \tfrac{1}{3}\right) \\ &\quad +3\lambda_{111}\left(\alpha_1\alpha_2\beta_1\beta_2 + \alpha_1\alpha_3\beta_1\beta_3 + \alpha_2\alpha_3\beta_2\beta_3\right)\end{aligned} \tag{3:7}$$

Where λ_{100} and λ_{111} are the values of the saturation magnetostriction when the crystal is magnetised along the [100] and [111] directions respectively, $\alpha_{1,2,3}$ are the direction cosines relative to the cube edges and $\beta_{1,2,3}$ are the direction cosines in the direction that Δl is measured. The magnetostrictive strain produced when the magnetisation direction is changed is typically of the order of 10^{-6} and for iron, $\lambda_{100} = 22 \times 10^{-6}$ and $\lambda_{111} = -21 \times 10^{-6}$, whilst for nickel $\lambda_{100} = -55 \times 10^{-6}$ and $\lambda_{111} = -23 \times 10^{-6}$ [28]. A positive value of magnetostriction means that the magnetisation of a ferromagnetic sample is increased by the application of tension, and so the material expands when it is magnetised. In contrast, a negative value of magnetostriction means that the magnetisation is decreased by tensions and as such the material contracts when it is magnetised.

It is often assumed, for simplicity, that the magnetostriction is isotropic - for example, in polycrystalline sample or amorphous alloys - in which case λ_s is the average of λ_{100} and λ_{111}. Thus, the fractional change in length of a ferromagnetic crystal reduces to:

$$\frac{\Delta l}{l} = \frac{3}{2}\lambda_s\left[\left(\alpha_1\beta_1 + \alpha_2\beta_2 + \alpha_3\beta_3\right)^2 - \frac{1}{3}\right] \tag{3:8}$$

Where λ_s is the saturation magnetostriction. This can be further reduced to:

$$\frac{\Delta l}{l} = \frac{3}{2}\lambda_s\left[\cos^2(\theta) - \frac{1}{3}\right] \tag{3:9}$$

Where θ is the angle between the saturation magnetisation and the direction in which Δl is measured. For iron and nickel, λ_s = -7x10^{-6} and -34x10^{-6}, respectively [48]. In general, the magnetoelastic energy density, ϕ_σ, is given by:

$$\phi_\sigma = \frac{3}{2}\left(\lambda_S \sigma \sin^2(\theta)\right) \tag{3:10}$$

Where σ is the magnetoelastic tensor and θ is the angle between the saturation magnetisation and the magnetoelastic tensor.

The magnetostriction constants of alloy systems can vary markedly with chemical composition. For binary nickel-iron alloys, the magnetocrystalline anisotropy depends sensitively upon the percentage nickel composition, as shown in Figure 3:4. The value of λ_{100} is zero at two compositions: $Ni_{46}Fe_{54}$ and $Ni_{83}Fe_{17}$, whilst the λ_{111} is zero at approximately 80% nickel. In addition, the magnetostriction becomes isotropic near 60% and 86% nickel content. The values of λ_{100} and λ_{111} are both close to zero for $Ni_{81}Fe_{19}$, in which K_1 (and also K_2) are both simultaneously very close to zero.

The physical origin of magnetostriction is the spin-orbit interaction and is described here as follows. An applied field will reorientate the spin moments and change the magnetisation direction and, because of the spin-orbit interaction, the electron orbitals also try to reorientate. Yet, the orbital momentum is almost entirely quenched in the 3*d* transition elements since the orbitals are fixed to the crystal lattice. Thus, the reorientation of the electron orbitals can only take place by a very small extent. It is for this reason that the typical changes in length caused by magnetostriction are of the order of 10^{-6} in the 3*d* ferromagnetic elements.

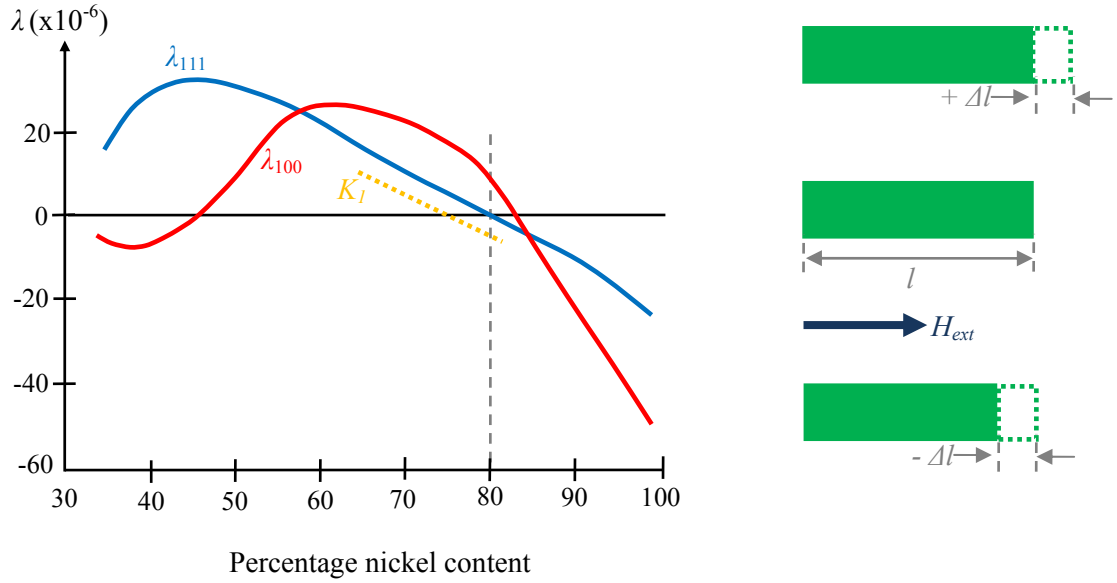

Figure 3:4. The variation of saturation magnetostriction with percentage nickel content in binary nickel-iron alloys, reproduced from [55]. The variation of the magnetocrystalline anisotropy constant K_1 is also included for comparison. The sketches show the change in relevant sample dimensions on the application of a magnetic field for positive and negative magnetostrictive effects. The dashed line at 80% nickel content is shown to highlight the behaviour of the magnetostriction and magnetocrystalline anisotropy constants for the NiFe alloy used within this study.

In the rare-earth metals the spin-orbit coupling is strong, and this results in a large reorientation of the electron orbits when the magnetisation direction is changed. Magnetostrictive effects in the rare-earth metals can thus cause considerable distortion.

A material which has a low value of K_1 and λ is expected to have high permeability; the combination of low value of K_1 decreases domain-wall energy (discussed in detail section 3.5) and a low value of λ means that microstresses become less effective. It is this combination that has made nickel-iron alloys of compositions close to $Ni_{80}Fe_{20}$ such a technologically important alloy. Kittel [48] highlights the correlation between magnetocrystalline anisotropy and magnetostriction, and developed the expression presented in (3:10) by considering the magnetocrystalline anisotropy energy as a function of the saturation magnetisation relative to the crystal axes and of the interatomic distance; that is, the strain. The amount of distortion then depends upon the direction of the magnetisation relative to the crystal axes. In general, a large value of the magnetocrystalline anisotropy constant K_1 is typically accompanied by a large value of the magnetostriction constant λ_s. This is the case in binary nickel-iron alloys where both constants tend to zero at approximately 80% nickel content.

3.4.5 Magnetostatic energy

As discussed previously in section 3.3, the magnetostatic energy is associated with stray field from a sample and is the sum of magnetic dipole-dipole fields. The magnetostatic energy is thus the energy associated with the magnetic field generated from the magnetic body itself. The magnetostatic energy density is written as:

$$\phi_s = \frac{\mu_0}{2} H_s \cdot M_s \tag{3:11}$$

Where H_s is the stray field which is associated with uncompensated free poles. The stray field tends to oppose the directions of the saturation magnetisation, M_s. The magnitude of the stray field depends sensitively upon the size and shape of the sample as outlined in section 3.3.2.

3.4.6 The Zeeman energy

The Zeeman energy density is written as:

$$\phi_{Zeeman} = -\mu_0 H_{ext} \cdot M_s \tag{3:12}$$

The Zeeman energy is the energy associated with the interaction of the saturation magnetisation with an externally applied field, H_{ext}. This energy is minimised when the saturation magnetisation is aligned parallel with the applied field and is maximised when the magnetisation is aligned anti-parallel to the applied field.

3.4.7 Summary of the energetic contributions to a ferromagnet

The energetic contributions to the total energy of a ferromagnetic system are summarised in Table 3:1.

Energy term	Description	Energy density expression
Exchange	Energy is minimised when spin magnetic moments are aligned parallel	$\phi_{\mathrm{A}} = A\sum_{i=1}^{3}\left(\nabla\alpha_i(r)^2\right)$
Magnetocrystalline anisotropy	Energy is minimised when M_{s} lies parallel to easy axes	$\phi_{\mathrm{k}} = K_1\left(\alpha_1^2\alpha_2^2+\alpha_2^2\alpha_3^2+\alpha_3^2\alpha_1^2\right)+K_2\left(\alpha_1^2\alpha_2^2\alpha_3^2\right)$ $\phi_{\mathrm{k}} = K_1\sin^2(\theta)+K_2\sin^4(\theta)$
Magnetostriction	The application of strain along specific directions of a crystal changes the direction of M_{s}	$\phi_{\sigma} = \frac{3}{2}\left(\lambda_{\mathrm{s}}\sigma\sin^2(\theta)\right)$
Magnetostatic	Energy due to stray magnetic fields associated with M_{s}	$\phi_{\mathrm{s}} = \frac{\mu_0}{2}H_{\mathrm{s}}\cdot M_{\mathrm{s}}$
Zeeman	Energy is minimised when M_{s} lies parallel to an externally applied field H_{ext}.	$\phi_{\mathrm{Zeeman}} = -\mu_0 H_{\mathrm{ext}}\cdot M_{\mathrm{s}}$

Table 3:1. Summary of the physical contributions to the free energy of a ferromagnet and the expressions for the energy density used in micromagnetics.

3.5 The energetics and structural properties of magnetic domain walls

The discussion in the previous sections within this chapter has shown how a ferromagnetic crystal may sub-divide into domains, where the specific orientation and size of domains is determined by the energetic contributions presented in Table 3:1. When a domain structure exists there must also be regions where the direction of the magnetisation changes from one domain to the next; these are called domain walls. Domain walls are not treated as separate entities within micromagnetic theory; rather, if the total energy of the ferromagnet is reduced by forming a domain structure then domain walls are a natural

consequence. Thus, domain walls will appear *if* their formation allows for a reduction in the total energy of the system.

In this section, the static properties of domain wall structures are discussed. The properties of interest include the micromagnetic structure and characteristic domain wall width, which are determined by the energy cost incurred by forming the wall. The discussion begins by considering the simplest domain wall structure, the Bloch wall, where the relationship between domain wall energy and micromagnetic structure is established. Following this, the effect of the thin film geometry on the domain wall energy and structure is discussed. Finally, the properties of domain walls in magnetically soft nanowire structures are described.

3.5.1 Bloch walls

A domain wall is a continuous transition region that separates adjacent domains in which the saturation magnetisation points in different directions. As shown in Figure 3:5, the change in magnetisation direction does not occur in one discontinuous jump across a single atomic plane; instead, the transition takes place gradually over many atomic planes such that the domain wall has a definite micromagnetic structure and a characteristic width, δ_{DW}. This section examines the general structural features of the transition region that lies between two adjacent domains in a bulk sample. Whilst this is not entirely physically realistic, it is a useful construction for developing a theoretical understanding of the influence of total domain wall energy on the micromagnetic structure and characteristic domain wall width.

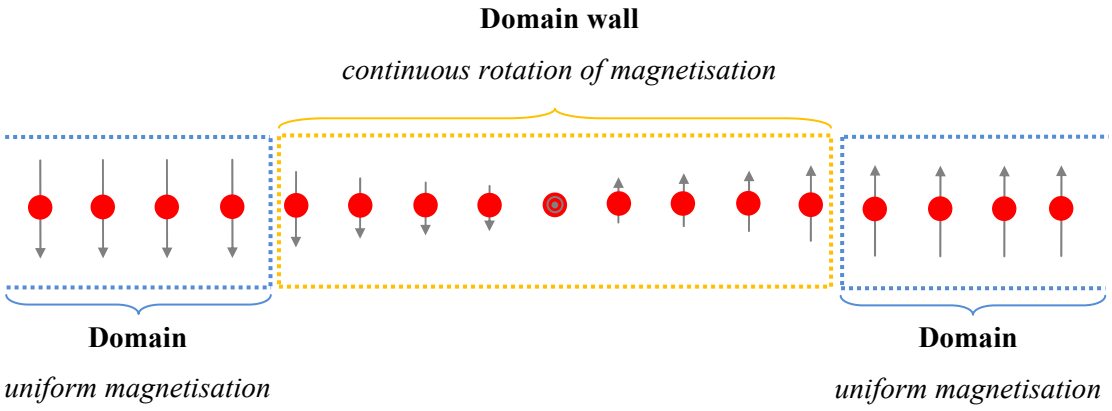

Figure 3:5. Plan view schematic showing the micromagnetic structure of a Bloch wall. The spin at the centre of the transition points out of the plane of the page.

For the purposes of discussion the contribution of magnetostatic energy to the total domain wall energy is neglected.

This assumption is acceptable provided that the domain wall is not near the surface of the ferromagnetic sample. When the magnetostatic energy contribution is neglected, it is assumed that the normal component of the saturation magnetisation remains constant throughout the wall, which means that the angle between neighbouring spins is also constant throughout the transition. However, when a domain wall is near the sample surface, the stray field from the uncompensated poles within the domain wall cannot be ignored and must be considered: this is important for thin films and is addressed in section 3.5.2. Insight into the micromagnetic structure of a Bloch wall in a bulk material can be gained by considering the competition between exchange energy and magnetostatic crystalline anisotropy energy.

The exchange energy seeks to make the transition between adjacent domains as broad as possible. Indeed, the exchange energy seeks to extend the 180° transition over N atomic planes, each with equal angles of 180°/N between adjacent spins. When N increases, the angle between neighbouring spins decreases and there is a corresponding decrease in exchange energy. The exchange energy per unit area associated with a gradual spin transition can be expressed as:

$$\sigma_{\mathrm{A}} = J_{\mathrm{exchange}} S^2 \left(\frac{\pi}{Na} \right)^2 N \tag{3:13}$$

Where J_{exchange} is the exchange integral, S is the spin angular momentum and a is the lattice parameter of the material. As N increases, however, the number of spin magnetic moments orientated in hard axes directions also increases and as such, there is a corresponding increase in magnetocrystalline anisotropy energy per unit area. For a material with uniaxial anisotropy, the magnetocrystalline anisotropy energy per unit area can be expressed as:

$$\sigma_{\mathrm{k}} = K_1 Na \tag{3:14}$$

Where K_1 is the magnetocrystalline anisotropy constant. The total energy per unit area of a 180° Bloch wall is thus:

$$\sigma_{\mathrm{DW}}^{\mathrm{Bloch}} = \sigma_{\mathrm{A}} + \sigma_{\mathrm{k}} \approx \frac{J_{\mathrm{exchange}} S^2}{N} \left(\frac{\pi}{a} \right)^2 + K_1 Na \tag{3:15}$$

The total wall energy per unit area is a minimum with respect to N when

$$N_0 = \sqrt{\frac{JS^2\pi^2}{K_1 a^3}} = \sqrt{\frac{\pi^2}{2a^2} \cdot \frac{A}{K_1}} \tag{3:16}$$

Where A is the exchange stiffness parameter and K_1 is the magnetocrystalline anisotropy constant. Inserting this value of N into equation (3:15) gives the optimum energy density for a 180° Bloch wall, which is:

$$\phi_{\mathrm{DW}}^{\mathrm{Bloch}} = 4\sqrt{AK_1} \tag{3:17}$$

The effect of the competition between the exchange and magnetocrystalline energies on the total domain wall energy is shown in Figure 3:6. N_0 is found to range from about 40 to nearly 10^4, and depends specifically upon the magnitude of the magnetocrystalline anisotropy constant K_1. The optimum wall width parameter $\delta_{\mathrm{DW}}^{\mathrm{Bloch}}$ can be estimated via:

$$\delta_{\mathrm{DW}}^{\mathrm{Bloch}} = Na = \left(\sqrt{\frac{\pi^2}{2a^2} \cdot \frac{A}{K_1}}\right) a \approx \pi\sqrt{\frac{A}{K_1}} \tag{3:18}$$

As K_1 decreases, the wall width increases. As discussed in section 3.4.3, K_1 decreases with increasing temperature, and so in a given material the wall width can be modified accordingly by changing the applied temperature. In addition, in alloy systems, the value of K_1 can be changed by changing the chemical composition and so the wall width parameter can be modified greatly in specific materials.

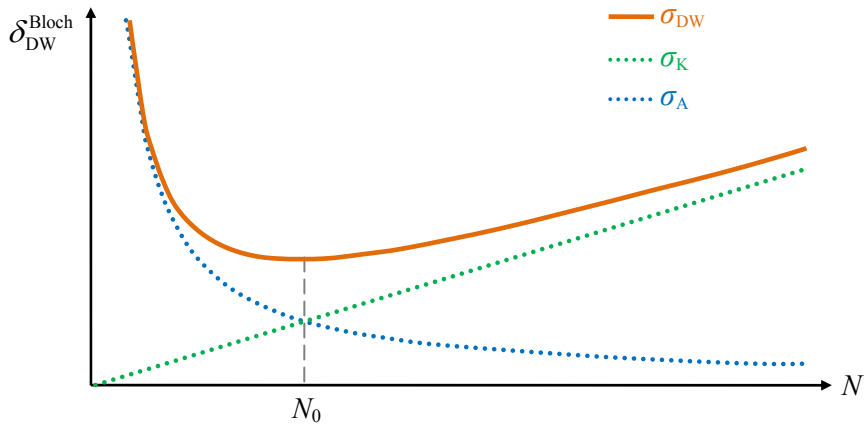

Figure 3:6. Minimisation of the sum of exchange energy and anisotropy energy densities. The domain wall energy is denoted in orange and the optimum wall energy occurs when the lines intercept. The total wall energy density is minimised at N_0.

Micromagnetic calculations can be used to provide to a more thorough determination of the wall width parameter. Following the analysis given in O'Handley [9], the magnetisation rotation may be described in spherical polar co-ordinates as:

$$\theta(x) = 2\arctan\left[\exp\left(\frac{\pi x}{\delta_{\mathrm{DW}}^{\mathrm{Bloch}}}\right)\right] \tag{3:19}$$

Where x corresponds to the direction of the saturation magnetisation within the domain, and $\delta_{\mathrm{DW}}^{\mathrm{Bloch}}$ is as defined in equation (3:18). As such, the domain wall width profile in the x direction and y directions, M_x and M_y are given by:

$$M_x = \sin\theta(x); M_y = \cos\theta(x) \tag{3:20}$$

Figure 3:7 presents magnetisation rotation profile along the x-axis for two different values of K_1. As a domain wall forms a *continuous* rotation of the magnetisation between adjacent domains, the wall width parameter is a difficult concept to define and as such there is no unique definition of a domain wall width. The most commonly used definition is that by Lilley [56], which is based upon the slope of the M_x profile and is highlighted in Figure 3:7 and corresponds to the $\pi\sqrt{A/K_1}$, as given by equation (3:18). There are several other definitions of the wall width parameter in the literature and in general the wall width definition employed depends upon the particular situation.

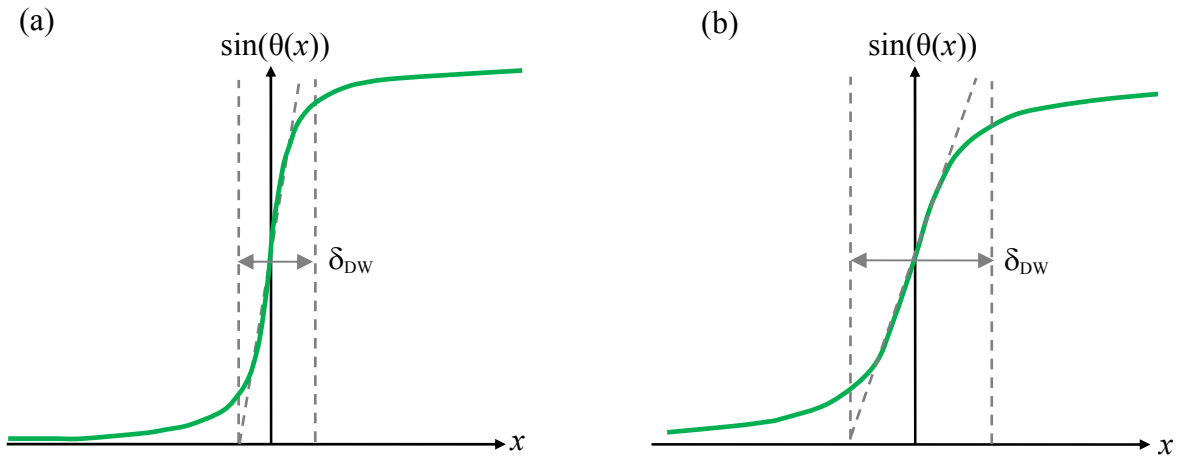

Figure 3:7. Schematic sketch of the magnetisation rotation along the x direction as described by equation (3:20) showing (a) the effect of large values of K_1 and (b) a small value of K_1. The definition of the wall width according to Lilley [56] is also indicated.

3.5.2 Domain walls in thin films

The concept of an infinitely extended domain wall is no longer valid when the thickness of the sample becomes comparable to the Bloch wall width. A magnetic film is geometrically confined in one dimension, and is described as thin if the thickness is comparable to the Bloch wall width parameter defined in the previous section. When this is the case, the effect of the large stray field and the associated magnetostatic energy can no longer be ignored.

When the thickness of the sample is comparable to the Bloch wall width, the associated magnetostatic energy becomes appreciable, relative to the exchange and anisotropy energies, due to the uncompensated poles formed where the wall intersects the surface. This means that it is no longer possible to neglect the interactions between the strips of free poles at the intersections of the wall with the surface of the specimen. In 1955 Néel showed that the domain wall energy is not a constant of the material, but instead also depends on the thickness of the sample when the thickness is less than a few hundred nanometres [58]. As a result, the domain wall energy and subsequent micromagnetic structure and width of domain walls in thin film materials are very different from those in bulk materials due to the anisotropic shape of thin films. A Néel wall is characterised by the fact that the magnetisation in the wall rotates from one domain to the next without leaving the plane of the film, as shown in Figure 3:8. An in-plane magnetisation rotation reduces the magnetostatic energy associated with uncompensated poles at the surface, which make a significant contribution when the film thickness is comparable to the Bloch wall width.

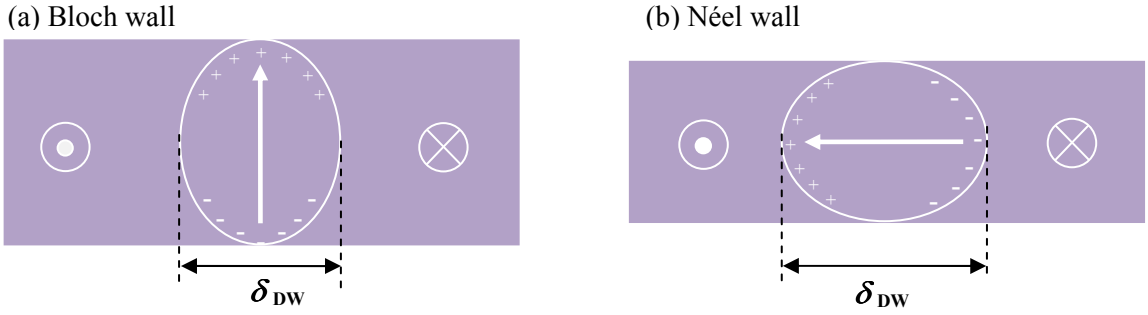

Figure 3:8. Side view schematic comparing the rotation of magnetisation in a (a) Bloch wall and (b) in a Néel wall. The elliptical cross-sections indicate the magnetic charges associated with uncompensated free poles.

A smaller magnetostatic energy at the internal face of the wall is accepted as the price for reducing the larger magnetostatic energy at the top surface. A more detailed schematic of the magnetisation rotation within a Néel wall is provided in Figure 3:9. In seeking to obtain the optimum wall energy associated with a Néel wall, the magnetostatic energy must also be included with contributions from the exchange and magnetocrystalline anisotropy energy and is expressed as:

$$\sigma_{\mathrm{DW}}^{\mathrm{Neel}} = 4\sqrt{A\left(K_1 + \frac{\mu_0}{2}M_{\mathrm{s}}^2\right)} \tag{3:21}$$

When the magnetocrystalline anisotropy constant is zero, as is the case for NiFe films with nominal composition close to $Ni_{80}Fe_{20}$, this reduces to:

$$\sigma_{\mathrm{DW}}^{\mathrm{Neel}} = \sqrt{8\mu_0 A M_{\mathrm{s}}^2} \tag{3:22}$$

The domain wall energy in thin $Ni_{80}Fe_{20}$ films thus consists mainly of the energy associated with the stray field and the exchange energy since the magnetocrystalline anisotropy energy can be neglected at this composition. Figure 3:10 compares the wall energy for Bloch and Néel walls in $Ni_{80}Fe_{20}$ thin films, as a function of film thickness, as reproduced from [57]. It can be seen that the Bloch wall energy increases for film thickness less than approximately 50 nm, when the Néel wall energy shows a corresponding decrease and thus becomes energetically favourable.

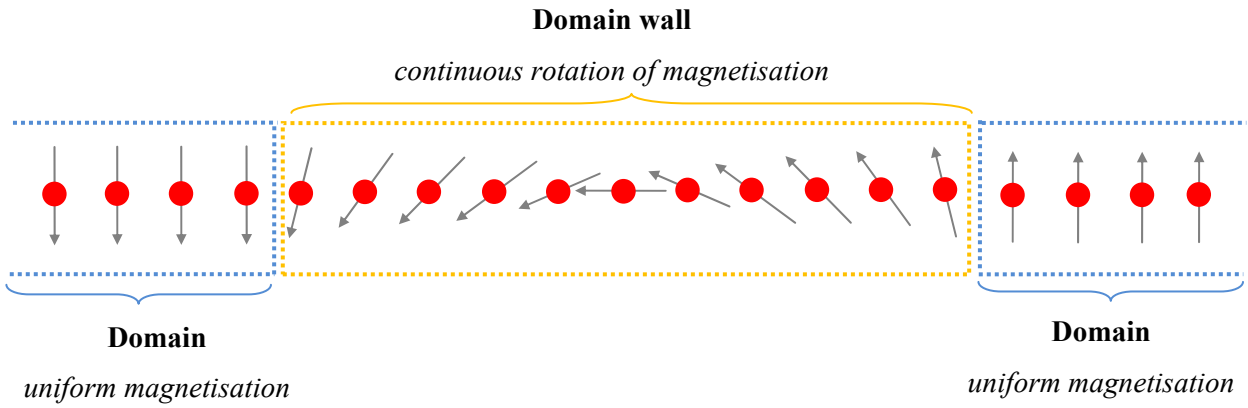

Figure 3:9. Schematic of the micromagnetic structure within a Néel wall, which is characterised by an in-plane rotation of magnetisation.

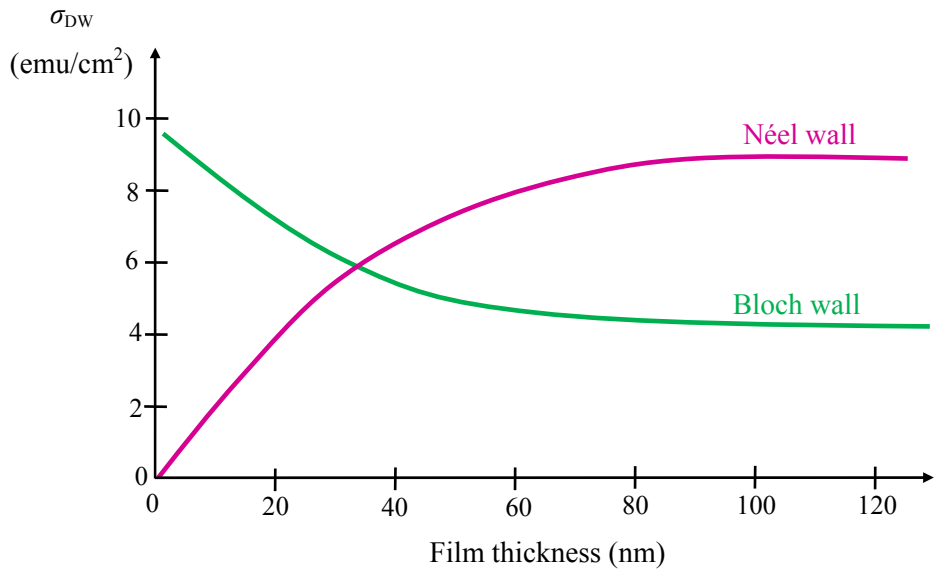

Figure 3:10. Comparison of the energy of Bloch wall and Néel walls as a function of film thickness for thin $Ni_{80}Fe_{20}$ films, reproduced from [57].

The width of a Néel wall is expressed as:

$$\delta_{DW}^{Neel} = \pi\sqrt{\left(\frac{A}{K_1} + \frac{2A}{\mu_0 M_s^2}\right)} \tag{3:23}$$

The calculated dependence of Bloch and Néel wall widths on film thickness is shown in Figure 3:11.

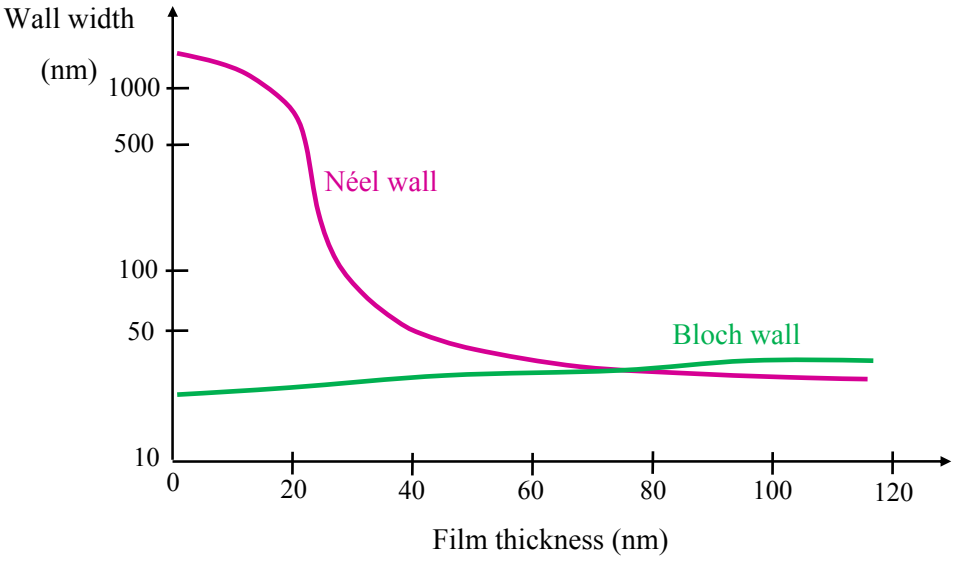

Figure 3:11. Variation of domain wall width as a function of film thickness for Bloch walls and Néel walls for thin $Ni_{80}Fe_{20}$ films, reproduced from [57].

It can be seen that the Néel wall width becomes significantly larger than the corresponding Bloch wall width as $Ni_{80}Fe_{20}$ film thickness decreases below approximately 50 nm, which is due to the nature of the in-plane rotation of magnetisation in a soft magnetic material. As the over-riding demand of the system is to reduce the energy associated with stray fields, a larger value of the wall width is accepted at the cost of reduced the magnetostatic energy at the surfaces of the thin film.

There are several types of Néel wall structures that may form in soft magnetic films aside from the simple structure considered here such as the cross-tie wall, for example, which was discovered by Huber *et al.* [59] and may be observed in very thin films. A phase diagram of the main wall types (with in-plane magnetisation rotation) is given by Hubert and Schäfer [25]. In general, there is a good agreement between experimental observations and theoretical predictions of the thickness at which Néel walls become favourable.

3.5.3 Domain walls in planar permalloy nanowire structures

A nanowire structure is geometrically confined along two dimensions. Typical nanowire thicknesses are a few tens of nanometres, whilst typical widths of the order of hundreds of nanometres. The axial length of such structures is significantly longer, and tends to be of the order of micrometres, and so is much less important. The nanowire geometry allows for much simpler domain wall structures to exist. For magnetic materials with weak intrinsic magnetocrystalline anisotropies such as $Ni_{81}Fe_{19}$ nanowires, the magnetisation is largely constrained by magnetostatic energy considerations to lie along the long axis of the wire with spins parallel to the surfaces and edges. The micromagnetic structure of a domain wall results from an energy minimisation process that includes material-dependent properties as well as the local geometry of the nanowire.

Experimental imaging techniques such as magnetic force microscopy and transmission electron microscopy combined with micromagnetic modelling reveal that magnetisation reversal of nanowires occurs by the propagation of a domain wall. The domains are separated by ‘head-to-head’ or ‘tail-to-tail’ domain walls, although it is worthwhile noting that there is no real difference between a head-to-head and a tail-to-tail domain wall. A schematic of the nanowire geometry and of the kinds of domain walls in shown in Figure 3:12.

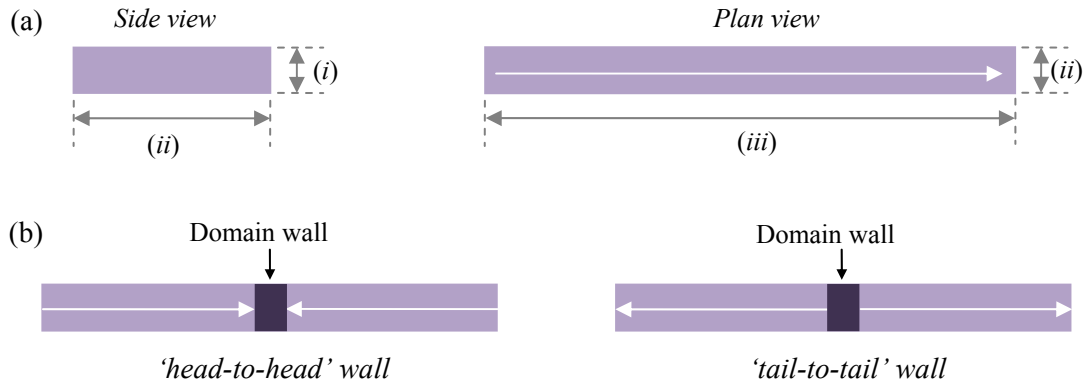

Figure 3:12. Schematic to show the nanowire structure (a) (*not to scale*) (*i*) nanowire thickness - of the order of tens of nanometres; (*ii*) nanowire width - of the order of hundreds of nanometres and (*iii*) axial length of nanowires - of the order of microns. Magnetisation reversal of nanowires occurs via the propagation of a domain wall, as shown in (b); which may either be 'head-to-head' or 'tail-to-tail'.

The internal structure of head-to-head domain walls was first studied using micromagnetic simulations by McMichael and Donahue [60], who discovered that there are two distinct domain wall structures: the transverse wall (TW) and the vortex wall (VW). Further investigation by Nakatani *et al.* [61] revealed that there is an intermediate state between the transverse and vortex wall, which is called the asymmetric transverse wall. Figure 3:13 shows the different types of domain wall that can exist in planar nanowire structures.

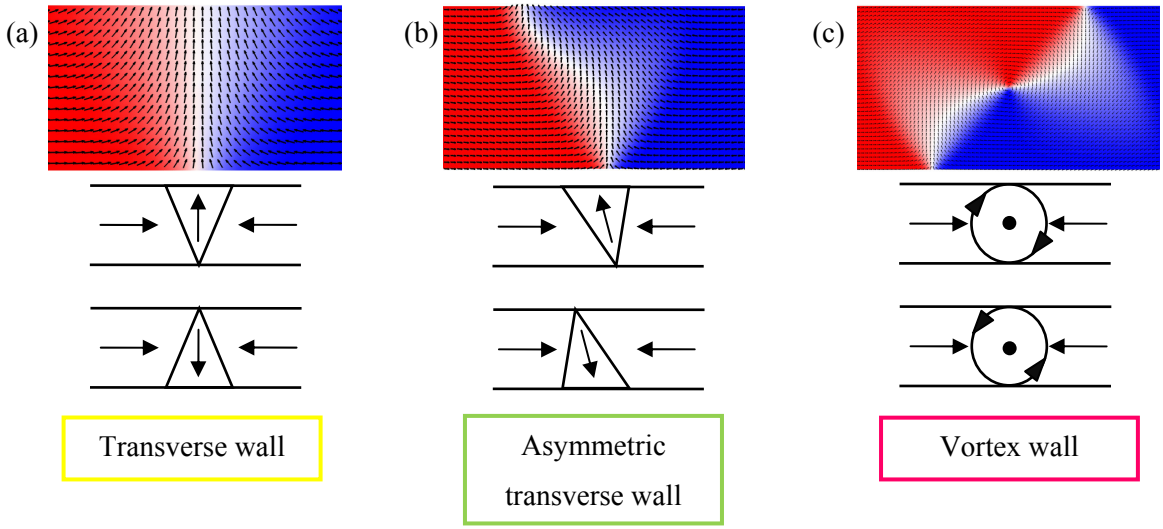

Figure 3:13. Micromagnetic simulations (*top*) and corresponding schematic representations (*bottom*) of the three domain wall structures that can exist in planar $Ni_{81}Fe_{19}$ nanowire structures. As wire thickness and width increases, the favourable wall structure changes from (a) a transverse wall to (b) an symmetric transverse wall and finally to (c) a vortex wall.

The simplest domain wall structure is the symmetric transverse wall in which the magnetic moments are orientated perpendicular to the nanowire axis. As the nanowire width and thickness increases the wall structure can become distorted and an asymmetric transverse wall becomes favourable. Increasing the nanowire width or thickness further allows the vortex wall to exist. The vortex wall is a flux closure structure since the magnetic moments exhibit a gradual rotation around the nanowire from one domain to the next. At the vortex core the moments point either upwards or downwards out of the nanowire plane.

In addition to its physical structure a domain wall also possesses chirality; where chirality refers to the sense of magnetisation rotation or the handedness within the domain wall. For a head-to-head transverse wall, for example, the magnetisation rotation may be either up or down, as shown in Figure 3:13. Similarly, for a vortex wall, the magnetisation rotation of the vortex may be either clockwise or counter-clockwise. In a symmetric nanowire structure these different chiralities are energetically equivalent states. Figure 3:14 presents the phase diagram by Nakatani [61] which is used to identify the type of domain wall structure present in $Ni_{80}Fe_{20}$ nanowires as a function of nanowire width and thickness. The boundary between the transverse and vortex wall states is found numerically to vary as:

$$w \cdot t = 61.37\Lambda^2 \qquad (3:24)$$

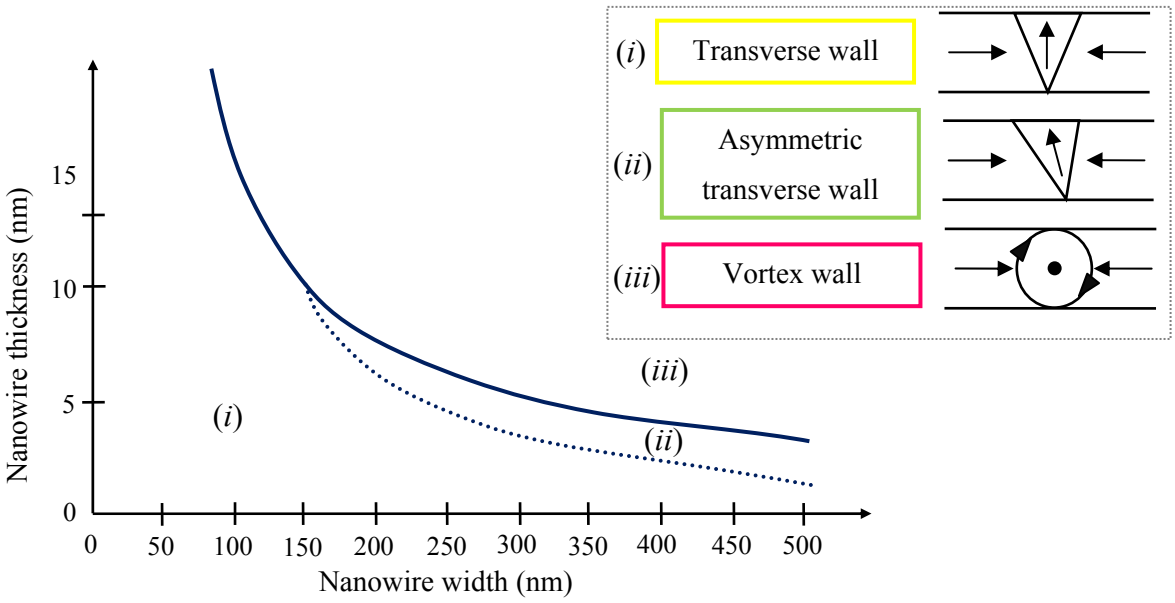

Figure 3:14. Phase diagram showing where the domain wall structures are most likely to exist in a $Ni_{81}Fe_{19}$ nanowire, reproduced from [61]. Simplified schematics of each wall structure are shown in the inset; these wall structures are shown in more detail in Figure 3:13.

Where w is the width of the nanowire, t is the nanowire thickness and Λ is the micromagnetic exchange length, defined as:

$$\Lambda = \sqrt{\frac{2A}{\mu_0 M_s^2}} \tag{3:25}$$

Where A is the exchange constant and M_s is the saturation magnetisation of the material. For $Ni_{81}Fe_{19}$, using $A = 13\text{x}10^{-12}$ J/m and $M_s = 860\text{x}10^3$ A/m yields an exchange length of approximately 5 nm. This length is very important for micromagnetic modelling and is discussed further in section 4.5.

Micromagnetic simulations reveal that the transition between the transverse wall and asymmetric transverse wall (i.e. going from (*i*) to (*ii*), as shown by the dotted line in Figure 3:14) is second order [61]. This means that it is not possible to distinguish between the two main domain wall structures when they are propagating under an applied magnetic field. The transition between the transverse wall and vortex wall (going from (*i*) to (*iii*) in Figure 3:14) is first order, which means that it is possible to distinguish between the two wall structures when the walls are propagating in an applied field.

When structural features such as notches are patterned within the nanowire, the spin structure tends to follow the local edges of these features. Notch structures alter the potential energy landscape that the domain wall experiences such that the domain wall structure that is favourable in the nanowire structure becomes trapped, or pinned. The pinning and propagation of domain walls in planar nanowires has become the focus of intense research. There are many proposed applications based on domain walls in nanowires, including both magnetic logic [62] and sensor [63] devices and more recently in magnetic memory concepts [64]. It can be seen in Figure 3:13 that the magnetisation varies significantly across the width of a nanowire for both transverse and vortex domain walls. The domain wall width for quasi-static domain walls in nanowires was estimated by Nakatani *et al.* in reference [61] by fitting the magnetisation profile to that of a 1D Bloch wall to yield:

$$\delta_{DW}^{TW} = \frac{w}{\pi}; \quad \delta_{DW}^{VW} = \frac{3w}{4} \tag{3:26}$$

These definitions indicate that the vortex wall is significantly wider than the transverse wall. Domain walls in planar nanowire structures are discussed in greater detail in chapter 7, where the pinning behaviour of domain walls in nanowires containing a single notch structure is investigated. The ambiguity surrounding the definition of wall width is

significant when identifying domain wall structure in planar nanowire structures using anisotropic magnetoresistance, as discussed in chapter 8. Indeed, the domain wall width is a critical parameter for both field and current-driven domain wall motion.

Chapter 4. Investigative techniques

4.1 Introduction

In this chapter, the techniques used to investigate the effect of geometrical confinement on the magnetic and magnetoresistance behaviour on of $Ni_{81}Fe_{19}$ thin films and nanowires presented in chapters 5 to 8 are discussed. A wide variety of investigative techniques are employed within this thesis including x-ray scattering, magneto-optical Kerr effect magnetometry, micromagnetic modelling and magnetoresistance measurements. For each technique, the relevant physical principles are described so that the analysis presented in chapters 5 to 8 can be understood. The experimental set up is then presented and the method of data collection outlined with key approaches to data analysis discussed as appropriate.

4.2 Preparation of thin films and nanostructures

4.2.1 Introduction

Advances in thin film preparation and lithographic fabrication technology of single atomic layers has pushed the critical dimensions of ferromagnetic structures further into the sub-micrometer regime and has allowed for the study of magnetism in one-and two-dimensional systems. In $Ni_{81}Fe_{19}$, as both the magnetocrystalline anisotropy and magnetostriction constants are simultaneously close to zero the magnetisation behaviour is primarily determined by the magnetostatics; that is, the shape of the element. For thin films, the magnetisation is confined to lie in-plane whilst for patterned nanostructures the domain structure follows the axial shape of the wire and any structural features that may be patterned along its length. In principle, the magnetic domain configuration in such structures is expected to be simplified as the dimensions of structures become comparable with both the exchange length and the domain wall width. Understanding the magnetisation processes in such magnetic structures is of fundamental interest and is important for device applications in magnetic memory [64] and magnetic logic devices [65].

Methods for thin film deposition include physical vapour deposition processes like thermal evaporation (as is used in this thesis), molecular beam epitaxy and sputtering due

to ion bombardment. The composition and structure of films can be controlled by the use of high vacuum deposition conditions. Techniques for creating nanoscale structures are classified as either 'bottom-up' or 'top-down', respectively. 'Bottom-up' refers to self-assembly or self-organisation methods, where short range interactions between large numbers of atomic, molecular, or nanoscale objects leads to long-range ordering. 'Top-down' techniques, on the other hand, rely on the direct writing of patterns by photolithography, electron-beam lithography or focussed ion-beam milling and can achieve large coherent areal coverage of nanoscale structures. Such techniques require a serial exposure of either the structures, or in the case of photolithography, a mask of the structures to be fabricated.

The following sections describe the preparation of samples including the thin film deposition and lateral patterning techniques used to fabricate samples for characterisation by x-ray scattering, magneto-optical Kerr effect magnetometry and magnetoresistance techniques.

4.2.2 Substrate preparation

Single crystal silicon wafers, topped with approximately 0.5 μm of hydrothermally grown SiO_2, were cut into square chips (of approximate area 10 mm^2) and elongated strips (approximate dimensions 27 mm x 3 mm) using a diamond scribe. Once cut, each chip/strip was washed in acetone for 60 seconds and then in isopropan-2-ol (IPA) for a further 60 seconds; each cleaning process was performed using ultrasonic agitation so as to remove any grease or debris from the surface of the chip. Each chip was then dried using a nitrogen gun to apply dry N_2 at glancing angle.

4.2.3 Thermal evaporation of thin films

Thin film samples studied in chapter 5 and 6 were prepared by thermal evaporation. Single layer $Ni_{81}Fe_{19}$ thin films were deposited onto the prepared substrates using a custom built high vacuum thermal evaporator system, a simplified schematic of which is shown in Figure 4:1. This system utilises a VAT turbo pump, backed up by an Edwards roughing pump so as to achieve base pressures of the order of 10^{-8} Torr, with typical growth pressures of the order 10^{-6} Torr as monitored by an ionisation gauge.

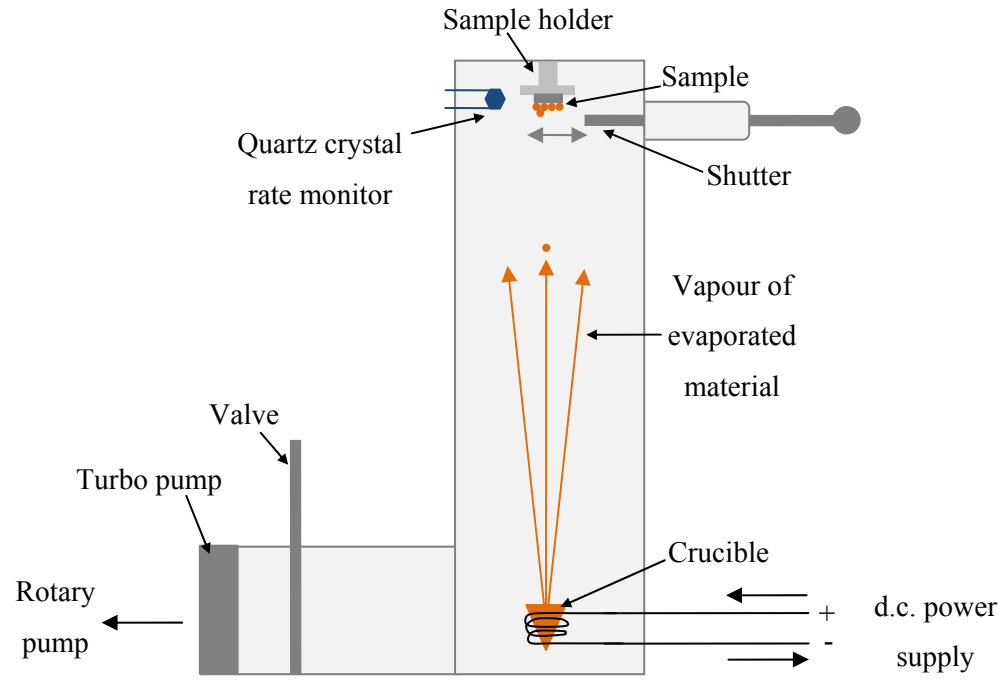

Figure 4:1. Schematic diagram of the side view of the thermal evaporator system.

The source material to be deposited was held in ceramic coated tungsten wire crucibles located at the base of the thermal evaporation system, which can hold a maximum of three crucibles. Substrates were secured to a holder, located at the top of the thermal evaporation system, using polymethylmethcrylate (PMMA) as an adhesive to minimise the amount of stress on the sample substrate during film growth.

Substrates were located a distance of approximately 0.5 m from the source crucible; a large separation between the substrate and the crucible permits a stable and uniform deposition over the entire substrate surface. Deposition of the source material was achieved by resistive heating of the crucible element, controlled by a Glassman d.c. power supply, which caused the powdered metal to melt and evaporate. Once a stable and appropriate deposition rate was achieved the shutter protecting the sample was opened and a film deposited onto the substrate.

Thickness was controlled by varying the power dissipated in the crucible, and the deposition rate was monitored using an *in situ* quartz crystal oscillator located close to the substrates, although it did not distort or block the rising plume of vaporised material. As material is deposited onto the quartz crystal its resonant frequency changes slightly; since frequency is inversely proportional to the square root of the mass of the oscillator, this allows for monitoring of the deposition down to the sub-nanometre regime.

Prior to each deposition, the crucible sources were 'baked-out' where the mechanical shutter was kept closed whilst the respective crucible sources were heated. The performance of a bake-out is beneficial for several reasons. In general, performing a bake-out increases the quality of the film deposited since it lessens the degree of oxide formation during film growth and allows for a lower base pressure to be obtained following the bake-out. In addition, this process also helps to remove any residual adsorbed water and other contaminants from the source materials since it helps to clean the interior of the evaporation chamber and heating of the crucible also causes the chamber to warm. Finally, this process allows the source current to be established for the actual deposition.

4.2.4 Description of samples

Thin film samples studied in chapters 5 and 6 had thicknesses which ranged from 3 nm to 40 nm. For each nominal film thickness, a total of three samples were deposited using different deposition rates. The rates of deposition were kept stable at 0.5 Å/s, 1.0 Å/s and 2.0 Å/s respectively, and were controlled by controlling the current applied to the crucible. Deposition of films occurred from a single ceramic coated tungsten wire crucible source, although for the highest rate of deposition two identical crucibles sources were used to achieve a stable deposition rate of 2.0 Å/s. The crucible source(s) were regularly topped up with powdered $Ni_{81}Fe_{19}$ between successive depositions.

The size and shape of the silicon substrate 'chips' was selected for characterisation of samples using specular x-ray reflectivity, x-ray diffraction and magneto-optical Kerr effect magnetometry. Magnetoresistance measurements were performed on elongated rectangular strips; the large aspect ratio of the strips was optimised to give a uniform current distribution along the long axis.

4.2.5 Patterning of planar nanowire structures

The nanowire samples studied in chapters 7 and 8 were prepared by electron-beam lithography. Electron-beam lithography uses a scanned electron beam to write structures in an electron-sensitive resist. Structures were designed using Raith specialist software which also controlled the electron beam in an FEI field-emission electron microscope. The basic features of the electron-beam lithography system used for patterning structures

studied in this thesis are shown in Figure 4:2. A tungsten cathode or field emission gun produces a beam of electrons which is focussed and deflected by a series of magnetic lenses to a specific point on the resist. The lenses are usually multipolar so that astigmatism of the beam can be eliminated. The beam spot size was determined by the degree of focussing; typical diameters are between five and ten nanometres for a field emission source. This technique has a much higher resolution than optical lithography, and is capable of producing structures as small as 10 nm [66]. The exposure region is primarily controlled by deflecting the beam using local high frequency magnetic fields from deflectors. Imaging of the surface was performed by measuring the intensity of scattered electrons as the beam is raster scanned across the sample.

The exposure process used to define nanowire structures is shown schematically in Figure 4:3. For a positive lithography resist such as polymethylmethcrylate (PMMA) it is the exposed regions of resist that are removed and thus become the areas whose features remain at the end of the process. The resist was spin-coated onto the substrate to a thickness of approximately 50 nm; a small ratio of film thickness to resist thickness was used to provide high quality edges.

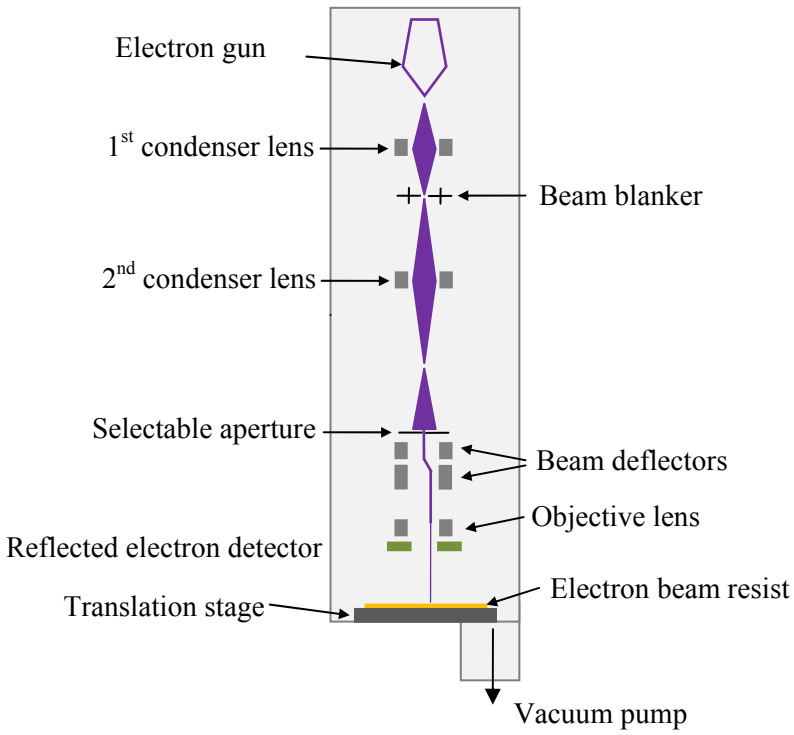

Figure 4:2. Simplified schematic of the FEI field emission electron microscope used in conjunction with specialist Raith software to design and write patterned nanostructures.

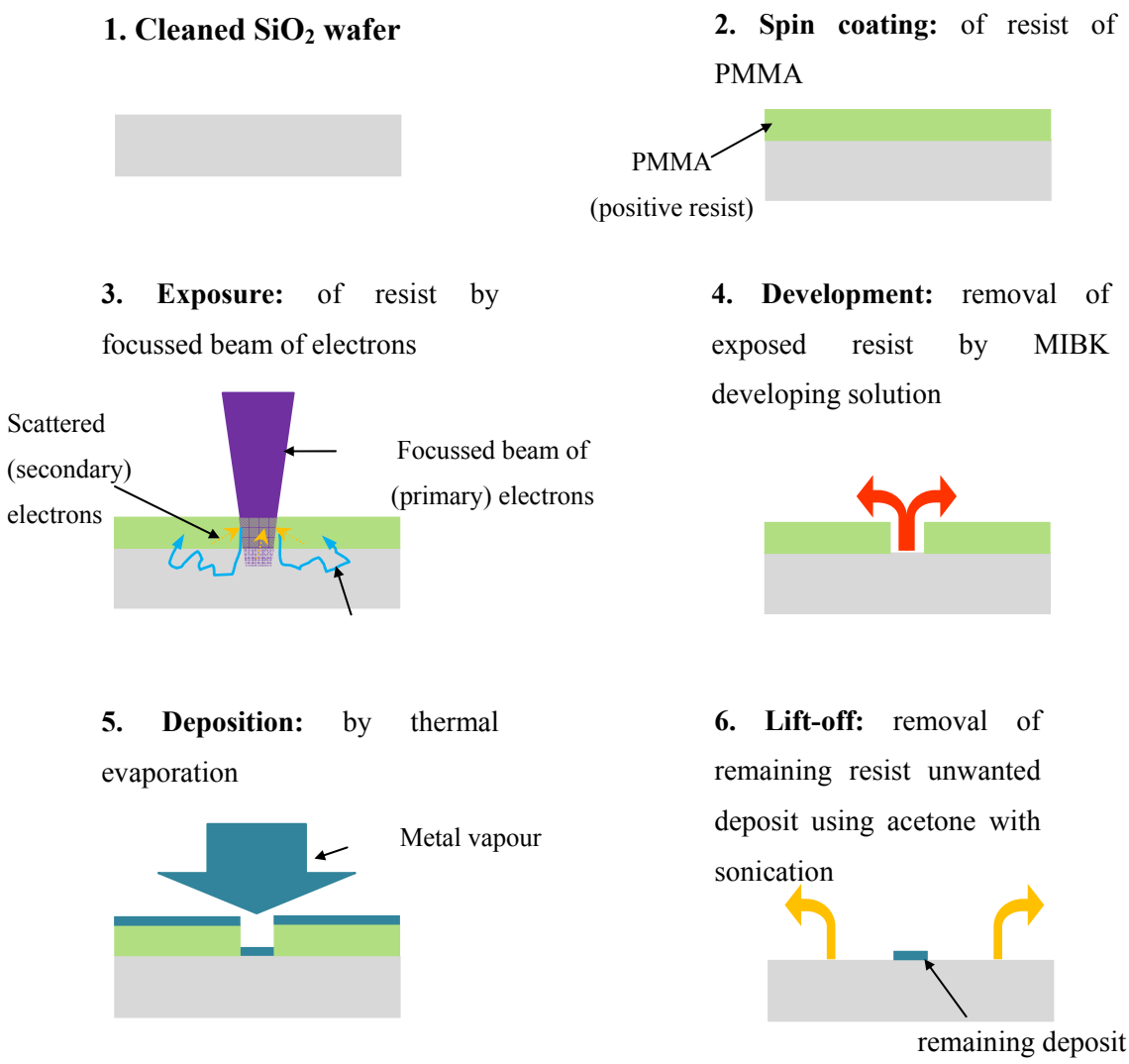

Figure 4:3. A schematic flow diagram to illustrate the six steps taken in the fabrication of planar nanowire elements using electron beam lithography and thermal evaporations.

The electron beam was moved across the sample and the substrate was exposed to the electron beam following a pattern defined in the Raith software; with a sufficient dose of electrons a given area of electron resist becomes soluble in the developer. Polymer chains are broken down when electron energies greater than 5 eV are used which means that the high energy electron beam does not directly cause changes in the resist. Instead, it is the secondary electrons which cause scission of the polymer chains into lower weight molecules which are soluble in a developing solution. Development in a 3:1 solution of IPA to methylisobutylketone (MIBK) under ultrasonic agitation is typical for a PMMA resist. This solution dissolves the away the PMMA that is weakened from electron exposure, whilst the ultrasonic agitation assists in the removal of solutions and effectively

removes any exposed areas of PMMA. The unexposed areas remained attached to the substrate and protected the remainder of the chip from being metalised.

Following development a thin film was deposited by thermal evaporation. The evaporated film coats the entire chip including the gaps between both the exposed and remaining unexposed PMMA. The final stage required any unexposed areas of remaining resist to be removed. During 'lift-off' the chip was placed in acetone under the action of ultrasonic agitation, which effectively removed any unexposed areas of PMMA and left lithographically defined nanostructures. Further details of the electron-beam lithography process used in Durham are given by Atkinson in [67].

4.3 X-ray scattering

4.3.1 Introduction

X-rays were discovered by Röntgen [68] in 1895 and have since become established as an invaluable probe of the structure of matter. X-ray scattering provides an excellent tool for the structural analysis of thin films as the wavelengths of x-rays are of the order of atomic distances. Furthermore, x-ray scattering is usually non-destructive and leaves the sample investigated intact.

Characterisation of the microstructure of $Ni_{81}Fe_{19}$ thin films presented in chapter 5 is achieved using two x-ray scattering techniques; grazing incidence specular x-ray reflectivity and high angle x-ray diffraction. Specular x-ray reflectivity measures electron density changes normal to the surface and has provided precise measurements of film thickness and information on interface widths. X-ray diffraction peaks have provided information on the out-of-plane crystallographic structure; in polycrystalline thin films such as $Ni_{81}Fe_{19}$, the diffraction peaks can reveal information on the preferred crystallographic orientation of crystallite grains as well as quantifying the size, shape and degree of strain present within the grains.

In the following sections the underlying theory and relevant principles behind the x-ray scattering techniques used to study the structural properties of $Ni_{81}Fe_{19}$ thin films are described. Full derivations are not provided since the focus is on understanding how x-ray scattering phenomena may be used to yield specific information on the structural properties of $Ni_{81}Fe_{19}$ thin films. This is followed by a description of experimental techniques and concludes with a description of the analysis techniques used.

X-ray scattering principles

In the classical description of scattering, an electron is forced to oscillate when placed in the electric field of an incident x-ray. The discussion presented in this thesis is limited to the classical description of scattering in which the re-radiated field is at the same frequency as the incident wave frequency and is referred to as elastic or Thomson scattering. An oscillating electron acts a source and re-radiates a spherical wavefront in all directions; as such, the scattering strength is normalised to the scattering of a single electron.

The discussion presented in the following sections is based upon three key assumptions. Firstly, it is assumed that scattering intensity of x-rays is weak, that is, once the x-ray has been scattered, re-scatter of the incident beam does not occur. This is the *kinematical* approximation, and is a reasonable assumption for most scattering geometries. Examples of weak scattering include the scatter of x-rays from very thin crystals, surface scattering and diffuse scattering. The kinematical assumption breaks down when the scattering is strong, for example, for the diffracted intensities and rocking curve widths of thick, near-perfect crystals. In such situations *dynamical* theory must be employed, which is beyond the scope of this study. Secondly, it is assumed that the point of observation for the scattered beam is at a large distance compared with the dimensions of any coherently illuminated scattering volume. Thirdly, it is assumed that the scattered waves from different atoms are essentially parallel and can all be labelled with a single wavevector $\mathbf{k}_{out}$. The combination of the second and third assumptions is known as the Fraunhofer, or far-field, approximation.

The scattering geometry

The scattering vector **q** is geometrically defined in Figure 4:4. This figure shows the experimental scattering geometry as relevant to both x-ray reflectivity and x-ray diffraction techniques. The scattering plane is normal to the sample surface and contains both the incident and scattered directions. In general, an incident wavevector $\mathbf{k}_{in}$ makes an angle α_{in} with the surface and the scattered wavevector $\mathbf{k}_{out}$ makes an angle $(2\theta - \alpha_{in})$. In elastic scattering the wavelength of the scattered wave is the same as that of the incident one, which allows the magnitude of the wavevector to be defined as $|\mathbf{k}| = 2\pi/\lambda$.

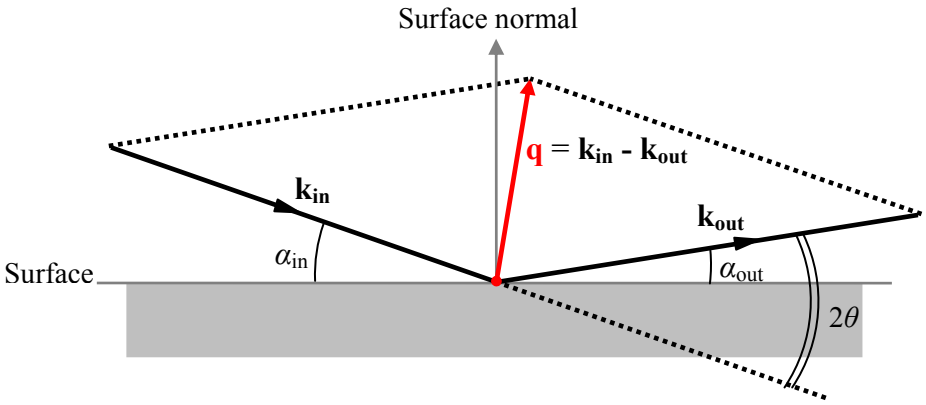

Figure 4:4. Definition of the scattering vector **q** and its relation to the incident and scattering wavevectors in the experimental geometry. 2θ relates the angle of the detector to the incident beam.

By convention, the scattering angle is labelled as 2θ; experimentally this relates the angle of the detector relative to the incident beam. The scattering vector **q** is related to the incident and reflected wavevectors by the relation:

$$\mathbf{q} = \mathbf{k}_{in} - \mathbf{k}_{out} \tag{4:1}$$

Where $\mathbf{k}_{in}$ and $\mathbf{k}_{out}$ are the wavevectors of the incident and scattered beam respectively. The scattering vector corresponds to a distance in reciprocal space and has units of inverse length. In specular x-ray reflectivity, the incident and scattered angles are equal.

The condition for grazing incidence is defined as that when the angle of incidence is either at or just above the critical angle for transmission into the material. For an x-ray beam at grazing incidence to the sample, the scattering vector **q** is small, which corresponds to a large real-space length vector. As such, x-ray reflectivity techniques are sensitive to the electron density profile over many hundreds of atomic layers. For films less than 1 μm thick, grazing incidence specular x-ray reflectivity measurements can provide valuable information of the thickness, density and roughness of the film normal to the surface of the sample.

In x-ray diffraction a strong scattered intensity is observed at specific angles of scattering, known as the Bragg angles. As both the scattering angles and corresponding scattering vector **q** are large, the distance probed in real space is small - typically of the order of Ångstroms. As such, x-ray diffraction measurements provide information on the interatomic structure of crystalline materials normal to the surface of the sample.

4.3.2 Principles of grazing incidence specular x-ray reflectivity

The reflectivity from a single interface is determined by both the difference in refractive index above and below the surface and by the width of the interface region. The refractive index is directly related to the scattering factor of a medium, which in turn depends upon the atomic number Z_A and the electron density, $\rho_A(\mathbf{r})$. This section describes the reflection and transmission behaviour of x-rays at an ideal interface, and provides a brief discussion as to how this behaviour can be generalised to n interfaces. An understanding of the physical process that occur when x-rays interact with a medium allows for confident interpretation of experimental results presented in chapter 5.

The refractive index of a material

The absolute index of refraction of a medium, n, is defined as the ratio of the phase velocity of an electromagnetic wave in a vacuum, c, to the phase velocity of the wave in matter, v:

$$n = \frac{\mathrm{c}}{v} \tag{4:2}$$

The refractive index of a material is written in the form:

$$n = 1 - \delta + i\beta \tag{4:3}$$

Where δ and β are coefficients related to the dispersion and absorption respectively. For x-ray radiation, both δ and β are small and positive and of the order of 10^{-6} and 10^{-8} respectively, yielding a refractive index ~ $1\text{x}10^{-5}$ less than unity. Equation (4:3) quantifies the deviation of the refractive index from unity, and may be expressed as:

$$n = 1 - \frac{r_0}{k^2}\sum_{\mathrm{A}}\rho_{\mathrm{A}}\left(Z_{\mathrm{A}} + f_{\mathrm{A}}^{'} - if_{\mathrm{A}}^{''}\right) \tag{4:4}$$

Where r_0 is the classical electron radius, ρ_A is the atomic number density, k is the wavevector and Z_A is the atomic number and $f_A^{'}$, $f_A^{''}$ correspond to the real and imaginary parts of the dispersion correction to the scattering (the subscript denotes the parameters relating to element A) [69]. This equation shows the refractive index depends primarily on the electronic density, which is given by $\rho_A Z_A$ for element A. Using values stated in [70], the electronic density of iron and nickel are 2.2073 electrons/Å^3 and 2.5588 electrons/Å^3 respectively; the electron density for $Ni_{81}Fe_{19}$ is deduced to be 2.4920 electrons/Å^3. As the amount of x-ray scattering is directly proportional to the electron density, accurate

determination of the refractive index of $Ni_{81}Fe_{19}$ allows the behaviour of x-rays at an interface between media of different electron density to be understood.

The reflection and transmission behaviour of x-rays at an interface

X-ray radiation incident from air onto a material interface sees the material as being optically less dense. As a result the transmitted beam is refracted away from the surface normal, as shown in Figure 4:5. This behaviour is described by Snell's law, which relates the incident grazing angle, α_i to the transmitted angle, α_t, via:

$$n_0 \cos\alpha_i = n_1 \cos\alpha_t \tag{4:5}$$

Where n_0 and n_1 are the refractive indices of the two materials, respectively. As the angle of incidence, α_i, decreases, the angle between the transmitted wave and the surface, α_t, also decreases.

Total external reflection will occur at the air-medium interface for x-rays incident on a medium at low grazing angles, as the angle of transmission is always less than the angle of incidence. The critical angle α_c is defined as the angle at which total external reflection ceases and the transmitted wave travels parallel to the surface. If the wave is incident from vacuum or air, $n_{air} \approx n_{vacuum} = 1$, the critical angle α_c (where $\alpha_t = 0$) can be derived from Snell's law:

$$\cos\alpha_c = n_1 \approx 1 - \frac{\alpha_c^2}{2} + \ldots \tag{4:6}$$

Within the kinematical theory, it is assumed that there is no absorption of the incident beam, which means that $\beta = 0$. Thus the critical angle is given by:

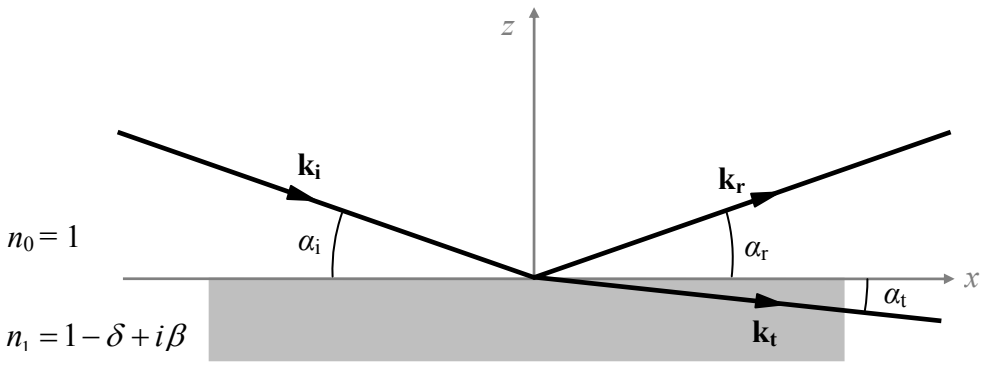

Figure 4:5. Reflection and transmission at an ideal interface between materials of different electron densities.

$$\alpha_c \approx \sqrt{2(1-n_1)} \approx \sqrt{2\delta} \tag{4:7}$$

Where δ is the real part of the deviation of the refractive index from unity, and is related to dispersion effects. Measurement of the critical angle yields directly the electron density in the near-surface region. For CuK_β radiation (8.905 keV) the dispersion constant for $Ni_{81}Fe_{19}$ is 2.0409 x 10^{-5} [71], which yields a critical angle of approximately ~ 0.37°.

The behaviour of an electromagnetic wave moving between media of different refractive indices is described by the Fresnel equations. Expressions for the Fresnel amplitude coefficients of the reflectivity and transmission are derived thoroughly in [69] and are stated in angular terms as:

$$r = \frac{n_0\alpha_{i,r} - n_1\alpha_t}{n_0\alpha_{i,r} + n_1\alpha_t} \tag{4:8}$$

$$t = \frac{2n_0\alpha_{i,r}}{n_0\alpha_{i,r} + n_1\alpha_t} \tag{4:9}$$

Experimentally it is the intensity of reflectivity and transmission that is measured; the corresponding intensity coefficients R and T are given by $R = |r|^2$ and $T = |t|^2$. At the critical angle, the incident beam is predominately transmitted into the sample and the reflectivity drops sharply as α_i^{-4}. This behaviour will change, however, if there is more than one possible reflection-transmission process.

Specular reflectivity from a single thin film on an infinite substrate

It is pertinent to now consider the reflection-transmission behaviour of x-rays incident on a single thin film upon an infinite substrate, as shown in Figure 4:6.

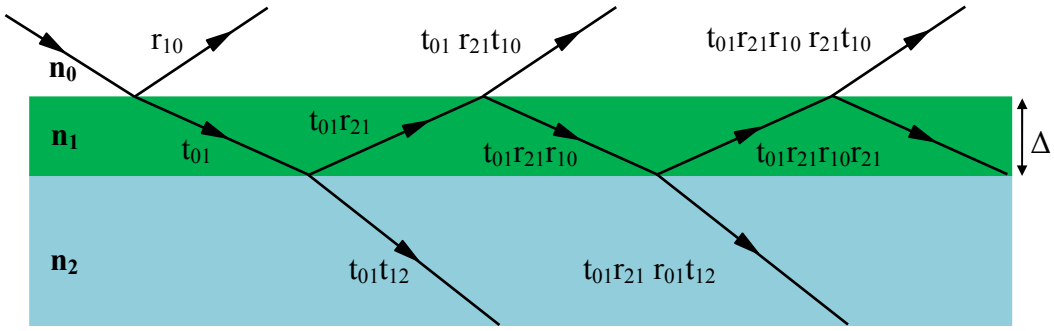

Figure 4:6. Reflection and transmission of incident x-rays in the case of a finite layer of thickness Δ and refractive index n_1 upon an infinitely thick substrate layer with refractive index n_2.

Due to the finite thickness of the thin film sample, denoted by Δ, and the presence of multiple interfaces, there are numerous reflection and transmission processes that can occur. The total reflectivity of the layer is an infinite sum of all possible reflections:

$$r_{\text{total}} = r_{10} + t_{01}r_{21}t_{10}p^2 + t_{01}r_{21}r_{10}r_{21}t_{10}p^4 + \ldots = r_{10} + t_{01}r_{21}t_{10}p^2\sum_{m=0}^{\infty}\left(r_{21}r_{10}p^2\right)^m \qquad (4:10)$$

Where p^2 is a phase factor given by $p^2 = \mathrm{e}^{(iq_1\Delta)}$ with $q_1 = 2k_1\sin\alpha_1$. The summation of the total reflectivity can be evaluated as a geometric series, which is expressed as:

$$r_{total} = r_{10} + \frac{t_{01}r_{21}t_{10}p^2}{1 + r_{10}r_{21}p^2} \qquad (4:11)$$

Examples of the simulated reflectivity for two perfectly sharp $Ni_{81}Fe_{19}$ layers 5 nm and 10 nm thick on an infinite silicon substrate are shown in Figure 4:7. In each simulation, a sharp drop in intensity occurs at the critical angle, after which there are a number of resulting interference fringes are known as Kiessig fringes [72]. Kiessig fringes result from interference between waves scattered from the bottom and top surfaces of thin films. Far from the critical angle, for a single film the period of the Kiessig fringes is inversely related to the film thickness Δ via:

$$\Delta = \frac{\lambda}{\alpha_{m+1} - \alpha_m} \qquad (4:12)$$

Where α_m is the location of the mth fringe. The number of Kiessig fringes is proportional to the thickness of the sample; as the thin film thickness increases the number of fringes also increases, as seen in Figure 4:7.

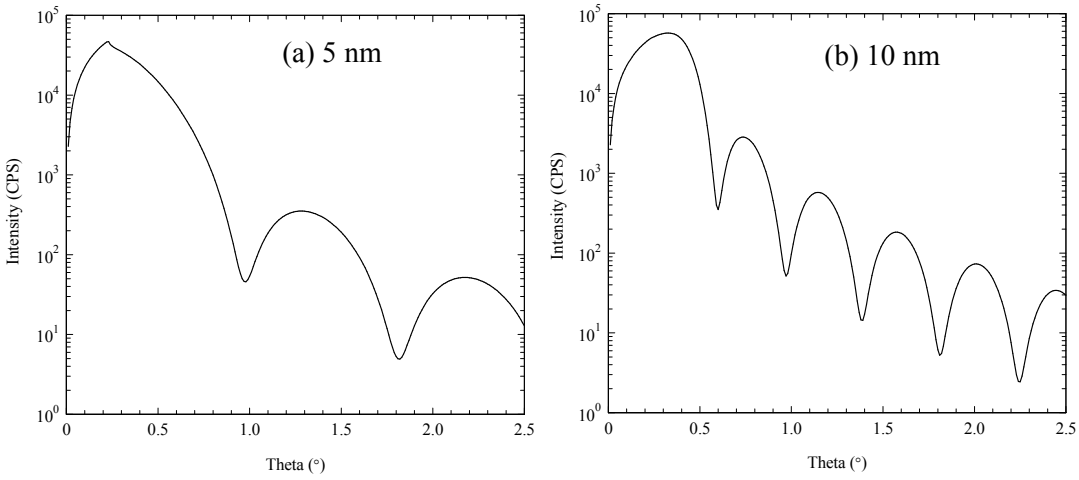

Figure 4:7. Simulated specular reflectivity from (a) a single 5 nm and (b) 10 nm layer of $Ni_{81}Fe_{19}$ on silicon substrate with a perfectly sharp interface.

For a given film thickness, the spacing of the fringes is almost constant (except at very low angles) and can be used to provide an estimate the film thickness. At very low angles, the fringes are a little more closely spaced due to the small effect of refractive index in the near surface region. The amplitude of the fringes is related to the topographic roughness and the chemical grading of the interfaces, as shown in Figure 4:8. In real systems, the interface between two materials is neither perfectly smooth nor chemically sharp with both effects leading to broadening of the Kiessig fringes. A specular reflectivity scan, however, is sensitive only to the average refractive index as a function of depth, z, and can therefore quantify only the value of the interface width; it is not possible to identify the type of interfacial roughness.

Grazing incidence specular x-ray reflectivity has been used to measure layer thickness, density and the interface width of $Ni_{81}Fe_{19}$ thin films. Sensitivity to the in-plane sample structure is gained when there is a component of the scattering vector in the plane of the sample as is the case of a transverse scan. Diffuse reflectivity scans must be used to separate the roughness from chemical intermixing. However, due to signal to noise conditions transverse scans typically require synchrotron radiation sources, and are beyond the scope of the work presented here.

Figure 4:8. Examples of the type of transition that can exist at an interface between two materials (a) topologically rough and (b) chemically graded interface.

4.3.3 Experimental set up for grazing incidence specular x-ray reflectivity

Specular x-ray reflectivity measurements presented in chapter 5 were made with a Bede GXR1 reflectometer using monochromated CuK_{β} radiation at a wavelength of 1.3922 Å; a schematic of the reflectometer equipment is shown in Figure 4:9. X-rays were produced from a sealed tube source containing a water-cooled copper target using a generating power of 1.6 kW (40 kV; 40mA).

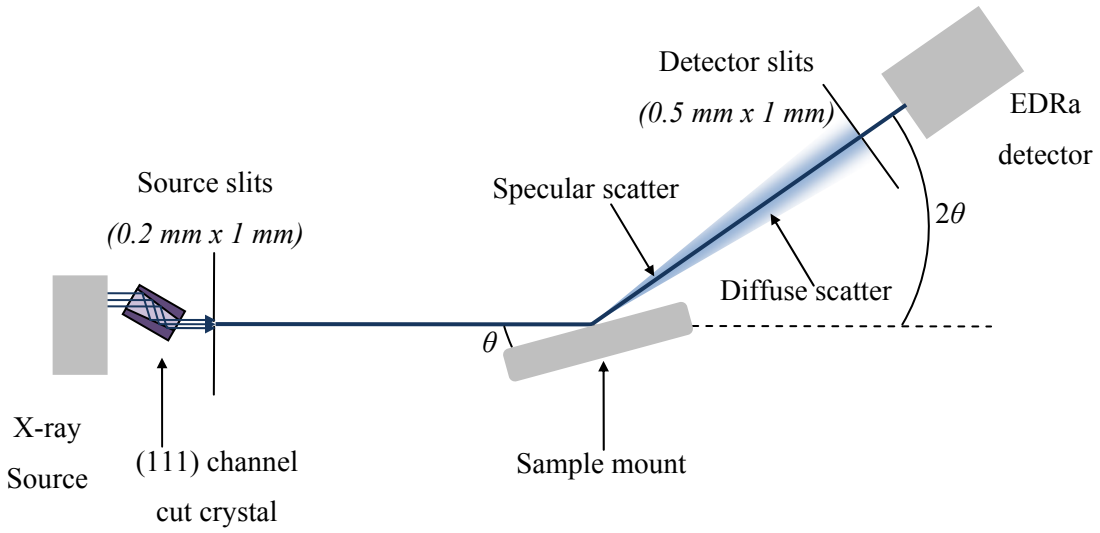

Figure 4:9. Plan view of the geometry of the set-up within the GXR1 reflectometer which utilises an EDRa scintillation detector. X-ray reflectivity measurements were obtained using CuK_β radiation at an energy of 8.905 keV.

The x-ray beam passes through a [111] asymmetric channel-cut silicon crystal which monochromated the incident beam to provide CuK_β radiation. The source slits were set to condition the x-ray beam to a spot size of 0.2 mm x 1 mm, with a divergence of approximately 0.01°. The large size of the x-ray beam spot allowed a large amount of the sample to be illuminated with a parallel beam of incident x-ray radiation. X-rays were incident on the sample at an angle θ, and the resulting intensity was measured using an EDRa detector located at 2θ. The angular acceptance of the detector was limited by a detector slit size of 0.5 mm.

For each thin film sample, a coupled θ-2θ specular scan was obtained over the range $0° < 2\theta < 6°$. In addition, a corresponding off-specular scan (which was offset from the specular condition by 1°) was also measured to provide information on the background signal. The true specular scan was obtained by subtracting the intensity of the off-specular scan from the specular scan; otherwise the specular scan does not provide accurate information on the nature of Kiessig interference fringes required to obtain detailed knowledge of the out-of-plane structural properties of thin films.

4.3.4 Data fitting techniques for grazing incidence x-ray reflectivity

Fitting of specular x-reflectivity scans was performed using the Bede REFS simulation software package [73]. Bede REFS is based upon the Parratt recursive formulism [74] and is used to simulate the x-ray reflectivity so that the thickness of thin film structures can be accurately quantified. This was done by employing genetic and evolutionary algorithms to fit the experimentally measured data; details of the algorithm can be found in [75]. In each simulation, the layer thickness, interface width and density were allowed to vary as free parameters with nominal values of film thickness introduced as starting values to ensure the simulation converges in a sensible time.

4.3.5 Principles of x-ray diffraction

In this section the physical principles of x-ray diffraction within the kinematical approximation are discussed. X-ray diffraction is the constructive interference of coherently scattered x-rays that are scattered from groups of electrons arranged in a periodically ordered array on the length scale of the wavelength of the incident radiation. The incident wave is assumed to be a plane wave, which means that the phase is constant over an extended wavefront perpendicular to the direction of travel. It is further assumed that when this wave interacts with a crystal lattice each atom re-radiates a spherical wavefront. For the majority of directions, these wavefronts will interfere destructively and sum to give overall total amplitude of zero. These wavefronts interfere constructively to produce diffraction peaks in a few specific directions only. This phenomenon is most apparent when the wavelength of the incident radiation is similar to the periodicity of the point scatters.

Bragg's law

The Bragg condition for the constructive interference of waves is shown in Figure 4:10. When the path difference between adjacent incident plane waves is equal to $n\lambda$, the x-rays scattered from the two centres are in phase and will interfere constructively in the far-field. This condition is met when the waves are incident at the Bragg angle, θ_B and is:

$$n\lambda = 2d_{hkl}\sin\theta_B \tag{4:13}$$

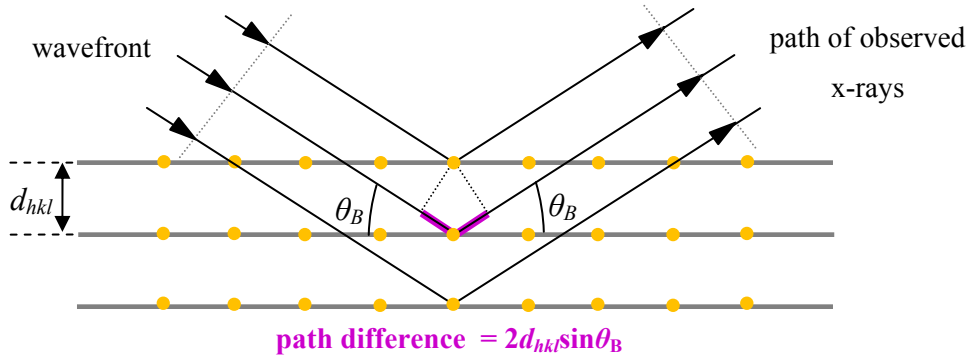

Figure 4:10. Geometrical construction for the derivation of Bragg's law, where orange dots correspond to scattering centres. The path difference is highlighted in purple.

Where d_{hkl} is the interplanar spacing and n is an integer related to the order of diffraction. This is Bragg's law [76], and is the simplest mathematical construction of diffraction phenomena. In a regular crystal lattice the Bragg condition will be simultaneously true for all point scatterers related by the same translational symmetry. As a consequence, there is a dramatic increase in the scattered x-ray amplitude which produces sharp diffraction peaks.

Reciprocal lattice and the Laue condition

Any vector in real space may be defined by the real space lattice vector, **R**, given by:

$$\mathbf{R} = n_1\mathbf{a}_1 + n_2\mathbf{a}_2 + n_3\mathbf{a}_3 \tag{4:14}$$

Where $\mathbf{a}_1, \mathbf{a}_2$ and $\mathbf{a}_3$ are three primitive basis vectors of the lattice. As x-ray diffraction provides information on the nature of reciprocal space, it is useful to define the reciprocal lattice vector, **G**, which is given by:

$$\mathbf{G} = h\mathbf{a}_1^* + k\mathbf{a}_2^* + l\mathbf{a}_3^* \tag{4:15}$$

Where (*h*,*k*,*l*) are the Miller indices. These are integers relating to the reciprocal lattice and correspond to the reciprocal of the distances from the origin to the plane that cuts the axes $\mathbf{a}_1^*, \mathbf{a}_2^*$ and $\mathbf{a}_3^*$ respectively, and $\mathbf{a}_1^*, \mathbf{a}_2^*$ and $\mathbf{a}_3^*$ are three perpendicular primitive basis vectors of the lattice. The reciprocal space lattice vectors are related to the real space lattice vectors by the relations:

$$\mathbf{a}_1^* = \frac{\mathbf{a}_2 \times \mathbf{a}_3}{\mathbf{a}_1 \cdot \mathbf{a}_2 \times \mathbf{a}_3} \quad \mathbf{a}_2^* = \frac{\mathbf{a}_3 \times \mathbf{a}_1}{\mathbf{a}_1 \cdot \mathbf{a}_2 \times \mathbf{a}_3} \quad \mathbf{a}_3^* = \frac{\mathbf{a}_1 \times \mathbf{a}_2}{\mathbf{a}_1 \cdot \mathbf{a}_2 \times \mathbf{a}_3} \tag{4:16}$$

The reciprocal lattice axes are perpendicular to the (100), (010) and (001) planes in the real space lattice. In general, all directions in real space are preserved in reciprocal space. Each reciprocal lattice point represents the whole set of planes of interplanar spacing d_{hkl}. For a cubic lattice, the interplanar spacing is given by:

$$d_{hkl} = \frac{a_0}{\sqrt{h^2 + k^2 + l^2}} \tag{4:17}$$

Where a_0 is the lattice parameter and (h,k,l) are the Miller indices.

The Laue condition [77] defines the location of diffraction peaks in reciprocal space relative to the crystal lattice, and is given by:

$$\mathbf{G} = \mathbf{q} \tag{4:18}$$

The Laue condition is a vector equation, which says that the scattered amplitude from a crystallite is non-vanishing only when the scattering vector **q** coincides with a reciprocal lattice vector. It is only when this condition is fulfilled that all of the phases of the scattered waves coherently sum to produce an intense signal. The Laue condition is completely equivalent to the Bragg condition. Assuming that the diffraction peaks are not limited by the resolution of the detector, the weak scattering from atoms is reinforced by successive planes of atoms scattering in phase. Strong intensity of a diffraction peak is achieved by this reinforcement; as such x-ray diffraction techniques integrate the scattering over many atomic layers.

Intensity of diffraction peaks

The Bragg reflections that are accessible in any x-ray diffraction experiment must be within the Ewald limiting sphere, which is defined by the x-ray wavelength. Furthermore, the number of diffraction peaks are confined to distinct points in reciprocal space as described by the Laue condition. The intensity at each diffraction peak is modulated by the absolute square of the unit cell structure factor and the multiplicity factor, which is determined by the crystal structure of the element.

When x-ray radiation is scattered from a crystal lattice, each of the atoms within the unit cell will scatter the incident radiation. However, because of the periodic arrangement of the atoms, the interference of scattered waves causes a distinct pattern of constructive and destructive interference to form. This pattern is determined by the structure factor,

F(*hkl*), which describes how an incident beam is scattered by atoms of a unit cell. The structure factor is given by:

$$\mathbf{F}(hkl) = \sum_{n=1}^{N} f_n \exp\left[2\pi i\left(hx_n + ky_n + lz_n\right)\right] \tag{4:19}$$

Where (*hkl*) are the Miller indices and f_n is the atomic form factor, for atom type *n*. The atomic form factor represents the scattering amplitude of a wave from a single atom and is proportional to the electron density. The atomic form factor depends upon the type of radiation and thus f_n for x-rays is not the same as that for neutron scattering. The structure factor accounts for the spatial distribution of the atoms within the unit cell. For face-centred cubic crystals the structure factor becomes:

$$\begin{aligned}\mathbf{F}_{fcc}(hkl) &= f_n\left[1 + \exp(\pi i\left(h+k\right)) + \exp(\pi i\left(h+l\right)) + \exp(\pi i\left(k+l\right))\right] \\ &= \begin{cases} 4f & \text{all } hkl \text{ even/odd} \\ 0 & hkl \text{ mixed} \end{cases}\end{aligned} \tag{4:20}$$

The multiplicity factor arises from there being more than one plane of the type {*hkl*}. Equation (4:19) describes the allowed Miller indices at which Bragg reflections will occur and thus relates the position of atoms within a unit cell to the intensity of a reflection. The allowed reflections for bulk $Ni_{81}Fe_{19}$ for CuK_α incident radiation (λ = 1.5406 Å) within the range $0° < 2\theta < 80°$ are listed in Table 4:1. The location of the silicon (004) peak from the substrate is also included since it is used as a fixed reference when locating the positions of diffraction peaks from $Ni_{81}Fe_{19}$ thin films.

Material composition	$a_{\mathbf{bulk}}$ **(Å)**	**Miller indices**	$2\theta_B$ **(°)**
$Ni_{81}Fe_{19}$	3.551	111	44.142
		002	51.429
		022	75.702
Si	5.431	004	69.131

Table 4:1. List of allowed Bragg reflections and angular location for CuK_α radiation incident on bulk $Ni_{81}Fe_{19}$ and Si. Values of bulk lattice parameters for $Ni_{81}Fe_{19}$ and Si taken from p. 104 [54] and [78], respectively.

It can be seen that for $Ni_{81}Fe_{19}$, which has a face-centred cubic structure, the lowest order planes that are allowed to diffract are the {111}, {002} and {022} families of planes. Higher order diffracting planes can occur, for example the (311) and (222) planes, although these occur at angles greater than the range of interest.

4.3.6 Experimental set up for high angle x-ray diffraction

High angle x-ray diffraction was used to measure the out-of-plane lattice parameter, grain size and preferred crystallite orientation of polycrystalline $Ni_{81}Fe_{19}$ thin films. All measurements were performed on a Bede D1 diffractometer using a MicroSource® that was filtered to produce predominantly CuK_α x-rays (1.5406 Å). The MicroSource® generates x-rays using an electromagnetically focussed and positioned electron beam that impacts on a water-cooled copper target at 80 W (40 kV; 2 mA). A schematic of the geometry used within the D1 diffractometer is shown in Figure 4:11.

The x-ray beam was focussed with a polycapillary optic, yielding a parallel beam with approximately 0.2° divergence, allowing a high intensity beam of x-rays to be produced.

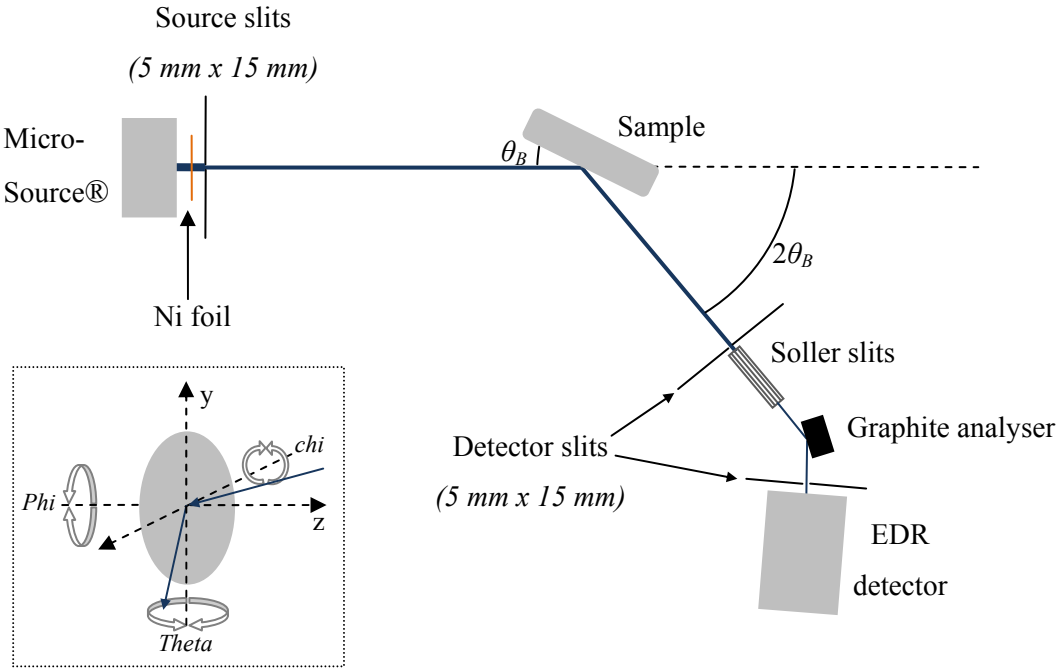

Figure 4:11. Plan view of the geometry of the Bede D1 diffractometer with MicroSource® which has a copper target and produced CuK_α radiation. The Ni foil was used to attenuate the $CuK_{\alpha 2}$ peak. The inset in the bottom left hand corner shows a side view of the sample mount in which the directions of rotation are marked.

The electron beam was electronically controlled in terms of focal spot dimension, position and profile. Once generated, the x-rays passed through a Ni foil in order to attenuate the $CuK_{\alpha 2}$ peak. The x-ray spot was limited by the width of the source slits. Following this, the x-rays were incident on the sample at an angle θ and the scattered intensity was analysed by a set of Soller slits at 2θ in front of a graphite analyser, which combined to give a total resolution of the instrumentation of approximately 0.15°. The detector was of scintillation type. Using the information given in Table 4:1, the detector was scanned across the range $0° < 2\theta < 80°$. A symmetric coupled θ-2θ curve was used to measure the position, width and intensity of the Bragg peak.

The scattered beam was conditioned using a set of Soller slits and a graphite analyser. Soller slits are a set of closely spaced parallel rectangular slits which collimate the beam by passing only parallel beam components and were used to limit the divergence of the diffracted beam so as to improve both the shape and resolution of the peaks. Following this, the scattered beam was incident upon a graphite analyser to further monochromate the scattered beam. The graphite crystal had a mosaic structure covering a relatively large range of incident angle. The different components of the scattered beam are diffracted radiation at different angles and all radiation other than the CuK_{α} radiation was attenuated. The combination of the Soller slits and the graphite results in a significant loss of intensity although the use of such filters improves the overall condition of the diffracted beam which is important when using x-ray diffraction to investigate the out-of-plane microstructure of thin films structures.

4.4 Magneto-optical Kerr magnetometry

4.4.1 Introduction

Magneto-optical effects are based upon small rotations of the plane of polarisation of light. Such effects were first reported by Faraday in 1845, [79] who observed that the plane of polarisation of light transmitted through a sample was rotated through an angle which was observed to depend upon the strength of the magnetisation within the sample. A similar effect is observed for light reflected from the surface of a sample; this is the Kerr effect and was first reported in 1877 [80, 81]. Both the Faraday and Kerr effects are proportional to the net magnetisation of the sample and provide non-invasive probes of the magnetisation state of a sample. Although MOKE magnetometry was originally developed

for the analysis of magnetic thin films, steady improvements in the sensitivity and the spatial and temporal resolution means that the technique is highly useful for the characterisation of patterned nanostructures [83].

In the following sections the underlying theory and relevant principles behind the magneto-optical Kerr effect are presented in which an understanding of the technique from both a macroscopic and microscopic viewpoint is developed. Following this, a description of experimental set up is provided, which includes a brief discussion of how nanostructures are located.

4.4.2 The geometry of the Kerr effect

The magneto-optical Kerr effect can be observed in three different magnetisation geometries, which are defined relative to plane of incident light as shown in Figure 4:12. In the longitudinal effect, as shown in Figure 4:12 (a), the magnetisation is parallel to the sample surface and parallel to the plane of incidence and reflection. Similarly, in the transverse effect, as shown in Figure 4:12 (b), the magnetisation is also in the plane of the sample although it is perpendicular to the plane of incidence. Finally, in the polar effect the magnetisation is perpendicular to the sample surface and the plane of incidence, as shown in Figure 4:12 (c). Both longitudinal and transverse MOKE measurements are performed at oblique angles of incidence whilst polar MOKE measurements are often performed at normal angles of incidence.

The longitudinal Kerr effect is a highly useful tool for characterising surface magnetic properties of structures with in-plane magnetisation and is a probe of magnetism on nanometre scales. All MOKE measurements presented in chapters 6 and 7 are taken using the longitudinal geometry, since the energetics of $Ni_{81}Fe_{19}$ thin film and planar nanowire structures mean the magnetisation direction lies parallel to the sample surface.

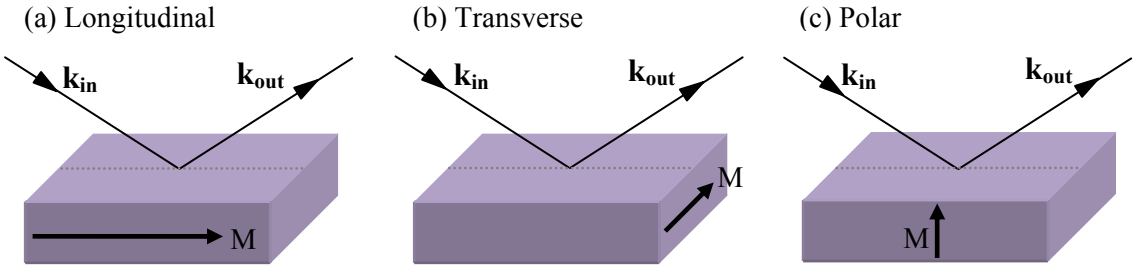

Figure 4:12. Schematic to show the three different magnetisation orientations (a) longitudinal, (b) transverse and (c) polar orientations the Kerr effect can be observed.

The use of this effect to study domains was first reported in 1953 by Fowler *et al*. [83] who observed domains on a (110) surface of silicon-iron crystal.

4.4.3 The longitudinal magneto-optical Kerr effect

When a beam of light propagates through a medium the electric field component of the light generates a motion of the electrons within the medium. An oscillating electron acts a source and re-radiates a spherical wavefront in all directions; in the classical description of the electron the re-radiated field is at the same frequency as the incident wave frequency. Linearly plane polarised light may be either *s*-polarised (in which the plane of polarisation is perpendicular to the plane of incidence) or *p*-polarised (in which the plane of polarisation is parallel to the plane of incidence), as shown in Figure 4:13. When linearly plane polarised light is incident upon a non-magnetic material, due to the motion of the electrons within the medium, light is re-radiated with the same plane of polarisation. However, when linearly plane polarised light is incident upon a magnetic material with in-plane, longitudinal magnetisation, the reflected light yields an orthogonally polarised component called the Kerr component.

In the magneto-optical Kerr effect, there is a rotation of the plane of polarisation of incident light upon reflection from a magnetisation sample, where the plane of polarisation refers to the direction of the electric vector of the incident radiation. The magnitude of the Kerr component is directly proportional to the magnetisation within the sample. For incident light with *p*-polarisation, the interaction with a magnetised sample results in the gain of a small component of *s*-polarised light on reflection from a magnetised sample (which may also be shifted in phase with respect to the *p*-component).

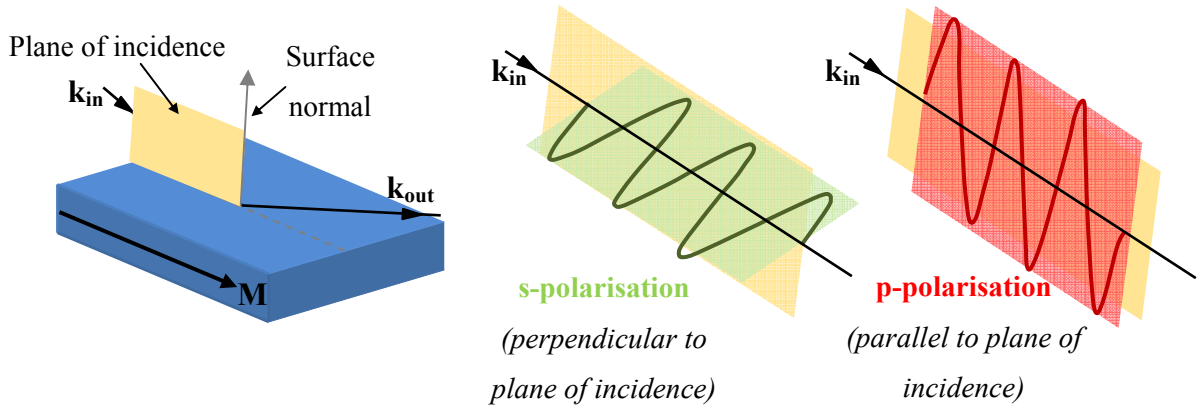

Figure 4:13. Schematic to show the *s*- and *p*-planes of polarisation within the longitudinal effect.

It is this which results in a rotation of the plane of polarisation of the incident beam.

4.4.4 Physical origin of the longitudinal Kerr effect

In this section an understanding of the physical origin of the Kerr component is developed by considering the optical properties of a medium. The optical properties of a medium are determined by its dielectric response, which on a microscopic level is determined by the motion of electrons within the medium, as shown in Figure 4:14.

(a) Left and right handed polarisations orbiting in phase

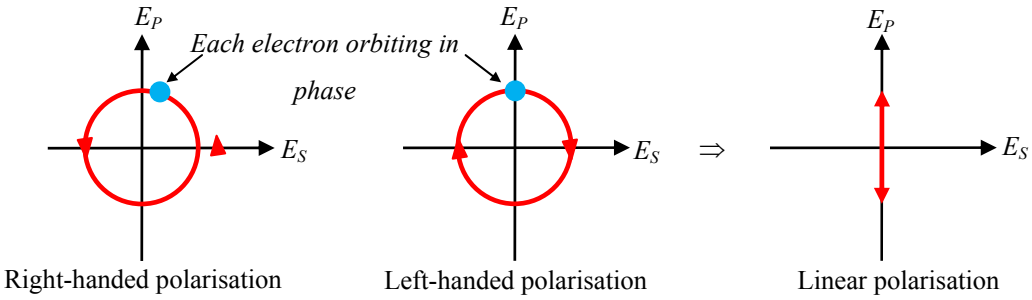

(b) **Phase shift:** rotation of plane of polarisation

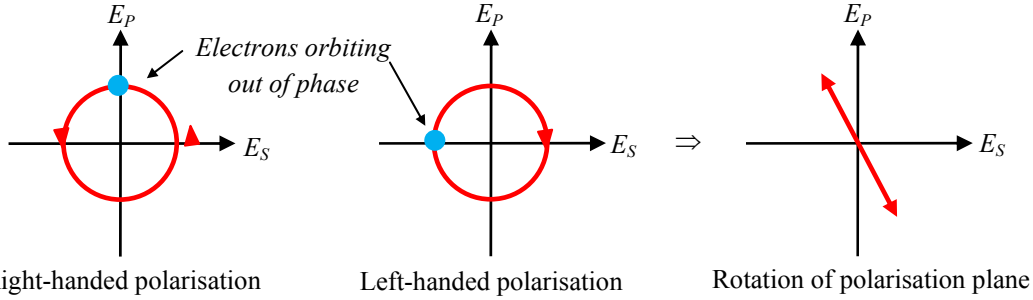

(c) **Preferential absorption:** ellipticity

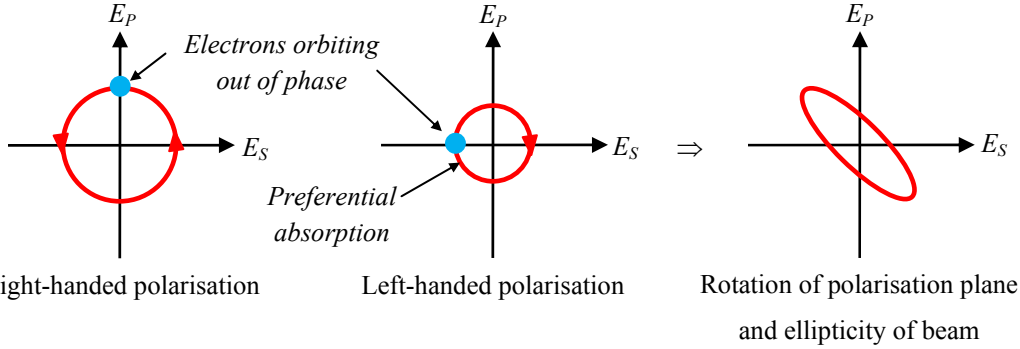

Figure 4:14. Schematic to show how the motion of electrons in a material gives rise to the rotation and elliptical components of the magneto-optical Kerr effect. A change in the motion of electrons changes the dielectric response of the material.

The dielectric response of a magnetic material

The dielectric law is written as:

$$\mathbf{D} = \boldsymbol{\varepsilon} \cdot \mathbf{E} \tag{4:21}$$

Where **D** is the electric displacement vector, **ε** is the dielectric permittivity tensor and **E** is the electric field vector. An electric field propagating in time and space is of the form:

$$\mathbf{E}(r,t) = E_0 \exp\left(ik\mathbf{n} \cdot \mathbf{r} - ickt\right) \tag{4:22}$$

Where k is the wavevector, **n** is a unit vector in the direction of propagation, **r** is the position vector, c is the speed of light in a vacuum and t is time. The generalised dielectric permittivity tensor is given in [25] and is of the form:

$$\boldsymbol{\varepsilon} = \varepsilon \begin{bmatrix} 1 & -iQ_V m_3 & iQ_V m_2 \\ iQ_V m_3 & 1 & -iQ_V m_1 \\ -iQ_V m_2 & iQ_V m_1 & 1 \end{bmatrix} + \begin{bmatrix} B_1 m_1^2 & B_1 m_1 m_2 & B_2 m_1 m_3 \\ B_2 m_1 m_2 & B_1 m_2^2 & B_2 m_2 m_3 \\ B_2 m_1 m_3 & B_2 m_2 m_3 & B_1 m_3^2 \end{bmatrix} \tag{4:23}$$

Where Q_v is the Voigt constant, which is a material dependent constant that describes the magneto-optical rotation of the plane of polarisation of light, B_1 and B_2 are constants and $m_{1,2,3}$ are the components of the unit vector of magnetisation along the cubic axes. In general, Q_v, B_1 and B_2 are not well known for the majority of materials, although for NiFe-systems, Q_v is of the order of 0.03 for the visible light range and is approximately proportional to the saturation magnetisation [86].

The dielectric tensor can be decomposed into a symmetric part (second matrix) and an antisymmetric part (first matrix). As the symmetric part of the dielectric tensor can be diagonalised, it does not give rise to magneto-optical effects [86] which only arise by considering the effect of the antisymmetric part of the dielectric tensor. Following the analysis given by Qiu and Bader in [84], the two normal modes of the antisymmetric part of the dielectric tensor are left-and right-handed circularly polarised light, with the refraction index given by:

$$n_{\pm} = \frac{\pm ck}{\omega} \tag{4:24}$$

Where the refractive index, n, is related to the dielectric tensor by $n = \sqrt{\varepsilon}$, c is the speed of light, k is the wavevector and ω is the angular frequency. The rotation of the plane of

polarisation of light that has travelled a distance L through a magnetised medium is given by:

$$\theta = \frac{kL}{2}\left(n_+ - n_-\right) \tag{4:25}$$

Where n_+ and n_- correspond to the refractive index of the left-handed and right-handed circularly polarised light, respectively. Using the definition of the refractive index given in equation (4:3), the real part of the above equation gives rise to the rotation shown in Figure 4:14 (b), whilst the imaginary part gives the ellipticity shown in Figure 4:14 (c).

Penetration depth

The magnitude of the MOKE signal is limited by the penetration depth of the laser into the sample, λ_{MOKE}, which is given by:

$$\lambda_{\mathrm{MOKE}} = \frac{1}{2k\beta} \tag{4:26}$$

Where k is the wavevector of the incident light and β is related to the absorption of the light in the material. The penetration depth (or skin depth) is the distance at which the intensity of the incident laser light is attenuated to 1/e of the initial value. Thus, equations (4:24) and (4:25) reveal that the rotation of the plane of polarisation is proportional to the thickness for film thickness much thinner than the penetration depth. For film thicknesses greater than the penetration depth these effects are complicated by absorptions of the medium. For incident light of wavelength 658 nm (as used within this study), β is equal to 3.37 and 3.82 for iron and nickel, respectively [86]. Using equation (4:26), this yields a penetration depth of approximately 14 nm. The Kerr response for films thinner than the penetration depth is directly proportional to the amount of magnetic material. In addition, it is strongly affected by the underlying substrate and the reflections that occur at the $Ni_{81}Fe_{19}$ substrate interface. At the penetration depth the signal is attenuated by 1/e due to absorption effects.

4.4.5 Experimental set up for longitudinal magneto-optical Kerr effect magnetometer

The magnetic behaviour of $Ni_{81}Fe_{19}$ thin films was measured using spatially resolved longitudinal magneto-optical Kerr effect magnetometry using an alternating magnetic field typically at 23 Hz and utilising a diode laser of wavelength 658 nm that was focussed to an

average spot size of 5 μm. A schematic of the MOKE magnetometer system is presented in Figure 4:15, in which the optical paths and principal optical components are clearly shown. There are two optical systems merged within this experimental apparatus which allows for both optical and magnetic interrogation of the sample without the need for sample repositioning. The output power of the laser was 30 mW although this was heavily attenuated with a captive attenuator such that the output power of the laser was less than 5 mW (class 3R). Light from the laser, passed through a beam expander and a Glan-Taylor polarising prism (with an extinction ratio < 10^{-5}) in order to enhance the beam polarisation ratio. The laser beam was focussed to a spot diameter of 5 µm upon the surface of the sample.

Samples were mounted upon an XY stage which was orientated at 45˚ relative to the incident light beam; as a result the focused laser spot was projected as an ellipse onto the sample, with the long axis orientated parallel to the sample surface. The position of the objective lens was adjusted until the focused spot had a sufficiently high central intensity without significant higher order modes being present. Incident light was linearly polarised and on reflection from a magnetic sample it emerged elliptically polarised. The reflected light passed through identical achromat lenses, a quarter-wave retardation plate (to remove any phase difference between the orthogonal reflected amplitudes and restore linearity).

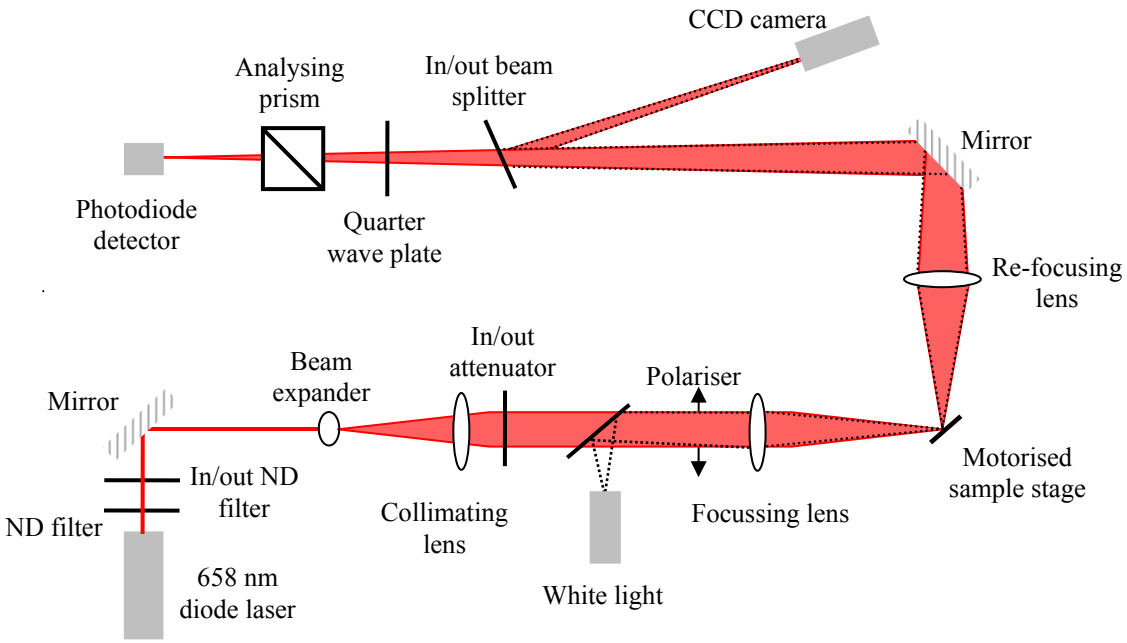

Figure 4:15. Schematic of the longitudinal magneto-optical Kerr effect magnetometry system used to probe the magnetic behaviour of thin films and nanowires. The laser has a wavelength of 658 nm and was focussed to a spot size of 5 µm.

Finally the beam passed through a Glan-Taylor polarising analyser from which the Kerr component of the reflected beam predominantly emerged.

The polarisation optics were optimised for measurements by first achieving the best extinction of the Kerr signal by iteratively rotating both the quarter-wave plate and analyser. Then, for measurements, the analyser was rotated by an appropriate angle away from extinction in order that polarisation changes can be distinguished as the intensity of light changed at the photodiode. The longitudinal Kerr rotation of permalloy is very small; typically around 0.01° which means that this was achieved when the two polarisers were almost crossed, meaning that most of the laser light was rejected. The light intensity transmitted through the polarising analyser was detected using a silicon photodiode and was recorded as the Kerr signal.

White light was introduced into the system so as to locate patterned nanostructures on the surface of the chip. As shown in Figure 4:15, white light was brought into the laser path prior to the sample using a pellicle between the first polariser and the sample surface. A beam splitter placed immediately before the quarter-wave plate allowed the surface of the sample to be imaged onto a CCD camera. A dichroic partial mirror protected the CCD chip from being saturated by the laser beam, and the white light was turned off before taking magnetic measurements. Magnetic fields were generated in the plane of the sample using an iron-core and air-spaced electromagnets. These were powered by Kepco BOP 20-5M power amplifiers, and were able to create a maximum magnetic field of ± 400 Oe. Waveforms were defined using a function generator, utilising a sinusoidal wave form.

Location of nanostructure

The location of individual nanostructures was identified using the procedure outlined here. Samples were mounted upon a computer controlled XY translation stage. Structure location was initially accomplished by focusing the laser spot as close as possible to the nanostructure of interest using the CCD image as a guide. The Kerr amplifier output was then connected to a lock-in amplifier and an alternating magnetic field of ~ 270 Hz was applied in the plane of the sample. The sample was then raster scanned through a two-dimensional grid beneath the laser spot and the lock-in amplifier signal was recorded for each position in the grid. This signal was effectively a measure of sample susceptibility, and thus allowed a susceptibility map of the sample to be generated. Since the magnetisation vector of the nanowires is constrained to lie along the long axis at

remanence, the application of an alternating field across the sample allowed the XY stage program to generate a contrast map of the ferromagnetic relative to paramagnetic background. Figure 4:16 presents a 20 μm x 20 μm scan with a pixel resolution of 1 μm used to located patterned nanowires.

In such susceptibility maps, the white areas correspond to the highest measured Kerr signal and denote local 'hot-spots' of magnetically active areas. Pink and red areas, on the other hand, represent increasingly lower signal magnitudes and as such correspond to regions of non-ferromagnetic material at room temperature. The bright area is larger than the wire width as it represents the convoluted response of the finite size of the laser spot and the nanostructure. This procedure allows particular regions of a structure to be selected for analysis, which was extremely useful for nanowire structures studied in chapter 7.

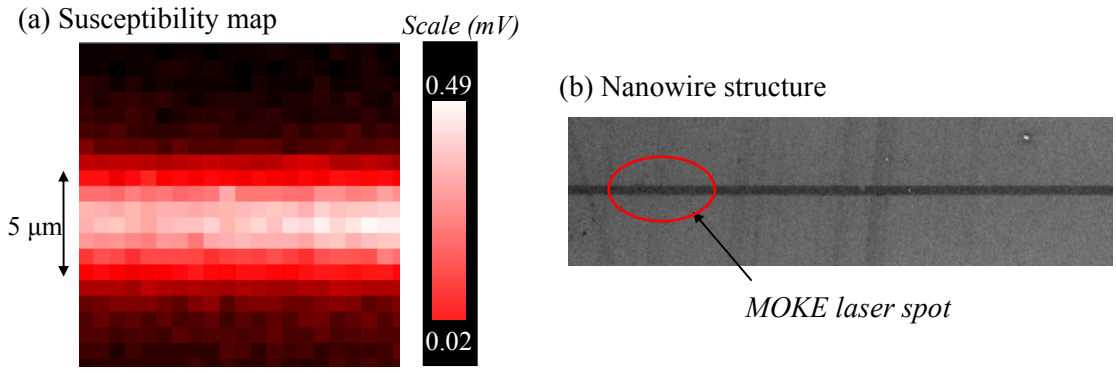

Figure 4:16. (a) Susceptibility map of a 20 μm x 20 μm square area taken from a $Ni_{81}Fe_{19}$ nanowire; each pixel in the map has a resolution of 1μm and (b) corresponding interpretation of location of the MOKE laser spot relative to the nanowire geometry.

4.5 Micromagnetic simulations

Micromagnetic modelling was used in chapters 7 and 8 to compliment MOKE magnetometry and to provide important insight into the magnetisation reversal via domain wall propagation. In addition, simulations have been used to provide information into the relationship between domain wall energy and micromagnetic structure. In this section, the underlying physical principles behind micromagnetic simulations and the techniques employed in order to perform physically meaningful micromagnetic modelling are discussed.

4.5.1 Field driven magnetisation reversal dynamics

For the purposed of micromagnetic calculations, whilst the magnetisation vector is assumed to be of constant magnitude, the direction is assumed to be a continuous function of position. Micromagnetics offers a rigorous approach to finding the arrangement of the magnetisation vector with the lowest total energy without making any initial assumptions [43]. The total free energy of a ferromagnetic system is given by:

$$E_{\text{total}} = \int_V \phi_{\text{total}} dV = 0 \tag{4:27}$$

Where ϕ_{total} is the total free energy density of the system and includes contributions from the exchange, magnetocrystalline anisotropy, magnetostriction, magnetoelastic, magnetostatic and Zeeman energies, as summarised in Table 3:1. In certain systems, some of these energetic terms can be discarded; for example, in $Ni_{81}Fe_{19}$ thin films and nanostructures, both the magnetocrystalline anisotropy and the magnetostriction energies are extremely close to zero and thus it is reasonable to ignore them from micromagnetic calculations (see sections 3.4.4 and 3.4.5). As a result, for $Ni_{81}Fe_{19}$, the total free energy includes contributions from exchange, magnetostatic and the Zeeman energy [43]. Moreover, for a given applied field, the configuration of the magnetic moments is that which gives the lowest total energy of the exchange and magnetostatic energies. As such, the field driving the motion of the moments is an effective one, since the applied field is only one of the terms that contribute to it. The effective field, $\mathbf{H}_{\text{eff}}$, is defined via:

$$\mathbf{H}_{\text{eff}} = -\frac{1}{\mu_0}\frac{\partial E_{\text{total}}}{\partial M} \tag{4:28}$$

Where E_{total} is the total free energy as defined in equation (4:27), M is the magnetisation and μ_0 is the permeability of free space. The effective field induces a torque on the magnetisation, given by:

$$\boldsymbol{\tau} = \mathbf{M} \times \mathbf{H}_{\text{eff}} \tag{4:29}$$

In thermodynamic equilibrium, the orientation of **M** at each point must be such that the total torque on each element $\boldsymbol{M}dV$ is zero. When the applied field is changed, this changes the effective field which in turn means that the torque at each point ceases to be zero. Dissipative processes must therefore occur in order for the system to tend toward

thermodynamic equilibrium; to do so may require a new equilibrium distribution of **M** to be established.

The motion of the magnetisation, **M**, in an effective field $\mathbf{H}_{\text{eff}}$, is described by the Landau-Lifshitz equation and is schematically illustrated in Figure 4:17. Due to the combination of the minimum energy principle and the constant magnetisation constraint, the torque on the magnetisation must vanish. For field-driven dynamic magnetisation behaviour, this condition can be expressed as:

$$\frac{d\mathbf{M}}{dt} = -\gamma\left(\mathbf{M}\times\mathbf{H}_{\text{eff}}\right) - \frac{\gamma\alpha}{M_{\text{s}}}\left(\mathbf{M}\times\left(\mathbf{M}\times\mathbf{H}_{\text{eff}}\right)\right) \tag{4:30}$$

The first term in this equation describes a precession of the magnetisation vector **M** about the effective field, with angular frequency equal to the Larmor frequency ω_{L}. During this motion the angle between the magnetisation and the effective field does not change. Typical precessional frequencies in ferromagnetic materials are of the order of GHz, although this depends upon the magnitude of the applied field.

It is known from experiment, however, that the magnetisation decays over time with losses arising from a combination of eddy currents, diffusion, spin scattering and sample imperfections. To account for these intrinsic losses, a phenomelogical damping parameter was introduced by Gilbert in 1955 [87], which represents local dissipative phenomena such as the relaxation due to magnetic impurities or the scattering of spin waves from lattice defects.

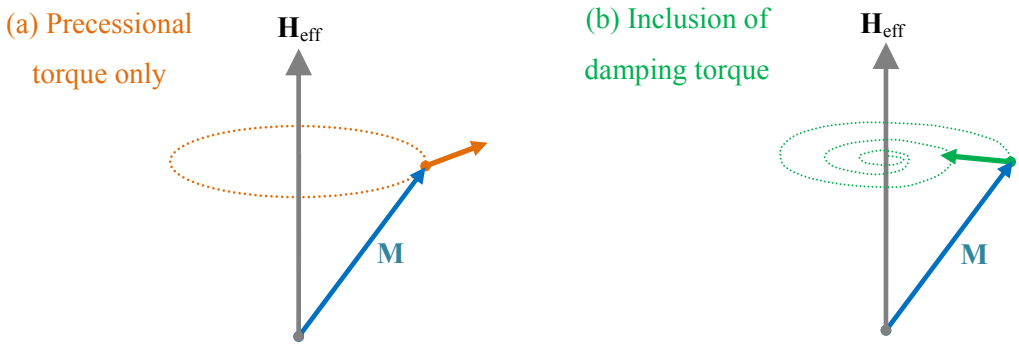

Figure 4:17. The different torques experienced by a magnetisation vector **M** precessing about an effective field $\mathbf{H}_{\text{eff}}$ as given by the Landau-Lifshitz equation. (a) Schematic to illustrate the action of the first term, which induces precessional motion of the magnetisation about the effective field; (b) the second term gives rise to a damping torque that eventually causes the magnetisation to align in the direction of the effective field.

This damping parameter gives rise to an associated torque, the damping torque, which allows the magnetisation to align itself parallel with the effective field, and corresponds to the second term in equation (4:30). Rigorous evaluation of the origin and magnitude of the damping parameter is one of the most complicated problems in modern solid-state magnetism due to the large variety of damping mechanisms in ferromagnets. In addition, in most cases it is difficult to separate the contributions to the energy dissipation rate measured experimentally.

4.5.2 Description of the micromagnetic framework

All micromagnetic simulations used within this thesis have been performed using the OOMMF micromagnetic simulation package, developed by Donahue and Porter in 1997 [88] which is freely available from [89].

The first stage in the modelling process is to define the problem to be solved; this is done by creating a MIF 1.1 file. The MIF file contains the material parameters, defines the geometry of the structure under investigation and describes the experimental parameters over which the simulation will run. It is important to use accurate parameters which are representative of the material under investigation so that the modelling provides physically meaningful results. The values of the physical parameters employed for $Ni_{81}Fe_{19}$ as used in this study were: saturation magnetisation, M_s = 860 x 10^3 A/m [53] exchange stiffness parameter, A = 13 x 10^{-12} J/m [28]; K_1 = 0 [52]. A value of α = 0.5 was used for the Gilbert damping parameter, which is believed to be significantly larger than what is typically observed and is because the primary use of micromagnetic modelling within this thesis is for the characterisation of quasi-static domain wall properties and pinning behaviour.

The use of a large value of the damping parameter encourages the system to reach equilibrium faster. Indeed, preliminary micromagnetic simulations show that for a more physically realistic value of α (of approximately 0.01 [90]) the system displays the same overall behaviour as given for α = 0.5 although the simulation time was greatly increased. This is because the domain wall motion becomes chaotic for fields above the Walker field, H_w. The Walker field is a threshold field above which Walker breakdown occurs in which the domain wall motion is limited by the precessional motion of the spins [91]. This causes stalling of the wall and a reduction in domain wall velocity is observed as the magnetic moment of the wall changes orientation via the nucleation of an anti-vortex wall structure [92]. However, since the investigation on domain wall properties present here

does not extend to domain wall propagation a larger than realistic value of the damping parameter does not affect the micromagnetically modelled behaviour.

4.5.3 Solution of the micromagnetic problem using the OOMMF 2D Solver

Once the problem to be solved is outlined in the MIF 1.1 file the computation engine then proceeds to integrate the Landau-Lifshitz equation given in (4:30). To do this, the micromagnetic problem was impressed upon a regular two dimensional grid of squares, with three dimensional spins positioned at the centre of each cell as shown in Figure 4:18. For the simulation to be physically meaningful, the cell size used should be of the order of the smallest definable feature on the scale of the structure under investigation. A sensible cell size for $Ni_{81}Fe_{19}$ nanowire structure should be of the order of the exchange length, which is defined as:

$$\Lambda = \sqrt{\frac{2A}{\mu_0 M_s^2}} \qquad (4:31)$$

Using the values of A and M_s provided in section 4.5.2 yields an exchange length of approximately 5 nm and as such also corresponds to the cell size employed in all simulations. Although a smaller cell sizes would be more physically realistic, the solver requires a significant amount of working memory. Typical simulations require 5MB + 1500 bytes per cell; so although a reduction in cell size is desirable, cell sizes smaller than 5 nm do not provide any additional physical insight yet significantly increases the simulation time. In OOMMF, the anisotropy and applied field energy terms were calculated assuming there is a constant magnetisation in each cell. The exchange energy was calculated using an eight-neighbour bilinear interpolation method as defined in [93] using Neumann boundary conditions.

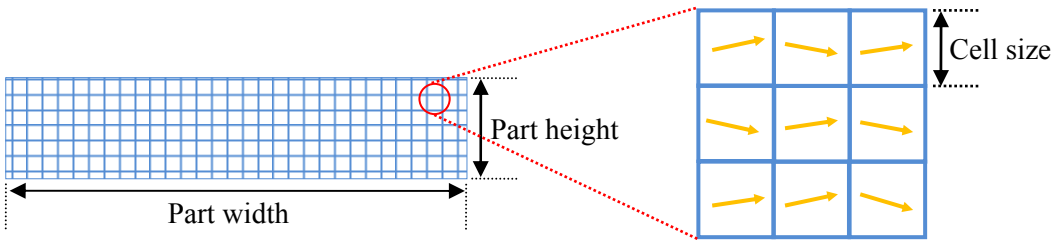

Figure 4:18. Schematic of the rectangular mesh used within the OOMMF micromagnetic modelling package (*left*) plan view of mesh; within each cell, the magnetisation is uniform. Exchange energy for each value of applied field is calculated by 8 nearest neighbours (*right*).

For each step, this was achieved by looking at the energetic cost of changing the angle of a spin by considering the effect of non-parallel spins on the eight nearest neighbours.

As the magnetostatic energy is a long range interaction this needs to be taken into account in the method of solution. The interaction of the demagnetising field is calculated as the convolution of the magnetisation against a kernel that describes the cell to cell magnetostatic interaction and is evaluated using fast Fourier transformation techniques. This kernel interprets the magnetisation as being constant within each cell [94, 95]. It is the calculation of the magnetostatic energy that requires the largest amount of working memory in the OOMMF software.

For each field step the Landau-Lifshitz equation is integrated using a second order predictor-corrector technique. The right hand side of equation given in (4:30) at the current and previous time step are extrapolated forward in a linear fashion for the current and previous time step and then integrated forward across a new time interval. A quadratic prediction for the magnetisation at the next time step is then obtained. The right hand side of equation (4:30) is then evaluated using this predicted value of magnetisation, which is then combined with the value at the current step to produce a linear interpolation of $d\mathbf{M}/dt$ across the new time interval. The time step is accepted if the total energy of the system decreases, and the maximum error between the predicted and final **M** is smaller than a nominal value. If the time step is rejected, then the step size is reduced and the integration procedure is repeated. If the time step is accepted, then the error between the predicted and final magnetisation is used to adjust the size of the next step. No fixed ratio between the previous and current time step is assumed. If the predictor-corrector solver fails to find a valid step then a fourth Runge-Kutta solver is used to prime the predictor-corrector toward a stable solution. For a given applied field, the integration continues forward in time until a specified control is reached. A solution is defined as stable if a small deviation from equilibrium yields a torque that restores the system to equilibrium; if the force increases the deviation still further then the solution is not stable. In the simulation work presented within this thesis a control point of 1×10^{-5} was used; this means that each time step was considered complete when the magnitude of torque on the magnetisation was $\leq 1 \times 10^{-5}$. This torque was calculated using $|m \times h| = |M \times H_{\text{eff}}|^2 / M_s^2$ and is thus a dimensionless value. Once this was achieved, the simulation progressed forward to finding a solution for the Landau-Lifshitz equation at the next time step.

Finally, all micromagnetic simulations are performed at 0 K; this removes the thermal fluctuations of spin magnetic moments which, if included, would further increase the simulation time; such an approach is justified in section 7.4. In addition, all simulations used mask structures that had perfectly smooth edges. The presence of a finite temperature combined with edge roughness present in real structures means that switching fields measured by micromagnetic modelling tend to be higher than those measured experimentally. This is due to the stochastic nature of spin magnetic moments associated with non-zero temperatures.

4.6 Electronic transport behaviour of ferromagnetic materials

This section outlines the physical principles of the dependence of electronic transport behaviour in the absence of an applied field in both non-ferromagnetic and ferromagnetic metals, which allows for a sound understanding of the differences in the magnetoresistance of non-ferromagnetic and ferromagnetic metals. Following this, a description of experimental set up used to measure the magnetoresistance of $Ni_{81}Fe_{19}$ thin films is provided. These measurements are presented in chapter 6 and incorporated into the model developed in chapter 8 to identify the presence and structure of domain walls in planar nanowires.

4.6.1 Electronic transport behaviour in metals

The physical properties of metallic materials can be understood using the Drude free electron model. In the Drude model, the valence electrons of the constituent atoms are assumed to behave as a 'sea' of conduction electrons that are able to move freely about the volume of the metal. The electrons that support conduction in metals typically consist of highly delocalised *s*-electrons, although only those electrons that lie above the Fermi energy, E_F, can contribute to electrical conduction. The electrical properties of metals are determined by the shape and the density of states of the bands near to and at the Fermi energy.

The electrical resistivity of a metal is determined by the rate of collisions of the conduction electrons; at low temperatures, the electrical resistivity is dominated by collisions with impurity atoms and other imperfections in the crystal lattice, whilst at room temperature the electrical resistance of most metals is dominated by collisions of the

conduction electrons with lattice vibrations (phonons). The electrical resistivity in a metal ρ is expressed as:

$$\rho = \frac{1}{\sigma} = \frac{m^*}{ne^2\tau} \tag{4:32}$$

Where σ is the electrical conductivity, m^* is the effective mass of the charge carriers (which is inversely proportional to the band curvature), n is the volume concentration of the free carriers, e is the electronic charge and τ is the relaxation time between successive scattering events, which is given by:

$$\tau = v_F l \tag{4:33}$$

Where v_F is the Fermi velocity and l is the mean free path of the conduction electrons, which is the distance travelled by an electron before it becomes scattered [1].

Figure 4:19 compares the shape of the density of states near to and at the Fermi level for alkali metals, non-ferromagnetic transition metals and ferromagnetic transition metals. In alkali metals, such as sodium, the valence electronic configuration is of the form s^1; the s band is highly delocalised and forms a continuous conduction band for electrons. Non-ferromagnetic transition metals as shown in Figure 4:19 (b), such as vanadium, possess a valence configuration of the form $d^n s^1$ and have both d and s states at the Fermi level.

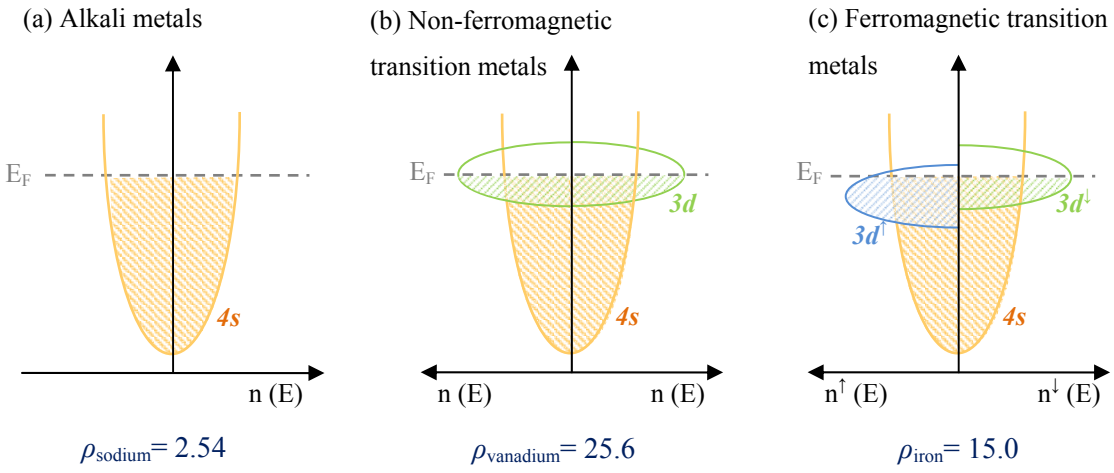

Figure 4:19. Schematic to show the electronic band structure and density of states for three classes of metals (a) simple alkali metals (b) non-ferromagnetic transition metals and (c) ferromagnetic transition metals. Examples of the electrical resistivity at the Debye temperature for each class of metal is provided (ρ is in $\mu\Omega$cm).

As shown in Figure 4:19 (c), a ferromagnetic transition metal also has both *d* and *s* states at the Fermi level, although as discussed in section 2.4.5, the *d* band is exchange split and so the valence electronic configuration is of the form $d^{n\uparrow}d^{n\downarrow}s^{1}$.

The two current model for ferromagnetic materials

The examples presented in Figure 4:19 suggest that the electrical resistivity at the Debye temperature is much larger when there are unoccupied *d* states at the Fermi level. At a given temperature, an increase in electrical resistivity takes place when the mean free path of the conduction electrons is reduced. The larger resistivity of ferromagnetic materials when compared to the simple alkali metals implies that the conduction electrons may be scattered to the unoccupied *d* states.

An understanding of the differences in electrical transport behaviour between ferromagnetic and non-ferromagnetic metals can be gained by considering the shape of the *s* and *d* bands of the ferromagnetic transition metals at the Fermi energy. Overlap of the *s* and *d* bands at the Fermi energy leads to hybridisation of the bands, and, as a result, the parabolic *s* bands acquire properties of the flatter *d* bands. Consequently, delocalised *s* electrons are able to scatter into localised *d* states of the same energy. Since there is a large density of states of the 3*d* band at the Fermi energy, this means that the probability of an *s* electron scattering into an unoccupied *d* state (*s*-*d* scattering) is several times greater than the probability of ordinary scattering. This increased probability for scattering into the *d* bands in turn reduces the mean free path of conduction electrons, and thus causes the electrical resistivity to increase. As the unoccupied *d* states are responsible for ferromagnetism, there is a direct connection between the magnetic properties and the electrical conductivity.

The first description of *s*-*d* scattering was provided by Mott [96] who suggested the current in a ferromagnet is made up of two parts, with separate contributions from majority (↑) and minority (↓) charge carriers. As explained in section 2.5.2, the effective number of Bohr magnetons, n_{eff}, provides information on the number of unpaired spins per atom and is deduced via:

$$n_{\text{eff}} = \frac{M_{\text{s}}(0)}{n\mu_{\text{B}}} \tag{4:34}$$

Where M_{s} (0) is the saturation magnetisation at $T = 0$ K, n is the number of atoms per unit volume and μ_{B} is the Bohr magneton. For iron, cobalt and nickel the values of n_{eff} are 2.22,

1.72 and 0.60 μ_B per atom, respectively. These values provide information on the density of states at the Fermi energy. As explained in section 2.5.2, in order to attain non-integral values of n_{eff}, the density of states for the exchange split spin-up and spin-down bands, $n^{\uparrow}(E)$ and $n^{\downarrow}(E)$, must be different, which means that the *s* to *d* scattering rates will be different for the spin-up and spin-down conduction electrons.

For temperatures below the Curie temperature, T_c, the spin direction of the charge carriers is conserved during the majority of scattering events; i.e. the spin-flip scattering is low. The two spin populations must therefore scatter independent spin currents. Electrical conduction takes place between two parallel paths for the majority (↑) and minority (↓) charge carriers respectively, as shown in Figure 4:20. For a single element ferromagnet, such as iron, the resistivity in each channel is the sum of the phonon, impurity, *s*-*d* and other scattering contributions. At low temperatures (below the Curie temperature), the resistivity of a ferromagnetic metal is given by:

$$\rho = \frac{\rho^{\uparrow}\rho^{\downarrow}}{\rho^{\uparrow} + \rho^{\downarrow}} \tag{4:35}$$

Where $\rho^{\uparrow}$ and $\rho^{\downarrow}$ are the values of resistivity of the majority and minority exchange split spin channels, respectively. Indeed, the independence of the spin channels is maintained if impurity or alloying elements are added to the ferromagnetic metal, provided there is little spin-flip scattering [97]. At low temperatures (below T_c) magnons (spin waves) are not strongly excited; it is magnons that mix spin-up and spin-down states. Spin-flip scattering is primarily caused by magnons [9]. Non-ferromagnetic metals exhibit a linear increase in electrical resistivity above the Debye temperature due to the increased thermal energy of phonons which increase the probability of a scattering event.

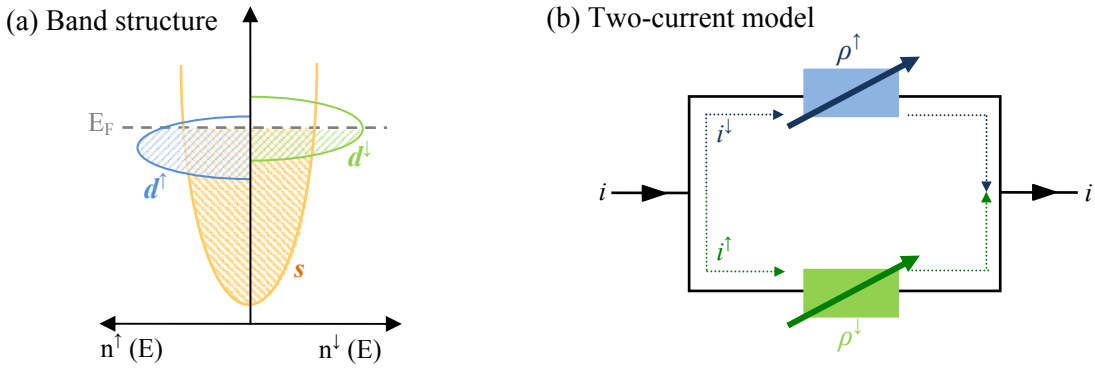

Figure 4:20. Schematic to illustrate (a) the exchange split 3*d* band structure of iron and (b) the two-current model of resistivity in iron, where $\rho^{\uparrow}$ and $\rho^{\downarrow}$ are the values of resistivity of the majority and minority exchange split spin channels, respectively.

In ferromagnetic materials, as temperature increases toward T_c the increase in the number of magnons causes mixing of the majority and minority spin channels. As such, a spin-up conduction electron can be scattered to a spin-down state by the annihilation of a magnon. As a consequence, this increases the total resistivity of the system since scattering events in the lower resistivity channel are increased.

4.6.2 Magnetoresistance behaviour in metals

In a non-ferromagnetic material, the presence of an externally applied field perpendicular to the current induces a Hall voltage in a direction orthogonal to both the current and magnetic field. An applied field causes a change in the longitudinal resistance of a material because the Hall effect causes charge carriers to deflect from the current direction. Due to the Lorentz force, the conduction electrons are forced into cyclotron orbits about the applied field. Once a charge carrier begins to orbit around the magnetic field, it no longer contributes to the current density until it is scattered. Once the conduction electron is scattered, it then begins its next cyclotron orbit, with an initial velocity biased towards the applied field. The effect of an applied field on the electrical resistivity thus depends upon the original resistivity; the longer the relaxation time τ, the larger the effect of an applied magnetic field. This is the 'ordinary' magnetoresistance effect which is analytically described by Kohler's rule:

$$\frac{\delta\rho}{\rho} \propto a\left(\frac{H}{\rho}\right)^2 \tag{4:36}$$

Where $\delta\rho$ is the change in resistivity, ρ is the resistivity of the material in the absence of an applied field and H is the applied field and a is a constant of proportionality. Experimentally, it is observed that the change in resistivity, $\delta\rho$, is a maximum when the applied field and the electric current are perpendicular and a minimum when they are parallel [9].

In a ferromagnetic material, this effect is often masked by the presence of a much larger phenomenon, known as the 'extraordinary' magnetoresistance effect. Extraordinary magnetoresistance effects are much stronger than the ordinary effects observed in non-magnetic metals due to the presence of a large spontaneous magnetisation, M, which is generally much stronger than an applied field, H. Due to spin-orbit effects, the magnetisation couples to the current density and there is an interaction between the spin

and the orbit of the electron motion. Kohler's rule can be extended for ferromagnetic materials as:

$$\frac{\delta\rho}{\rho} \propto a\left(\frac{H}{\rho}\right)^2 + b\left(\frac{M}{\rho}\right)^2 \tag{4:37}$$

Where b is a constant of proportionality.

Anisotropic magnetoresistance behaviour in ferromagnetic materials

The discussion of magnetoresistance effects in this section is restricted to the changes in electrical resistance in ferromagnetic metals associated with the direction of magnetisation relative to the applied current: this is known as anisotropic magnetoresistance. This effect was discovered in 1857 by Thomson [98] and is sometimes called the orientation effect since it depends upon the orientation of the magnetisation to the applied current. In general, the resistance of a ferromagnetic varies as:

$$\rho(\theta) = \rho_\perp + \delta\rho\cos^2(\theta) \tag{4:38}$$

The change in resistivity, $\delta\rho$, is a minimum when the magnetisation and the electric current and perpendicular, ($\rho_\perp$) and is a maximum when they are parallel ($\rho_\parallel$) [99, 100] Values of $\rho_\parallel$ and $\rho_\perp$ using can be measured experimentally in typical scans as shown in Figure 4:21. The change in resistivity between the parallel and perpendicular states, $\delta\rho$, is defined by the relation:

$$\delta\rho = \rho_\parallel - \rho_\perp \tag{4:39}$$

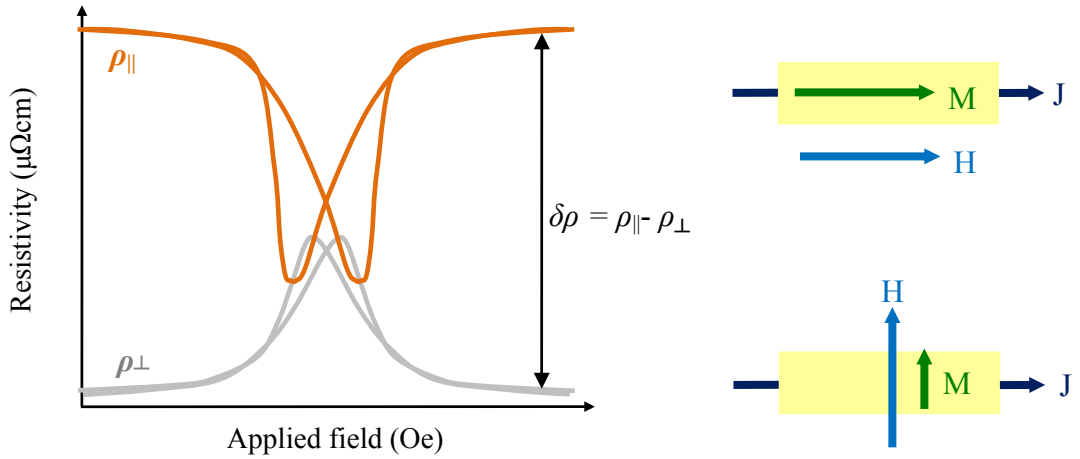

Figure 4:21. Example of the anisotropic resistance in $Ni_{81}Fe_{19}$ taken at room temperature with corresponding schematics to show the orientation of the magnetisation and the current density J.

The resistivity of the zero field state depends upon the exact domain configuration [97]. Since this, in turn, depends upon the history of the sample, it is not well defined even for a given sample at a given temperature. To account for this, it is usual to define ρ_{ave} using a combination of $\rho_{\parallel}$ and $\rho_{\perp}$ via:

$$\rho_{ave} = \frac{1}{3}\left(\rho_{\parallel} + 2\rho_{\perp}\right) \tag{4:40}$$

This allows for the anisotropic magnetoresistance (AMR) ratio to be defined [99] as:

$$\frac{\delta\rho}{\rho_{ave}} = \frac{\rho_{\parallel} - \rho_{\perp}}{\frac{1}{3}\left(\rho_{\parallel} + 2\rho_{\perp}\right)} \tag{4:41}$$

The AMR ratio of bulk nickel-iron alloys is shown in Figure 4:22. The AMR ratio depends sensitively on the percentage nickel content, and has a maximum of 5% for $Ni_{90}Fe_{10}$; whilst for $Ni_{81}Fe_{19}$ it is close to the maximum and is approximately 4% in bulk materials.

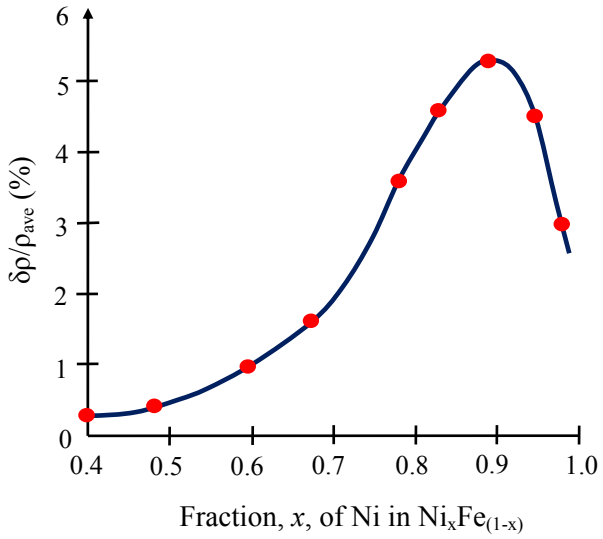

Figure 4:22. Anisotropic magnetoresistance ratio in percent for $Ni_xFe_{(1-x)}$ alloys at room temperature, taken from Bozorth [53].

4.6.3 Microscopic origin of anisotropic magnetoresistance

An explanation for the microscopic origin of the anisotropic magnetoresistance effect was proposed by Smit in 1951 [100] who proposed that such effects can only arise because of the spin-orbit interaction. The electrical resistivity properties of transition metals are understood using the Mott two-current model and at low temperatures, there is no mixing of the spin channels such that $\rho(\uparrow) \neq \rho(\downarrow)$. Smit proposed that in order to observe

anisotropic magnetoresistance where $\rho_{\parallel} > \rho_{\perp}$, spin-flip scattering must occur. Moreover, since the AMR ratio tends to zero as T is increased to the Curie temperature, the origin of the spin-flip scattering cannot be due to magnons.

According to Smit, the spin-orbit interaction provides a way to mix spin-up and spin-down states so that s↑ electrons can be scattered into empty *d* states. As the 3*d* orbitals are fixed to the lattice, the distribution of holes transverse is not equal to the distribution longitudinal. As such, this implies that holes in the *d*-orbits are not evenly distributed, with a deficit of hole-orbits perpendicular to the magnetisation. Thus, the transition probability for an *s*-electron is smallest for a conduction electron moving perpendicular to the plane of the orbit. However, since there are relatively few holes in orbits perpendicular to the magnetisation, it follows that *s*-electrons moving in the direction of the magnetisation are more easily trapped compared to those electrons moving in a parallel direction. Since electrical resistance is mainly determined by the scattering of the electrons moving in the direction of the current, it can be concluded that $R_{\parallel} > R_{\perp}$.

4.6.4 Experimental set up for anisotropic magnetoresistance measurements

Magnetoresistance measurement on $Ni_{81}Fe_{19}$ thin films and planar nanowire structures were performed using a custom built magnetoresistance system, a description of which can be found in [101]. In this system, a LabVIEW program was used to control the instrumentation, and to record the measured data. An overview of the experimental hardware used to perform measurements is shown in Figure 4:23. The sample was placed in the electrically and thermally shielded cover within the electromagnet.

The magnetoresistance measurements of thin films presented in chapter 6 were made using a conventional linear four point technique on samples that were shaped with a large aspect ratio of approximate dimensions 27 mm x 3 mm. A linear four point probe technique was used to eliminate the contribution of the resistance of the wiring and contacts from the measurement of the sample. The arrangement of the contacts was such that the outer two probes supplied current to the samples, whilst the inner probes were the voltage contacts. The sample geometry ensured that the distribution of electric current was isotropic across the entire width of the chip. The electrical resistance was measured using an applied current of 4 mA.

(a) Overview of hardware

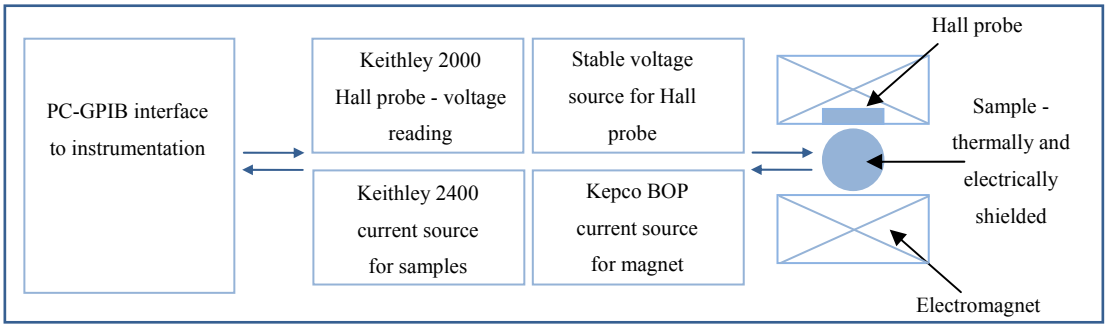

(b) Screenshot of front end display

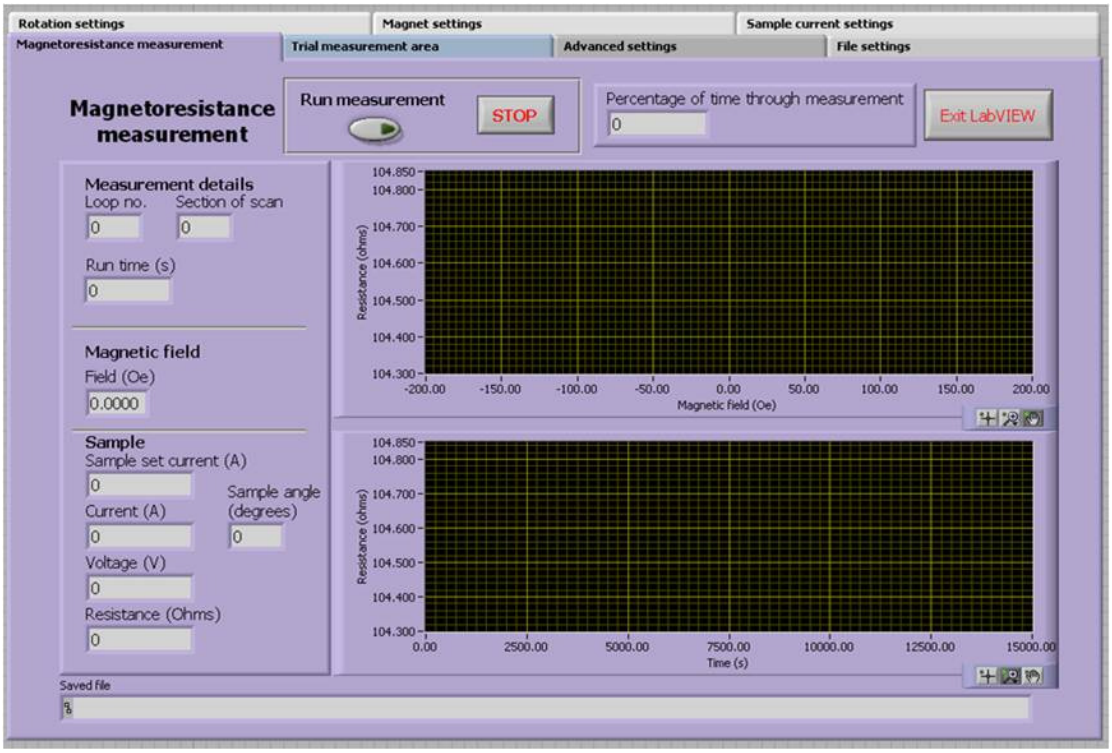

Figure 4:23. (a) Schematic of the hardware used to measure the magnetoresistance of $Ni_{81}Fe_{19}$ thin films and nanowire structures and (b) screenshot to show the front panel of the LabVIEW software. In this program the data is displayed in real time and the measurement can be started and stopped from the front panel.

This is equivalent to a current density of between approximately 10^7 Am^{-2} and 10^8 Am^{-2} for all film thicknesses, which is below the value of current density at which spin torque effects are observed to occur [102]. Measured voltages were in the range of 1.9591 V for a 3.02 nm thin film to 3.75 x 10^{-8} V for a 43.36 nm thin film. A measurement of voltage versus current between 0.1 mA and 4 mA was performed to ensure that the contacts were Ohmic. The voltage across the chip was made using probes with a (7.05 ± 0.05) mm separation and was measured using a Keithley nanovoltmeter.

Electrical connection to the sample was made using gold-plated phosphor bronze spring loaded probes as shown in Figure 4:24. The contacts were made from gold-plated phosphor bronze with a 1.3 mm rounded tip [103]. Good mechanical contact to the sample was ensured by compressing the spring probes by approximately half the available compression distance and fastening tightly in place as shown in Figure 4:24 (a). The rounded tip of the probes, combined with the manufacturer's specification that the maximum spring force applied by the probes was equal to 1.47 N [103], meant that no damage was visible on the sample surface after the magnetoresistance measurement had been made.

As the surface of the $Ni_{81}Fe_{19}$ samples did not have a gold capping layer, and an oxide layer was therefore expected to form (see section 5.2). To ensure that the oxide barrier did not affect the calculated resistivity, the contact resistance to the sample was carefully considered. Two techniques were used to check the contact resistance. The first technique measured the two point resistance between the four linear contacts in order of distance between the contacts. By measuring the resistance between contacts 1 and 2, 1 and 3, then 1 and 4, a graph could be plotted of the total measured two point resistance versus distance between contacts. This was then extrapolated to zero distance between the contacts. At zero distance, the total resistance has no contribution from sample resistance and all that remains is twice the contact resistance [104]. The value measured for a single contact was approximately 15 Ω.

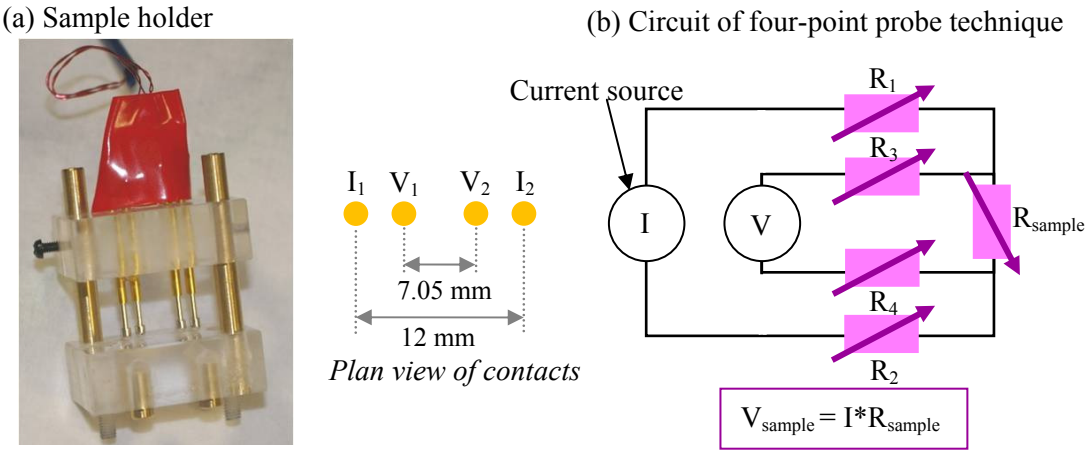

Figure 4:24. (a) Photograph of sample holder and corresponding plan view schematic of the electrical contacts used to measure the magnetoresistance of $Ni_{81}Fe_{19}$ thin films and (b) voltage and current contact geometries for measurements of electrical resistance in thin films using a 4-point probe technique. The probe tips were 1.3 mm in diameter with a contact resistance of 50 mΩ and a spring force of 1.47 N [103].

This was the same value for both a sample capped with 3 nm gold and for an uncapped sample containing a surface oxide layer.

The second technique used to support the contact resistance measured above, was to extrapolate the resistance of the sample between the outer two contacts of the four point probe based on the four point resistance measurement between the inner voltage contacts. The resistivity of the sample was calculated for the spacing between the inner contacts and then recalculated for the spacing of the outer contacts. Using this method, a resistance of approximately 63 Ω was calculated which when compared to the measured two point resistance gave a difference of 24 Ω, corresponding to approximately 12 Ω per contact. Despite such a crude approximation, the two methods give values which are of a similar order of magnitude. This confirms the assertion that that the contact resistance is removed from the measured resistance through the use of the four point measurement technique.

During all measurements, the applied current remained on whilst the applied magnetic field was gradually increased/decreased accordingly at a steady rate of 0.05 Oe/s. An initial test run was performed for each orientation of magnetic field with respect to the applied current for both parallel and perpendicular measurements. Following this, two full magnetisation sweeps were performed; with the magnetic field in each sweep ranging from -200 Oe to +200 Oe. For each sample, the values of saturation resistance for the each orientation were averaged across the two sweeps. The number of sweeps performed was limited by the Joule heating of the sample, which only became noticeable for film thicknesses less than 10 nm when the measurements displayed a linear increase in resistance as a function of time. Since it took approximately an hour per full resistance sweep, it was possible to fit a linear line of best fit to the sample resistance time data, as shown in Figure 4:25. Knowledge of the increase in sample resistance with time allowed for the measured data to be corrected for Joule heating.

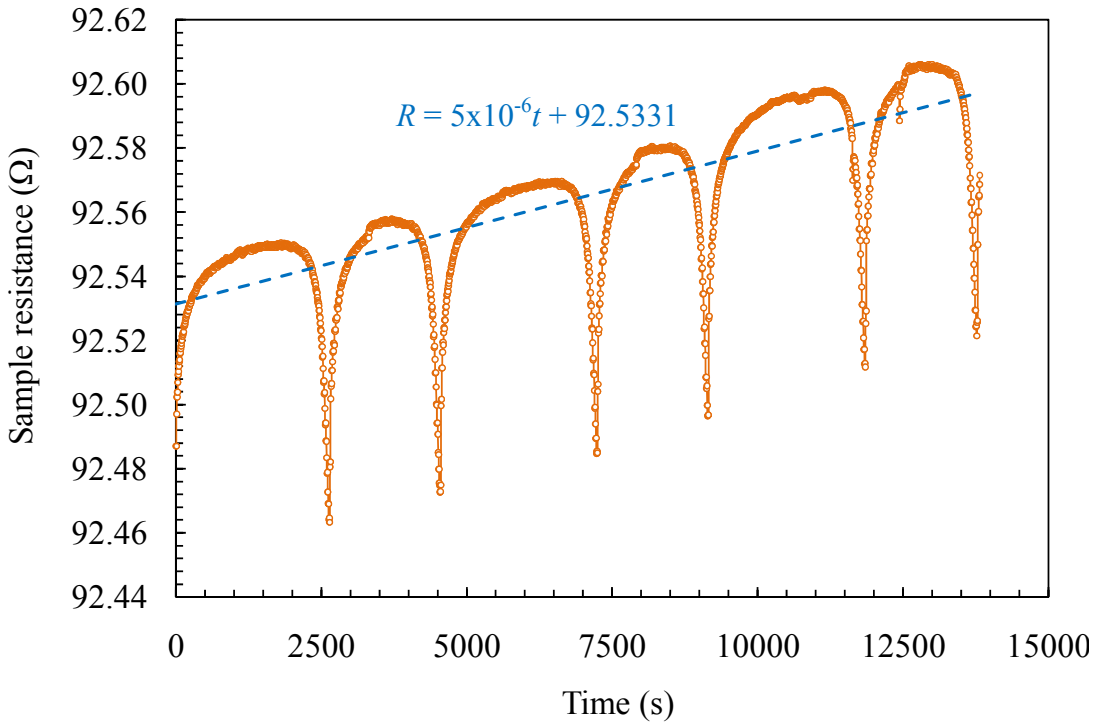

Figure 4:25. Resistance versus time graph for an 11.40 nm thin film to show the effect of Joule heating on the sample resistance. The data shown is for the parallel orientation of the applied current and sample magnetisation, and the large periodic jumps in resistance correspond to magnetisation reversal within the sample. The data were corrected by subtracting the gradient of the slope from the measured resistance.

Chapter 5. The structural properties of $Ni_{81}Fe_{19}$ thin films

5.1 Introduction

Much attention has been given to magnetic phenomena in thin films over the past twenty years. An increased understanding of thin film magnetism has brought important contributions to the fundamental understanding of the physics of magnetism in tandem with the development of critical applications in data storage technology. Example thin film devices that are of technological importance include giant magnetoresistance (GMR) and tunnelling magnetoresistance (TMR) sensors and devices; an example of which includes the study of the large magnetoresistance effects in Fe/MgO/Fe magnetic tunnel junctions [105, 106]. In addition, there are several sensor and memory devices that have been developed that are based on both thin films and nanowire structures, examples of which include references [64, 65 and 107]. The drive to realise increasingly smaller memory bits on magnetic media and to create ever smaller magnetic devices means that the influence of reduced size and surface effects become increasingly important in the design of such structures as bulk behaviour cannot be assumed.

Experimental and theoretical studies of well characterised epitaxial structures based on iron and nickel illustrate how the fundamental magnetic properties such as the magnetic moment [108] and magnetic anisotropies [109] may change markedly in thin films as compared to their bulk counterparts. As fundamental properties such as magnetostriction, magneto-optical effects and the magnetoresistance are caused by spin-orbit effects, the nature of the atomic structure, strain and crystallinity are crucial in determining the observed magnetic properties of thin films. Both the degree of texture and crystallite grain size present within thin films are known to affect magnetoresistance behaviour; indeed, it has been reported that such structural properties are sensitive to the preparation technique and film deposition rate [99].

An investigation of the structural properties of $Ni_{81}Fe_{19}$ thin films thermally evaporated on pre-oxidised silicon substrates using three stable deposition rates is presented in this chapter. Grazing incidence specular x-ray reflectivity measurements were used to provide details of the $SiO_2/Ni_{81}Fe_{19}$ interface as a function of film thickness, as well as providing precise measurements of the $Ni_{81}Fe_{19}$ layer and the nature of any surface oxide layer that may have formed. The location, full width half maxima (FWHM)

and intensity of Bragg diffraction peaks were used to provide information on the strain and texture present within the films as a function of film thickness and comparisons to bulk values have been made. Information on the microstructure of the films was provided using a combination of high angle x-ray diffraction measurements and high-resolution transmission electron microscopy. The magnetic and magnetoresistance behaviour of these films are studied in chapter 6.

5.1.1 Description of samples

Thin films with nominal composition $Ni_{81}Fe_{19}$ were thermally evaporated onto pre-oxidised silicon substrates at a growth pressure of 10^{-6} Torr using the method described in section 4.2.3. Film thickness ranged from 3 nm to 40 nm and for each film thickness a total of three samples were deposited using different stable deposition rates of 0.5 Å/s, 1.0 Å/s and 2.0 Å/s, respectively. For each deposition, thin films were simultaneously deposited onto a square chip (of approximate dimensions 10 mm^2) and two elongated strips (of approximate dimensions 27 mm x 3 mm), as shown in Figure 5:1. The geometry of the chips was optimised to allow for characterisation of thin film samples using grazing incidence specular x-ray reflectivity, x-ray diffraction and magneto-optical Kerr effect magnetometry. Magnetoresistance measurements presented in chapter 6 were performed on the strips; the large aspect ratio was chosen so as to allow a uniform current distribution and to provide reliable magnetoresistance results.

Precise measurements of sample composition were obtained using an Oxford Instruments wavelength dispersive x-ray analysis (WDX) as part of a Hitachi SU-70 field emission gun scanning electron microscope (SEM).

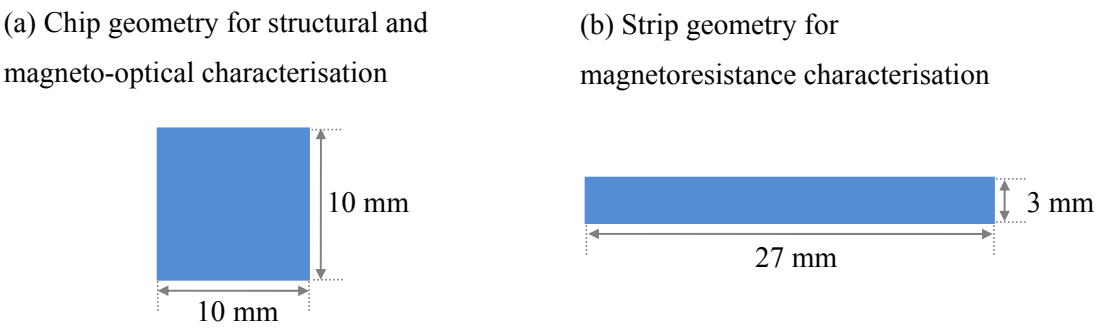

Figure 5:1. Schematic to illustrate the sample geometry used for characterisation of (a) the structural properties characterisation and (b) the magnetic behaviour of $Ni_{81}Fe_{19}$ thin films.

All samples were found to have a composition that was extremely close to that of the nominal composition, with actual compositions varying between $Ni_{81}Fe_{19}$ and $Ni_{83}Fe_{17}$. It is suggested that such deviations from the nominal $Ni_{81}Fe_{19}$ composition of up to 2% is due to the differences in melting temperature of nickel and iron which are 1728 K and 1811 K [1] in air respectively; although these are expected to be slightly lower under high vacuum conditions. However, as there was not a thermocouple present within the equipment it is not possible to have precise knowledge of the exact temperature. Nonetheless, although the measured chemical compositions are slightly nickel rich, the deviations from the nominal composition are not expected to significantly change the physical properties of the thin films.

According to the data presented by Bozorth in references [52, 53 and 55], there is negligible difference between the saturation magnetisation M_s for bulk $Ni_{82}Fe_{18}$ and $Ni_{83}Fe_{17}$ and $Ni_{81}Fe_{19}$. There is also little deviation in the magnitude and sign of the magnetocrystalline anisotropy and magnetostriction constants which are extremely close to zero and show very little change to the values for $Ni_{81}Fe_{19}$. Finally, there is little change in the bulk lattice parameter between these compositions. It is suggested that such small deviations will not affect either the magnetic properties or the lattice parameter and as such values of M_s, K_1, λ_{100}, λ_{111} and a for $Ni_{81}Fe_{19}$ have been used to parameterise all film structures within this study.

5.2 Study of $Ni_{81}Fe_{19}$ thin film sample structure

Grazing incidence specular x-ray reflectivity measurements were made on $Ni_{81}Fe_{19}$ thin films using a Bede GXR1 reflectometer as described in section 4.3.3. All measurements were interpreted by fitting the measured specular reflectivity using the Bede REFS simulation code [73], as described in section 4.3.4.

5.2.1 Overview of sample structure

As all $Ni_{81}Fe_{19}$ films were deposited under vacuum conditions and characterised externally, a thin surface oxide layer was expected to form on removal from the vacuum chamber. As the scattered intensity is related to the Fourier transform of the layer structure, when more than one layer exists each layer will contribute a period to the scattering profile corresponding to the inverse of the individual layer thickness. Thus,

inclusion of the oxide layer in the model structure is imperative to obtaining a good fit between experimentally measured results and simulation.

Figure 5:2 compares experimentally measured specular x-ray reflectivity data for two thin film thicknesses with best fit simulations for $Ni_{81}Fe_{19}$ films both with and without an upper surface oxide layer. Although both models accurately produce the correct number of Kiessig fringes, the light blue curve ($Ni_{81}Fe_{19}/Fe_2O_3$) better reproduces the amplitude of the measured reflectivity curves when compared to the red curve ($Ni_{81}Fe_{19}$ only), which is particularly clear at higher angles. For the thin film samples presented in Figure 5:2, it was observed that the goodness of fit is lower, and therefore the fit is better, when the surface oxidation layer is considered. For example, the goodness of fit (GOF) reduces from 0.142 to 0.112 for a 7 nm thick film and from 0.151 to 0.104 for a 10 nm film on the inclusion of a surface oxide layer.

The goodness of fit parameter in the Bede REFS simulation code [73] is deduced using data fitting techniques based upon χ^2 statistics and is a single number that is used to provide a measure of the quality of the best fit simulation agrees with the experimental data. If the best fit simulation describes all of the details of the sample structure then, in the absence of Poisson noise, the minimum goodness of fit will be zero. However, due to the presence of noise in experimental data the minimum goodness of fit is greater zero even for a perfect model. The goodness of fit is extremely useful for investigating the sensitivity of the experimentally measured reflectivity data to each parameter within the model [73].

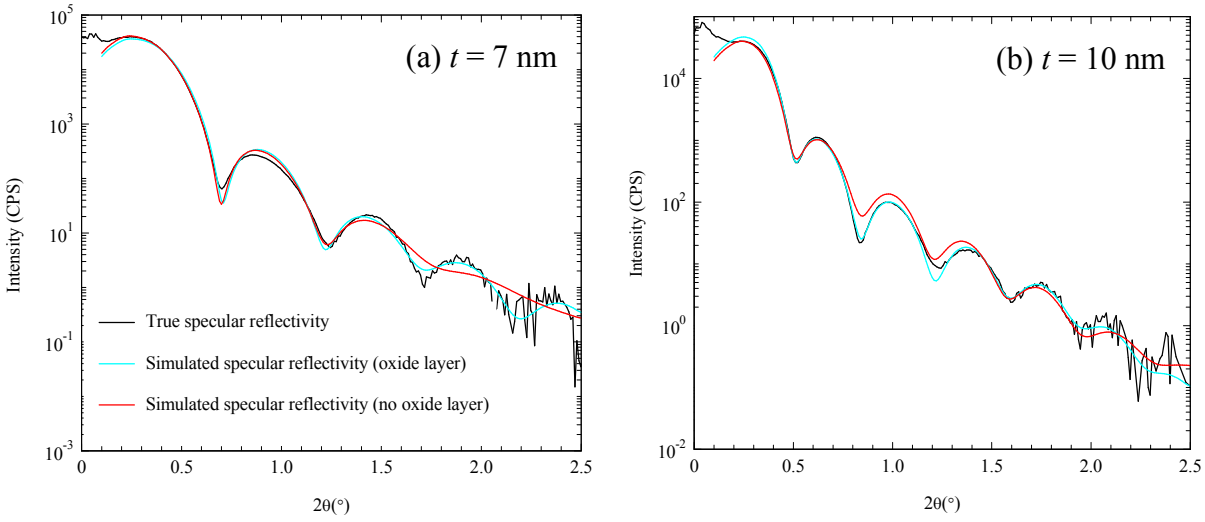

Figure 5:2. Measured and best fit simulated specular x-ray reflectivity scans for $Ni_{81}Fe_{19}$ thin films with and without a surface oxidation layer for (a) nominal $Ni_{81}Fe_{19}$ thickness of 7 nm deposited at a rate of 0.5 Å/s and (b) nominal $Ni_{81}Fe_{19}$ film thickness of 10 nm deposited at a rate 1.0 Å/s.

However, due to variations in experimental conditions, sample structure and Poisson noise it is not possible to compare the goodness of fit for different experimental data.

Due to the variant valence states in the iron there are several compositions and structural forms of iron oxide. As the amount of x-ray scattering is sensitive to the number of electrons present, it is only possible to identify a reduction in electron density, which is likely to be the result of a surface oxide layer. The precise chemical composition or indeed the phase cannot be determined exactly through such simulations. It was not possible to quantify the precise chemical composition using WDX analysis since typical oxide layer thicknesses of ~ 1 nm thick made it difficult to obtain a large enough signal required for precise compositional analysis. It is assumed that the oxide layer has zero spontaneous moment and a magnetisation much less than the $Ni_{81}Fe_{19}$ layer and a nominal composition Fe_2O_3 is used from here on. It is further assumed that the oxide layer is electrically insulating, and thus only the thickness of the $Ni_{81}Fe_{19}$ layer is used when investigating the thickness dependence of structural and magnetic properties presented both in this chapter and chapter 6.

Indeed, whilst the composition of the oxide layer was chosen to be Fe_2O_3, no difference in the simulated reflectivity data was observed if the oxide composition was chosen to be NiO instead. This is due to the values of electron density values in iron and nickel; as discussed previously in section 4.3.2, these correspond to 2.2073 electrons/$Å^3$ and 2.5588 electrons/$Å^3$, respectively. The difference in the electron density between iron and nickel is essentially negligible to an incident x-ray.

5.2.2 Grazing incidence x-ray reflectivity results

Figure 5:3 presents experimentally measured grazing incidence x-ray reflectivity data and corresponding best fit simulations for $Ni_{81}Fe_{19}$ thin films deposited at a rate of 0.5 Å/s. Simulation curves were obtained by recursively fitting the layer thickness, interface width and density of the $Ni_{81}Fe_{19}/Fe_2O_3$ layers as free parameters and as previously described in section 4.3.4. All simulations were based on the nominal structure of the as-deposited films and included a surface oxide layer of 1 nm. The simulations were deemed complete when both the free parameters and the goodness of fit parameter remained constant for more than 10,000 generations. The parameters used to obtain the best fit simulations for films deposited at 0.5 Å/s, 1.0 Å/s and 2.0 Å/s are provided in Table 5:1,Table 5:2 and Table 5:3, respectively.

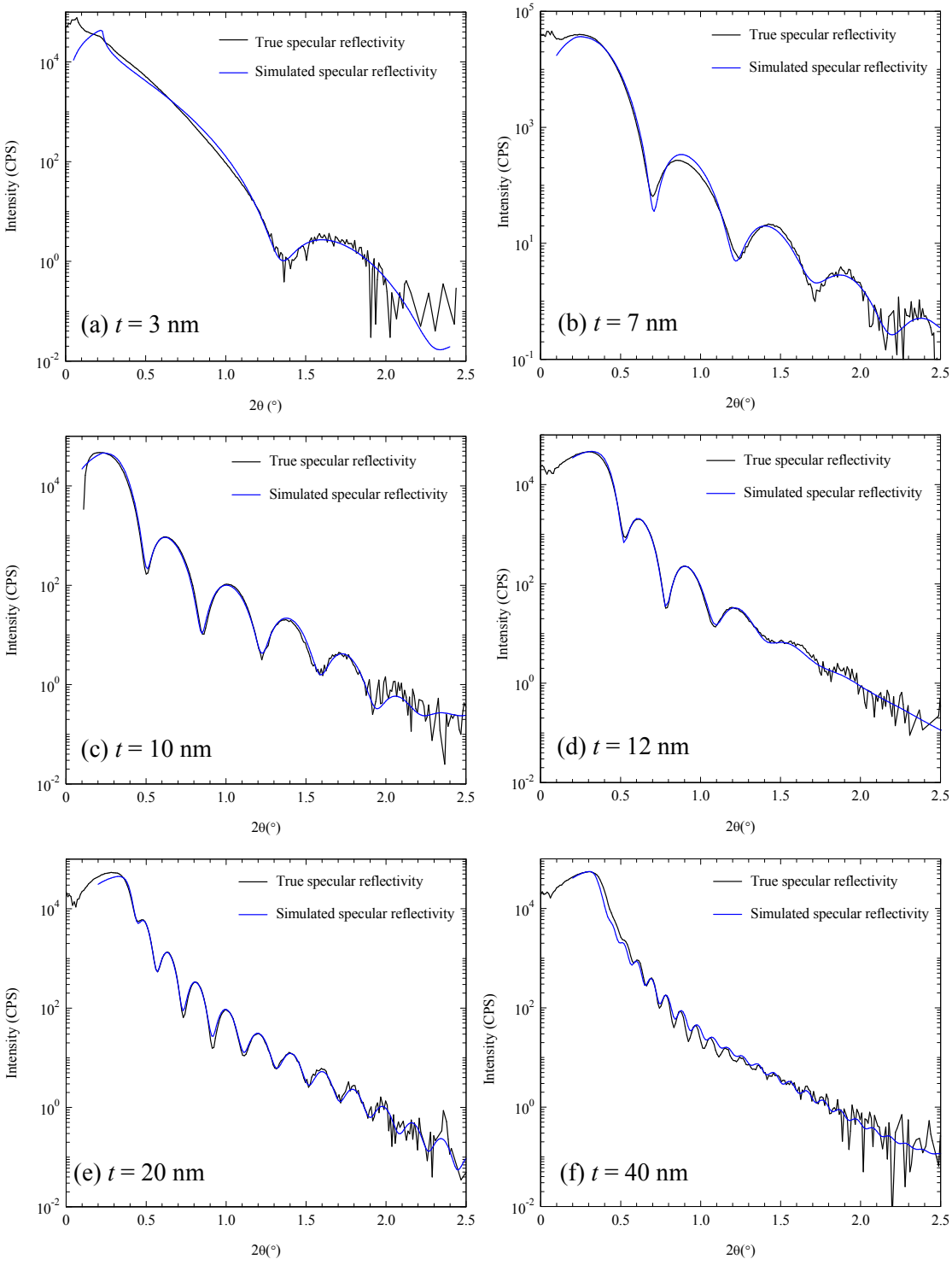

Figure 5:3. Measured specular x-ray reflectivity data (*black curve*) and corresponding simulated reflectivity data (*blue curve*) calculated using Bede REFS simulation software for thin films of nominal film thickness (a) 3 nm (b) 7 nm (c) 10 nm (d) 12 nm (e) 20 nm and (f) 40 nm all deposited at a rate of 0.5 Å/s.

Deposition rate 0.5 Å/s		**Recursively fitted parameters**			
Nominal thickness (nm)	Total thickness (nm)	Layer	Layer thickness (nm)	Interface width (nm)	Layer density (%)
3	3.97 ± 0.03	SiO_2	∞	0.75 ± 0.02	100
		$Ni_{81}Fe_{19}$	3.12 ± 0.03	0.72 ± 0.02	80.0 ± 1.6
		Fe_2O_3	0.85 ± 0.02	0.52 ± 0.02	49.3 ± 0.2
4	7.70 ± 0.01	SiO2	∞	0.69 ± 0.03	100
		$Ni_{81}Fe_{19}$	4.80 ± 0.01	1.24 ± 0.09	100
		Fe_2O_3	2.89 ± 0.01	0.49 ± 0.01	29.2 ± 0.1
5	6.02 ± 0.05	SiO_2	∞	0.46 ± 0.05	100
		$Ni_{81}Fe_{19}$	5.90 ± 0.03	2.18 ± 0.03	85.3 ± 1.6
		Fe_2O_3	0.12 ± 0.04	0.63 ± 0.05	49.0
6	8.47 ± 0.10	SiO_2	∞	0.58 ± 0.03	100
		$Ni_{81}Fe_{19}$	6.51 ± 0.10	1.13 ± 0.15	100
		Fe_2O_3	1.90 ± 0.02	0.49 ± 0.1	10.0 ± 0.3
7	8.25 ± 0.06	SiO_2	∞	0.52 ± 0.01	100
		$Ni_{81}Fe_{19}$	7.36 ± 0.04	0.97 ± 0.05	90.0 ± 1.3
		Fe_2O_3	0.89 ± 0.04	0.38 ± 0.04	20.1 ± 0.7
10	14.26 ± 0.06	SiO_2	∞	0.65 ± 0.01	100
		$Ni_{81}Fe_{19}$	11.36 ± 0.03	0.67 ± 0.01	66.0 ± 0.2
		Fe_2O_3	2.85 ± 0.05	0.10 ± 0.05	11.2 ± 0.2
12	13.55 ± 0.03	SiO_2	∞	0.52 ± 0.09	100
		$Ni_{81}Fe_{19}$	12.70 ± 0.25	1.10 ± 0.04	92.3 ± 1.2
		Fe_2O_3	0.85 ± 0.01	1.14 ± 0.07	59.7 ± 0.5
20	23.76 ± 0.08	SiO_2	∞	0.53 ± 0.05	100
		$Ni_{81}Fe_{19}$	21.36 ± 0.05	1.09 ± 0.04	90.0 ± 0.9
		Fe_2O_3	2.40 ± 0.06	0.30 ± 0.27	9.5 ± 0.1
40	42.02 ± 0.28	SiO_2	∞	0.59 ± 0.03	100
		$Ni_{81}Fe_{19}$	40.39 ± 0.24	1.33 ± 0.08	77.6 ± 1.0
		Fe_2O_3	1.63± 0.10	0.78 ± 0.03	30.0 ± 0.1

Table 5:1. Best fit parameters used in the simulation of specular reflectivity of $Ni_{81}Fe_{19}$ thin films deposited at 0.5 Å/s onto pre-oxidised silicon substrates. The interface widths provided refer to the $SiO_2/Ni_{81}Fe_{19}$, $Ni_{81}Fe_{19}/ Fe_2O_3$ interface and the Fe_2O_3/air interface, respectively.

Deposition rate 1.0 Å/s		**Recursively fitted parameters**			
Nominal thickness (nm)	Total thickness (nm)	Layer	Layer thickness (nm)	Interface width (nm)	Layer density (%)
3	3.45 ± 0.06	SiO_2	∞	0.72 ± 0.02	100
		$Ni_{81}Fe_{19}$	3.12 ± 0.03	2.00	99
		Fe_2O_3	0.33 ± 0.05	0.67 ± 0.05	58.4 ± 5.9
5	6.64 ± 0.08	SiO_2	∞	0.66 ± 0.02	100
		$Ni_{81}Fe_{19}$	5.58 ± 0.08	1.18 ± 0.07	86.5 ± 1.8
		Fe_2O_3	1.06	0.96	25.4
7	10.20 ± 0.06	SiO_2	∞	1.00 ± 0.07	100
		$Ni_{81}Fe_{19}$	7.88 ± 0.05	0.72± 0.01	99.1
		Fe_2O_3	2.31	2.70 ± 0.40	15.2
10	12.53 ± 0.12	SiO_2	∞	0.44 ± 0.10	100
		$Ni_{81}Fe_{19}$	11.47 ± 0.09	0.82 ± 0.05	71.2
		Fe_2O_3	1.06 ± 0.08	1.80 ± 0.80	16.5
12	13.30 ± 0.11	SiO_2	∞	0.64 ± 0.01	100
		$Ni_{81}Fe_{19}$	13.16 ± 0.11	1.22 ± 0.06	93.1 ± 2.0
		Fe_2O_3	0.14 ± 0.03	0.26	6.9
15	16.43 ± 0.16	SiO_2	∞	0.58 ± 0.04	100
		$Ni_{81}Fe_{19}$	15.64 ± 0.11	1.22	92.2 ± 1.9
		Fe_2O_3	0.80 ± 0.12	1.00 ± 0.08	100
20	21.69 ± 0.16	SiO_2	∞	0.49 ± 0.02	100
		$Ni_{81}Fe_{19}$	20.63 ± 0.34	1.37 ± 0.09	87.3 ± 0.9
		Fe_2O_3	1.06 ± 0.08	0.38 ± 0.17	8.4 ± 0.4
40	42.57 ± 0.76	SiO_2	∞	1.00 ± 0.07	100
		$Ni_{81}Fe_{19}$	40.50 ± 0.47	1.00	100
		Fe_2O_3	2.06 ± 0.6	0.76	100

Table 5:2. Best fit parameters used in the simulation of specular reflectivity of $Ni_{81}Fe_{19}$ thin films deposited at 1.0 Å/s onto pre-oxidised silicon substrates. The interface widths provided refer to the $SiO_2/Ni_{81}Fe_{19}$, $Ni_{81}Fe_{19}/ Fe_2O_3$ interface and the Fe_2O_3/air interface, respectively.

Deposition rate 2.0 Å/s		**Recursively fitted parameters**			
Nominal thickness (nm)	Total thickness (nm)	Layer	Layer thickness (nm)	Interface width (nm)	Layer density (%)
3	3.87 ± 0.03	SiO_2	∞	0.86 ± 0.02	100
		$Ni_{81}Fe_{19}$	3.02 ± 0.03	0.70 ± 0.02	80.0 ± 0.3
		Fe_2O_3	0.85 ± 0.02	0.52 ± 0.01	49.3 ± 0.2
5	6.07 ± 0.02	SiO_2	∞	0.51 ± 0.04	100
		$Ni_{81}Fe_{19}$	5.00 ± 0.02	0.69 ± 0.01	84.9 ± 1.2
		Fe_2O_3	1.07 ± 0.01	0.24 ± 0.02	36.1 ± 1.3
7	8.27 ± 0.08	SiO_2	∞	1.00 ± 0.04	100
		$Ni_{81}Fe_{19}$	7.35 ± 0.08	0.75 ± 0.01	100
		Fe_2O_3	0.91 ± 0.01	0.28 ± 0.01	8.1
10	13.50 ± 0.06	SiO_2	∞	0.77 ± 0.02	100
		$Ni_{81}Fe_{19}$	11.50 ± 0.04	0.66 ± 0.01	67.2 ± 0.9
		Fe_2O_3	2.40 ± 0.04	0.10	11.7
12	16.40 ± 0.09	SiO_2	∞	0.65 ± 0.03	100
		$Ni_{81}Fe_{19}$	13.40 ± 0.09	1.17	100
		Fe_2O_3	3.00 ± 0.09	2.00	40.3
15	16.48 ± 0.16	SiO_2	∞	0.62 ± 0.03	100
		$Ni_{81}Fe_{19}$	15.60 ± 0.11	1.21	90.2 ± 0.8
		Fe_2O_3	0.88 ± 0.12	1.00 ± 0.08	96.0
20	22.70 ± 0.05	SiO_2	∞	0.59 ± 0.04	100
		$Ni_{81}Fe_{19}$	21.75 ± 0.11	1.45 ± 0.10	71.2 ± 0.7
		Fe_2O_3	0.95 ± 0.2	0.91 ± 0.21	36.2 ± 0.8
40	45.02 ± 0.12	SiO_2	∞	0.62 ± 0.08	100
		$Ni_{81}Fe_{19}$	43.36 ± 0.09	1.15	81.2
		Fe_2O_3	1.68 ± 0.08	0.58 ± 0.07	24.6

Table 5:3. Best fit parameters used in the simulation of specular reflectivity of $Ni_{81}Fe_{19}$ thin films deposited at 2.0 Å/s onto pre-oxidised silicon substrates. The interface widths provided refer to the $SiO_2/Ni_{81}Fe_{19}$, $Ni_{81}Fe_{19}/ Fe_2O_3$ interface and the Fe_2O_3/air interface, respectively.

5.2.3 *Analysis of layer thicknesses*

Figure 5:4 presents the total measured sample thickness ($Ni_{81}Fe_{19}$ layer and Fe_2O_3 layer) as a function of nominal film thickness for all deposition rates. A linear line of best fit to all the data suggests that the total film thickness is up to 4% greater than nominal film thickness, which is attributed to the presence of a low density surface oxide layer. The non-zero intercept is also attributed to the presence of the oxide layer. The line of best fit has an R^2 value of 0.99 which suggests that there is no systematic dependence of the total film thickness upon the deposition rate, and that the *in-situ* rate monitor is well calibrated for all deposition rates.

Figure 5:5 compares the thicknesses of the constituent $Ni_{81}Fe_{19}$ and Fe_2O_3 layers as a function of nominal film thickness for all sample deposition rates. Considering the $Ni_{81}Fe_{19}$ layer initially, there is no systematic dependence of the measured film thickness upon the deposition rate. A line of best fit to all the data has an R^2 value of > 0.99, with a gradient of (3 ± 1) %, and an intercept of (0.48 ± 0.21) nm. The non-zero intercept is consistent with the values of the $SiO_2/Ni_{81}Fe_{19}$ and $Ni_{81}Fe_{19}/Fe_2O_3$ interface widths provided in Tables 5.1 to 5.3, respectively.

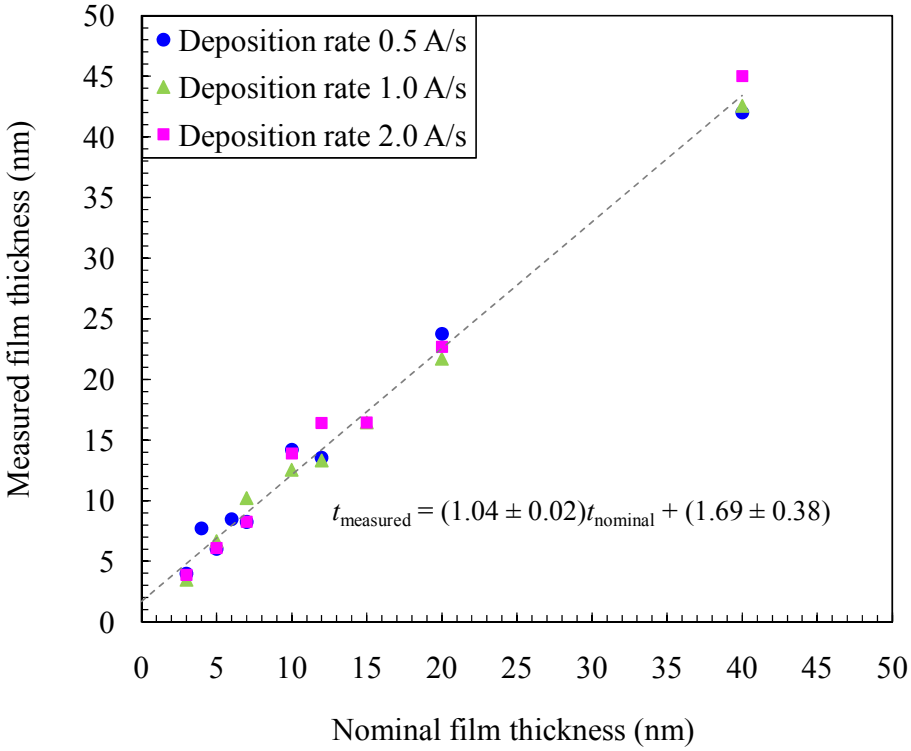

Figure 5:4. Nominal film thickness versus total film thickness ($Ni_{81}Fe_{19}$ layer and Fe_2O_3layer) for thin films deposited at 0.5 Å/s (●), 1.0 Å/s (▲) and 2.0 Å/s (■), respectively. The line of best fit is the best fit to all the data. Error bars are not visible since they are smaller than data points.

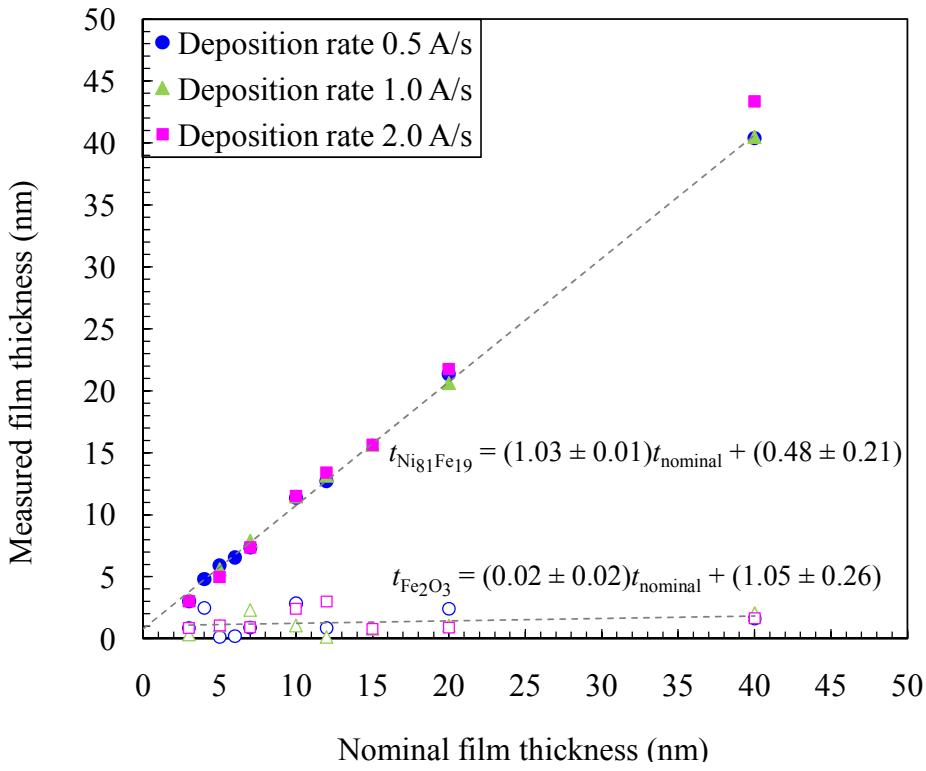

Figure 5:5. Nominal film thickness versus measured $Ni_{81}Fe_{19}$ layer (*solid symbols*) and Fe_2O_3 (*open symbols*) thickness, for thin films deposited at 0.5 Å/s (●), 1.0 Å/s (▲) and 2.0 Å/s (■), respectively. The lines of best fit are the best fit to all the data. Error bars are not visible since they are smaller than data points.

In general, the thickness of the surface oxide layer is independent of nickel-iron film thickness and has a typical thickness of ~ 1 nm, although there are several exceptions to this. Specular x-ray reflectivity measurements on those films with a larger oxide layer were made several months after both film deposition and measurements of the remainder of the samples. It is known that thin film quality degrades over time as the oxide layer expands [110]; as such the anomalies in the thicknesses of the oxide layer are attributed to the consequence of the aging of films.

5.2.4 Analysis of $SiO_2/Ni_{81}Fe_{19}$ and $Ni_{81}Fe_{19}/Fe_2O_3$ interface widths

Interfacial roughness can alter the thin film properties at the interface. An interface is an area of reduced symmetry and so at the interface the atomic layers of each material bond differently when compared to the bulk. Altered bonding can lead to magnetoelastic effects and therefore magnetostriction [111, 112, 113], and thus knowledge of the nature of the

interfaces of the $Ni_{81}Fe_{19}$ layers is important for understanding the magnetic properties of these films are presented and discussed in chapter 6.

Figure 5:6 presents the ratio of the interface width at the substrate to the film thickness. Although all simulations suggest that the $SiO_2/Ni_{81}Fe_{19}$ interface is less than 1 nm, with typical values around 0.5 nm, it can be seen that for film thicknesses less than 10 nm the interface width represents an increasing larger proportion of the total $Ni_{81}Fe_{19}$ film thickness. As specular x-ray reflectivity only measures the structure in the plane normal to the sample, it is not possible to distinguish between topological roughness and chemical intermixing of the layers at the interface. It is likely that the interface width parameters are a combination of each of these factors. Following the analysis of Kim and Silva in [112], it is suggested that the interface width-to-thickness ratio is important and may cause changes in the magnetostriction constant at the interface between the substrate and the film. Since magnetostriction is caused by spin-orbit effects the nature of the bonding environment at the interface is important for understanding magnetoresistance behaviour, which is also caused by spin-orbit effects and is addressed in further detail in chapter 6.

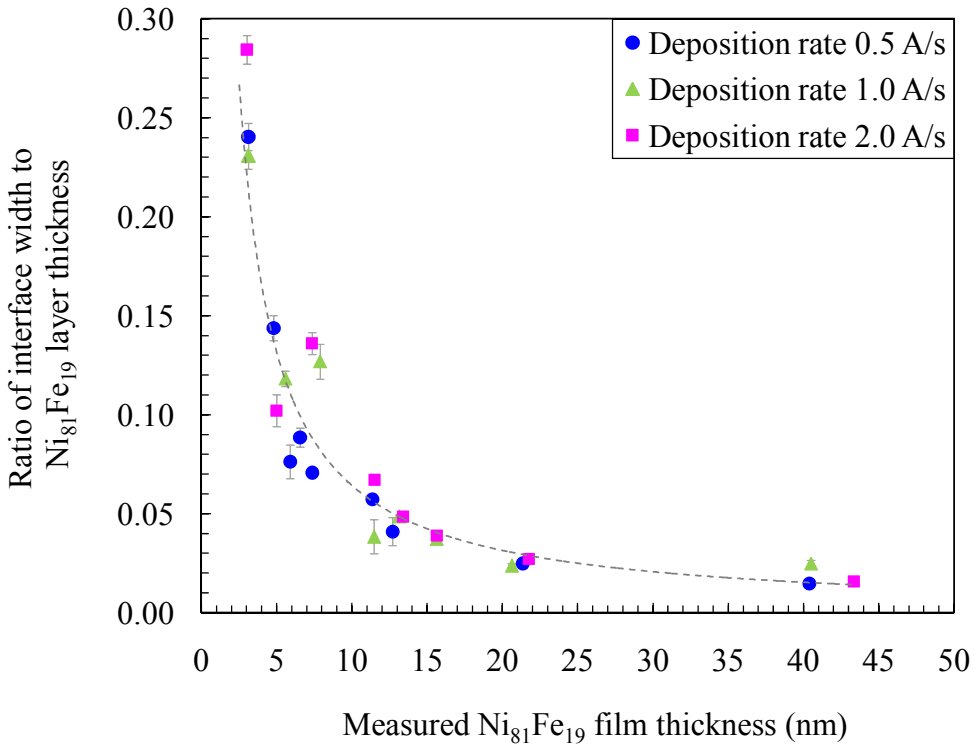

Figure 5:6. Ratio of $SiO_2/Ni_{81}Fe_{19}$ interface width to $Ni_{81}Fe_{19}$ film thickness for thin films deposited at 0.5 Å/s (●), 1.0 Å/s (▲) and 2.0 Å/s (■), respectively. The line is a guide to the eye only. Error bars are present on all data, although they are several they are smaller than data points and thus are not visible.

The width of the $Ni_{81}Fe_{19}/Fe_2O_3$ interfaces presented in Table 5:1 to 5:3 indicate that all films are continuous in the direction normal to the substrate. As discussed earlier in section 5.2.1, a thin surface oxide layer is expected to form on the $Ni_{81}Fe_{19}$ layer on removal from the thermal evaporator vacuum chamber. Best-fit simulations estimate the density of the oxide layer to be less than 50% that of the density of bulk Fe_2O_3. It is suggested that the observed reduction in oxide layer density are the result of a combination of several factors. Firstly, as typical interface widths are seen to be comparable in thickness to the layer itself it is suggested that the surface oxidation layer is a gradual transition and that this interface is largely due to chemical intermixing. Furthermore, a decrease in the layer density may arise as a result of surface roughness (with typical out-of-plane widths between 0.5 nm and 1 nm); although such surface roughness is likely to be a combination of topological roughness and chemical intermixing of the $Ni_{81}Fe_{19}$ and Fe_2O_3 layer. The magnitude of surface roughness is not expected to significantly affect either the magnetic or magnetoresistance properties of the films. Finally, as discussed in section 4.3.5, the intensity of measured diffraction peaks depends sensitively upon the layer thickness. Since typical surface oxide layer thicknesses are approximately 1 nm it is suggested that the contribution of the oxide layer to the x-ray diffraction measurements will be negligible.

5.3 Characterisation of the microstructural properties of $Ni_{81}Fe_{19}$ thin films

The following sections describe the measurement and characterisation of x-ray diffraction peaks from polycrystalline $Ni_{81}Fe_{19}$ thin films, which in turn have been used to derive information on the nature of the microstructure. High angle x-ray diffraction has been used to measure the texture (preferred orientation), out-of-plane lattice parameter, and average out-of-plane crystallite grain size of polycrystalline $Ni_{81}Fe_{19}$ thin films. All measurements were performed on a Bede D1 diffractometer and MicroSource® x-ray generator that was monochromated to produce CuK_α x-ray radiation ($\lambda = 1.5406$ Å), as outlined in section 4.3.6.

5.3.1 Determination of peak position and preferred orientation

Both the position and shape of Bragg diffraction peaks provide information on the crystallographic orientation of the film normal to the sample surface. The intensity of the

measured diffraction peaks is determined by both the sample thickness and the presence of a preferred crystallite orientation. Figure 5:7 presents coupled θ-2θ x-ray diffraction scans for $Ni_{81}Fe_{19}$ thin films deposited on a pre-oxidised silicon substrate as a function of film thickness. All points were measured with a count time of 20 seconds, with a step size of 0.05°. It can be seen that there are three diffraction peaks located at $2\theta \approx 44°$, 52° and 69° respectively; the first two are believed to correspond to the diffraction of x-rays from the $Ni_{81}Fe_{19}$ (111) and (002) planes, whilst the latter corresponds to the Si (004) peak from the Si substrate. The diffraction peak from the (022) peak is not visible since it lies beneath the tail of the (004) peak from the silicon.

For a randomly dispersed powder diffraction sample, the relative integrated intensities beneath the measured Bragg diffraction peaks can be determined from the square of the structure factor (equal to $4f^2$ for face-centre cubic structures) and the multiplicity factor. The multiplicity factor arises from there being more than one plane of the type $\{hkl\}$.

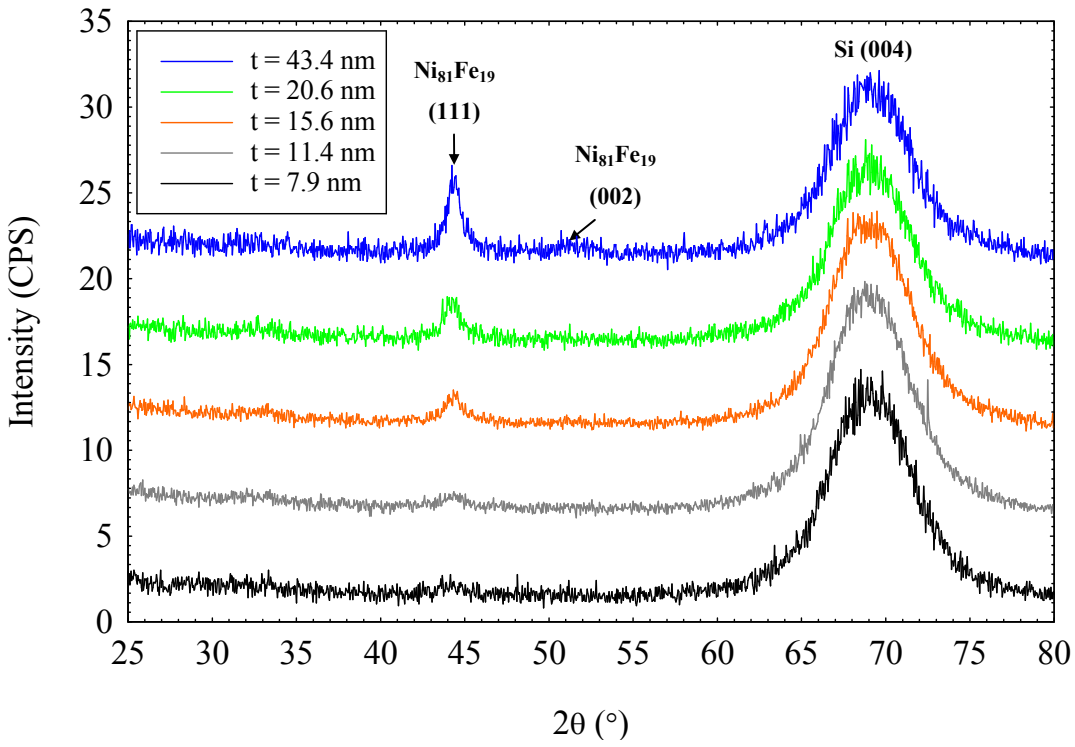

Figure 5:7. Offset coupled θ-2θ x-ray diffraction curves for $Ni_{81}Fe_{19}$ thin films as measured using CuK_α radiation on the Bede D1 diffractometer and MicroSource®. Successive scans are offset by 5 for clarity. All points were measured with a count time of 20 seconds with a step size of 0.05°. Thin films deposition rates were as follows: t = 7.9 nm (1.0 Å/s), t = 11.4 nm (0.5 Å/s), t = 15.6 nm (2.0 Å/s), t = 20.6 nm (1.0 Å/s) and t = 43.4 nm (2.0 Å/s), respectively.

For the {111} family of reflections, for example, the multiplicity factor is 8 since diffraction can occur from $(111),(11\bar{1}),(1\bar{1}1),(\bar{1}11),(1\bar{1}\bar{1}),(\bar{1}1\bar{1}),(\bar{1}\bar{1}1),(\bar{1}\bar{1}\bar{1})$ planes, which multiplies the probability that such a chance orientation occurs by a factor of 8. Multiplicity factors for the {002} and {022} sets of planes can be deduced in a similar fashion and correspond to 6 and 12, respectively. It can be seen in Figure 5:7 that the intensity of the (111) peak is significantly larger than that of the (002) peak; indeed, this is most noticeable in measured data from the 43.3 nm thin film.

It is a characteristic structural feature of thin polycrystalline films that, for a given measurement direction, certain crystallographic lattice planes can occur with greater probability than others, for example see reference [114]. This phenomenon is termed either 'preferred orientation' or 'texture' (the terms are used interchangeably here) and its effect on the measured x-ray diffraction data is illustrated in Figure 5:8. Metal thin films tend to have a preferred orientation; indeed, $Ni_{81}Fe_{19}$ films deposited on SiO_2 tend to have (111) texture [115].

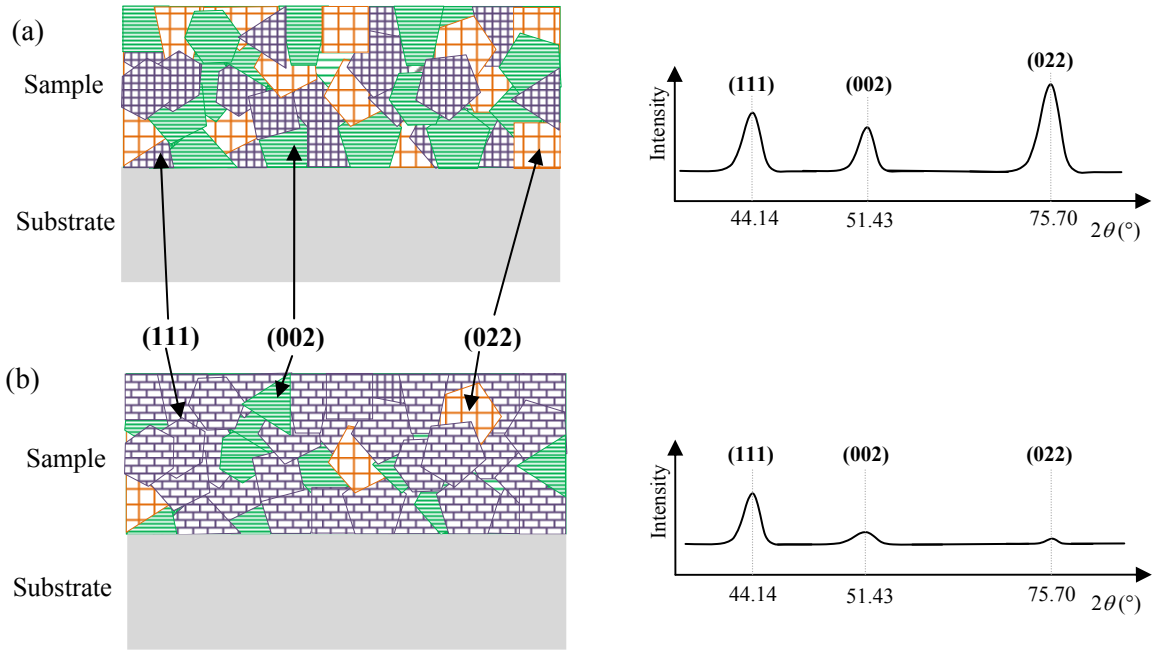

Figure 5:8. Schematic to show possible crystallite grain structure within $Ni_{81}Fe_{19}$ thin films. Truly polycrystalline $Ni_{81}Fe_{19}$ samples have an isotropic distribution of allowed grain orientations as shown in (a), where the corresponding integrated intensity is the product of the structure factor ($4f^2$ for fcc structures) and the multiplicity factor. In (b), the $Ni_{81}Fe_{19}$ thin film is largely (111) textured which distorts the measured intensities accordingly. In the symmetric x-ray diffraction geometry, x-rays diffract from crystallographic planes that are parallel to the sample surface.

The presence of texture has a significant influence on the diffraction pattern; density enhanced lattice planes will be associated with a pronounced enhancement of the intensity of certain diffraction peaks at the expense of others when compared to the diffraction peaks from a powder sample, as shown in Figure 5:8 (b). Aside from the multiplicity factor, the film thickness also contributes to the relative intensity of diffraction peaks. In thin film samples, the Bragg diffraction peaks are not nearly as sharp, nor as intense, as observed in thicker samples of the corresponding crystals. In the kinematical limit, as film thickness decreases, the height of the diffraction peak also decreases and the integrated intensity is directly proportional to the number of atoms within the sample, N^2.

5.3.2 Analysis of peak position

Quantification of the best fit peak position, shape and width of x-ray diffraction peaks was used to extract information on the nature of the microstructure of the associated diffracting planes. To do so, it was necessary to develop a suitable fit to the measured data from which the required information can be extracted. In particular, in order to develop an explanation of magnetoresistance data presented in chapter 6, it is necessary to identify and quantify the presence of microstrain within the thin films.

Broadly speaking, the presence of microstrain is characterised by a Gaussian profile, whilst a Lorentzian profile suggests the presence of broadening due to a small grain size only. With this in mind, one attempt to develop a best fit to the experimental data measured in this study was obtained by the combination of a linear background and a Pearson VII curve, which is of the form:

$$y(x) = \frac{a_0}{\pi a_2 \left[1 + \left(\frac{x - a_1}{a_2} \right)^2 \right]^{a_3}} \qquad (5:1)$$

Where a_0 is the peak height; a_1 is the peak centre; a_2 is related to the half width at half maximum (HWHM) and a_3 is related to the lineshape. As the value of the lineshape parameter is allowed to vary, a Pearson VII curve can be either purely Lorentzian ($a_3 = 2$), purely Gaussian ($a_3 = \infty$), or a combination of the two. The inclusion of a free lineshape parameter was used to provide detailed information on changes in lineshape profile and thus provides useful information on the nature of microstrain present within the films

studied here. Further information on the use of a Pearson VII curve to extract information from x-ray diffraction peaks is available in [114].

The peak position and full width half maximum (FWHM) for each diffraction peak has been obtained by fitting a line of best fit to the measured data and was performed using the Levenberg-Marquardt algorithm. This is an iterative technique that locates the minimum of a multivariate function using a standard non-linear least-squares process that computes the first derivatives of functions. The goodness of fit is quantified by the reduced χ^2 parameter, and so the fitting method seeks for a global minimum of χ^2 [116]. In each fit there are a total of six free parameters.

Symmetric coupled θ-2θ curves centred about the $Ni_{81}Fe_{19}$ (111) peak with best fit data are presented in Figure 5:9, Figure 5:10 and Figure 5:11 for film thicknesses from 7.9 nm to 21.8 nm. All points were measured with a count time of 45 seconds; with a step size of 0.01°. It can be seen that as film thickness increases, the measured intensity of the (111) x-ray diffraction peak increases, as is expected.

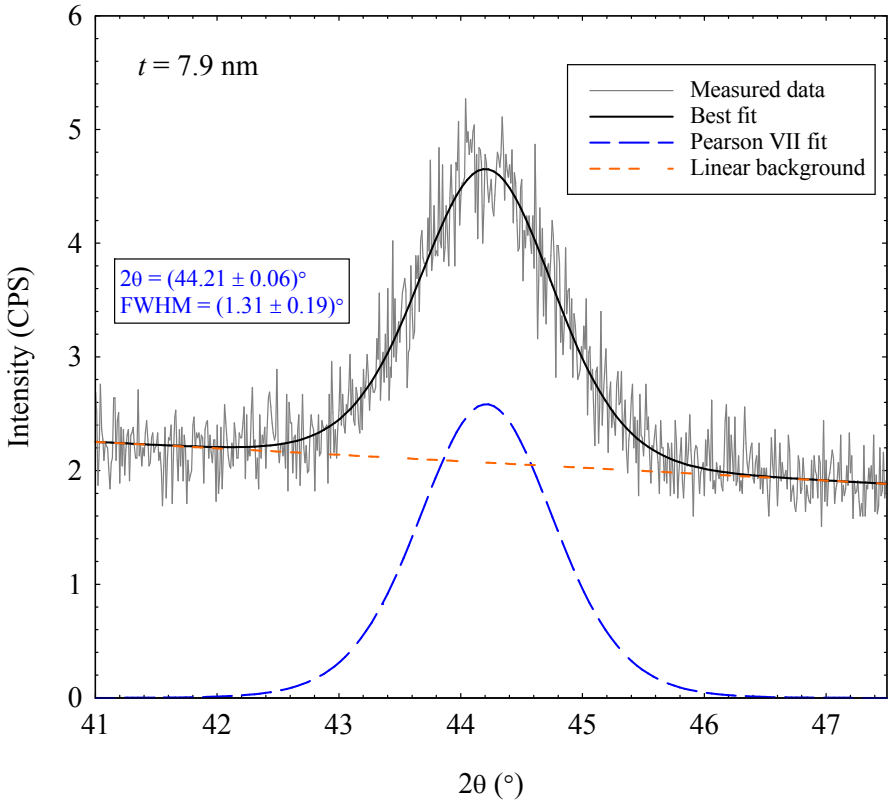

Figure 5:9. Symmetric coupled θ-2θ x-ray diffraction curve about the $Ni_{81}Fe_{19}$ 111 peak for a 7.9 nm film deposited at a rate of 1.0 Å/s. The best fit is given by a Pearson VII curve on top of a linear background and yields a reduced χ^2 values of 0.027.

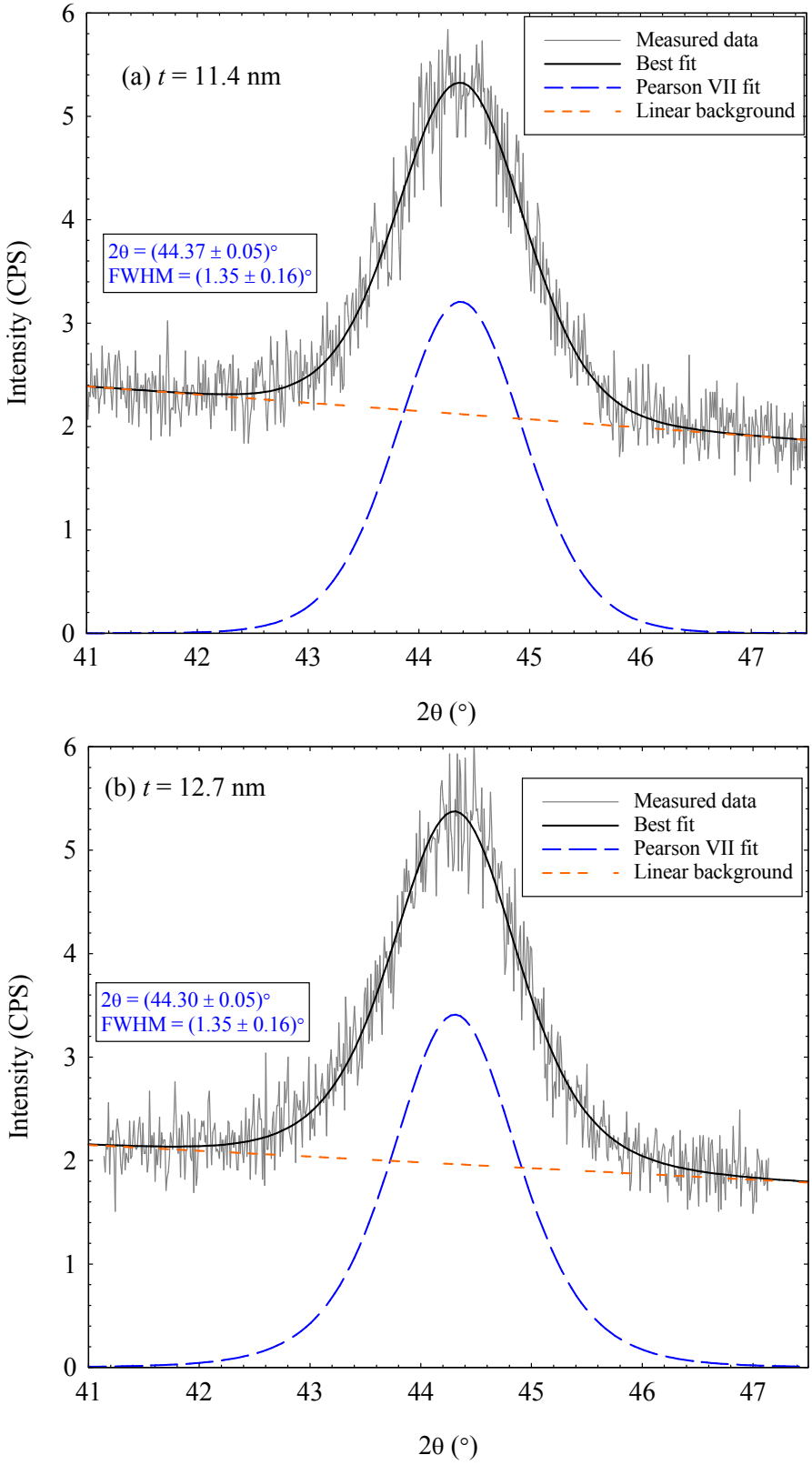

Figure 5:10. Symmetric coupled θ-2θ x-ray diffraction curves about the $Ni_{81}Fe_{19}$ 111 peak for (a) an 11.4 nm film deposited at a rate of 0.5 Å/s and (b) a 12.7 nm film deposited at a rate of 0.5 Å/s For each, the best fit is given by a Pearson VII curve on top of a linear background. The reduced χ^2 values of these fits are 0.023 and 0.019, respectively.

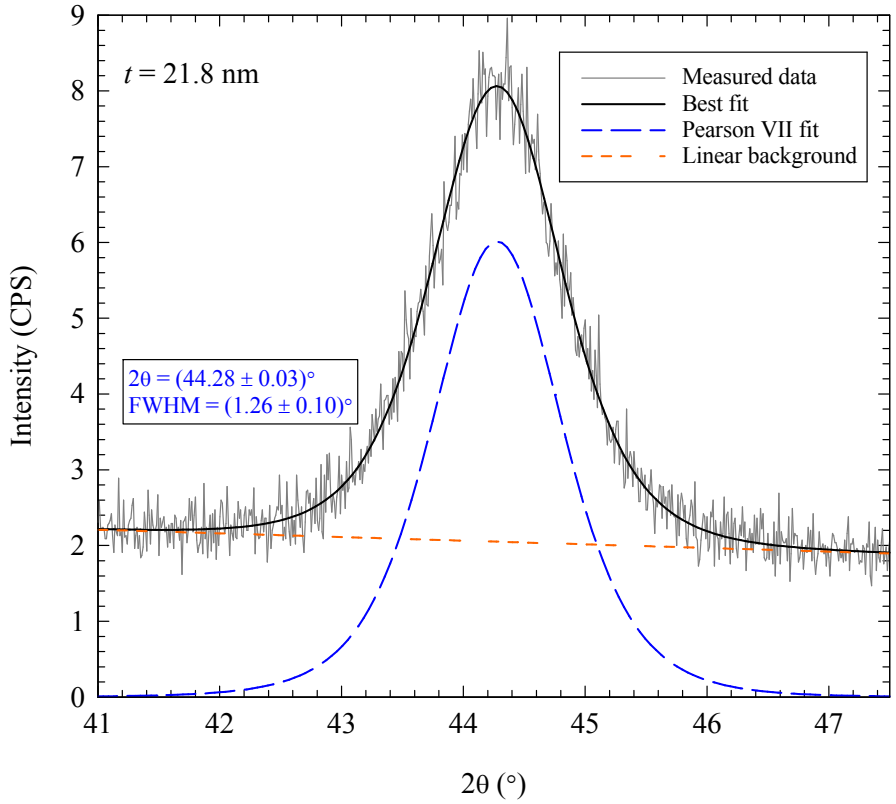

Figure 5:11. Symmetric coupled θ-2θ x-ray diffraction curves about the $Ni_{81}Fe_{19}$ 111 peak for a 21.8 nm film deposited at a rate of 2.0 Å/s. The best fit is given by a Pearson VII curve on top of a linear background and has a reduced χ^2 values of 0.023.

The width of the measured diffraction peaks is closely related to the lineshape parameter (a_3), and as the film thickness increases the lineshape was observed to change from a Gaussian shaped curve as seen in Figure 5:9 and Figure 5:10 (a) to a sharper and more Lorentzian like curve seen in Figure 5:11. Although some broadening of the diffraction peak was expected to occur due to the decrease in film thickness, whilst the *shape* of the peak changes the *width* of the peak shows little change as the film thickness decreases. The FWHM is typically 1°, and it is suggested that this is due to small crystallite grains that are not columnar and is discussed further in section 5.3.3.

The position of the (111) peak for bulk $Ni_{81}Fe_{19}$ is expected to occur at 44.142°, as described in section 4.3.5 (Table 4:1). The location of all peak positions have been measured with respect to the silicon (004) peak, which occurs at 69.129°: thus any changes in the peak position of the $Ni_{81}Fe_{19}$ (111) peak with an unchanged silicon (004) peak are believed to be real and not due to misalignment of the equipment. Figure 5:12 compares the best fit position of the (111) peak as a function of film thickness for $Ni_{81}Fe_{19}$ thin films.

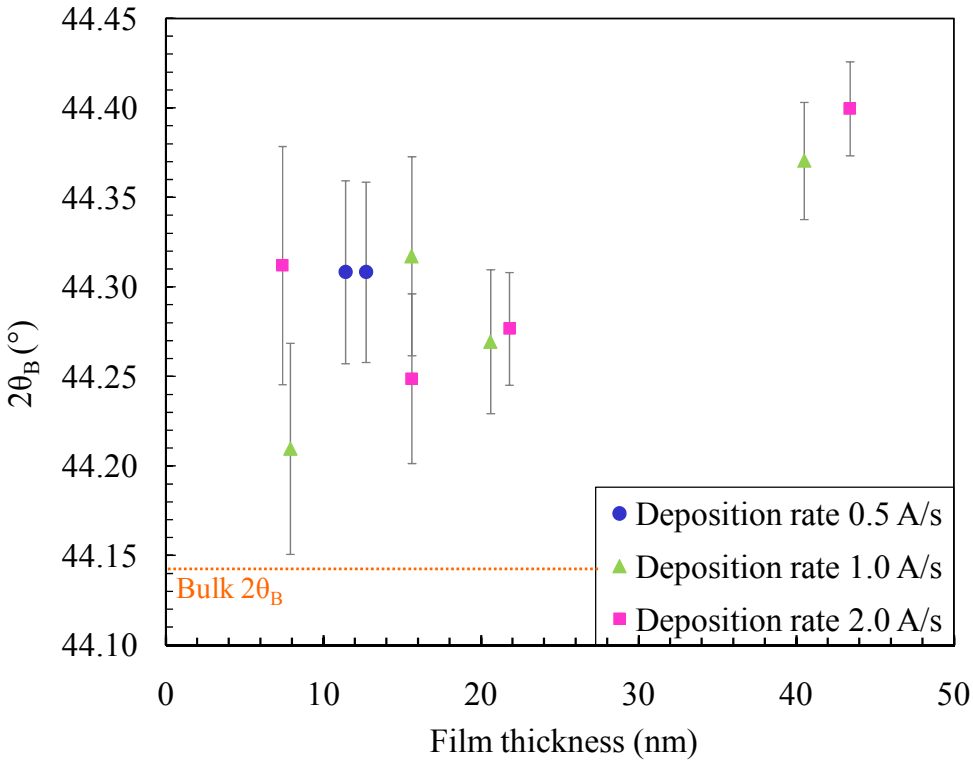

Figure 5:12. Peak positions of the $Ni_{81}Fe_{19}$ (111) peak as measured from best fit Pearson VII curves to experimental data. The (111) peak position for bulk $Ni_{81}Fe_{19}$ is expected to occur at 44.142° and is indicated by the orange dotted line for comparison.

It can be seen that the (111) peak occurs at a higher angle than the bulk value for all thin film thicknesses, with no systematic correlation between deposition rate and peak position. As the angular position of a Bragg peak, θ_B, is determined by the out-of-plane spacing of the atom planes associated with a reciprocal lattice vector, the location of θ_B can be modified by the presence of strain within the sample. As discussed in section 5.2.1, experimental data presented by Bozorth in references [53, 55] suggests that small variations in chemical composition of up to 2% are not expected to change the lattice parameter. Thus, any change in the interplanar spacing associated with specific macroscopic directions is expected to be due to the presence of strain within the sample. The peak position can be used to calculate both the out-of-plane d_{hkl} spacing using Bragg's law, from which the out-of-plane lattice parameter can be deduced via:

$$d_{hkl} = \frac{a}{\sqrt{\left(h^2 + k^2 + l^2\right)}} \tag{5:2}$$

Figure 5:13 presents the out-of-plane lattice parameter values for $Ni_{81}Fe_{19}$ thin films.

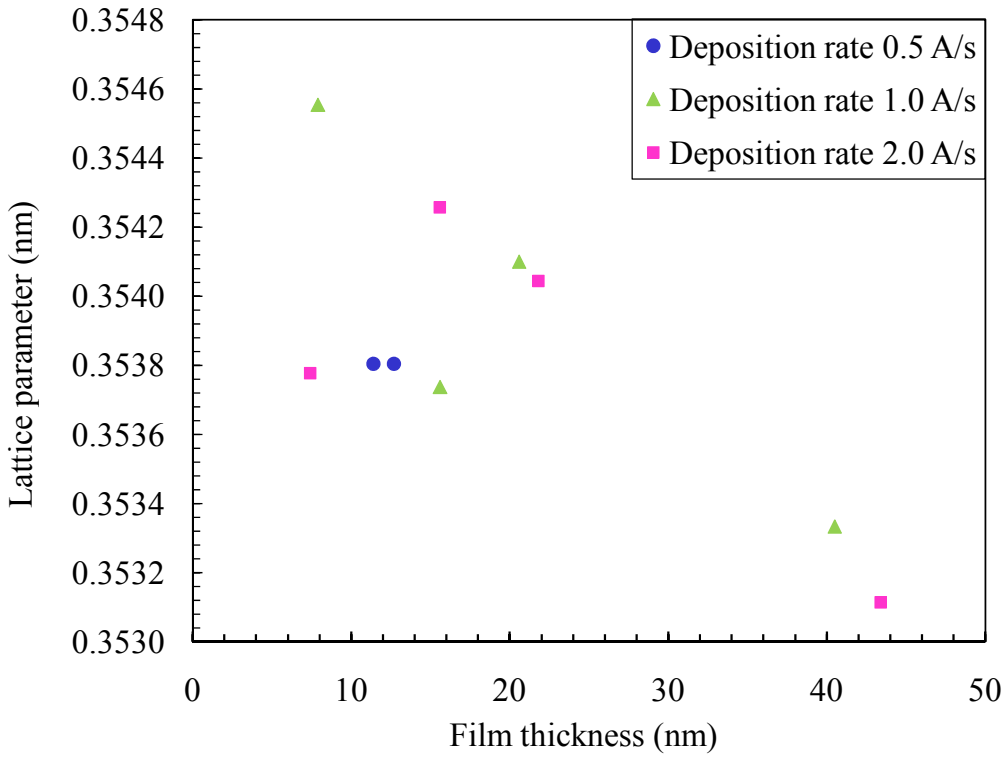

Figure 5:13. Calculated lattice parameter of $Ni_{81}Fe_{19}$ thin films as deduced from peak position measured using Pearson VII fits. Error bars are smaller than data points. Bulk lattice parameter of $Ni_{81}Fe_{19}$ is expected to occur at 0.3551 nm, as given in [53].

All values are lower than the bulk lattice parameter, which has a value of $a_{bulk} = 0.3551$ nm [53]. The largest strain of the lattice parameter occurs in the 40 nm film deposited at 2.0 Å/s, which is 0.56% smaller than that of the bulk lattice parameter. The average out-of-plane lattice parameter is (0.3538 ± 0.0002) nm, where the error quoted here is the standard error on the data. This value is 0.37% smaller than that of the bulk. The shift in measured peak position and consequent reduction in lattice parameter is evidence that the thin film samples are under some form of strain, which is of particular importance for $Ni_{81}Fe_{19}$ thin films in which the magnetostriction is not quite zero. Thus any stress present within the film due to the growth conditions could affect the magnetic and magnetoresistance behaviour, and is discussed in section 6.4.

The observed change in the lineshape from a Gaussian to Lorentzian-like profile with increasing film thickness suggests that there is some microstrain present within thinner films and is possibly a result of strain at the substrate interface. Indeed, close inspection of the peaks presented in Figure 5:10 suggests there may be two peaks present within the central peak. As this is not limited by the resolution of the detector - equal to

0.15°- it is suggested that the $Ni_{81}Fe_{19}$ layer is comprised of two layers; an initial layer that is strained at the interface, above which the lattice parameter has a value that is closer to the bulk value. An alternative method of fitting the x-ray diffraction peaks was therefore applied by fitting two Lorentzian curves, each of the form:

$$y(x) = \frac{a_0}{\pi a_2 \left[1 + \left(\frac{x - a_1}{a_2}\right)^2\right]} \tag{5:3}$$

Where a_0 is the peak height; a_1 is the peak centre; a_2 is related to the HWHM; thus in each fit there are a total of eight free parameters. Best fit data are shown in Figure 5:14, Figure 5:15 and Figure 5:16, and values of reduced χ^2 are provided accordingly. The combination of two Lorentzian curves yields a good overall fit to the measured data, with all fits producing reduced χ^2 of less than one and smaller than the corresponding χ^2 for a single Pearson VII fit.

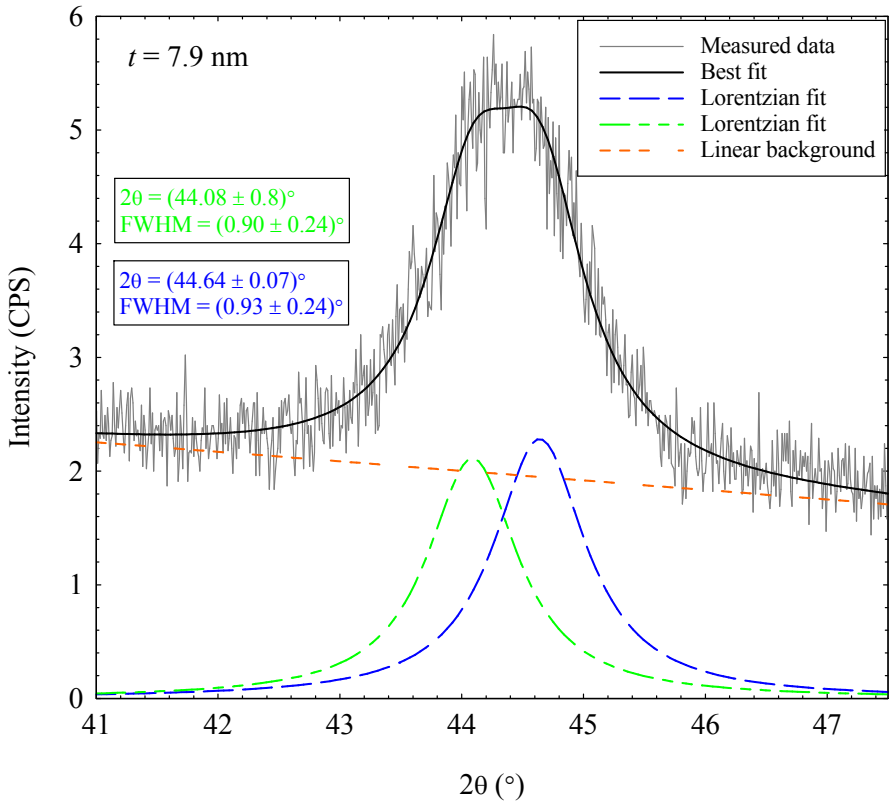

Figure 5:14. Symmetric coupled θ-2θ x-ray diffraction curve about the $Ni_{81}Fe_{19}$ (111) peak for a 7.9 nm thin film deposited at a rate of 1.0 Å/s. The best fit is given by two Lorentzian curves on top of a linear background. The reduced χ^2 value of this fit is 0.025.

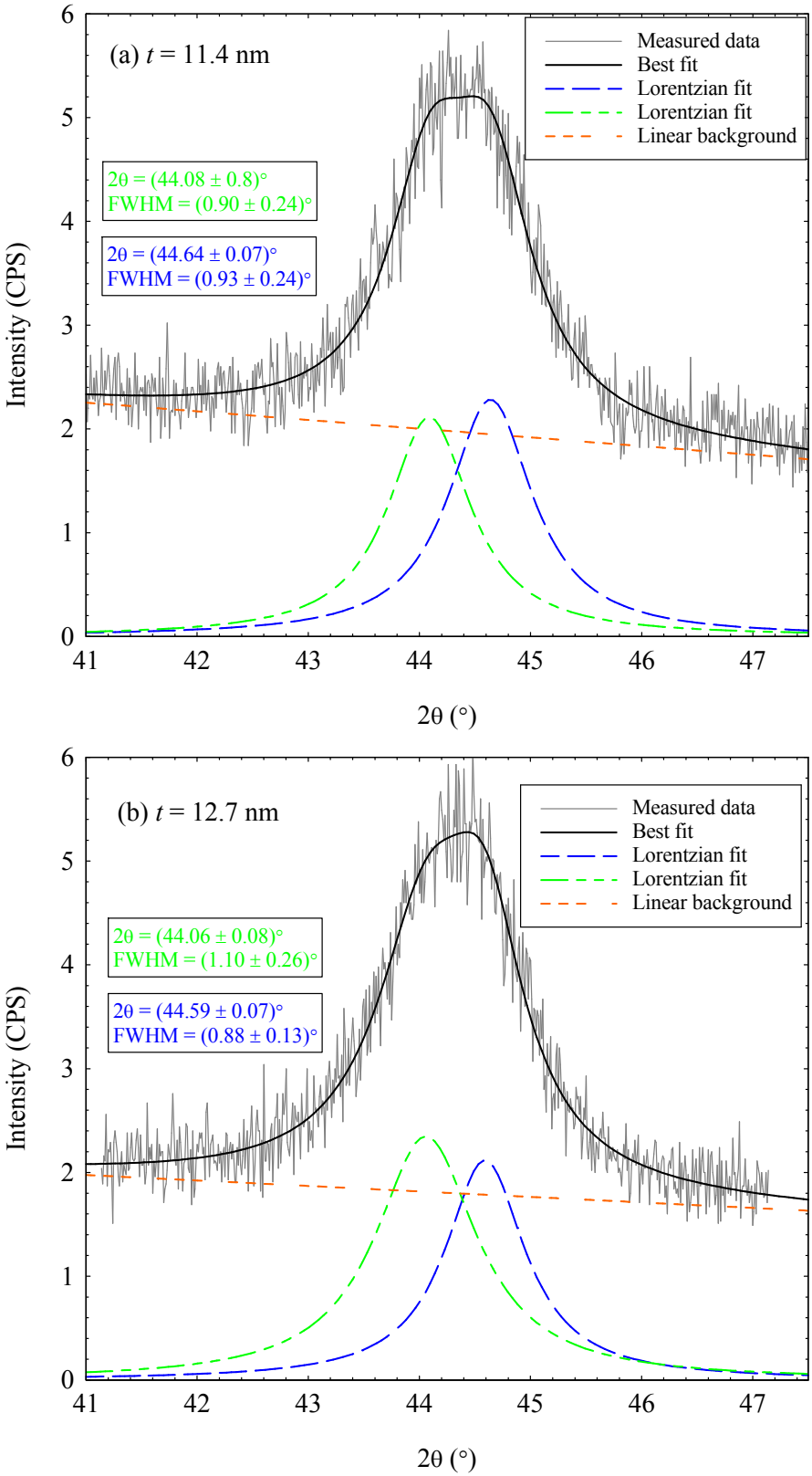

Figure 5:15. Symmetric coupled θ-2θ x-ray diffraction curves about the $Ni_{81}Fe_{19}$ (111) peak for (a) an 11.4 nm thin film deposited at a rate of 0.5 Å/s and (b) a 12.7 nm thin film deposited at a rate of 0.5 Å/s. The best fits are given by two Lorentzian curves on top of a linear background. The reduced χ^2 value of these fits are 0.023 and 0.019, respectively.

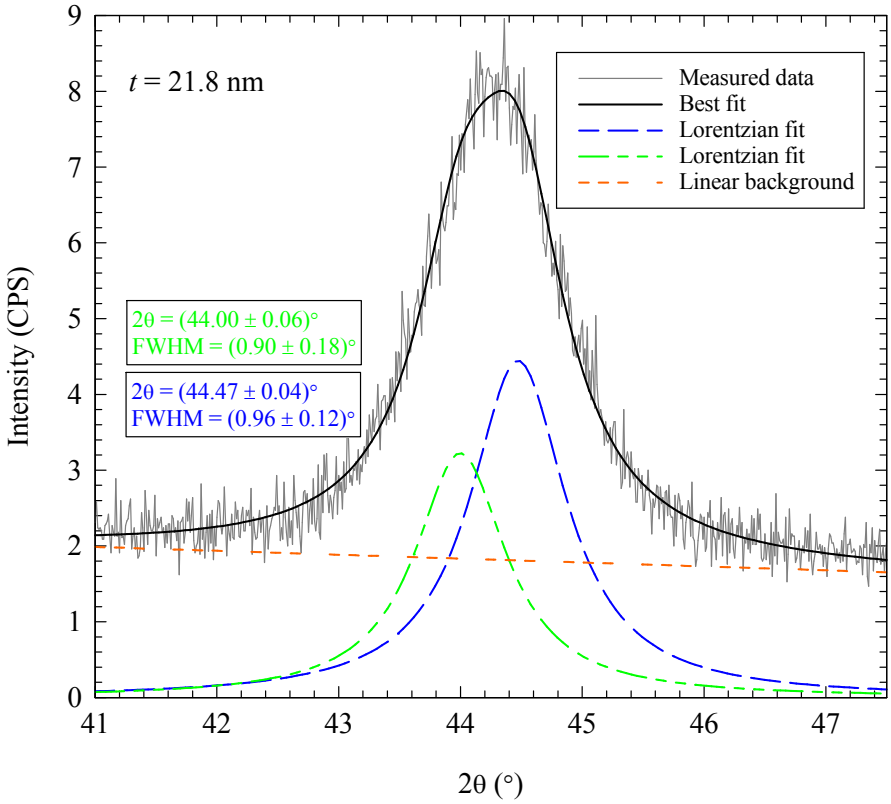

Figure 5:16. Symmetric coupled θ-2θ x-ray diffraction curve about the $Ni_{81}Fe_{19}$ (111) peak for a 21.8 nm thin film deposited at a rate of 2.0 Å/s. The best fit is given by two Lorentzian curves on top of a linear background, and the reduced χ^2 values of this fit is 0.023.

The best fit peak positions obtained from the individual Lorentzian curves are presented in Figure 5:17 (a).

In general, for $t < 20$ nm, the two constituent peaks are located at approximately 44.0° and 44.6° whilst for the 40 nm films (not shown here), the two peaks are located at approximately 44.3° and 44.8°. The constituent best fit peaks show a change in Bragg angle; one exhibits a negative shift from the bulk value whilst the other peak exhibits a positive shift. Furthermore, the height of the lower Bragg angle decreases as film thickness increases whilst the height of the upper Bragg angle shows an increase in height as film thickness increases. It is suggested that these two peak positions given by this analysis must correspond to diffraction from two $Ni_{81}Fe_{19}$ layers with different out-of-plane lattice parameters. The corresponding out-of-plane lattice parameters have been deduced using equations (5:2) and (5:3) and are presented in Figure 5:17 (b).

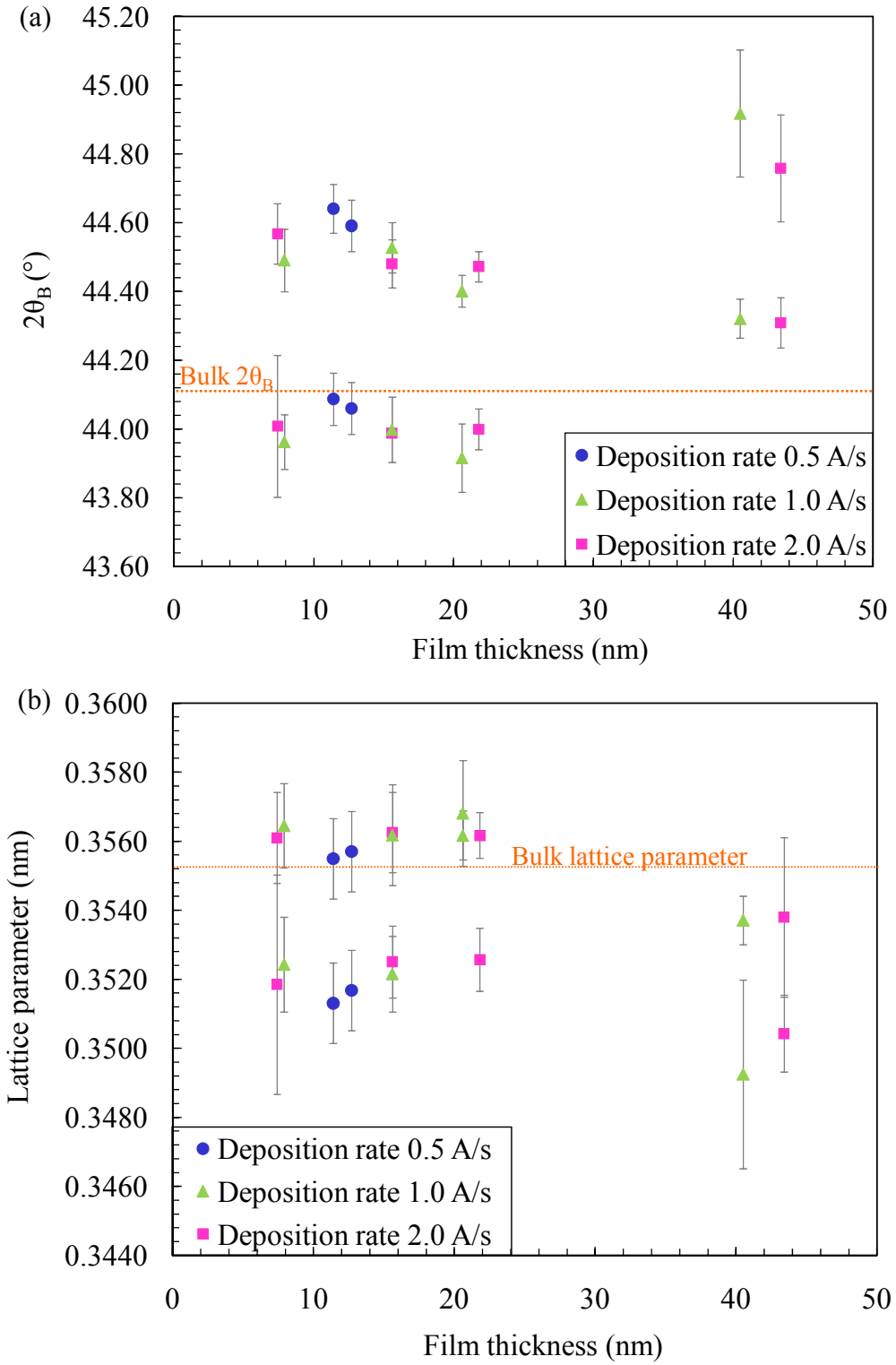

Figure 5:17. (a) Best fit values of peak position when using a combination of two Lorentzian curves to fit to the measured data. The peak position for bulk $Ni_{81}Fe_{19}$ is indicated by the orange line for comparison. (b) Calculated lattice parameter of $Ni_{81}Fe_{19}$ thin films as deduced from peak position measured two Lorentzian curves to fit the $Ni_{81}Fe_{19}$ (111) diffraction peak as shown in Figures 5:14, 5:15 and 5:16. The out-of-plane lattice parameter for bulk $Ni_{81}Fe_{19}$ is expected to occur at 0.3551 nm [53] and is shown by the orange for comparison.

The first Lorentzian fit yields an average out-of-plane lattice parameter (0.3557 ± 0.0004) nm whilst the second yields an average out-of-plane lattice parameter of (0.3516 ± 0.0004) nm. The errors quoted here are the standard error for each data set. Thus, values of lattice parameter deduced by this analysis suggest the presence of an initial $Ni_{81}Fe_{19}$ layer that has an out-of-plane lattice parameter which is larger than bulk by 0.17%, and another layer which is smaller than the bulk by 0.99%.

It is important to note that in order such changes in lattice parameter are not due to changes in chemical composition. The lattice constants of bulk NiFe alloys are reported by Bozorth in reference [53]; the average lattice parameters deduced via the use of a double Lorentzian fit would be obtained by chemical compositions closer to approximately $Ni_{70}Fe_{30}$ and $Ni_{95}Fe_5$, respectively. As such large variations in composition were not observed in WDX analysis of these films, and thus it is suggested that the change in out-of-plane lattice parameter is due to the presence of stress at the substrate interface. Furthermore, as the height of the peak corresponding to the layer in tension decreases as the film thickness increases it is suggested that this layer is only a few nanometres thick.

Since the width of the $SiO_2/Ni_{81}Fe_{19}$ interface comprises a greater proportion of the total film thickness for film thickness less than 10 nm (see Figure 5:6), it is further suggested that the initial few nanometres of growth are under a tensile strain as a result of the shortening of bond lengths at this interface. In addition, for films thicker than 20 nm, both Lorentzian peaks correspond to out-of-plane lattice parameters that are smaller than that of the bulk, and are similar to those values given by single Pearson VII fits. The presence of a thin, strained $Ni_{81}Fe_{19}$ layer at the substrate interface is a potentially significant result and is important to the interpretation of magnetoresistance data presented in chapter 6 (section 6.5). Values of peak position and out-of-plane lattice parameter for these two different approaches of peak fitting are presented in Table 5:4.

Film parameters		**Single Pearson VII fit**		**Double Lorentzian fit**	
Deposition rate (Å/s)	**Film thickness (nm)**	**$2\theta_B$ (°)**	**a (nm)**	**$2\theta_B$ (°)**	**a (nm)**
1.0	7.88 ± 0.05	44.21 ± 0.06	0.3546 ± 0.0009	43.96 ± 0.08	0.3564 ± 0.0012
				44.49 ± 0.09	0.3524 ± 0.0014
2.0	7.35 ± 0.08	44.31 ± 0.07	0.3538 ± 0.0010	44.01 ± 0.11	0.3561 ± 0.0031
				44.57 ± 0.09	0.3518 ± 0.0013
0.5	11.36 ± 0.03	44.31 ± 0.07	0.3533 ± 0.0008	44.09 ± 0.08	0.3555 ± 0.0012
				44.64 ± 0.07	0.3513 ± 0.0011
0.5	12.70 ± 0.25	44.31 ± 0.07	0.3538 ± 0.0008	44.06 ± 0.07	0.3557 ± 0.0012
				44.59 ± 0.07	0.3517 ± 0.0011
1.0	15.64 ± 0.11	44.32 ± 0.06	0.3537 ± 0.0008	44.00 ± 0.09	0.3562 ± 0.0015
				44.52 ± 0.07	0.3522 ± 0.0011
2.0	15.64 ± 0.11	44.25 ± 0.05	0.3543 ± 0.0007	43.99 ± 0.08	0.3563 ± 0.0012
				44.48 ± 0.07	0.3525 ± 0.0010
1.0	20.63 ± 0.34	44.27 ± 0.04	0.3541 ± 0.0006	43.92 ± 0.10	0.3568 ± 0.0015
				44.40 ± 0.04	0.3531 ± 0.0007
2.0	21.75 ± 0.11	44.28 ± 0.04	0.3540 ± 0.0005	44.00 ± 0.06	0.3562 ± 0.0009
				44.47 ± 0.04	0.3526 ± 0.0007
1.0	40.39 ± 0.24	44.40 ± 0.03	0.3533 ± 0.0005	44.32 ± 0.06	0.3537 ± 0.0009
				44.92 ± 0.19	0.3492 ± 0.0027
2.0	43.36 ± 0.09	44.37 ± 0.03	0.3531 ± 0.0004	44.31 ± 0.07	0.3538 ± 0.0011
				44.76 ± 0.15	0.3504 ± 0.0023

Table 5:4. Comparison of best fit Bragg peak position parameters and the corresponding out-of-plane lattice parameters for the $Ni_{81}Fe_{19}$ (111) diffraction peak deduced from single fit Pearson VII curves and double fit Lorentzian curves.

5.3.3 Determination of grain size

The broadening of a Bragg diffraction peak due to finite crystallite size is described by the Scherrer relation [117], which is given by:

$$\Delta(2\theta) = \frac{\kappa\lambda}{D\cos\theta_B} \tag{5:4}$$

Where $\Delta(2\theta)$ is the full width at half maximum of the diffraction peak, λ is the wavelength of the incident radiation, κ is a constant related to the line shape of the diffraction peak and D is the crystallite size normal to the sample surface. Figure 5:18 and Figure 5:19 present average out-of-plane crystallite grain size within $Ni_{81}Fe_{19}$ thin films using values of FWHM deduced from both the Pearson VII fit and double Lorentzian fits, respectively. For each graph, the out-of-plane grain size shows only a weak linear dependence to the film thickness with grain size increasing slightly as film thickness increases. The average crystallite grain size does not scale with film thickness; instead each fitting method suggests that the grains are typically less than 10 nm for all film thicknesses investigated within this study.

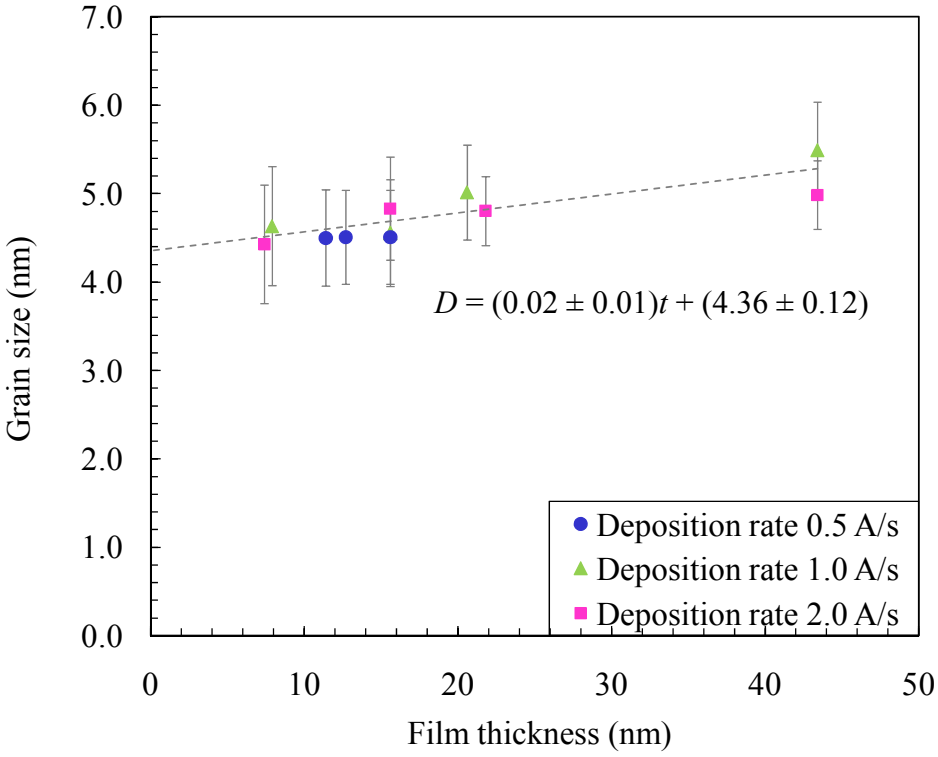

Figure 5:18. Average out-of-plane crystallite grain size within $Ni_{81}Fe_{19}$ thin films as calculated from full-width half maxima from fits to experimental data to experimental data of the $Ni_{81}Fe_{19}$ (111) diffraction peak using a single Pearson VII curve.

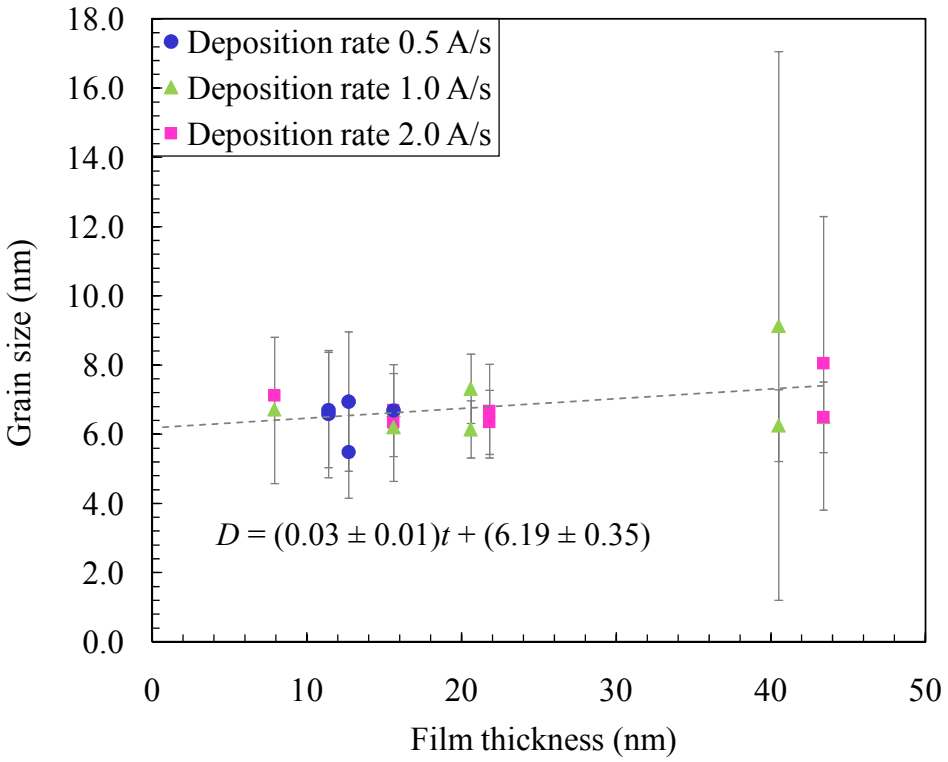

Figure 5:19. Average out-of-plane crystallite grain size within $Ni_{81}Fe_{19}$ thin films as calculated from full-width half maxima from fits to experimental data of the $Ni_{81}Fe_{19}$ (111) diffraction peak using a double Lorentzian fit.

This is a consequence of the fact that all films were thermally evaporated onto cold substrates and is evidence that the grain growth is not columnar.

It is well known that the average crystallite size is sensitive to the preparation technique and may be affected by the rate of deposition, the substrate material, as well as the presence of seeding layers, heating of the substrate during deposition and the use of post-deposition annealing [99]. In general, average crystallite size tends to increase if seeding layers (such as chromium or tantalum) are used. In addition, there is an increase in grain size if there is heating of the substrate during deposition. The consequences of a small crystallite grain size are considered in greater detail in the discussion of magnetoresistance data presented in chapter 6.

Table 5:5 presents FWHM and the corresponding average out-of-plane grain size data for $Ni_{81}Fe_{19}$ thin films deduced using best fit data from a single Pearson VII fit and a double Lorentzian fit, respectively. Measurements of the lateral grain size were obtained using high resolution transmission electron microscopy and are presented in section 5.4.

Film parameters		**Single Pearson VII fit**		**Double Lorentzian fit**	
Deposition rate (Å/s)	**Film thickness (nm)**	**FWHM (°)**	**Grain size (nm)**	**FWHM (°)**	**Grain size (nm)**
1.0	7.88 ± 0.05	1.31 ± 0.20	4.63 ± 0.67	0.91 ± 0.21	6.68 ± 1.53
				0.89 ± 0.21	6.61 ± 1.54
2.0	7.35 ± 0.08	1.37 ± 0.02	4.42 ± 0.07	0.90 ± 0.29	6.71 ± 2.14
				0.85 ± 0.25	7.13 ± 2.10
0.5	11.36 ± 0.03	1.35 ± 0.16	4.50 ± 0.53	0.90 ± 0.25	6.70 ± 1.84
				0.92 ± 0.23	6.59 ± 1.67
0.5	12.70 ± 0.25	1.35 ± 0.02	4.51 ± 0.05	1.11 ± 0.27	5.48 ± 1.33
				0.87 ± 0.25	6.95 ± 2.01
1.0	15.64 ± 0.11	1.33 ± 0.18	4.56 ± 0.60	0.91 ± 0.33	6.68 ± 2.46
				0.98 ± 0.25	6.21 ± 1.56
2.0	15.64 ± 0.11	1.26 ± 0.15	4.83 ± 0.58	0.90 ± 0.25	6.70 ± 1.87
				0.95 ± 0.24	6.34 ± 1.57
1.0	20.63 ± 0.34	1.21 ± 0.13	5.02 ± 0.54	0.83 ± 0.34	7.32 ± 2.97
				0.99 ± 0.13	6.14 ± 0.82
2.0	21.75 ± 0.11	1.27 ± 0.10	4.81 ± 0.39	0.91 ± 0.18	6.68 ± 1.35
				0.96 ± 0.14	6.35 ± 0.92
1.0	40.39 ± 0.24	1.11 ± 0.11	5.50 ± 0.55	0.97 ± 0.16	6.25 ± 1.03
				0.67 ± 0.58	9.13 ± 7.93
2.0	43.36 ± 0.09	1.13 ± 0.09	4.99 ± 0.39	0.93± 0.15	6.50 ± 1.01
				0.75 ± 0.40	8.05 ± 4.24

Table 5:5. Comparison of average out-of-plane crystallite grain size deduced via the Scherrer analysis using full width half maximum (FWHM) values obtained using a single Pearson VII fit and a double Lorentzian fit to the $Ni_{81}Fe_{19}$ (111) diffraction peak.

5.4 High resolution transmission electron microscopy

High resolution transmission electron microscopy (TEM) imaging on 20 nm $Ni_{81}Fe_{19}$ samples thermally evaporated onto silicon nitride membranes was performed by Dr. B. G. Mendis in the Electron Microscopy Facility at Durham University [118]. The sample was nominally identical to a 20 nm sample deposited at a rate of 0.5 Å/s onto a pre-oxidised silicon substrate, although it is recognised that the substrate may modify the grain growth.

TEM imaging is a microscopy technique whereby an electron beam is transmitted through a thin electron transparent sample allowing imaging and electron diffraction patterns to be generated. TEM imaging is complementary to x-ray diffraction in that it provides high resolution images of small regions of the sample. Figure 5:20 presents the diffraction pattern obtained from a nominally 20 nm thick $Ni_{81}Fe_{19}$ film. The series of rings observed in this image correspond to the diffraction of electrons from favourably orientated crystallites; the fact that rings rather than spots are observed is a consequence of the polycrystalline nature of the $Ni_{81}Fe_{19}$ thin film. Assignment of the rings was done by Dr. B. G. Mendis [118]. Analysis of the radius of each individual ring allows the identification of the d_{hkl} for diffracting planes to be identified using:

$$d_{hkl} = \frac{\lambda L}{R} \tag{5:5}$$

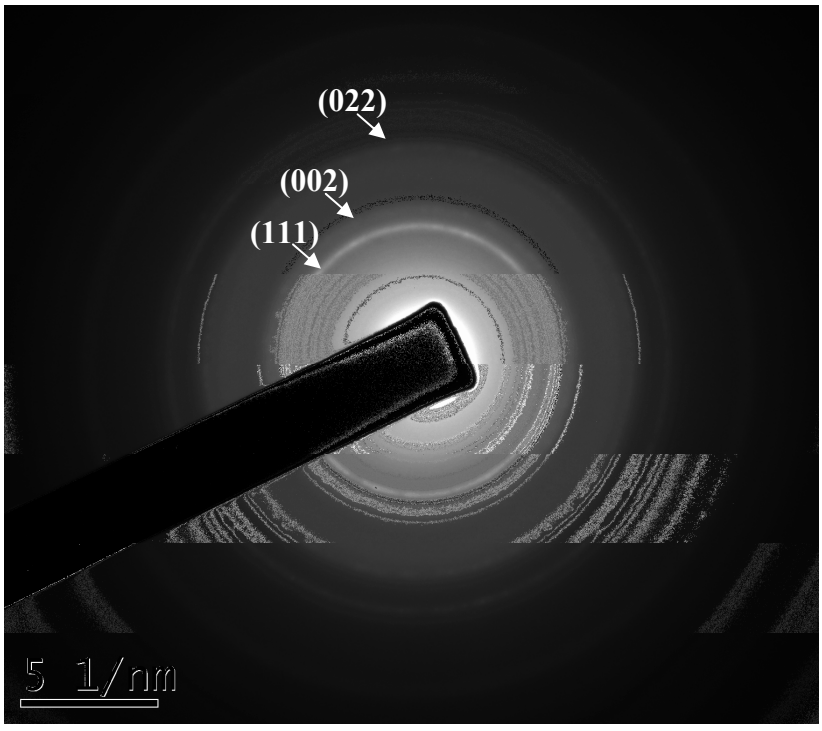

Figure 5:20. Electron diffraction pattern of 20 nm $Ni_{81}Fe_{19}$ thin film. The scale bar is in units of reciprocal space. Image and assignment of diffraction rings by B. G. Mendis, Durham University [118].

Where λ is the electron wavelength, L is the camera length of the electron microscope and R is the radius of each diffraction ring. In Figure 5:20 these correspond to the (111), (002) and (022) planes, respectively. However, the intensity of the (111) ring is brighter than that of the corresponding (002) and (022) rings which suggests the films have a strong (111) texture and is in agreement with the data presented in Figure 5:7. Figure 5:21 presents a high resolution bright field transmission electron microscopy image of the sample surface. All dark points on the images correspond to strongly diffracting planes. Crystallites can be identified in Figure 5:22 by areas surrounded by yellow lines and a variety of grain sizes can be observed. Typical in-plane grain sizes correspond to generally less than 10 nm, which is in good agreement with the out-of-plane analysis presented in the previous section indicated equidimensional crystallites.

Figure 5:23 presents a dark field high-resolution transmission electron microscopy image of the film, in which the variety in grain size can be clearly seen. All bright features correspond to favourably orientated grains that are diffracting. The variation in grain size can be seen more clearly in the dark field image and is observed to range from crystallites as small as 3 nm to up to approximately 10 nm.

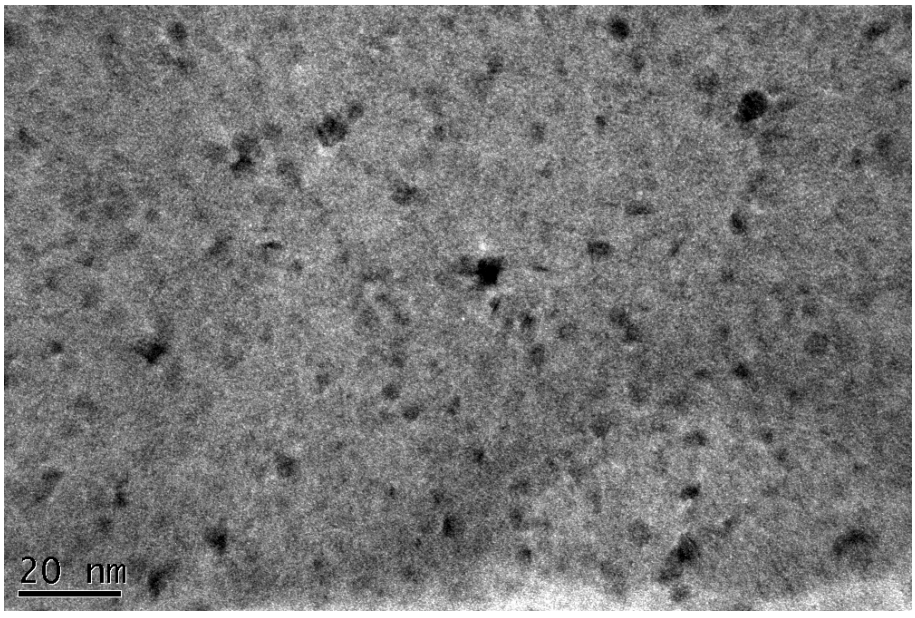

Figure 5:21. Bright field transmission electron microscopy image of a 20 nm $Ni_{81}Fe_{19}$ thin film. All dark features correspond to favourably orientated grains that are strongly diffracting. Image by B. G. Mendis, Durham University [118].

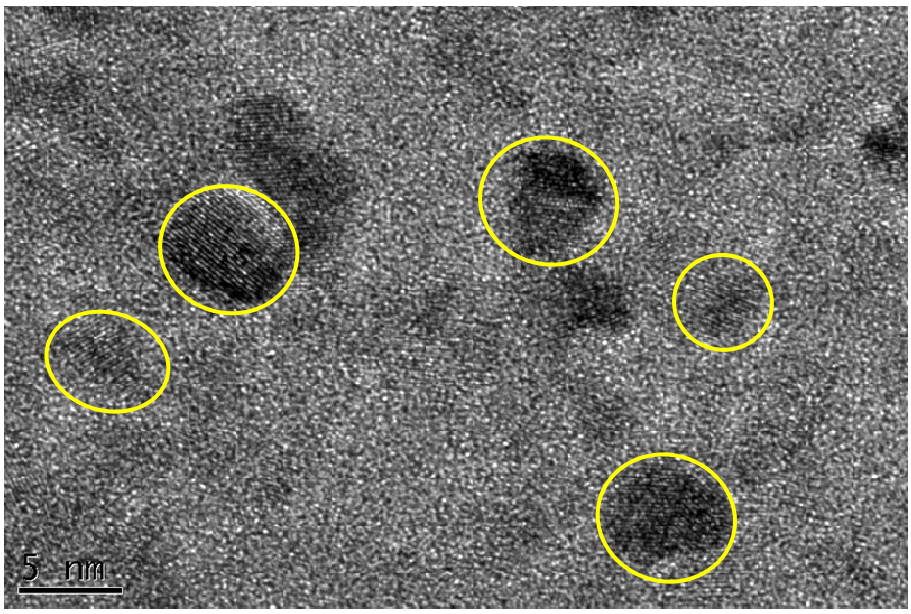

Figure 5:22. Bright field high resolution transmission electron microscopy image of a 20 nm $Ni_{81}Fe_{19}$ thin film. All dark features correspond to favourably orientated grains that are diffracting. Areas circled with a yellow ring highlight areas where the diffracting planes are tilted away from one another which are an indication of mosaic within the thin film. Image by B. G. Mendis, Durham University [118].

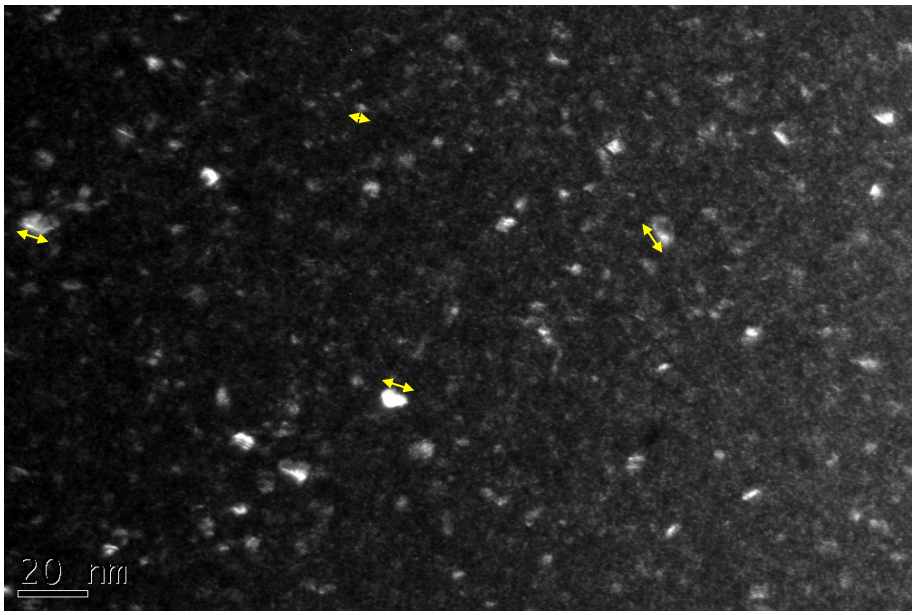

Figure 5:23. Dark field high resolution transmission electron microscopy image of a 20 nm $Ni_{81}Fe_{19}$ thin film. All bright features correspond to favourably orientated grains that are diffracting. The variety in grain size can be seen more clearly in the dark field image and can be seen to range from approximately 3 nm to approximately 10 nm. Image by B. G. Mendis, Durham University [118].

5.5 Chapter conclusion

In this chapter x-ray scattering measurements have been used to study the out-of-plane structure of $Ni_{81}Fe_{19}$ thin films. Thin films in the range 3 nm to 40 nm were fabricated using thermal evaporation at stable deposition rates of 0.5 Å/s, 1.0 Å/s and 2.0 Å/s onto pre-oxidised silicon substrates. Specular x-ray reflectivity measurements have been used to measure the film structure normal to the sample surface and best-fit simulations have been used to quantify the film thickness and interface widths. All films were found to contain a thin oxide layer (of suggested nominal composition Fe_2O_3) approximately 1 nm thick, which was independent of deposition rate and perhaps increases over time.

Direct interpretation of x-ray diffraction peaks has shown that the films are largely (111) textured. The location of the Bragg angle for the (111) plane is shifted from that of the bulk for all film thicknesses investigated. It is suggested that the growth of the initial few nanometres $Ni_{81}Fe_{19}$ upon SiO_2 is strained by up to 0.17% from that of the bulk due to the shortening of bonds at the $Ni_{81}Fe_{19}/SiO_2$ interface. It is further suggested that as film thickness increases beyond the initial few nanometres the $Ni_{81}Fe_{19}$ layer relaxes, and has an out-of-plane lattice parameter that is 0.99% less than that of the bulk lattice parameter. A combination of x-ray diffraction measurements and high resolution transmission electron microscopy have shown that the microstructure of the all films is characterised by a small crystallite grain size which shows a small increase as film thickness increases and is independent of the film deposition rate. The effect of the microstructure of $Ni_{81}Fe_{19}$ thin films on the magnetic and magnetoresistance behaviour is described in chapter 6.

Chapter 6. The magnetic and magnetoresistance behaviour of $Ni_{81}Fe_{19}$ thin films

6.1 Introduction

The anisotropic magnetoresistance (AMR) behaviour in $Ni_{81}Fe_{19}$ thin films has been the focus of a large number of experimental and theoretical studies over the past forty years [119, 120, 121, and 122] and yet remains a modern and active topic of research [123, 124]. Indeed, the research and development of NiFe films and sensors based upon AMR still continues to attract much attention at present [125, 126, 127 and 128]. In such devices, the output signals are proportional to the anisotropic magnetoresistance, $\delta\rho$, whilst the AMR ratio, $\delta\rho/\rho_{ave}$, is considered a reasonable figure of merit for application purposes since the power dissipation is proportional to thin film resistivity, ρ_{ave}. Thorough knowledge of the thickness dependence of the resistivity parameters and their sensitivity to preparation techniques is thus crucial for optimising the performance of such devices.

From a fundamental viewpoint, AMR measurements provide important insight into the relationship between the magnetic behaviour and the microstructure of the thin film. It is well reported in the literature that the magnetoresistance behaviour in thin films can be strongly affected by the film composition, texture, and crystallite grain size [99]. Furthermore, in NiFe alloys, there is a strongly correlation between the number of Bohr magnetons present within the alloy and the maximum AMR ratio. This was first suggested by Snoek [129], who called attention to the maxima in AMR ratio, and highlighted that it corresponded to compositions at which there are approximately one Bohr magneton per atom in the alloy (at compositions close to $Ni_{81}Fe_{19}$). At such compositions there is also zero magnetocrystalline anisotropy [52] and zero magnetostriction [55]. From such correlations, it is suggested that AMR is the result of spin-orbit interactions [99, 100], with the sensitive relationship between magnetostriction, magnetocrystalline anisotropy, and AMR behaviour is complicated and not fully understood.

In this chapter, the magnetic and magnetoresistance behaviour of $Ni_{81}Fe_{19}$ thin films that were structurally characterised in chapter 5 is presented. The thickness dependence of the magnetic and magneto-optic behaviour of $Ni_{81}Fe_{19}$ thin films have been studied using a combination of magneto-optical Kerr effect and vibrating sample magnetometry measurements, with information regarding the presence of magnetic

anisotropy and the value of thin film coercivity provided from the shape of MOKE hysteresis loops. The effect of film thickness on electrical resistivity and anisotropic magnetoresistance behaviour was investigated, and the corresponding values of the anisotropic magnetoresistance have been deduced. The chapter concludes with a discussion that brings together key structural, magnetic and magnetoresistance behaviour deduced from chapter 5 and 6 in which the values measured here are compared to both bulk values and thin film values provided in the literature.

6.2 Study of the magnetisation behaviour, anisotropy and coercivity of $Ni_{81}Fe_{19}$ thin films

Longitudinal magneto-optical Kerr effect magnetometry measurements were obtained from $Ni_{81}Fe_{19}$ thin film samples using a laser of wavelength 658 nm that was focussed to a 5 μm spot, as described in section 4.4.5. All samples were approximately 10 mm^2.

6.2.1 Thickness dependence of the magnetisation and magneto-optical behaviour of $Ni_{81}Fe_{19}$ thin films

Figure 6:1 presents the normalised average measured MOKE signal as a function of film thickness, in which all values have been normalised to the intensity measured from the thickest film sample to allow for comparison between all films. As the MOKE laser spot was focussed to 5 μm, MOKE hysteresis loops were measured at a minimum of five random locations for each thin film sample so that any variation in the magneto-optic response of across the film due to the presence of defects and/or local variations in values of out-of-plane roughness could be observed. It was found, however, that such variations were small and in general, variations in MOKE signal of less than 5% were typically observed. It is important to note that although MOKE signals do not directly represent the magnetisation and instead are proportional to the amount of magnetised material present.

It can be seen that the normalised MOKE magnetisation increases linearly for $t \leq 15$ nm, above which the data asymptotically approaches the maximum. The behaviour observed here is consistent with results reported by Qiu and Bader [84] and by Moog *et al.* [130, 131]. The initial linear increase is expected as the Kerr effect is directly proportional to the increasing amount of magnetic material.

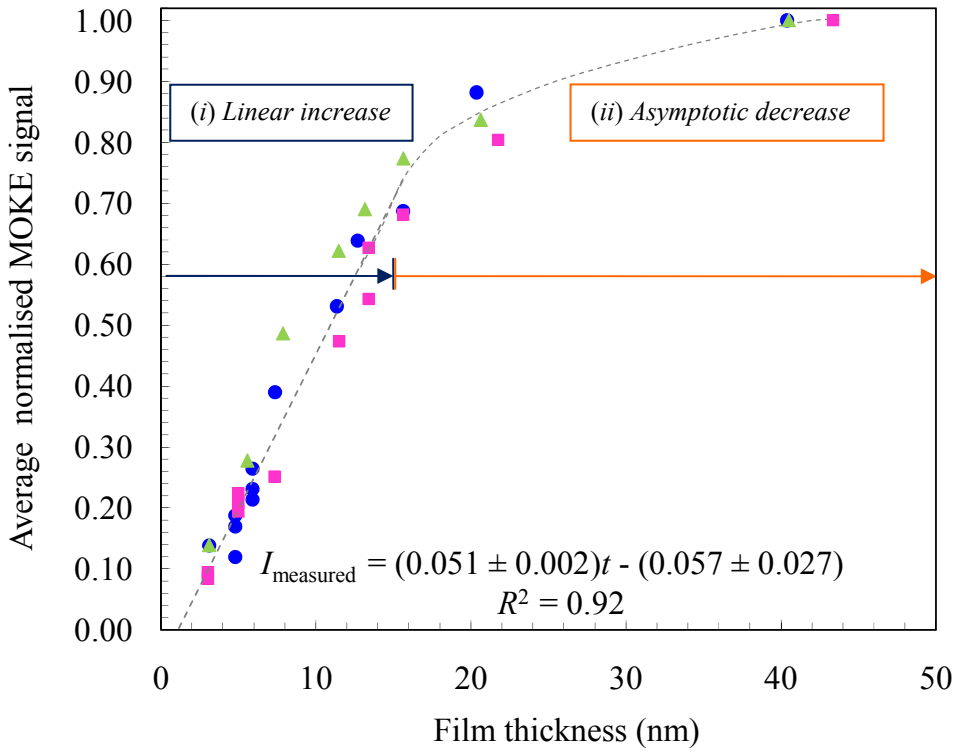

Figure 6:1. Normalised average measured MOKE signal measured as a function of film thickness for films deposited at a rate of 0.5 Å/s (●), 1.0 Å/s (▲) and 2.0 Å/s (■), respectively. All MOKE signals were measured at an applied field of ± 40 Oe. Error bars are not visible since they are smaller than data points. There are two distinct regions; (*i*) linear increase in normalised MOKE signal and (*ii*) an asymptotic approach toward the maximum. The line of best fit is to all films with a nominal thickness 15 nm or less; above 15 nm the line is a guide to the eye only.

As the film thickness increases beyond 15 nm, the signal begins to saturate due to the absorption of light which limits the sensitivity to any further increase in the amount of magnetic material. In section 4.4.4, the penetration depth for 658 nm light incident on $Ni_{81}Fe_{19}$ was deduced to be 14 nm; above which the signal intensity is expected to show a 1/e decrease due to absorption affects. There is a good agreement between the thickness dependence of the linear regime measured here and the expected value of the penetration depth. In addition, it can be seen that there is a strong dependence of the normalised MOKE signal upon film thickness, with no systematic dependence of the normalised signal upon the deposition rate.

As the magneto-optic response is determined by the dielectric response of the film, it is recognised that variations in film composition, out-of-plane roughness and surface oxide layer thickness could potentially affect the dielectric responses of different films of the same nominal dimensions and thus make cross-comparison between MOKE signals

from different samples difficult. However, it can be seen that the differences between samples measured here is minimal as the magneto-optical response of all thin film samples display largely consistent behaviour.

A linear line of best fit to the normalised MOKE signal for $t < 15$ nm can be used to identify the presence and magnitude of a magnetic dead layer. A magnetic dead layer is characterised by a loss of magnetic moment, and if present, tends to occur at the substrate interface. As previously described in section 2.4.4, ferromagnetism is sensitive to interatomic spacing; hence any significant change in bond lengths at the substrate interface due to stress can give rise to a magnetically dead layer [132, 133]. If there were no losses of magnetic moment at the interface, the linear dependence of the normalised MOKE signal should go through the origin. The line of best fit presented to the data in Figure 6:1 suggests that the presence of a magnetically dead layer (0.89 ± 0.42) nm thick.

Further investigation into the presence of a magnetic dead layer was performed using vibrating sample magnetometry (VSM). In this technique, a sample is within a uniform magnetic field which induces a magnetic dipole moment. The magnetic moment is measured by oscillating the sample near a detection coil and synchronously detecting the induced voltage. A relatively large oscillation amplitude (typically between 1-3 mm peak) is used, and the sample is oscillated at a frequency of 40 Hz. As the frequency of the electrical signal has the same frequency of vibration, the amplitude of the signal is proportional to the magnetic moment. As VSM measurements provide direct measurements of the magnetic moment from the entire sample, rather than from localised regions, such measurements have been used to complement MOKE magnetometry measurements.

VSM measurements were made in the Rutherford Appleton Laboratory using a Quantum Design PPMS-9 system, and were performed by A. Ridler [134]. All measurements were taken at saturation in an applied field of 1 T in the longitudinal configuration, i.e. the magnetic field, VSM vibration and magnetic moment were all directed along the vertical axis. Figure 6:2 presents the variation of magnetic moment per cross-sectional area measured from a selection of $Ni_{81}Fe_{19}$ thin films deposited on 5 mm^2 pre-oxidised silicon substrates at a stable deposition rate of 0.5 Å/s. In addition, expected values of magnetic moment are also shown, which have been deduced using a bulk value of $M_s = 860$ emu/cm^3 [53].

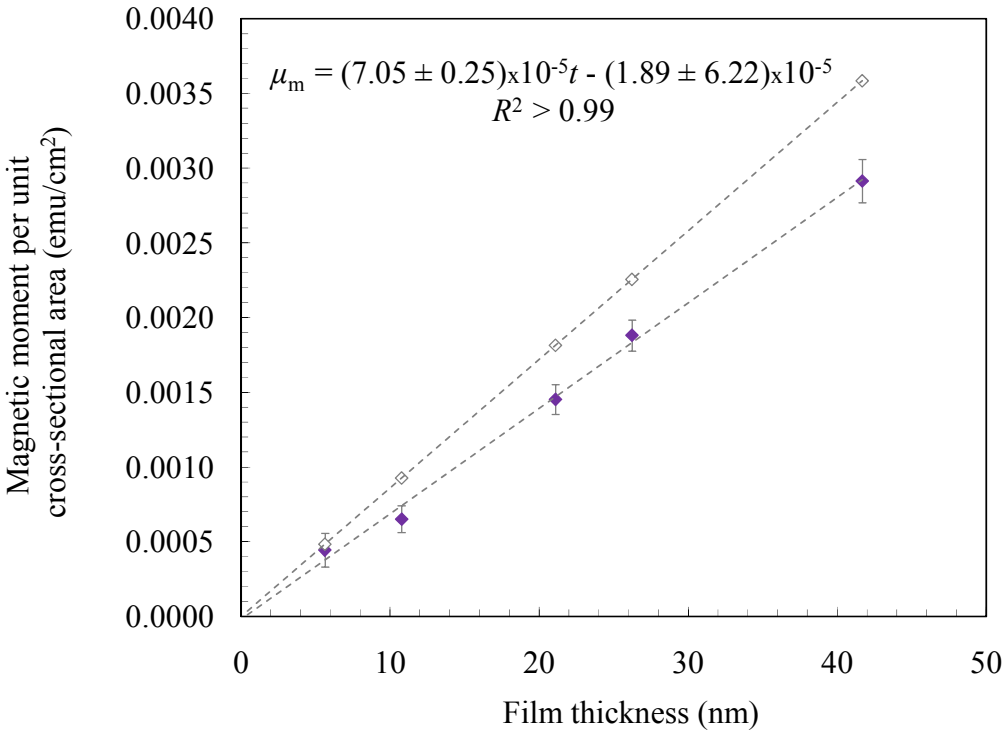

Figure 6:2. Variation of magnetic moment per cross-sectional area with film thickness for a selection of $Ni_{81}Fe_{19}$ thin films deposited at a rate of 0.5 Å/s measured using vibrating sample magnetometry (♦). Measurements were performed by A. Ridler in Rutherford Appleton Laboratory [134]. Expected values of magnetic moment are also shown (◊) which have been deduced using a bulk value of M_s = 860 emu/cm^3 [53].

A linear increase in observed magnetic moment with film thickness is observed, which is as expected since VSM provides a direct measurement of the magnetic response of the entire film. The observed magnetic moment values are lower than the expected values with the differences attributed to a reduction in M_s to approximately 710 emu/cm^3. As precise information on the film thickness was not provided by A. Ridler in [134], it is not possible to know whether the film thickness this corresponds to the total film thickness or that of the $Ni_{81}Fe_{19}$ layer only. Indeed, if it is assumed that the film thickness corresponds to the total thickness, then the $Ni_{81}Fe_{19}$ film thickness can be estimated using values reported in Tables 5:1 to 5:3. Values of the expected magnetic moment of each thin film deduced using the bulk value of M_s and the reduced film thicknesses are much closer to what was observed experimentally. It is therefore suggested that the reduction in magnetic moment in the thin films is largely due to the presence of the surface oxide layer.

If there were no losses of magnetic moment at the interface, the linear dependence of the normalised MOKE signal should go through the origin. The line of best fit

presented to the data in Figure 6:2 suggests that the presence of a magnetically dead layer of (0.27 ± 0.89) nm. As a zero intercept is within the error on this value, it is suggested that the $Ni_{81}Fe_{19}$ films investigated here do not contain a magnetic dead layer.

Structural measurements presented in chapter 5 suggested that all films were continuous in the direction normal to the sample, with a $SiO_2/Ni_{81}Fe_{19}$ interface approximately 0.5 nm wide. Indeed, this interface width is thought to be a combination of both topological roughness and chemical intermixing and, since the values of the magnetic dead layer are within the interface width, it is suggested that the non-zero intercept measured by MOKE could be related to the nature of the interface. X-ray diffraction measurements suggested that the initial few nanometres of $Ni_{81}Fe_{19}$ have an out-of-plane lattice parameter that is 0.17% larger to than that of the bulk. It is suggested that it is not large enough to affect the lattice spacing conditions required for ferromagnetism. Indeed, calculations of the value of r_a/r_{3d} show that the initial layers are located slightly to the right of $Ni_{81}Fe_{19}$ on the Bethe-Slater curve presented in Figure 2:9. However, as the MOKE response of a film depends upon the dielectric properties of the film and is not a direct measurement of the sample magnetisation, whereas VSM directly measures the magnetic moment of the film, it is suggested that all film thicknesses under investigation here are fully ferromagnetic at the substrate interface and there is no magnetic dead layer.

6.2.2 Dependence of magneto-optical Kerr effect magnetometry loops shape and coercivity on $Ni_{81}Fe_{19}$ film thickness

The shape of the MOKE hysteresis curve may be affected by the presence of magnetic anisotropy, which can include contributions from magnetocrystalline anisotropy as well as shape and stress anisotropy. Whilst the former is intrinsic to the material, and is expected to be close to zero for $Ni_{81}Fe_{19}$, both shape and stress anisotropy may be affected by the sample geometry, the substrate conditions and the deposition parameters [7]. MOKE hysteresis loops were measured at several random locations for each chip and were also made at successive rotations of 90° about the original starting position so as to investigate anisotropy effects within the film. Figure 6:3 presents example hysteresis loops taken at 0° and 90° taken from a selection of film thicknesses. In general, although a small range of MOKE hysteresis behaviour is observed, there is no systematic dependence upon either the film thickness or deposition rate.

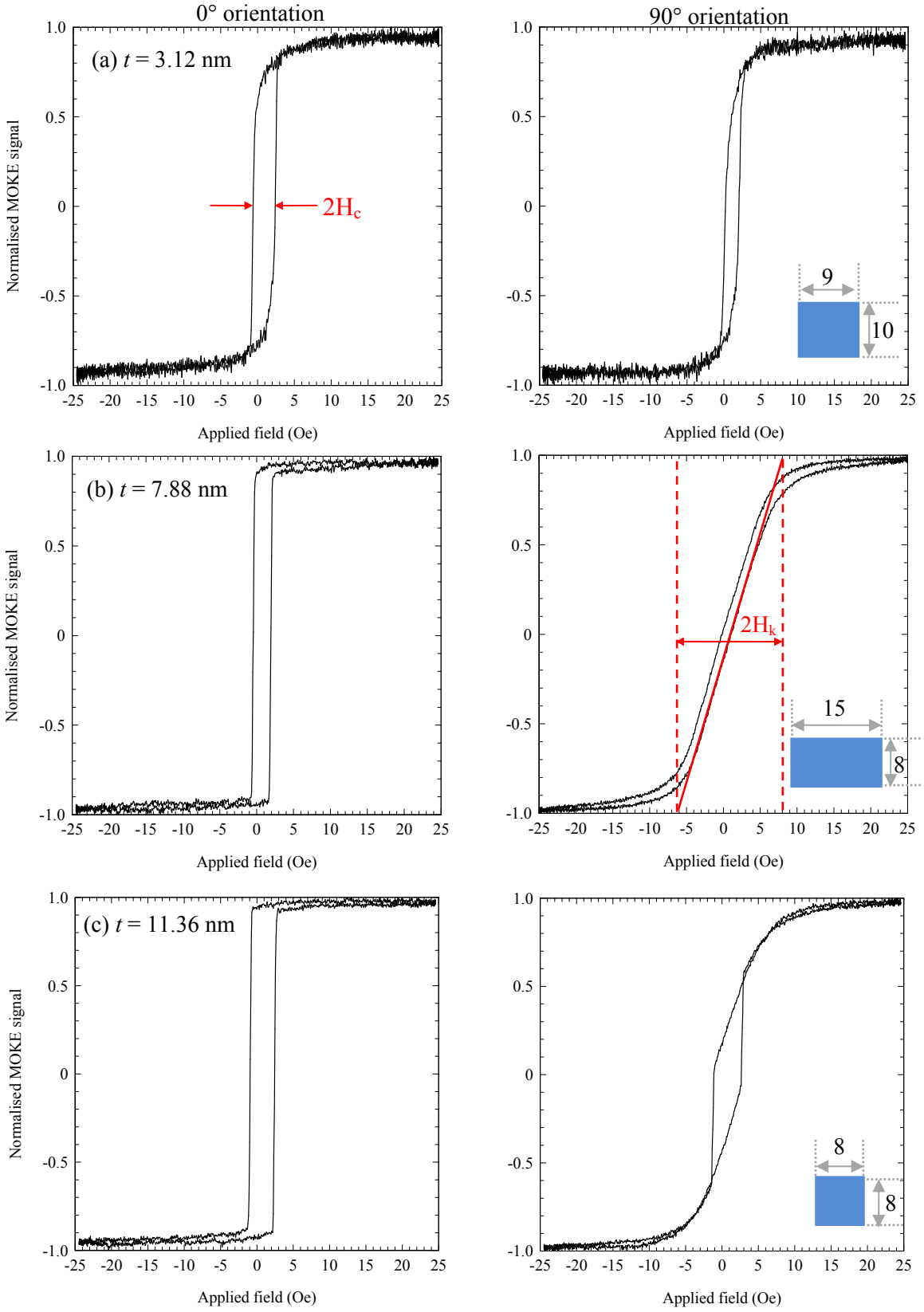

Figure 6:3. Normalised MOKE hysteresis loops showing typical behaviour for the samples at 0° (*left*) and 90° (*right*), for $Ni_{81}Fe_{19}$ thin films of thickness (a) 3.12 nm deposited at a rate of 0.5 Å/s (b) 7.88 nm deposited at a rate of 1.0 Å/s and (c) 11.36 nm deposited at a rate of 0.5 Å/s. The inset shows a scale schematic of the sample, where all lengths are given in mm.

It can be seen that some loops display definite 'easy' and 'hard' axes magnetisation behaviour (as shown in Figure 6:3 (b)), which are indicative of the presence of uniaxial magnetic anisotropy. Such behaviour, however, is limited to only 6 samples. The vast majority of samples display behaviour similar to that shown in Figure 6:3 (a), which are representative of an isotropic distribution of anisotropy within the films. As $Ni_{81}Fe_{19}$ is an extremely soft material, it is suggested that the differences in loop shape may be the result of stress related effects due to the presence of strain at the substrate interface. However, since uniaxial behaviour was only observed in 6 samples, it is suggested that such behaviour is more likely to be due to small changes in sample shape could result in a small amount of shape anisotropy.

Whilst all chips were intended to be square in shape, and approximately 10 mm^2, some chips were more rectangular than others and had dimensions closer to 8 mm x 15 mm. As small differences in the shape would change the demagnetising factor, it is suggested that such changes are predominantly responsible for the changes in loop shape observed here. Indeed, when the more rectangular samples were deliberately broken to form a square, a change in loop shape from Figure 6:3 (b) to Figure 6:3 (c) was observed. The average measured value of the uniaxial anisotropy, H_k, is 7 Oe and so the magnetic anisotropy present within the films studied here is small.

Figure 6:4 presents the average value of coercivity, H_c, as a function of film thickness for films with an isotropic distribution of anisotropy. The majority of samples have an average coercivity between 2 - 3 Oe. Although there is no strong correlation between H_c and film thickness the coercivity shows the most variation for $t < 10$ nm. In this regime, the film coercivity shows a slight decrease as film thickness decreases. Indeed, whilst the two 3 nm films deposited at a rate of 2.0 Å/s are extremely soft - more so than the 3 nm films deposited at the lower rates of 0.5 Å/s and 1.0 Å/s - and in general, there is also no strong correlation between the average coercivity and the deposition rate. The values of H_c presented here vary differently from results published by Akhter *et al.* [135], who observe a relatively large increase in average coercivity for $t < 5$ nm. Furthermore, the authors conclude that the samples are not continuous for $t < 5$ nm, which leads to a large increase in non-magnetic 'holes' which causes a corresponding increase in coercivity. The absence of such an increase in the data presented here further suggests that all $Ni_{81}Fe_{19}$ films are continuous in the plane of the applied field. This is in good agreement with x-ray reflectivity measurements provided in section 5.2.

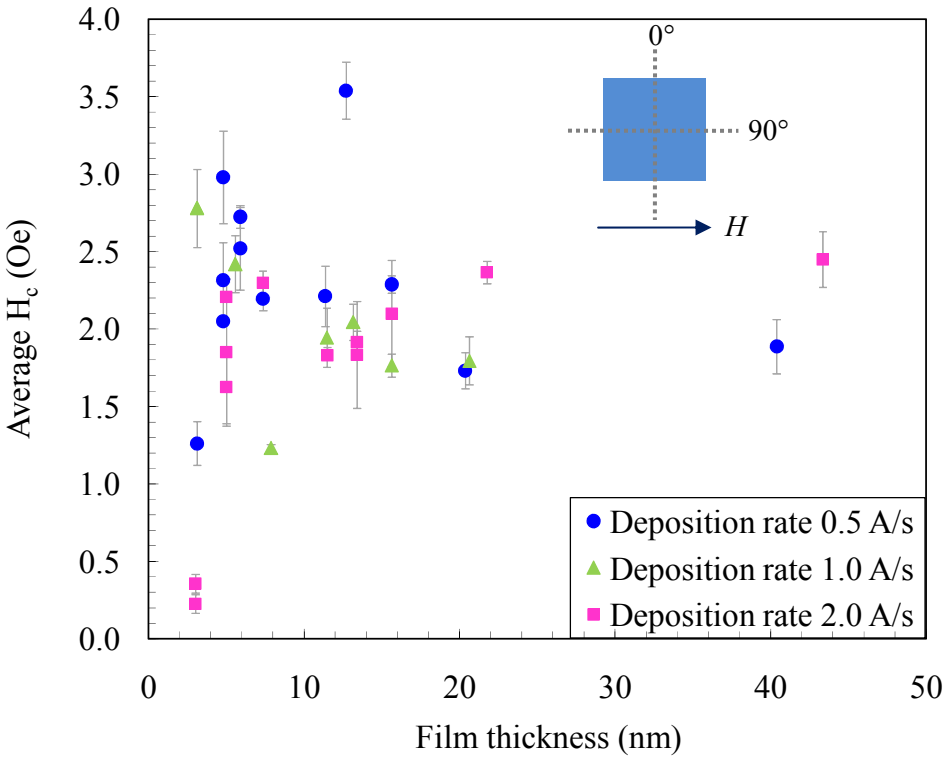

Figure 6:4. Average values of coercivity as a function of $Ni_{81}Fe_{19}$ thin films as measured from MOKE magnetometry loops at random locations on the chip surface. The inset shows shape of the typical chip geometry.

6.3 Study of the resistance and magnetoresistance behaviour of $Ni_{81}Fe_9$ thin films

Anisotropic magnetoresistance measurements were made on $Ni_{81}Fe_{19}$ thin film samples shaped into elongated strips (of approximate dimensions 27 mm x 3 mm) using a four-point probe technique described in section 4.4.5.

6.3.1 Dependence of resistance and resistivity behaviour on $Ni_{81}Fe_{19}$ film thickness

Figure 6:5 presents example magnetoresistance behaviour measured for an applied current parallel ($R_{\parallel}$) and perpendicular ($R_{\perp}$) to an applied magnetic field for (a) a 5.58 nm thin film deposited at 1.0 Å/s and (b) a 43.36 nm thin film deposited at 2.0 Å/s.

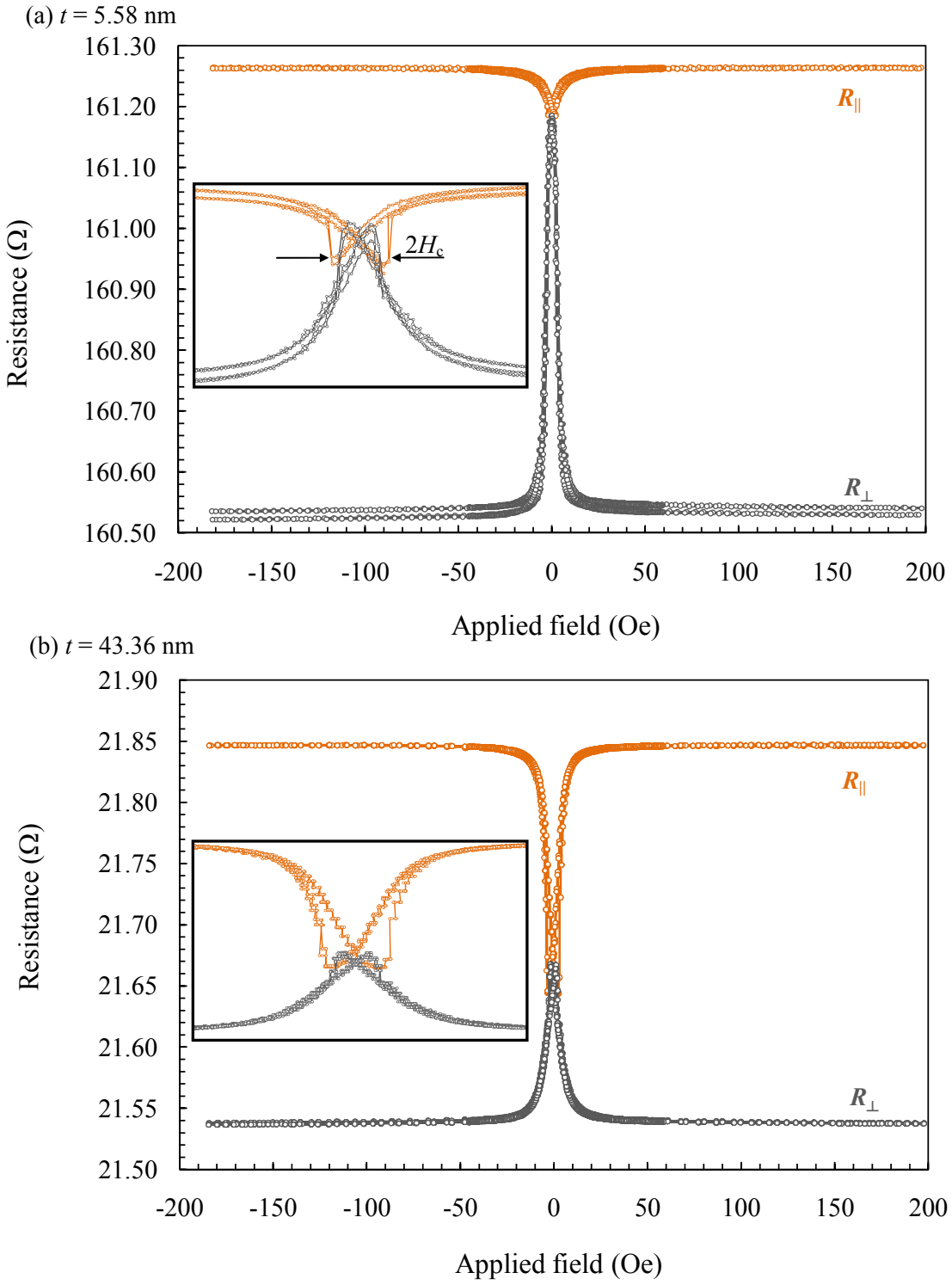

Figure 6:5. Example magnetoresistance data for $Ni_{81}Fe_{19}$ thin films of thickness (a) 5.58 nm deposited at a rate of 1.0 Å/s and (b) 43.36 nm deposited at a rate of 2.0 Å/s. The inset shows an enlarged image of the behaviour between -20 Oe and +20 Oe. Mean values of $R_{\|}$ and $R_{\perp}$ are deduced from average values of the resistance between +50 to +200 Oe and -50 to -200 Oe, respectively. The differences in the values of $R_{\perp}$ at high fields in (a) are the result of Joule heating within the sample and are not hysteretic effects. The discretisation of steps in R vs. H that can be seen in the inset is due to the finite sampling of the current as the applied field was ramped at a constant rate.

The shape and relative intensity of both $R_{\parallel}$ and $R_{\perp}$ are consistent with the majority of magnetic moments orientated along the axial length of the sample, which is due to the large aspect ratio of the chip. The sharp change in electrical resistance observed in parallel sweeps at applied fields close to zero is a signature of a sharp magnetisation reversal process and provides information on the coercivity of the sample. Conversely, when the applied field is perpendicular to the current, the change in resistance at close to zero applied field is less sharp and typically more rounded, which suggests that reversal of the spin magnetic moments occurs gradually and may be expected as the magnetisation is being driven along a hard axis.

In general, the change in $R_{\perp}$ between zero applied field and at saturation increases as film thickness decreases, which is suggested to be a consequence of the spin confinement caused by the decreasing film thickness. As film thickness decreases, the spin magnetic moments are confined to lie within the plane of the film. This means that during magnetisation reversal the moments are forced to point across the width of the strip, as opposed to out of the plane which can occur for thicker film samples. Average values of H_c measured from magnetoresistance data measured with electric current and applied field parallel are presented in Figure 6:6.

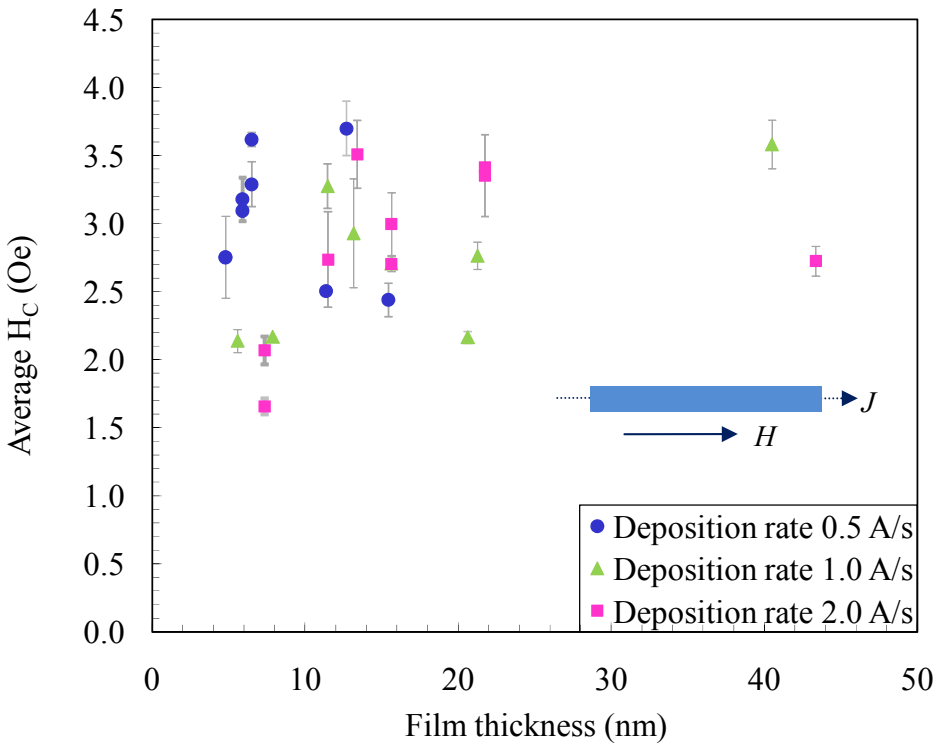

Figure 6:6. Average measured thin film coercivity as measured from magnetoresistance measurements for an electric current and applied field aligned parallel as shown in the inset.

There is good agreement between the data measured here and that measured from MOKE hysteresis loops presented in Figure 6:4. Indeed, as expected, all films are very soft with average values of coercivity between 2 and 3 Oe. It is suggested that the small variation in coercivity for specific film thickness is likely to be the result of small variations in sample shape, although there is little variation in H_c for film thicknesses below 10 nm as was observed for the coercivity behaviour measured by MOKE. There is no systematic dependence of H_c on either the deposition rate which shows a good agreement between MOKE and MR data.

Figure 6:7 presents the average thin film resistance as a function of $Ni_{81}Fe_{19}$ thickness measured for all deposition rates. The average thin film resistance, R_{ave}, was defined using:

$$R_{ave} = \tfrac{1}{3}\left(R_{\parallel} + 2R_{\perp}\right) \qquad (6:1)$$

Where $R_{\parallel}$ and $R_{\perp}$ correspond to the values of saturation resistance parallel and perpendicular to the applied field.

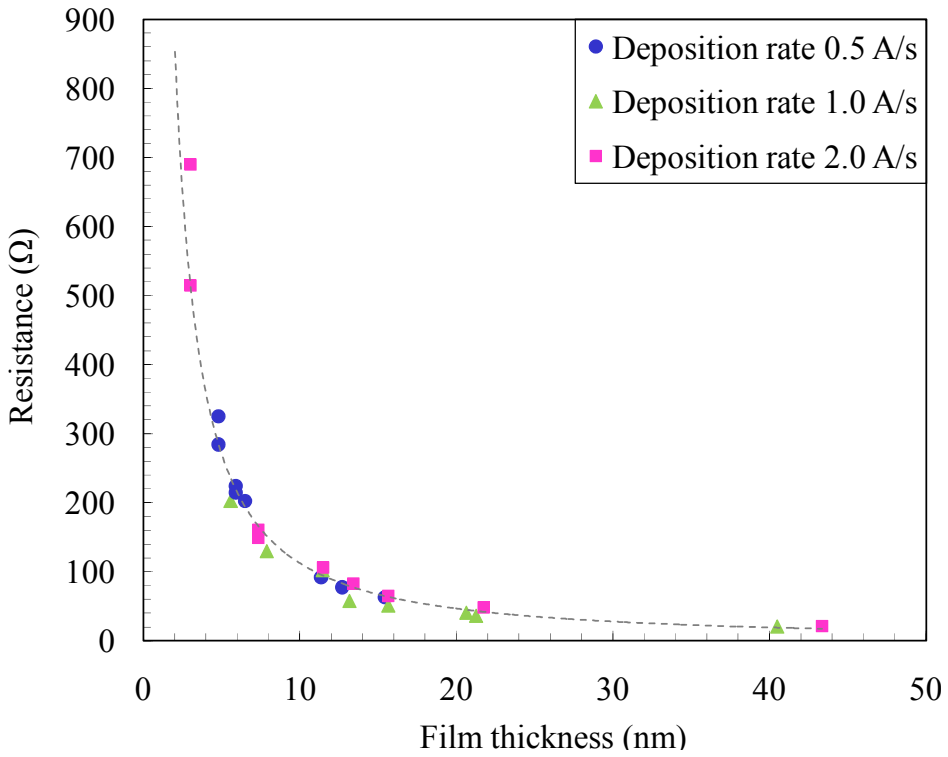

Figure 6:7. Average measured $Ni_{81}Fe_{19}$ resistance as a function of film thickness, deduced using $R_{ave} = \tfrac{1}{3}\left(R_{\parallel} + 2R_{\perp}\right)$. Typical errors on the measured resistance values are of the order of 1 x 10^{-4} %, and thus error bars are not visible since they are smaller than data points. The line is a guide to the eye only.

These values were deduced from average values of the resistance at saturation (from between +50 to +200 Oe and likewise for the negative fields). It was necessary to define R_{ave} by this relation since the zero field resistance depends upon the exact domain configuration which in turn depends upon the history of the sample and on the exact temperature [97].

There is a strong thickness dependence of resistance. It is clear that the average resistance increases as film thickness decreases. This is quite a shallow increases for $t >$ 10 nm, and becomes much sharper for $t < 10$ nm. The strong correlation between film resistance and film thickness is due to the effect of geometrical confinement of the sample in the direction of the surface which limits the mean free path of the conduction electrons. Values of the thin film resistivity were deduced using the relation:

$$\rho_{ave} = \frac{R_{ave} \cdot L}{A} \tag{6:2}$$

Where L is the separation of the voltage measuring probes (7.05 ± 0.05) mm and A is the cross-sectional area of the strip (i.e. the film thickness multiplied by the strip width). Figure 6:8 presents the average resistivity as a function of thin film thickness; values of resistivity are presented in units of μΩcm in order to give more sensible numbers and in order to allow ease of comparison with data presented in the literature. The values of average resistivity presented in Figure 6:8 exhibit a similar trend to that observed for the average resistance data presented in Figure 6:7, in that as film thickness decreases the resistivity increases. This increase is fairly shallow for all film thicknesses, although this increase becomes slightly sharper for $t < 10$ nm.

It is well known that resistivity increases as thin film thickness decreases. This phenomenon is known as the size effect. A magnetic film is defined as thin if the thickness t is less than the mean free path of the conduction electron in the bulk material, l_0. As such, the resistivity noticeably increases when the mean free path of the conduction electrons is comparable to the film thickness. In order for this to occur electrons must be diffusely scattered at the surface. Fuchs and Sondheimer [136, 139] deduced expressions for the thin film resistivity within the condition of diffuse scattering of conduction electrons at the boundaries of the film. For very thin films, where $t < l_0$, the resistivity is described by:

$$\rho_{ave} = \frac{4 l_0 \rho_0}{3} \cdot \frac{1}{\left[\ln(l_0/t) + 0.423\right]} \tag{6:3}$$

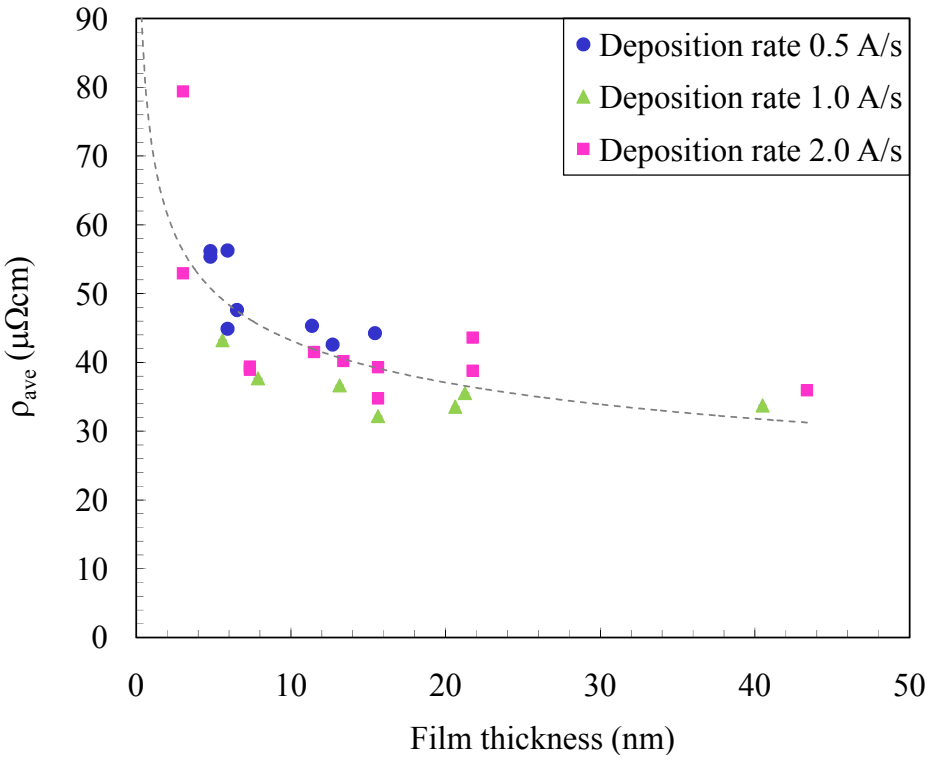

Figure 6:8. Average $Ni_{81}Fe_{19}$ thin film resistivity as a function of film thickness, deduced using measured values of R_{ave} presented in Figure 6:7. The standard errors on the deduced resistivity values are of the order of 0.1%, and thus error bars are not visible since they are smaller than data points. The line is a guide to the eye only.

For thicker films, $l_0 < t$, the corresponding resistivity is given by:

$$\rho_{ave} = \rho_0 \left[1 + \tfrac{3}{8}(l_0/t)\right] \qquad (6:4)$$

Where ρ_{ave} is the measured value and ρ_0 is the bulk resistivity. Kaya reports that that bulk $Ni_{80}Fe_{20}$ has a resistivity of 14 μΩcm [140].

Figure 6:9 presents $\rho_{ave}\, t$ as a function of $Ni_{81}Fe_{19}$ film thickness. There is a very strong linear dependence of $\rho_{ave}\, t$ upon t; manipulation of (6:4) shows that a best fit line can yield both the projected bulk resistivity, ρ_0, and the mean free path, l_0. Such an analysis gives values of the bulk resistivity for $Ni_{81}Fe_{19}$ films of (33.02 ± 1.05) μΩcm and a corresponding mean free path of (7.10 ± 0.53) nm. Whilst the bulk value of resistivity is significantly larger than that given by Kaya in [140] for bulk $Ni_{80}Fe_{20}$, this may be explained in part by the relatively small mean free path of the electrons which is believed to be limited by the presence of very small crystallites, which present an additional obstacle from which the electrons are scattered [141].

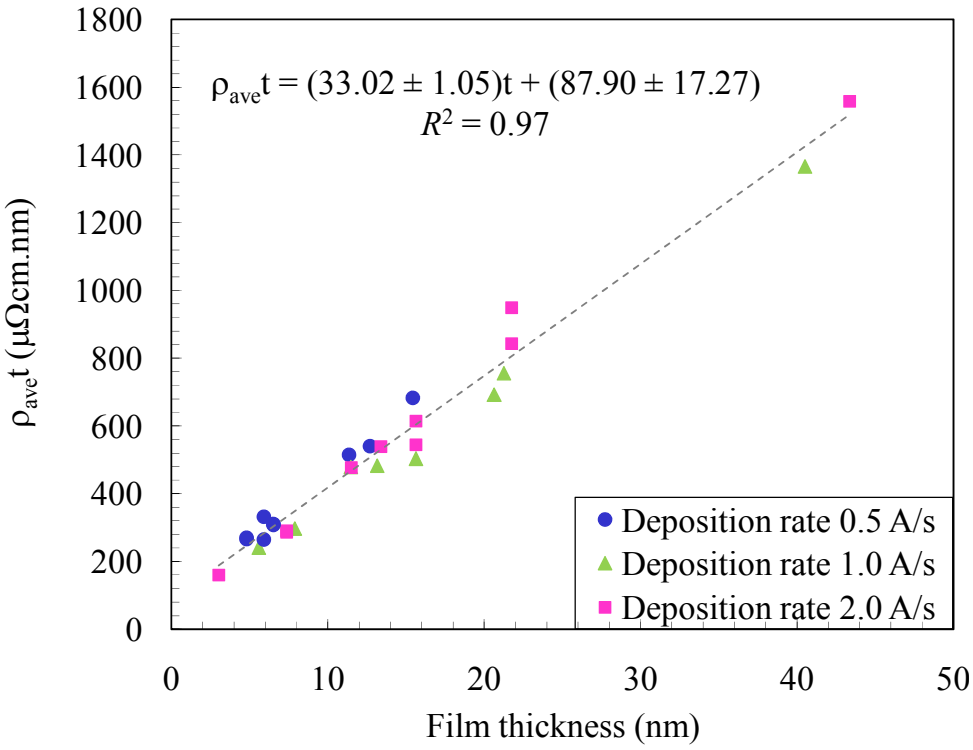

Figure 6:9. Dependence of $\rho_{ave}t$ as a function of $Ni_{81}Fe_{19}$ film thickness. The line of best fit is to all the data, and can be used to give values of the bulk resistivity and mean free path by the Fuchs-Sondheimer expression for thin film resistivity given in equation (6:4).

Indeed, the average grain size deduced here is in good agreement with that given by the Scherrer analysis to x-ray diffraction peaks presented in section 5.3.3 and also by high resolution transmission electron microscopy presented in section 5.4.

6.3.2 Dependence of anisotropic magnetoresistance on $Ni_{81}Fe_{19}$ film thickness

Anisotropic magnetoresistance is defined as difference between the resistivity for current and magnetisation parallel ($\rho_{\parallel}$) and current and magnetisation orientated perpendicular ($\rho_{\perp}$) and is given by:

$$\delta\rho = \rho_{\parallel} - \rho_{\perp} \tag{6:5}$$

Anisotropic magnetoresistance data for $Ni_{81}Fe_{19}$ films measured in this study are presented in Figure 6:10. In this figure it can be seen that $\delta\rho$ exhibits a strong dependence on film thickness. For $t > 20$ nm, this dependence is only slight; however as film thickness decreases, $\delta\rho$ decreases rapidly and tends toward zero for $t < 7$ nm.

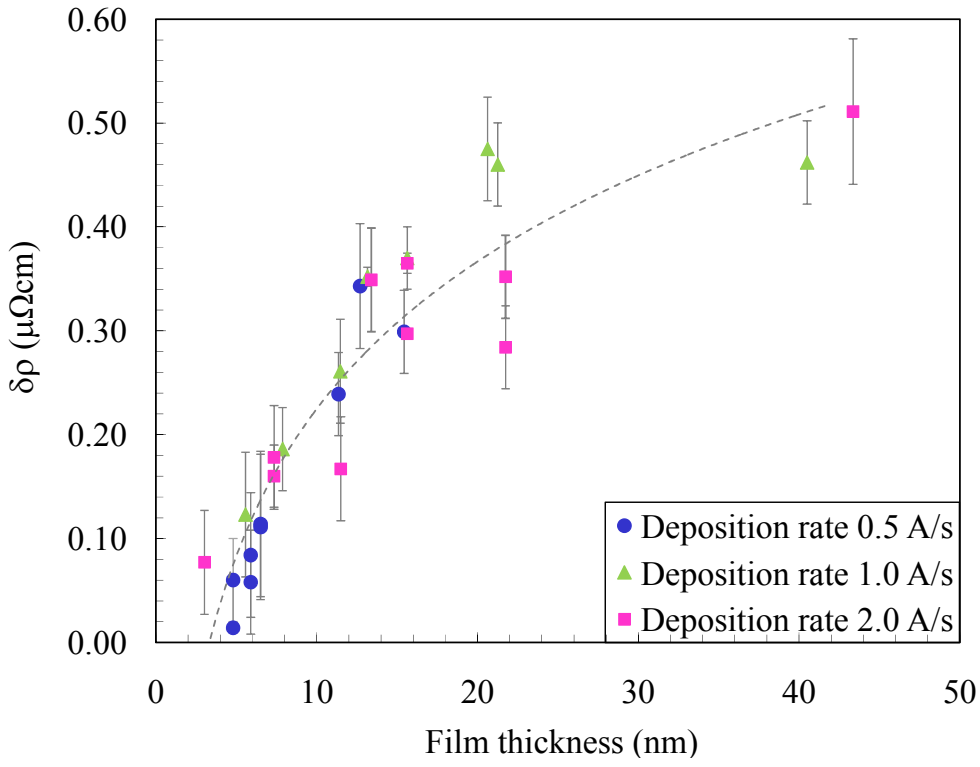

Figure 6:10. Anisotropic magnetoresistance as a function of film thickness for $Ni_{81}Fe_{19}$ thin films. The line is a guide to the eye only.

In McGuire [99] it is stressed that for permalloy $\delta\rho$ should be independent of film thickness, which is clearly not the case for the films investigated here. If a loss of anisotropic magnetoresistance occurred only in the thinnest films then it might be interpreted as a consequence of a magnetic dead layer, however, there is a very strong trend toward zero presented here occurs for $t \leq 10$ nm, which suggests that something more fundamental is occurring. Indeed, at 10 nm there is no doubt that the films are ferromagnetic. Comparison of literature values of $\delta\rho$ is discussed in further detail in section 6.4.

The anisotropic magnetoresistance ratio is defined as:

$$\frac{\delta\rho}{\rho_{\text{ave}}} = \frac{\rho_{\parallel} - \rho_{\perp}}{\frac{1}{3}\left(\rho_{\parallel} + 2\rho_{\perp}\right)} \tag{6:6}$$

Figure 6:11 presents values of the percentage anisotropic magnetoresistance ratio as a function of film thickness. The AMR ratio is strongly thickness dependent and shows a sharp decrease as film thickness decreases.

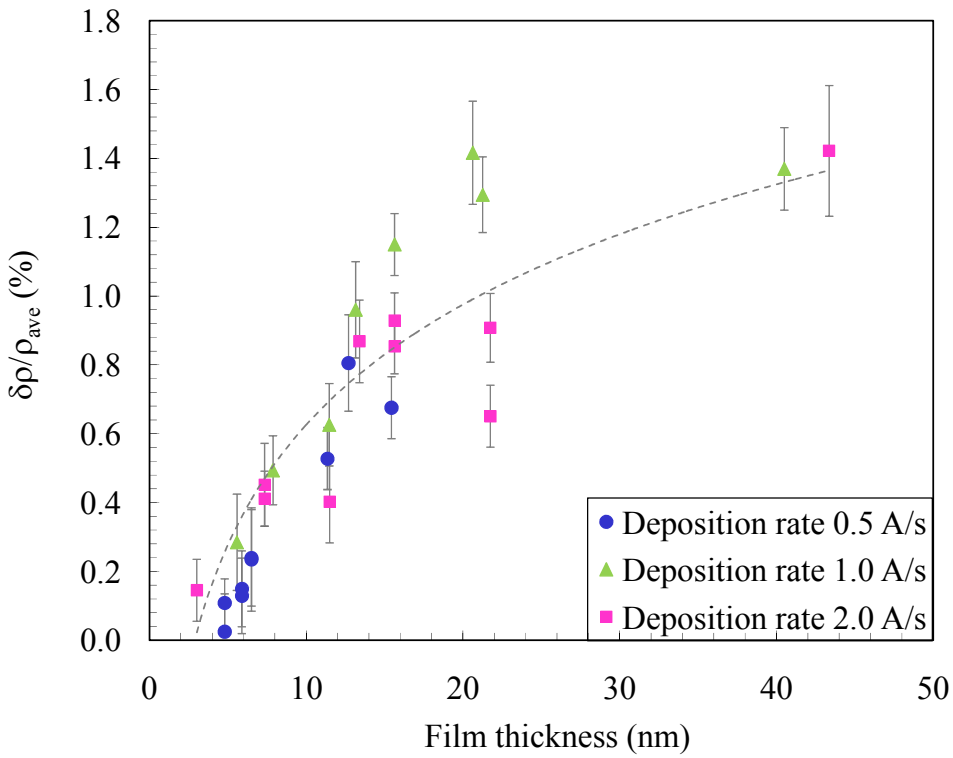

Figure 6:11. Percentage anisotropic magnetoresistance ratio, $\delta\rho/\rho_{ave}$, for $Ni_{81}Fe_{19}$ thin films deposited on pre-oxidised silicon substrates as a function of film thickness. The line is a guide to the eye only.

In bulk $Ni_{81}Fe_{19}$, the AMR ratio is expected to be close to 4% [53], although in thin films it is expected to be smaller and is measured to be closer to 3% [119]. This decrease is largely attributed to the strong thickness dependence of resistivity. The data presented in Figure 6:11 is very similar to that presented in Figure 6:10 as the AMR ratio tends to zero for $t < 7$ nm. It is suggested that AMR ratio is largely determined by the strong dependence of $\delta\rho$, and is not just a consequence of the increase in resistivity as film thickness decreases. In [99], McGuire emphasises that values of $\delta\rho/\rho_{ave}$ depends only on ρ_{ave}, although this is clearly not the case here.

Other authors have seen a similar decrease in the anisotropic magnetoresistance ratio in thin $Ni_{80}Fe_{20}$ films; Krzyk *et al.* [124] report on the anisotropic magnetoresistance of ultrathin permalloy films deposited on pre-oxidised silicon substrates and probed *in situ*. The authors suggest that the films are continuous for film thicknesses greater than approximately 2 nm, and for 3 nm films the AMR ratio is reported as 0.04%, whilst for 4 nm films the AMR ratio is reported as 0.065%, which are similar to those measured in this study. Values of AMR presented in the literature are discussed in more detail in section 6.4.

6.3.3 Summary of resistivity and anisotropic magnetoresistance data for $Ni_{81}Fe_{19}$ thin films

Thin film resistivity for parallel and perpendicular ($\rho_{\|}$, $\rho_{\perp}$) orientation of current and magnetisation were each deduced using $\rho = R \cdot L/A$, where L corresponds to the separation of the voltage probes and A is the cross-sectional area of the thin film **(**equation (6:1)). Measurement of the parallel and perpendicular resistitive allowed for the average thin film resistivity, $\rho_{ave,}$ to be deduced using equation (6:2). Anisotropic magnetoresistance data were deduced using equations (6:5) and (6:6).

Thin film resistivity and anisotropic magnetoresistance data for all $Ni_{81}Fe_{19}$ thin films studied within this investigated are summarised in Table 6:1, Table 6:2 and Table 6:3, respectively.

Film thickness (nm)	$\rho_{\|}$ **(μΩcm)**	$\rho_{\perp}$ **(μΩcm)**	ρ_{ave} **(μΩcm)**	$\delta\rho$ **(μΩcm)**	$\frac{\delta\rho}{\rho_{ave}}$ **(%)**
4.80 ± 0.01	56.16 ± 0.04	56.18 ± 0.04	56.17 ± 0.05	0.01 ± 0.05	0.02 ± 0.11
4.80 ± 0.01	55.40 ± 0.03	55.34 ± 0.03	55.36 ± 0.04	0.06 ± 0.04	0.11 ± 0.07
5.90 ± 0.03	44.92 ± 0.04	44.86 ± 0.04	44.89 ± 0.05	0.06 ± 0.05	0.13 ± 0.11
5.90 ± 0.03	56.33 ± 0.04	56.25 ± 0.04	56.28 ± 0.06	0.08 ± 0.06	0.15 ± 0.11
6.51 ± 0.01	47.42 ± 0.05	47.31 ± 0.05	47.34 ± 0.07	0.11 ± 0.07	0.24 ± 0.14
6.51 ± 0.01	47.70 ± 0.05	47.59 ± 0.05	47.63 ± 0.07	0.11 ± 0.07	0.24 ± 0.15
11.36 ± 0.34	45.48 ± 0.03	45.24 ± 0.03	45.32 ± 0.04	0.24 ± 0.04	0.52 ± 0.09
12.70 ± 2.46	42.81 ± 0.04	42.47 ± 0.04	42.58 ± 0.06	0.34 ± 0.06	0.81 ± 0.14
15.43 ± 0.05	44.45 ± 0.03	44.15 ± 0.03	44.25 ± 0.04	0.30 ± 0.04	0.68 ± 0.09

Table 6:1. Thin film resistivity, anisotropic magnetoresistance and anisotropic magnetoresistance ratio data for thin films deposited at a rate of 0.5 Å/s.

Film thickness (nm)	$\rho_{\parallel}$ **(μΩcm)**	$\rho_{\perp}$ **(μΩcm)**	ρ_{ave} **(μΩcm)**	$\delta\rho$ **(μΩcm)**	$\frac{\delta\rho}{\rho_{ave}}$ **(%)**
5.58 ± 0.08	43.29 ± 0.04	43.17 ± 0.04	43.21 ± 0.06	0.12 ± 0.06	0.28 ± 0.14
7.88 ± 0.05	37.80 ± 0.03	37.62 ± 0.03	37.68 ± 0.04	0.19 ± 0.04	0.49 ± 0.10
11.47 ± 0.09	41.87 ± 0.03	41.61 ± 0.03	41.69 ± 0.05	0.26 ± 0.05	0.63 ± 0.12
13.16 ± 0.11	36.89 ± 0.03	36.54 ± 0.03	36.66 ± 0.05	0.35 ± 0.05	0.96 ± 0.14
15.64 ± 0.11	32.42 ± 0.02	32.05 ± 0.02	32.18 ± 0.03	0.37 ± 0.03	1.15 ± 0.09
20.63 ± 0.34	33.86 ± 0.03	33.38 ± 0.03	33.54 ± 0.05	0.47 ± 0.05	1.42 ± 0.15
20.63 ± 0.34	35.85 ± 0.03	35.39 ± 0.03	35.54 ± 0.04	0.46 ± 0.04	1.29 ± 0.11
40.50 ± 0.47	34.03 ± 0.03	33.57 ± 0.03	33.70 ± 0.04	0.46 ± 0.04	1.37 ± 0.12

Table 6:2. Thin film resistivity, anisotropic magnetoresistance and anisotropic magnetoresistance ratio data for thin films deposited at 1.0 Å/s.

Film thickness (nm)	$\rho_{\parallel}$ **(μΩcm)**	$\rho_{\perp}$ **(μΩcm)**	ρ_{ave} **(μΩcm)**	$\delta\rho$ **(μΩcm)**	$\frac{\delta\rho}{\rho_{ave}}$ **(%)**
3.02 ± 0.03	53.02 ± 0.05	52.93 ± 0.05	52.95 ± 0.05	0.08 ± 0.05	0.15 ± 0.09
7.35 ± 0.08	39.02 ± 0.02	38.86 ± 0.02	38.91 ± 0.03	0.16 ± 0.03	0.41 ± 0.08
7.35 ± 0.08	39.51 ± 0.04	39.33 ± 0.04	39.39 ± 0.05	0.18 ± 0.05	0.45 ± 0.12
11.50 ± 0.04	41.61 ± 0.04	41.45 ± 0.04	41.50 ± 0.05	0.17 ± 0.05	0.40 ± 0.12
13.40 ± 0.09	40.42 ± 0.03	40.07 ± 0.03	40.19 ± 0.05	0.35 ± 0.05	0.87 ± 0.12
15.64 ± 0.16	39.54 ± 0.02	39.18 ± 0.02	39.30 ± 0.03	0.37 ± 0.03	0.93 ± 0.08
15.64 ± 0.16	34.97 ± 0.03	34.67 ± 0.03	34.77 ± 0.04	0.30 ± 0.04	0.85 ± 0.11
21.75 ± 0.11	39.02 ± 0.03	38.66 ± 0.03	38.78 ± 0.04	0.35 ± 0.04	0.91 ± 0.10
21.75 ± 0.11	43.81 ± 0.03	43.52 ± 0.03	43.62 ± 0.04	0.28 ± 0.04	0.65 ± 0.09
43.36 ± 0.08	36.28 ± 0.05	35.77 ± 0.05	35.94 ± 0.07	0.51 ± 0.07	1.42 ± 0.19

Table 6:3. Thin film resistivity, anisotropic magnetoresistance and anisotropic magnetoresistance ratio data for thin films deposited at 2.0 Å/s.

6.4 Discussion of $Ni_{81}Fe_{19}$ resistance and magnetoresistance reported in the literature

Figure 6:12 presents resistivity data as a function of film thickness for thicknesses below 50 nm for both $Ni_{82}Fe_{18}$ and $Ni_{81}Fe_{19}$ measured by several workers [119, 120, 121, 122 and 126]. Each data set shows that as film thickness decreases the resistivity increases, as is expected due to the Fuchs size effect. The resistivity data is consistent across these studies, with the exception of the Williams and Mitchell data, (b) [120] which is noticeably offset from the other data sets, particularly for $t < 30$ nm. In this case, the larger values of resistivity are attributed to the very high deposition rate (1000 Å/s), which is believed to induce a large amount of strain within the films. Madayas *et al.* [122] report on single crystal $Ni_{81}Fe_{19}$ films that exhibit a lower resistivity than the corresponding polycrystalline films, which can be seen in data sets (c) and (d) respectively. This is attributed to the reduced presence of grain boundaries. Grain boundaries mark the interface of two crystallites that have different orientations and thus interrupt the periodicity of the lattice.

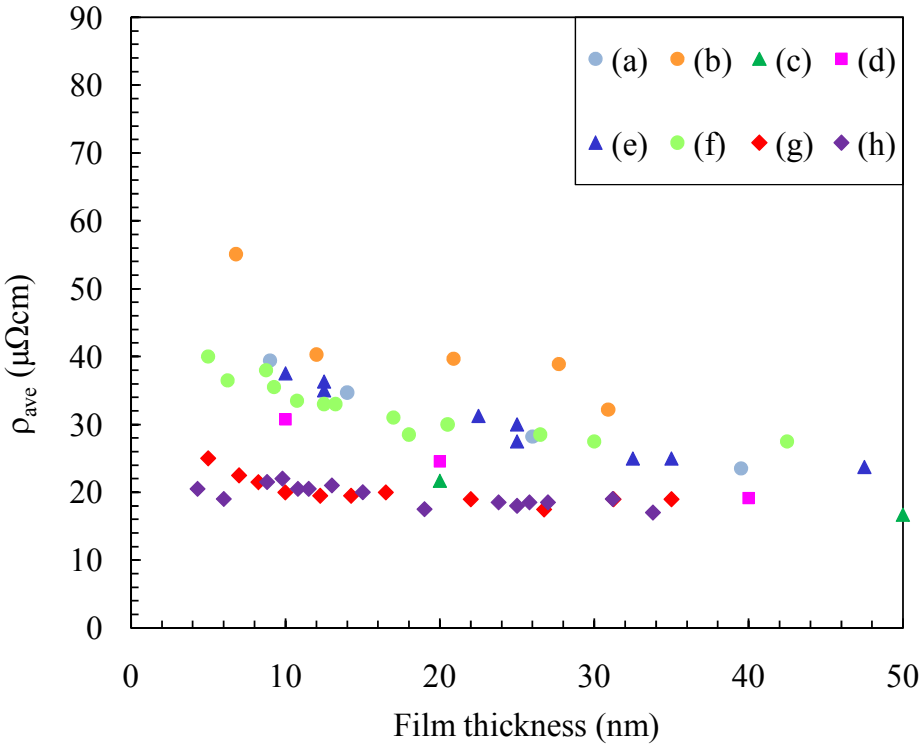

Figure 6:12. Thin film resistivity as a function of film thickness for eight data sets for permalloy films reported in the literature. Details of the legend are explained in Table 6:4, in which detailed information on the preparation conditions is also provided. Errors have not been reported with thin film resistivity data and hence are not present within this figure.

Legend entry	Workers	Film composition	Comment on preparation
(a)	Mitchell *et al.* (1964) [119]	$Ni_{82}Fe_{18}$	Thermal evaporation at ~ 17Å/s onto glass substrate heated at 300°C during deposition. Magnetic field 25 Oe in the plane applied during deposition
(b)	Williams *et al*. (1968) [120]	$Ni_{82}Fe_{18}$	Thermal evaporation at 1000Å/s onto glass substrate heated at 300°C during deposition. Magnetic field 2500 Oe in the plane applied during deposition
(c)	Madayas *et al*. (1974) [121]	$Ni_{80}Fe_{20}$	Thermal evaporation onto (100)-orientated MgO substrates heated to 300°C during deposition
(d)	Madayas *et al*. (1974) [121]	$Ni_{80}Fe_{20}$	Thermal evaporation onto oxidised silicon substrates. Post-deposition annealing of films at a temperature of 300°C for 2 hours
(e)	Miyazaki *et al.* (1989) [122]	$Ni_{82}Fe_{18}$	Thermal evaporation at a rate of 10 Å/s in the presence of a magnetic field of 25 Oe onto substrates heated to 350°C
(f)	Lee *et al.* (2000) [122]	$Ni_{81}Fe_{19}$	Sputter deposited onto glass substrates
(g)	Lee *et al.* (2000) [122]	$Ni_{81}Fe_{19}$	Sputter deposited on glass substrates with a 45 Å under layer of $Ni_{49}Fe_{12}Cr_{39}$
(h)	Lee *et al.* (2000) [122]	$Ni_{81}Fe_{19}$	Sputter deposited on glass substrates with a 45 Å under layer of $Ni_{56}Cr_{44}$

Table 6:4. Details of the preparation conditions for corresponding data presented in Figure 6:12.

Thus, in addition to the film thickness the nature of the microstructure may also significantly affect the measured resistivity values. For very thin films, Madayas and

Shatzkes [141] suggest that a significant proportion of the total resistivity originates from scattering at grain boundaries in addition to increased surface scattering.

Several workers have attempted to improve the average crystallite size and so decrease the amount of associated scattering with small crystallites by depositing films at elevated substrate temperatures ((a), (b), (c)), performing post-deposition annealing ((d) and (e)) and also by depositing on top of NiFeCr (g) and NiCr (h) under-layers. Of these, the most noticeable change in the resistivity is achieved when $Ni_{81}Fe_{19}$ films are deposited on a thin NiFeCr or NiCr seed layer of approximately 45 Å. This results in a large change in resistivity when compared to $Ni_{81}Fe_{19}$ as-deposited directly onto the substrate as shown in data set (f). This large change is attributed to the formation of large (111) textured grains, which subsequently results in a reduction in the grain boundary scattering.

A large (111) texture was reported in $Ni_{82}Fe_{18}$ films investigated by Miyazaki *et al.* in [122] an is quantitatively similar for deposition onto heated substrates reported in [122] and post-deposition annealed films also reported in [121] although the decrease in resistivity observed in very thin films is considerably less than that reported by Lee *et al.* in [126]. Other authors have used Ta seeding layers to induce a (111) texture; although the use of a Ta seed layer has been reported to result in a loss of magnetic moment equivalent to a magnetic dead layer approximately (1.6 ± 0.2) nm [133]. The addition of a thin Al_2O_3 buffer layer between the Ta and NiFe is suggested to suppress the formation of a magnetically dead layer [128], and also significantly enhances the specular reflection of conduction electrons due to the interface sharpening [142]. Ding *et al.* [128] report an increase in the AMR ratio as a direct result of the improvement to the interface sharpness, despite a weak (111) texture, suggesting that crystallite grain size and texture are not the only factors to influence the electrical properties of thin magnetic films and highlighting the importance of diffuse scatter. Figure 6:13 presents values of anisotropic magnetoresistance data, $\delta\rho$, as a function of film thickness for $t < 50$ nm for both $Ni_{82}Fe_{18}$ and $Ni_{81}Fe_{19}$ measured by Mitchell *et al.*, Williams and Mitchell and Miyzaki *et al.* [119, 120, and 122].

Whilst there is considerably much less data available for $\delta\rho$ data within the literature, it is clear that the anisotropic magnetoresistance reported by these authors is larger than that reported within this study. Although there is no data presented in Figure 6:13 for $t < 10$ nm, the values given for $t = 10$ nm are approximately twice that measured in this study and were presented in Figure 6:10.

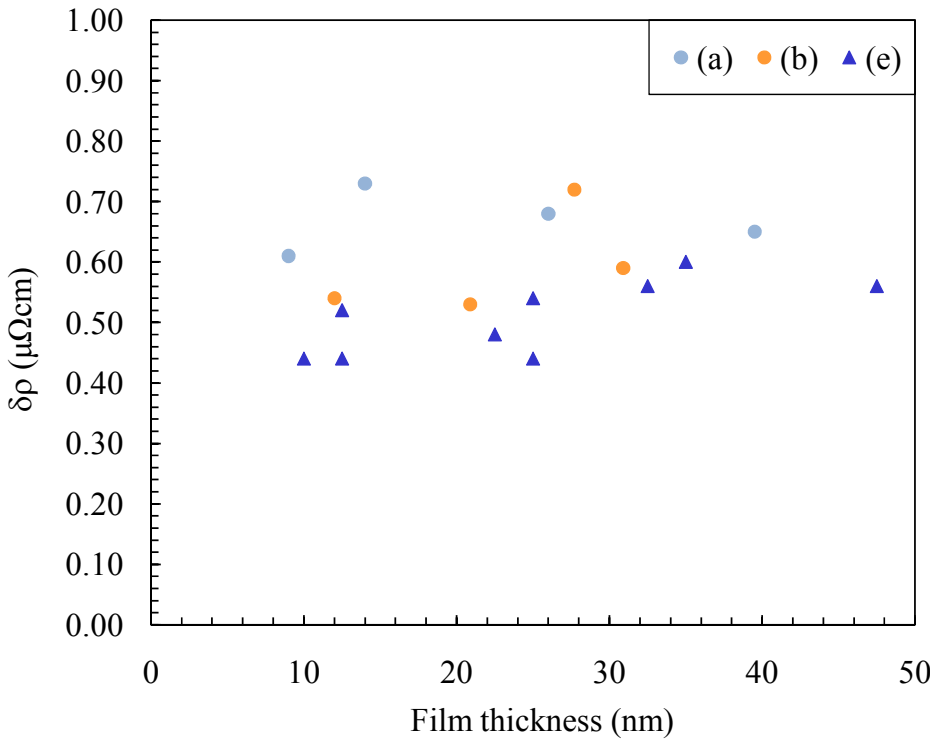

Figure 6:13. Anisotropic magnetoresistance as a function of film thickness for three data sets for permalloy films as reported in the literature. The legend is explained in Table 6:4, which also provides information on the preparation conditions. Details of errors have not been reported with anisotropic magnetoresistance data and hence are not present within this figure.

In addition, the anisotropic magnetoresistance exhibits only a weak thickness dependence, which is also in contrast to the data presented in Figure 6:10.

The data presented by Williams and Mitchell [120] shows a slight dependence of $\delta\rho$ on film thickness, which is attributed to the high rate of deposition of the films. Indeed, the authors believe that the high rate of deposition (1000 Å/s) results in a systematic contamination of bottom layers of $Ni_{81}Fe_{19}$ thin films with decomposed substrate constituents. As a result of the dissipated energy of the metal atoms during deposition, it is suggested that these contaminants (silicon and oxygen) are able to diffuse a short distance into the films. Consequently, the authors conclude that the contamination of a few tenths of a percent would affect the anisotropic magnetoresistance of thinner films, but would become less of an effect with increasing film thickness. The films in this study, however, were not deposited at such elevated rates and do not show any systematic dependence upon the deposition rate, so it is unlikely that the same argument can be applied for the disappearance of the magnetoresistance in the films studied here.

6.5 Interpretation and discussion of the relationship between microstructure and magnetoresistance behaviour of $Ni_{81}Fe_{19}$ thin films

The thickness dependence of the resistivity phenomena studied here can be understood in terms of two main size effects. The first of these size effects is related to film thickness (Fuchs-Sondheimer scattering [136, 139]) whilst the second is related to grain size (Mayadas-Shatzkes scattering [141]). The combination of each of these effects causes a reduction in the mean free path of the conduction electrons and a subsequent increase in the resistivity of the thin film; both effects are observable in the resistivity data for the $Ni_{81}Fe_{19}$ films studied here.

In the literature, it is widely accepted that the reduction in AMR ratio, $\delta\rho/\rho_{ave}$, in thin films is due solely to the increase in film resistivity; indeed McGuire [99] states that the value of magnetoresistance should not depend upon film thickness. Whilst the AMR ratio of the $Ni_{81}Fe_{19}$ films presented in this study is observed to be strongly thickness dependent, this is largely determined by the strong thickness dependence of the $\delta\rho$, rather than the resistivity, ρ_{ave}. Indeed, both the AMR and the AMR ratio of the $Ni_{81}Fe_{19}$ films studied here each tend toward zero for $t < 10$ nm.

The importance of preparation conditions upon values of both thin film resistivity and AMR is also emphasised in the literature and was discussed in section 6.4. However, in this study, there is little systematic dependence on deposition rate. Moreover, there is reasonable agreement between thin film resistivity measured here and data sets (a) to (e) presented in Figure 6:12, despite large differences in deposition rate and the substrate conditions and even for post deposition annealing. There are, however, significant differences between the values of AMR previously reported by other workers and those observed in this study. Although there is a lack of AMR data for $t < 10$ nm, the values measured by other workers are approximately double that observed here for similar thicknesses and do not show any strong dependence upon film thickness.

It is well known that the observed characteristic ferromagnetic properties possessed by binary nickel-iron alloys can be manipulated by changing the chemical composition of the alloy. For the alloys with compositions close to $Ni_{80}Fe_{20}$ both the magnetocrystalline anisotropy constant, K_1, and the magnetostriction, λ_s, are simultaneously close to zero. The anisotropic magnetoresistance in ferromagnetic materials is also sensitive to composition and the simultaneous occurrence of such phenomena was highlighted by Snoek [129]. As each of these physical phenomena is due to the spin-orbit interaction, it is

suggested that disappearance of anisotropic magnetoresistance observed here is associated with a change in one of the other physical properties. An explanation of the disappearance of AMR with decreasing film thickness is developed here which is based upon key microstructural information obtained in chapter 5 and the magnetic properties observed in this chapter.

The loss of AMR due to discontinuous films and the presence of a magnetic dead layer have been ruled out through a combination of specular x-ray reflectivity, MOKE and VSM measurements. Best fit simulations to specular x-ray reflectivity measurements presented in section 5.2 suggest that typical widths of the $SiO_2/Ni_{81}Fe_{19}$ interface are approximately 0.5 nm. Although this represents a larger portion of the film thickness for $t < 10$ nm, which may cause strain of the $Ni_{81}Fe_{19}$ layer at the substrate, it is not large enough to cause discontinuous films for even the thinnest film samples studied here. The magnitude of MOKE magnetometry signals presented in section 6.2 show a linear increase as film thickness increases, up to the penetration depth of the laser. Although a line of best fit to the measured data does not go through the origin, it does for VSM data which is a measurement of the magnetic moment of the whole sample. Since the value of the magnetic dead layer suggested by the MOKE data is within the width of the $SiO_2/Ni_{81}Fe_{19}$ interface it is not possible to conclusively state the presence of a dead layer. Furthermore, the shape of MOKE hysteresis loops taken from random locations and sample orientations suggest that there is no systematic magnetic anisotropy present. The majority of thin film samples are found to have an isotropic distribution of anisotropy, which is expected in NiFe films of this composition.

X-ray diffraction data presented in section 5.3 showed that at the atomic layers, the out-of-plane lattice parameter bonds differently at the substrate interface when compared to that in the bulk. Indeed, changes in the angular location of the x-ray diffraction peak suggested that the out-of-plane lattice parameter within the initial few nanometres of $Ni_{81}Fe_{19}$ is strained by up to 0.17%.

Any change in the bonding can lead to magnetoelastic effects, and hence magnetostriction it is thus suggested that any deformation of the out-of-plane lattice parameter could alter the magnetostriction. The magnetostriction of a ferromagnet is parameterised by λ_s, which is directly proportional to the change in length, $\Delta l/l$, produced when the sample is magnetised to saturation. Several authors have studied the thickness dependence of the saturation magnetostriction in $Ni_{81}Fe_{19}$ thin films on SiO_2 substrates

[111, 112, 113 and 143], and have observed a strong thickness dependence for $t < 40$ nm. In [143], Ounadjela *et al.* observe that the magnetostriction in $Ni_{81}Fe_{19}$ films becomes increasingly negative for $t < 20$ nm. The data reported by Kim and Silva [112] suggests that $Ni_{81}Fe_{19}$ thin films exhibit near zero magnetostriction for $t > 7$ nm, below which the magnetostriction becomes increasingly negative. This can be understood by considering the phenomenological model suggested by Néel for magnetostriction [144]:

$$\lambda_s = \lambda_s^{bulk} + \frac{\lambda_s^{surface}}{t} \tag{6:7}$$

Where λ_s is the total magnetostriction, which is the sum of the bulk term λ_s^{bulk} and a surface term $\lambda_s^{surface}$. In thick samples, the bulk volume term dominates whilst the surface term dominates as film thickness decreases.

In order to observe AMR, the conduction bands must be anisotropic with respect to the magnetic field direction. As both the magnetostriction and anisotropic magnetoresistance are both related to spin-orbit effects, it is not unreasonable to expect that a change in the magnetostriction constant due to the microstructure of the film could affect the magnetoresistance properties for $t < 7$ nm. Thus, it is suggested that the disappearance of the magnetoresistance observed in this study is a direct consequence of a thickness dependence of the magnetostriction. The cause of this thickness dependence is unknown; however, based on the results presented here, it is suggested result of strain of the initial $Ni_{81}Fe_{19}$ layers at the SiO_2 interface causes a change in the magnetostriction such that it affects the anisotropic magnetoresistance.

6.6 Chapter conclusion

In this chapter, a combination of MOKE and VSM magnetometry and electrical resistance measurements have been used to study the magnetic and magnetoresistance behaviour of $Ni_{81}Fe_{19}$ thin films. The intensity of normalised MOKE magnetisation measurements is proportional to film thickness until the penetration depth of the incident laser light is reached. This is observed to correspond to approximately 15 nm for incident light of wavelength 658 nm, as used here. Beyond this thickness the signal is affected by absorption effects. MOKE hysteresis loop shapes suggest that there is no systematic anisotropy present, whilst coercivity measurements show that all films are very soft as is expected for $Ni_{81}Fe_{19}$ thin films. The lack of a systematic dependence of coercivity upon

film thickness, down to the thinnest films, combined with the clear thickness dependence of both the MOKE and VSM signals suggests that all films are ferromagnetic and continuous, and further suggests that there is no magnetic dead layer present within the films.

Electrical resistance measurements show that the thin film resistivity, ρ_{ave}, increases as film thickness decreases, which is consistent with the Fuchs-Sondheimer size effect model. In general, thin film resistivity observed here is larger than reported previously in the literature. As the average out-of-plane and lateral grain size corresponds to ~7 nm, which also corresponds to that of the average mean free path, it is suggested that the larger values of thin film resistivity observed here is largely the result of the increased scattering associated with small crystallite grains. Other factors such as interfacial roughness between the $SiO_2/Ni_{81}Fe_{19}$ and $Ni_{81}Fe_{19}/Fe_2O_3$ layers could also contribute to an increase in thin film resistivity. Anisotropic magnetoresistance, $\delta\rho$, is observed to be strongly dependent upon on film thickness and tends toward zero for $t < 7$ nm. This thickness dependence is larger than has previously reported in the literature, where it is suggested that $\delta\rho$ should be independent of film thickness for $Ni_{81}Fe_{19}$ films. The anisotropic magnetoresistance ratio, $\delta\rho/\rho_{ave}$, measured in this study is an order of magnitude smaller than has previously been reported for bulk $Ni_{81}Fe_{19}$ which is attributed to the strong thickness dependence of the anisotropic magnetoresistance. Results from x-ray diffraction measurements presented in chapter 5 are used to provide an explanation for the disappearance of AMR observed here. It is suggested that this is due to the change in the out-of-plane lattice parameter, and the associated strain, present in the initial layers of $Ni_{81}Fe_{19}$ at the $SiO_2/Ni_{81}Fe_{19}$ interface which causes a change in the magnetostriction constant, λ_s. It is suggested that any change in the magnetostriction in $N_{i81}Fe_{19}$ will cause a change in the anisotropic magnetoresistance, since both effects are due to the spin-orbit interaction.

Chapter 7. Domain wall pinning behaviour in $Ni_{81}Fe_{19}$ planar nanowire structures

7.1 Introduction

The pinning and propagation of domain walls in planar nanowires has become the focus of intense research, with many proposed applications including both magnetic logic [62] and sensor [63] devices and more recently in magnetic memory concepts [64, 145]. In these devices, information is encoded in the magnetisation direction of domains in planar nanowires, with the nucleation and propagation of domain walls in nanowires allowing for the input, manipulation and readout of stored information. Such devices require a high level of control of domain wall propagation behaviour, which can be achieved through local pinning centres that provide well defined stable locations and thus confine domain wall propagation.

Domain walls have been considered to behave as quasi-particles [146] that can be controlled by external magnetic fields, spin-polarised currents and lithographically patterned variations in the nanowire geometry. The micromagnetic spin structure of a domain wall results from an energy minimisation process that includes material dependent properties as well as the local geometry of the nanowire. For magnetic materials with weak intrinsic anisotropies such as cobalt rich CoFe-based amorphous alloys or polycrystalline permalloy nanowires (with a nominal composition around $Ni_{80}Fe_{20}$) the magnetisation is largely constrained by magnetostatic energy considerations so as to lie along the axial length of the wire with spins parallel to the surfaces and edges. The magnetisation direction in such magnetically soft nanowires is thus defined by the geometry of the nanowire, and when structural features such as notches are patterned within the nanowire the spin structure tends to follow the local edges of these features.

Artificially structured variations in the nanowire geometry such as a notch can be introduced to engineer domain wall pinning and have allowed some of the more fundamental properties of domain walls to be determined. These structural features yield a pinning potential energy landscape in which the quasi-particle can move under the action of a magnetic field and spin-polarised currents. By analogy with a mechanical oscillator, the domain wall has been considered as a particle confined in a simple parabolic potential, the bottom of which is assumed to correspond to the physical centre of the notch [146]. In

contrast to this simplistic approach, a detailed knowledge of the pinning potential created by different notches is a vital step towards understanding both the fundamental properties of domain walls, and also towards the optimisation of domain wall pinning behaviour that is required for magnetic memory devices. Understanding and controlling the field driven motion of domain walls in nanowires is an important preliminary step to studying their current driven dynamics [147, 148]. As such, quantitative correlation between the depinning field and pinning site geometry is highly relevant to both field and spin-polarised current induced domain wall behaviour and may ultimately lead to optimising the control and efficiency of these devices. In this chapter, a systematic investigation into the relationship between wire width, notch geometry and field driven domain wall pinning behaviour is presented.

7.2 The effect of nanowire width on domain wall injection behaviour

7.2.1 Description of the nanowire structure

As the magnetisation direction in magnetically soft nanowires is defined by the geometry of the nanowire, the spin structure tends to follow the local edges of these features. Manipulation of the physical structure allows the domain wall propagation to be controlled. The lowest energy state of a nanowire is that of uniform magnetisation; when a nanowire is uniformly magnetised the spins at the ends are orientated to some extent across the width of the strip in either the c-state or s-state configuration as shown in Figure 7:1. Such arrangements are formed so as to reduce the magnetostatic energy associated with a large, uniformly magnetised nanowire. Since these spins are orientated across the width of the strip they are easier to switch magnetisation direction compared to those that are orientated along the axial length. When a magnetic field is applied in the plane of the nanowire switching of the nanowire occurs by domain walls that are nucleated at each end of the nanowire.

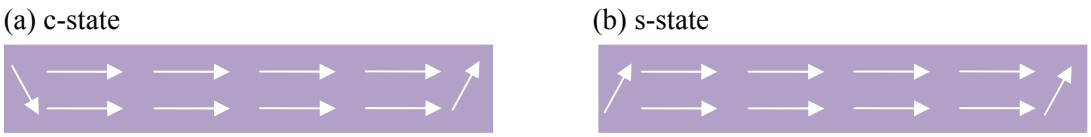

Figure 7:1. Schematic to show orientation of spin magnetic moments in a uniformly magnetised nanowire strip (without nucleation pad or pointed end) for a (a) c-state and (b) s-state configuration.

Once nucleated, these domain walls then propagate along the length of the nanowire toward the centre of the nanowire, where they proceed to annihilate each other.

The magnetic field required to nucleate a domain wall in a nanowire of uniform width is large, and can be significantly reduced by the addition of a micron-scaled nucleation pad to one end [149]. Furthermore, by tapering the opposite end of the nanowire to a sharp point it becomes magnetically very hard and thus a larger magnetic field is required to reverse the magnetisation direction at this end [150]. Modification of the ends of the nanowire to include these features means that a domain wall can be introduced from the nucleation pad. Once the wall is introduced, it can propagate along the length of the nanowire to the pointed end where it is annihilated. Such a design not only allows for domain walls to be nucleated at a lower field, but also ensures domain wall propagation occurs in the same direction on successive field reversal cycles.

Planar magnetic nanowire samples were fabricated on pre-oxidised silicon substrates using electron-beam lithography, followed by thin-film deposition and lift-off techniques as outlined in section 4.2. Thin films were deposited by thermal evaporation from a single $Ni_{81}Fe_{19}$ source from a base pressure of 10^{-7} Torr and a growth pressure of 10^{-6} Torr at a rate of 0.5 Å/s, using the method described in section 4.2.5. The nanowires investigated here were all 10 nm thick, with nominal nanowire widths ranging from 200 nm to 600 nm. All nanowire structures were fabricated with a large nucleation pad on one end, of approximate dimensions 3 μm x 11 μm, whilst the other end was tapered to a point. Each nanowire contained a single asymmetrically patterned pinning structure; the pinning structures were of two different geometries in the form of triangular and rectangular shaped notches.

A scanning electron microscopy image of a typical nanowire structure is presented in Figure 7:2, in which the key structural features used to control domain wall propagation are highlighted. It is worthwhile pointing out that the speckles of various different sizes present in Figure 7:2 are thought to be residual from the cleaning processes used during sample fabrication and believed to be non-magnetic. The following sections describe the nucleation of domain walls and the subsequent pinning behaviour at the nucleation-pad interface and at notch pinning structures.

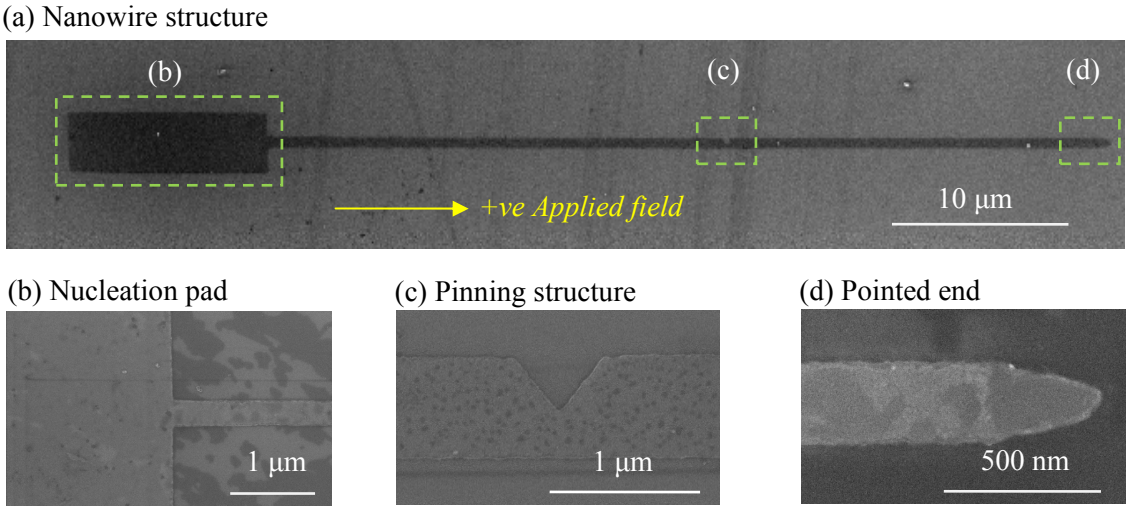

Figure 7:2. Scanning electron microscopy images of a nanowire structure (a) nominally 400 nm wide containing a 3 x 11 µm nucleation pad; enlarged images (b) of nucleation pad-wire interface for a 200 nm wide nanowire; (c) triangular notch pinning structure in a 600 nm wide nanowire and (d) pointed end to annihilate domain wall structures and ensure domain wall propagation is from nucleation pad on successive magnetisation reversal cycles. Typical root mean square edge roughness was approximately 10 nm.

7.2.2 Switching behaviour of the nucleation pad

The switching behaviour of the nucleation pad was investigated by placing the MOKE laser spot as shown in Figure 7:3. Examples of normalised MOKE hysteresis loops measured from nucleation pads attached to nanowires of two different widths are presented in Figure 7:4. Both MOKE hysteresis loops are characterised a sharp switching transition between magnetisation directions. For the nucleation pad attached to a nanowire 285 nm wide switching occurs at (18 ± 2) Oe, whilst the pad attached to a nanowire 710 nm wide switches at an applied field of (16 ± 2) Oe. As the MOKE data is time averaged over several hundred field reversal cycles, this suggests that the switching is reproducible.

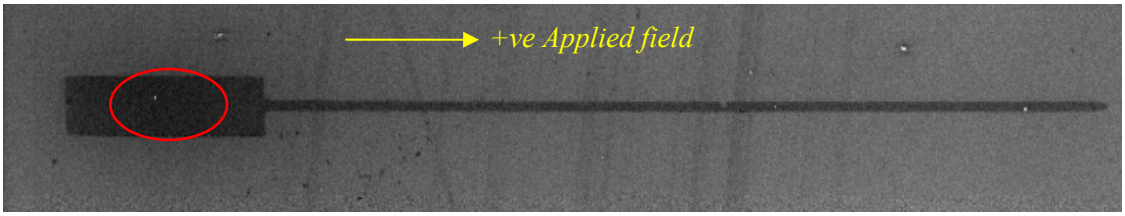

Figure 7:3. Schematic to show the location of the laser spot during measurements of magnetisation reversal in the nucleation pad.

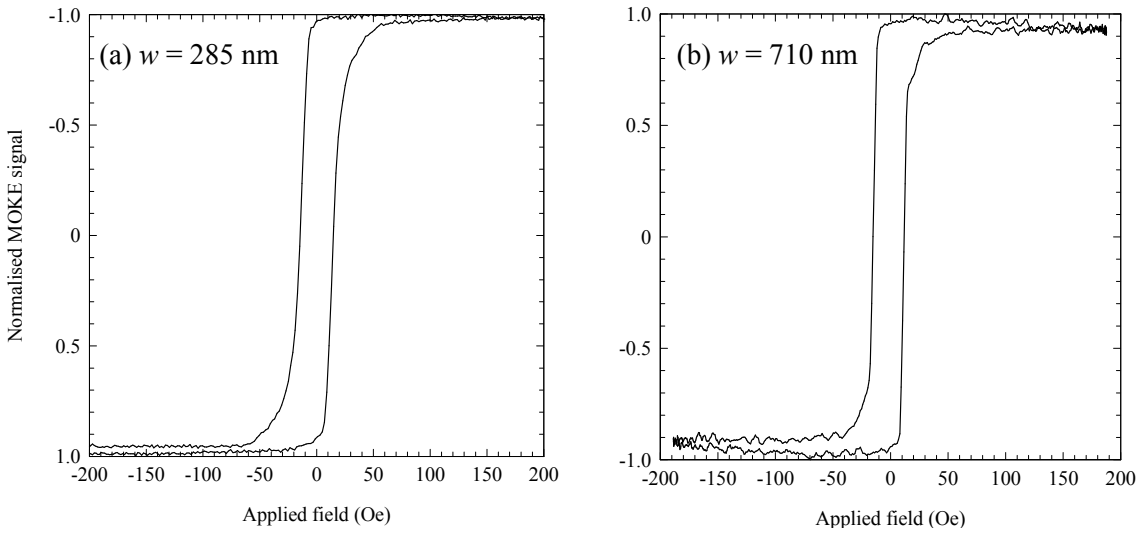

Figure 7:4. Normalised MOKE hysteresis loops measuring the switching field of the nucleation pads attached to nanowires of two different widths, taken with the laser spot positioned shown in Figure 7:3. The different noise levels present are a result of the different lengths of time averaging. The magnetic field was not measured directly during the experiment. The offset in the loops at $H = 0$ is the result of a small amount of residual field present within the coils due to the manner in which the current to the coils supplying the magnetic field is increased/decreased and is not representative of the switching behaviour of the pad.

The average switching field for many different nucleation pads of the same nominal dimensions are shown in Figure 7:5.

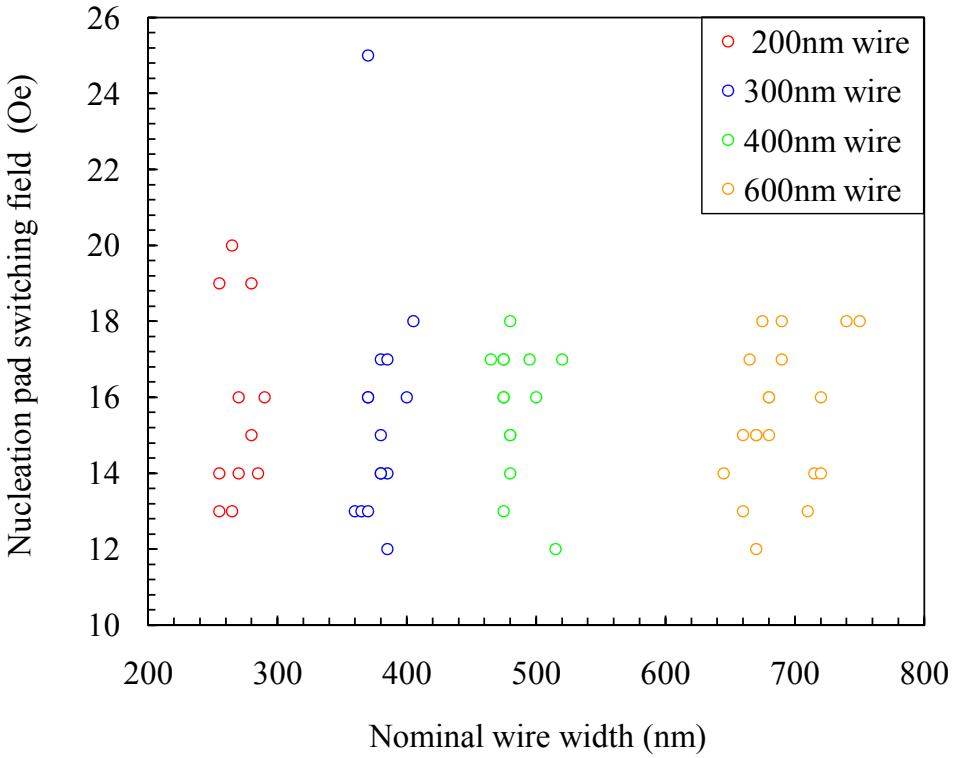

Figure 7:5. Switching field for nucleation pads of the same nominal dimensions (3 µm wide, 11 µm long) as a function of nominal nanowire width for 10 nm thick nanowire structures.

The average switching field of different nucleation pads of the same nominal dimensions is approximately 16 Oe, with a spread of ± 6 Oe. There is no obvious dependence of the switching field of the pad upon the nanowire width, which is to be expected since the switching behaviour of the nucleation pad is solely determined by magnetostatics. The small range in measured switching fields between different pads of the same nominal dimensions is attributed to a combination of variations in the lithography and the possibility that some structures may not have been completely aligned parallel to the direction of the applied field during MOKE measurements. Variations in the lateral dimensions due to edge roughness (with typical rms edge roughness approximately 10 nm) could affect the demagnetising factor, and consequently the switching field. In addition, if the nanowires are not completely aligned parallel then this can result in a transverse component of the applied field could affect the magnitude of the axial switching field.

7.2.3 The effect of nanowire width on domain wall injection behaviour

Once the magnetisation within the nucleation pad has switched direction a domain wall will form at the pad-wire junction. This is because the micromagnetic spin structure of a domain wall is highly sensitive to the lateral dimensions of the nanowire, as described in section 3.5.3. A domain wall will pin at the pad-wire junction if the spin structure of the wall in the pad is not energetically favourable within the nanowire and if the applied field is not too large. Due to the large difference between the widths of the nucleation pad and the nanowire, the micromagnetic structure of the domain wall must re-orientate such that it becomes energetically favourable within the reduced dimensions of the nanowire. As such, the domain wall will remain pinned at the pad-wire junction until the applied field is increased. The field required to depin the wall and inject into the nanowire was measured by placing the focussed MOKE laser spot over the junction between the nucleation pad and the nanowire as shown in Figure 7:6.

Figure 7:6. Schematic to show location of the laser spot used to measure domain wall injection from the nucleation pad to the nanowire. The arrows indicate the formation of a head-to-head domain wall that is pinned at the pad-wire interface.

Normalised MOKE hysteresis loops measuring the average domain wall injection field for a selection of different nanowire widths are shown in Figure 7:7. It can be seen that there are two distinct switching fields within each MOKE hysteresis loop. The first switching field, H_1, occurs between (10 ± 2) Oe and (20 ± 2) Oe in each nanowire structure and does not appear to depend upon the nanowire width. Based on the results presented in section 7.2.2, it is suggested that this corresponds to the switching field of the nucleation pad. The second switching field, labelled H_2, is observed to depend upon the width of the nanowire and is suggested to correspond to the injection field of the domain wall.

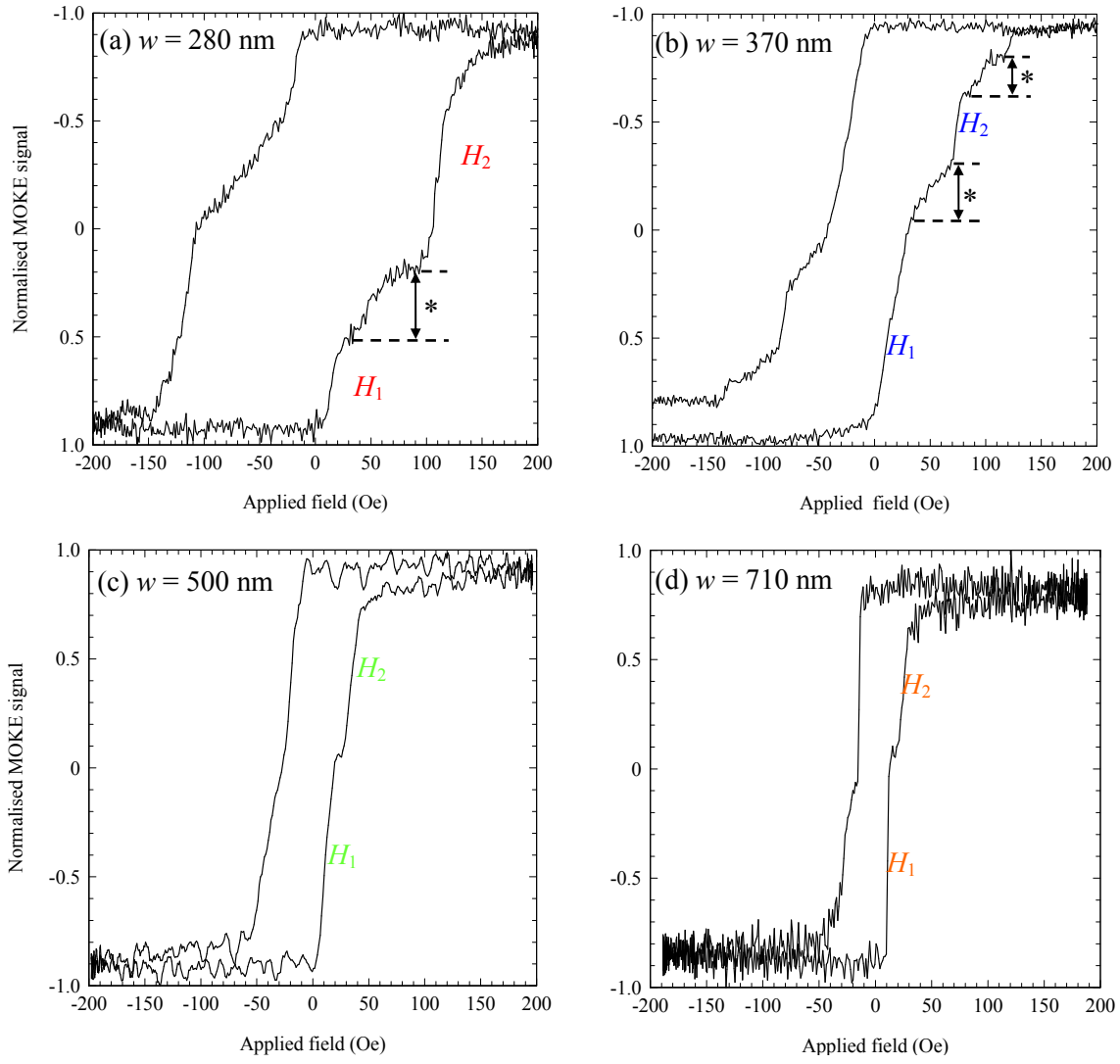

Figure 7:7. Normalised MOKE hysteresis loops measuring domain wall injection field as a function of nanowire width, measured using the focused MOKE laser spot positioned as shown in Figure 7:6. In each loop, the event labelled H_1 corresponds to the switching field of the pad, whilst H_2 corresponds to the domain wall injection field. It is suggested that the events labelled with an asterisk correspond to the re-orientation of spins within the domain wall as it remains pinned.

At injection, the domain wall is depinned from the pad-wire interface and proceeds to propagate along the nanowire.

The average injection field for different nanowire structures as measured from MOKE hysteresis loops is presented in Figure 7:8. It can be seen that as the wire width decreases, the average field required to depin a domain wall and 'inject' it into the nanowire increases. This increase is very slight for wire widths wider than 400 nm and becomes much more rapid for wire widths narrower than 400 nm. For wire widths wider than 400 nm, large variations in nanowire widths yield small differences in the average injection fields for different wire widths. Figure 7:8 shows that for 500 nm and 710 nm wide nanowires the average injection field is measured to be (34 ± 2) Oe and (25 ± 2) Oe, respectively. Indeed, for nanowires wires nominally 400 nm wide, the spread in average measured the injection fields is approximately 24 Oe. However, for wire widths narrower than 400 nm the increase in injection field becomes more rapid. For example, the average injection field of a 370 nm wide nanowire is measured as (59 ± 2) Oe whilst for a 280 nm wide wire, the injection field is much larger, at (110 ± 2) Oe. Furthermore, it can be seen that small variations in wire width yield large variations in the average injection field.

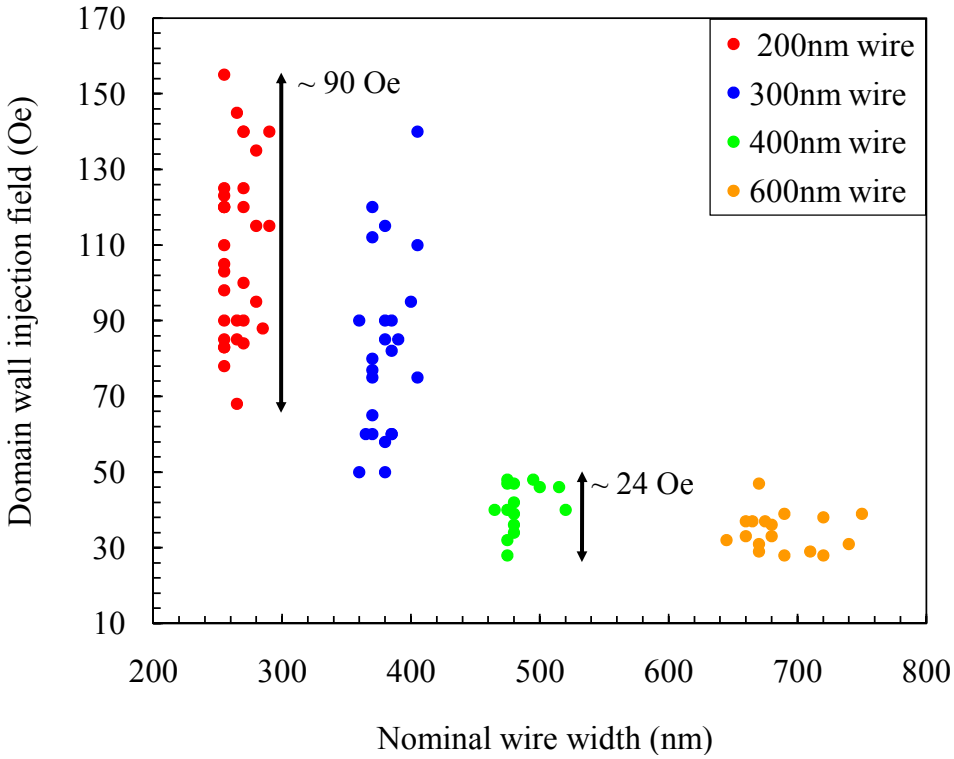

Figure 7:8. Comparison of the average injection fields measured from MOKE hysteresis loops of different nanowires of the same nominal dimensions. All nanowires are 10 nm thick.

Indeed, for nanowires with a nominal width of 200 nm, the measured injection fields have a spread of approximately 90 Oe.

An understanding of the domain wall injection fields can be gained by considering the energetics of the pinned domain wall at the pad-wire interface. A domain wall pinned at the pad-wire interface can be treated as a quasi-particle trapped in symmetric parabolic potential well as shown in Figure 7:9. The depth of the potential well is determined by the width of the nanowire; as the nanowire width decreases the depth of the pinning potential increases and a larger applied field is required to depin the wall from the pad-wire interface. Once the wall is nucleated within the pad it will remain pinned at the pad-wire interface until the applied field is large enough to provide enough energy for the wall to depin. The application of an applied magnetic field tilts the potential energy landscape as an applied field changes the potential energy of the domain wall. A domain wall depins from the pad-wire interface, and so becomes injected into the nanowire, when the potential well is sufficiently tilted up so as to tip the quasi-particle over and out of the top of the well.

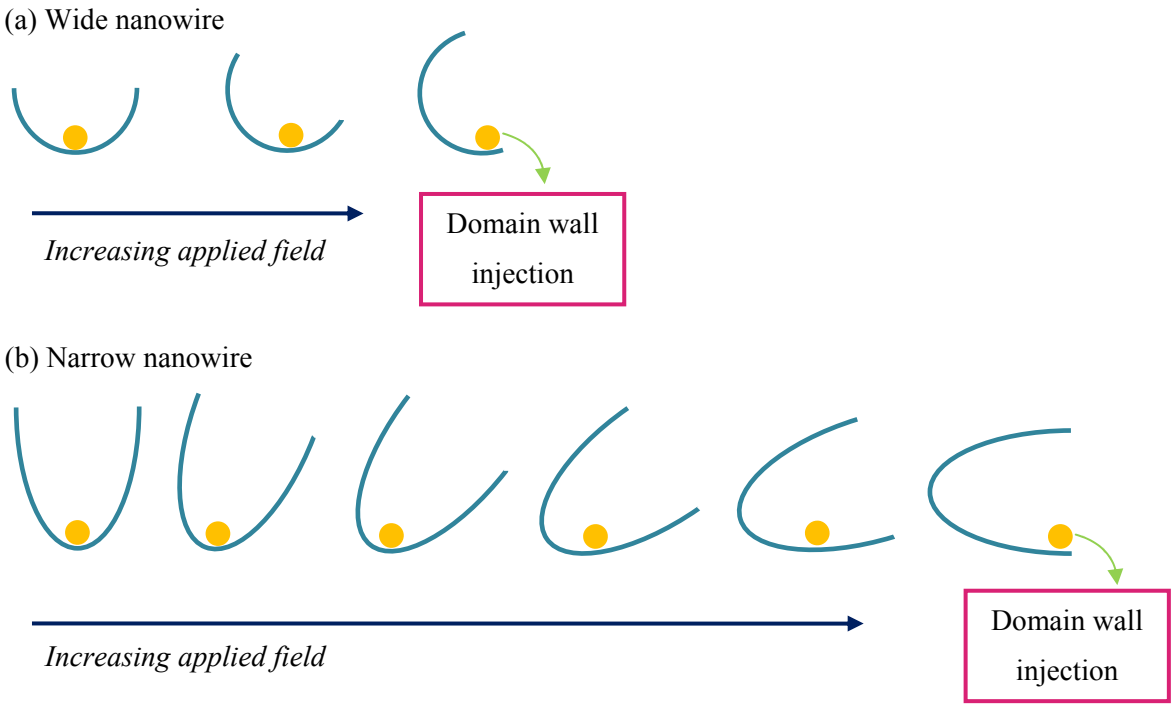

Figure 7:9. Schematic of domain wall injection, in which the domain wall is illustrated as a quasi-particle pinned in a potential well. A domain wall pinned at the junction between the nucleation pad and a wide nanowire can be compared to that of a wall in a shallow potential well, as shown in (a). A wall pinned at the junction between the nucleation pad and a narrow wire is like a particle pinned in deep potential well as shown in (b).

Whilst this analogy serves as a good explanation for why the domain wall injection field increases as wire width decreases, it does not explain why the measured injection field in nanowires with $w < 400$ nm is sensitive to small changes in lateral wire width.

Consider the MOKE hysteresis loops presented in Figure 7:10 in which domain wall injection in nanowires of nominal width of 200 nm are presented.

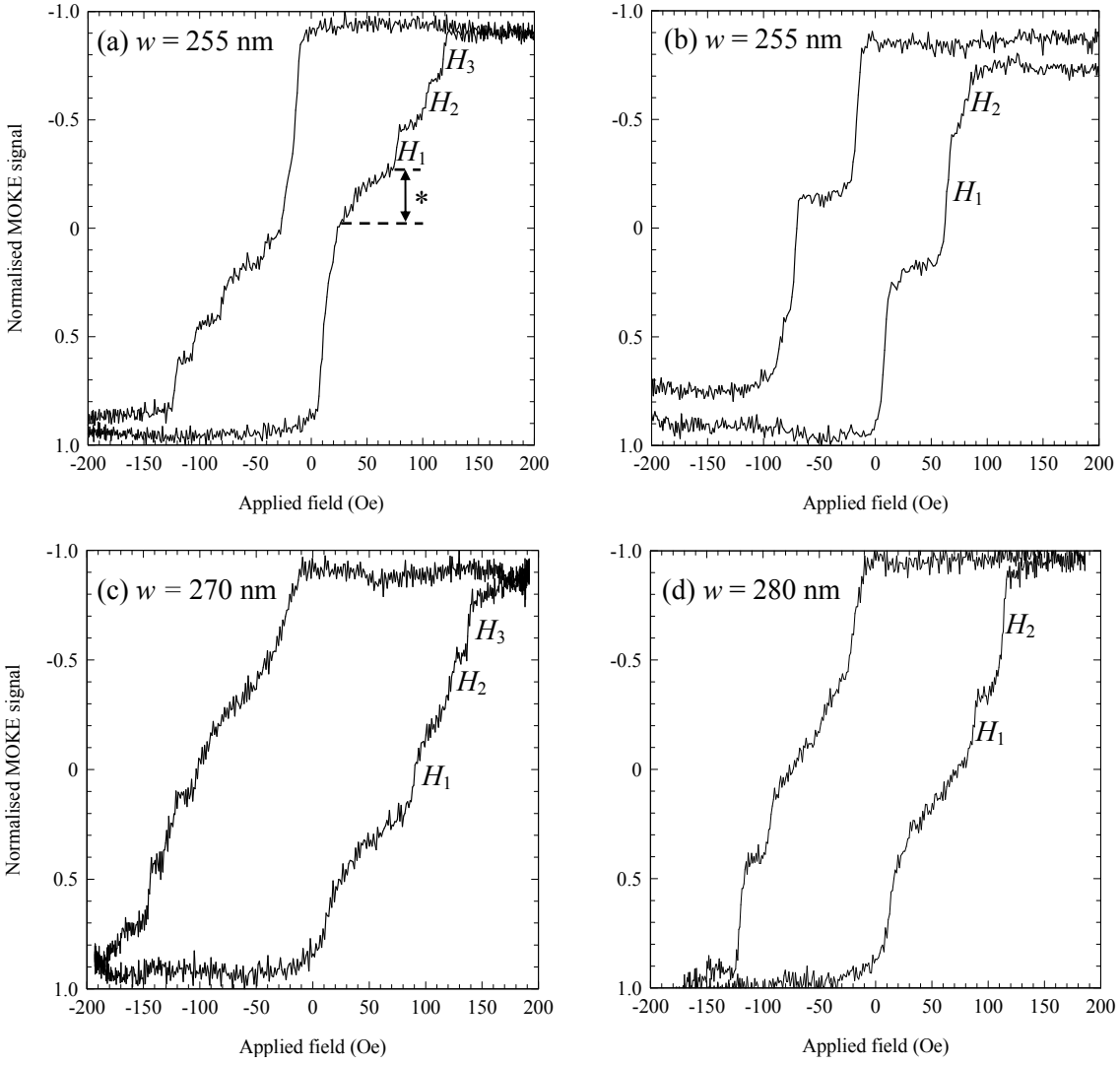

Figure 7:10. Example normalised MOKE hysteresis loops measuring domain wall injection into different wires of the same nominal dimensions. Actual wire widths as measured by scanning electron microscopy are provided for comparison. For each loop, there are several different switching steps labelled H_1 to H_3 inclusive; these are thought to correspond to different domain wall injection fields. It is suggested that those events similar to that labelled with an asterisk correspond to the re-orientation of spins within the domain wall as it remains pinned. The MOKE hysteresis loop presented in (b) does not close due to drift in the signal, which is a consequence of the time averaging process. Drift of the MOKE signal tended to occur when measuring the magnetisation reversal properties of the narrower nanowires as the signal had to be time averaged for longer in order to reduce the noise levels associated with less magnetic material.

In each loop there are multiple switching fields, labelled H_1 to H_3 inclusive, which indicates that there are multiple fields at which domain wall injection from the pad into the nanowire occurs. Such steps are also visible in MOKE hysteresis loops taken from wires of nominal width 300 nm, although for all wires wider than 400 nm injection takes place by a single switching event similar to those shown in Figure 7:7 (c) and (d). This observation suggests that for a given nanowire width, there are a discrete number of applied fields at which a domain wall will depin from the pad-wire interface. These observations cannot be explained using the simple particle in a potential well analysis presented in Figure 7:9.

7.2.4 Analysis of the dependence of domain wall energy upon domain wall structure using micromagnetic modelling

Further insights into domain wall injection behaviour have been obtained using quasi-static micromagnetic simulations to study the relationship between the domain wall energy and its micromagnetic spin structure. Using the phase diagram reported by Nakatani *et al.* in reference [61] as a guide, one of two basic domain wall structures (transverse wall or vortex wall, respectively) was artificially introduced into a rectangular shaped element 6 μm long and 10 nm thick. The nanowire width, w, was varied from 50 nm up to 400 nm. For each wire width the domain wall structure was allowed to relax to its equilibrium configuration at zero-applied field. In addition, for each wire structure a simulation was also performed at positive saturation; that is, for a wire that contains no domain wall. The energy of the domain wall, E_{DW}, was determined using:

$$E_{\mathrm{DW}} = E_{\mathrm{DW}}^{\mathrm{total}} - E_{\mathrm{No\ DW}}^{\mathrm{total}} \tag{7:1}$$

In doing this, both the exchange and magnetostatic energies associated with the flat end shapes of the rectangular element were accounted for. This energy value was then divided by the cross-sectional area of the planar nanowire, wt, so as to normalise all domain wall energies relative to one another.

The results presented here focus on head-to-head domain walls only. Corresponding simulations for tail-to-tail domain walls yield identical results to those presented for head-to-head domain walls. In addition, only transverse walls in which the wall moments point upwards, and vortex walls with clockwise spin structure have been investigated as domain walls of the opposite chirality (downwards for the transverse wall

and counter-clockwise for the vortex wall) yield identical results in a symmetric spin structure. Such results indicate that the two chiralities of each domain wall structure are energetically degenerate in a symmetric nanowire structure. The importance of domain wall chirality is discussed in greater detail in section 7.3.3.

The internal micromagnetic spin structure of transverse and vortex walls produced from micromagnetic simulations are compared in Figure 7:11; knowledge of the physical structure is particularly useful when interpreting the variation of energies with wire width. It is well known that the micromagnetic structure of a domain wall is highly sensitive to the transverse dimensions of the wire [60, 61]. Since the formation of a domain wall costs a finite amount of energy, the preferred domain wall structure for any given nanowire will be that which incurs the lowest total energy cost. Figure 7:12 compares the variation of total energy of vortex walls and transverse walls, which also shows the variation of the constituent magnetostatic and exchange energies.

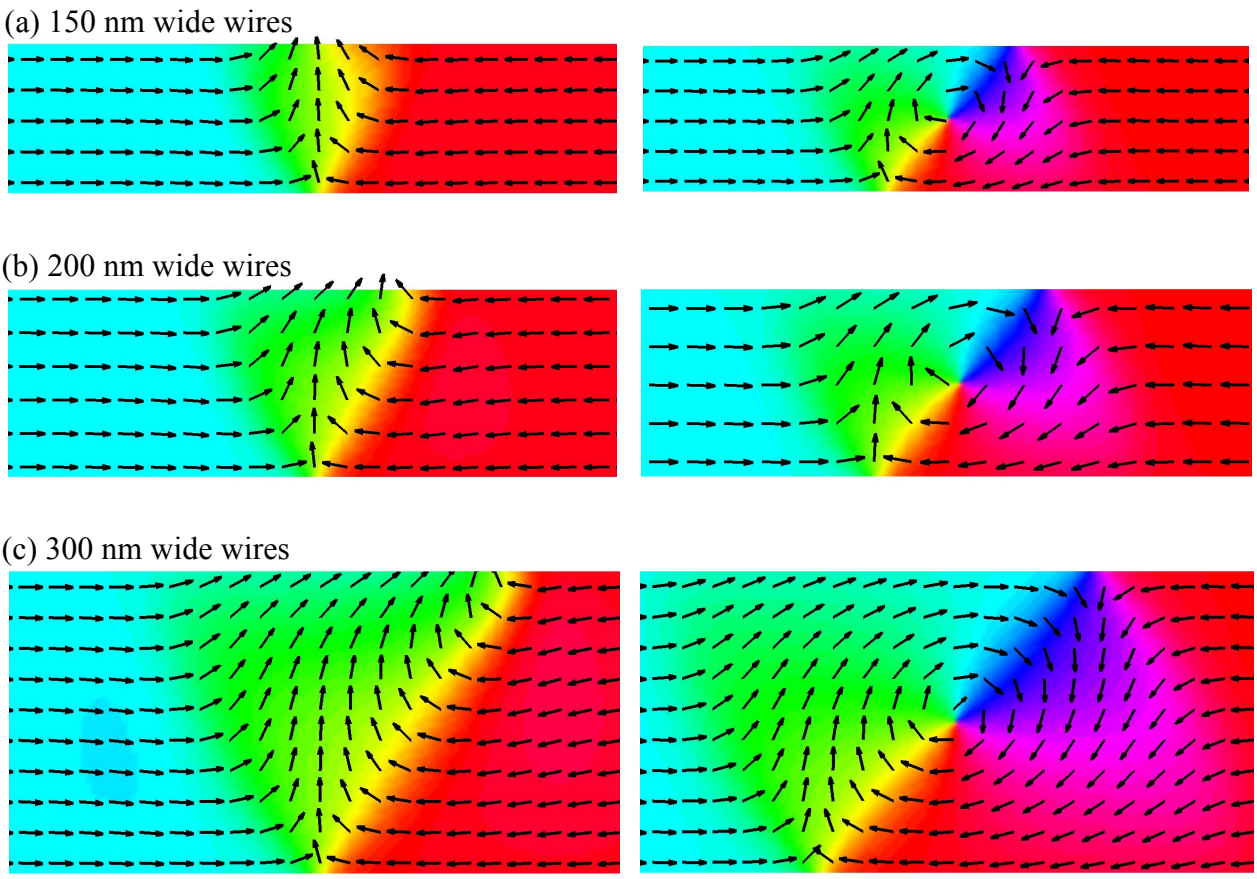

Figure 7:11. Detailed micromagnetic structure of (*left*) transverse and (*right*) vortex domain wall structures in a 10 nm thick nanowire; (a) 150 nm wide wires, (b) 200 nm wide wires and (c) 300 nm wide wires, respectively. The colours represent directions of magnetisation rotation within the domain wall and are shown as a guide to the eye.

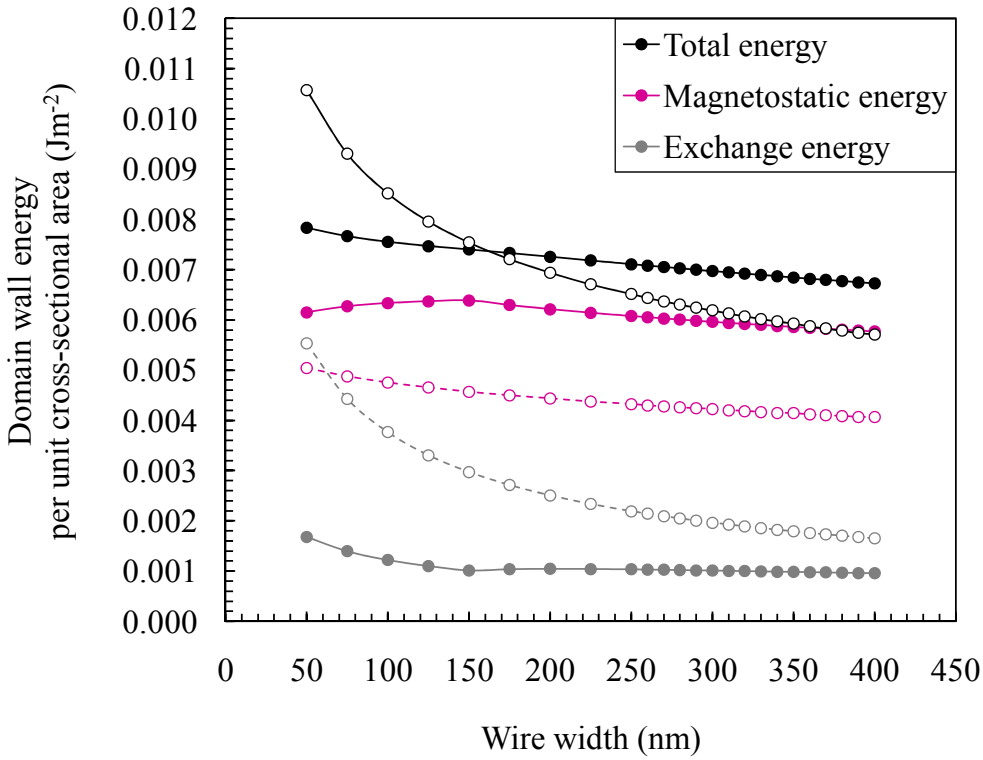

Figure 7:12. Comparison of the total energy, magnetostatic energy and exchange energy per unit cross-sectional area for transverse walls (*solid symbols*) and vortex walls (*open symbols*) in a 10 nm thick nanowire as deduced from OOMMF micromagnetic simulations.

Based on the micromagnetic simulations presented here, a transverse domain wall (●) is the energetically favourable state for a wire width, w = 150 nm since it is 1.9% lower in energy than the corresponding vortex wall (○). As wire width increases to 175 nm, the total energy of the transverse wall decreases with increasing wire width, whilst the energy of the vortex wall decreases more rapidly and thus becomes the energetically favourable domain wall structure. For a 200 nm wide nanowire, the transverse wall is 4.5% higher in energy than the vortex wall. As the wire width continues to increase the vortex wall becomes increasingly favourable in energy and by 400 nm the transverse wall is higher in energy by approximately 15%. Further understanding of the dependence of the total domain wall energy on nanowire width can be gained by considering the variation of both the magnetostatic and exchange energies. The relationship between nanowire width, wall structure and exchange energy is considered initially.

As wire width increases the exchange energy per unit area decreases for both transverse and vortex walls, although this decrease is much more rapid for vortex walls than for transverse walls. The exchange energy is associated with the number of spin magnetic moments within the wall and on the size of the angle between adjacent spins.

Figure 7:11 shows that the domain wall width scales approximately with wire width. In addition, for a given wire width, the vortex wall is always wider than the corresponding transverse wall. Both domain wall structures comprise of a 180° transition, and so the large value of exchange energy for both transverse and vortex walls for $w < 100$ nm is attributed to the larger angles between adjacent spins that are present within the narrower walls. The exchange energy within a vortex wall (○) is considerably higher for narrower wires for two main reasons; firstly, the wall is wider than the transverse wall and so contains more spins, and secondly, the wall is constrained resulting in large angles between adjacent spins which is a result of the narrow width. When the width, w, > 200 nm, there is no further decrease in the exchange energy of transverse walls (●), although for vortex walls the exchange energy continues to decrease despite the number of spins within the wall increasing. As seen in Figure 7:11, this is because the increasing wire width allows the wall to expand in width, which in turn allows for a much more gradual rotation of magnetisation. Thus, even though there are *more* spins within the wall, there are no large angles between adjacent spins as there are for the transverse wall.

A description of the exchange energy alone does not explain why a vortex wall becomes the energetically favourable structure. As $w > 175$ nm, the vortex wall becomes energetically favourable because of the significant reduction in magnetostatic energy that the vortex configuration offers when compared to that of the corresponding transverse structure. For all wire widths, the magnetostatic energy associated with transverse walls (●) is larger than that for vortex walls (○); this can be understood by considering the schematic presented in Figure 7:13. As discussed in section 3.3.1, the magnetostatic energy is associated with the stray field that arises from uncompensated free poles from a magnetic body. The large magnetostatic energy associated with transverse walls arises because the spin magnetic moments are orientated transverse to the long axis of the nanowire. This means that on the upper and lower sides of the nanowire there are uncompensated free poles along the strip width.

Figure 7:13. Schematic illustration to show how the magnetostatic energy associated with (a) the transverse wall structure and (b) the vortex wall structure.

As wire width increases, the number of spins within the wall increases and so there are an increasing number of spins orientated across the strip width. In contrast, for the vortex wall structure, the stray field is reduced by having a gradual in-plane rotation of spin magnetic moments. Such a spin structure is essentially a flux-closed state, which minimises the number of free poles upon the upper and lower portions of the nanowire. In addition, there is also a small vortex core which points out of the plane of the nanowire which also makes a finite contribution to the magnetostatic energy. However, as the vortex core tends to comprise of a few magnetic moments only, the core is not a large source of stray field. As such, the magnetostatic energy of a vortex wall in a 10 nm thick nanowire is always less than that associated with a transverse wall in the same nanowire structure.

In Figure 7:12, it can be seen that for a transverse wall the magnetostatic energy (●) is significantly larger than the exchange energy (●) and increases as wire width increases for $w < 150$ nm. For $w > 150$ nm the magnetostatic energy shows a slight decrease as wire width increases. To reduce this large stray field, the transverse wall changes structure slightly to become an asymmetric transverse wall, as seen in Figure 7:11 (b) and (c). The magnetostatic energy is reduced by orientating a large proportion of spins at lower angles with respect to the top edge, although the 'backbone' of the wall structure still contains some high angle spins orientated across the wire width. Conversely, for vortex walls, the magnetostatic energy, (○) decreases as the width increases for all wire widths. As the wire widths increases above 400 nm, the transverse wall becomes increasingly energetically unfavourable, which is attributed to the increasing cost of magnetostatic energy. Indeed, when $w = 500$ nm, micromagnetic simulations of transverse wall structures do not converge toward a stable solution which suggests that such a wall structure is too energetically expensive to exist in when $w > 400$ nm for 10 nm thick nanowires.

It is suggested that for wire widths between 150 nm and 400 nm both domain wall structures can be supported with the higher energy structure existing as a metastable state. It is further suggested that the large spread in injection fields observed in Figure 7:10 for $w < 400$ nm is due to the injection of different domain wall structures. Consider the MOKE hysteresis loops presented in Figure 7:10 for the 255 nm wide wire. Using the energies extracted from micromagnetic simulations presented in Figure 7:12, the transverse wall structure is higher in energy by approximately 8.3%. It is suggested that the lower

injection fields correspond to the injection of vortex wall structures since these are the energetically favourable state, whilst the higher injection fields correspond to injection of energetically unfavourable transverse wall structures. Since all micromagnetic simulations are performed at zero temperature in wires with perfect edge structures it is not unreasonable, therefore, to propose that the effect of finite temperature, combined with random edge roughness from the lithography process could make an unfavourable wall structure favourable in some field reversal cycles. Further discussion on the effects of the effects of thermal activation energy is presented in section 7.4.

The co-existence of metastable domain wall structures in a nanowire is also highly sensitive to the nanowire thickness. Figure 7:14 presents the total domain wall energy of both transverse and vortex domain wall structures in a 300 nm wide wire for nanowire thicknesses from 3 nm to 15 nm inclusive. As the nanowire thickness increases, the domain wall energy also increases for both transverse (●) and vortex (○) wall structures, although this increase is greater for the transverse walls than for vortex walls. For 300 nm wide, 3 nm thick nanowires, the transverse domain wall is approximately 17% lower in energy than the vortex wall and is thus the energetically favourable state.

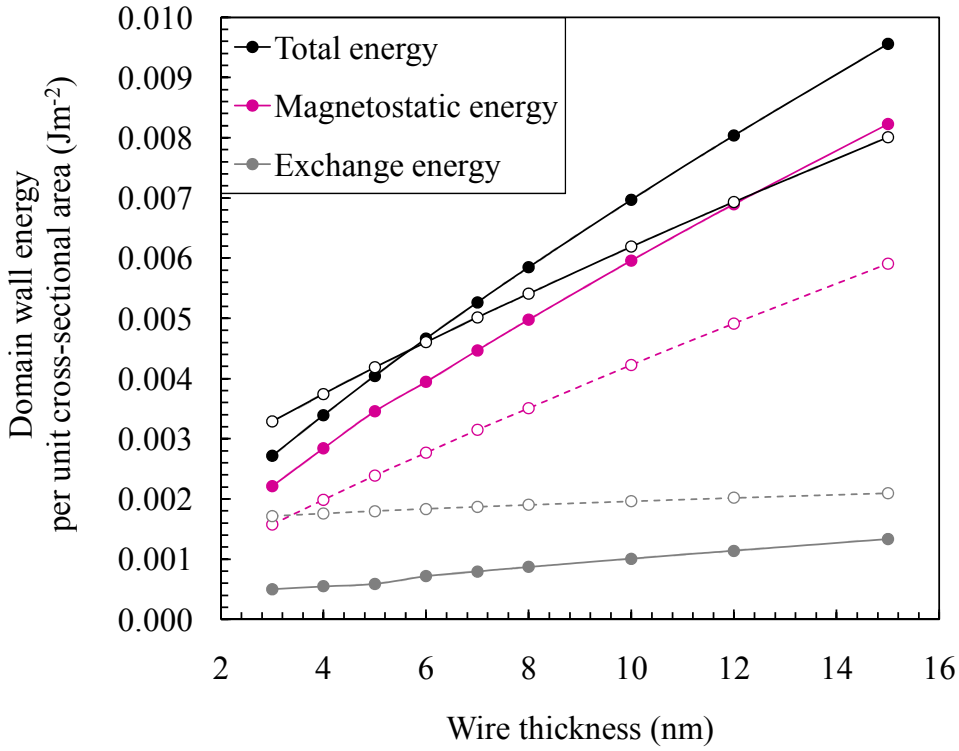

Figure 7:14. Comparison of total domain wall energy for transverse (*solid symbols*) and vortex (*open symbols*) domain wall structures in a 300 nm wide nanowire as a function of film thickness.

As wire thickness increases the difference in energy between wall structures decreases and for 5 nm thick nanowires the vortex wall is only 3% higher energy than a transverse wall. Vortex walls become energetically favourable in 300 nm wide wires for wire thicknesses greater than 7 nm, and as the wire thickness is further increased to 15 nm the transverse wall is approximately 20% more expensive in energy than the corresponding vortex wall. It is therefore expected that both transverse walls and vortex walls can co-exist as metastable states in 300 nm wide nanowire structures less than 10 nm in thickness. Above this thickness, the transverse wall becomes increasingly unfavourable when compared to the energy of the vortex wall structure.

The ability for different wall structures to co-exist as metastable states is largely dictated by the cost in magnetostatic energy associated with the particular wall structure. Although both walls exhibit an increase in the magnetostatic energy as wire thickness increases, Figure 7:14 shows that this increase is much more rapid for transverse walls than for vortex walls. Thus, although the exchange energy associated with the vortex wall structure is larger than that of the transverse wall, this is accepted because of the significant reduction in magnetostatic energy this wall structure offers.

Figure 7:15 compares the total domain wall energy as a function of wire width for nanowire widths between 50 nm and 600 nm and thicknesses from 5 to 15 nm. For a given thickness, the domain wall energy decreases as wire width increases. In general, for narrow wires, the transverse wall structures have a lower energy, and are thus the energetically favourable structure. As wire width increases, the vortex wall structure offers the lower energy state and is thus the more energetically favourable structure. As the nanowire thickness increases the domain wall energy increases for each type of domain wall structure. For each thickness investigated, there is a considerable range of wire widths that can support both transverse walls and vortex walls with only small differences in energy at zero temperature. Thus, at room temperature, it is expected that such structures could co-exist as metastable states. The existence of multiple wall structures in wires of these dimensions is inferred from experimental observations of different magnitudes of the anisotropic magnetoresistance signal [148] and is the basis of the investigations reported in chapter 8.

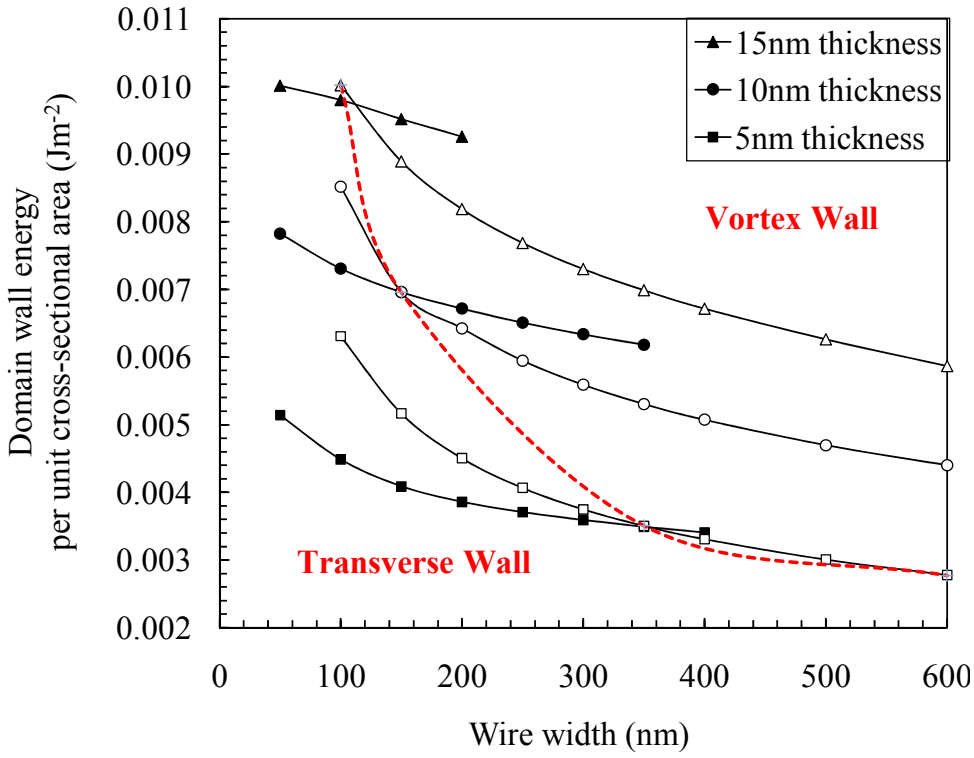

Figure 7:15. Plot of domain wall energy per unit cross-sectional area as a function of nanowire width as deduced by OOMMF micromagnetic simulations. Solid symbols correspond to transverse walls whilst open symbols correspond to vortex walls. There is very good agreement between the energies given from micromagnetic simulations presented here and the Nakatani phase diagram [61].

There is good quantitative agreement between these independent simulations and those of Nakatani *et al.* [61] which adds confidence in using micromagnetic simulations for further analysis of domain wall pinning behaviour in pinning sites and is discussed in the following sections.

7.3 The effect of notch geometry and domain wall structure on domain wall pinning behaviour

When structural features such as notches are patterned within magnetically soft nanowires, the spin structure tends to follow the local edges of these features. As has already been seen, the domain wall structure is sensitive to the cross-sectional dimensions of the nanowire; the addition of a notch locally perturbs the potential energy landscape experienced by a propagation domain wall. A domain wall will pin at a notch if the micromagnetic spin structure of the domain wall is not energetically stable within the reduced dimensions of the notch. If the notch is not deep enough, then it may not perturb

the energy landscape enough to result in the pinning of a domain wall. Depinning of a domain wall can be achieved through application of a spin polarised current or by the application of an applied magnetic field. As previously seen in section 7.2.5, a pinned domain wall can be considered as a quasi-particle trapped in a parabolic potential well, the depth of which is determined by both the wall structure and the wire width. By this analogy, the application of a spin-polarised current depins a domain wall by supplying kinetic energy to the wall, whilst the application of a magnetic field tilts the potential energy landscape to depin a domain wall.

A precise understanding of how the domain wall potential energy landscape is modified by different geometrical variations is currently lacking. As magnetostatic energy is dominant for materials with weak magnetocrystalline anisotropy and negligible magnetostriction it is reasonable to suppose that varying the notch geometry will allow for modification of the domain wall potential energy landscape. Detailed knowledge of the pinning potential created by different notches is a vital step towards understanding the fundamental properties of domain walls, and also towards the optimisation of domain wall pinning behaviour that is required for magnetic memory devices. This section reports on the depinning of domain walls from two notch geometries of comparable size to both each other and to the length scales of a domain wall in 300 nm wide, 10 nm thick nanowire structures.

7.3.1 Description of notch geometries

In order to study the effect of notch geometry on domain wall pinning behaviour, nanowires were fabricated containing single notches of both triangular and rectangular shape as shown in Figure 7:16 (a). All notch structures were located approximately 25 μm from the nucleation pad, so as to allow the MOKE laser spot to measure the magnetisation reversal behaviour of the nanowire before and after the notch, as shown in Figure 7:16 (b). This allowed the effect of the notch on domain wall propagation to be investigated. The dimensions of the notch structures were chosen to be comparable with the extent of the domain wall width using the one dimensional wall parameters as a guide.

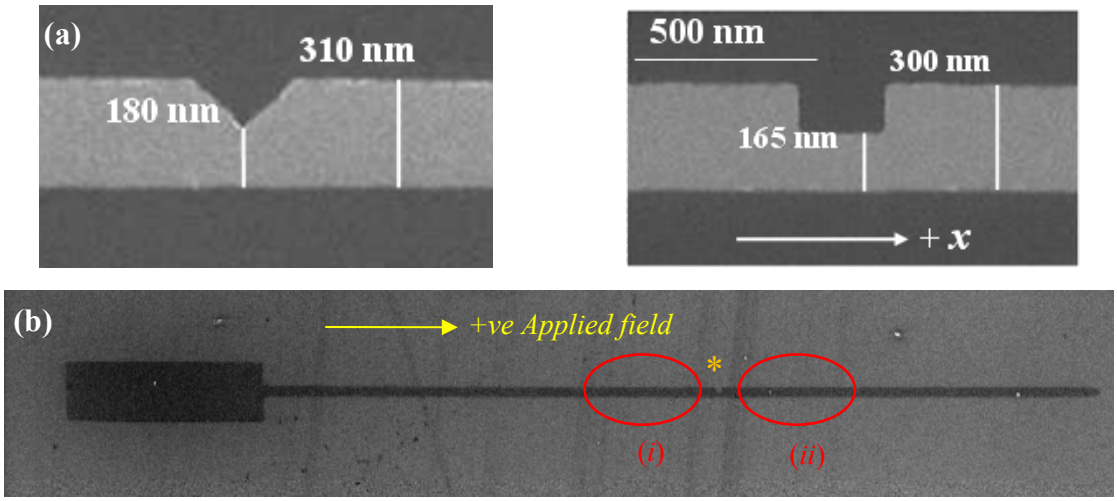

Figure 7:16. (a) Scanning electron microscopy images of a triangular notch structure (*left*) and a rectangular notch (*right*) used to pin domain walls. (b) Schematic to show the location of the laser spot during measurements of domain wall pinning behaviour at notch structures patterned along the length of the nanowire. The nature of domain wall pinning behaviour can be deduced by comparing MOKE hysteresis loops taken at (*i*) and (*ii*).

As previously discussed in section 3.5.5, these are described by:

$$\delta_{DW}^{TW} = \frac{w}{\pi}; \quad \delta_{DW}^{VW} = \frac{3w}{4} \tag{7:2}$$

Where δ_{DW}^{TW} is the width of the transverse wall, δ_{DW}^{VW} is the vortex wall width and w is the wire width. For the 300 nm wide wires investigated here the notch dimensions were all 300 nm long and 150 nm deep; such notch dimensions were used so as to present an abrupt change to the potential energy landscape. In addition, it was expected that a given wall structure would experience different pinning interactions depending on the geometrical structure of the notch due to magnetostatic interactions. It is supposed, therefore, that structural pinning features with different shapes but of comparable size to both each other and to the length scales of a domain wall within a planar nanowire may present different energetic barriers to a propagating domain wall.

7.3.2 Dependence of domain wall depinning field behaviour on notch geometry

Figure 7:17 presents the magnetic field required to depin a domain wall from triangular (▲) and rectangular notches (■) as a function of nanowire width, as measured with the MOKE laser spot in position (*ii*) as shown in Figure 7:16 (b).

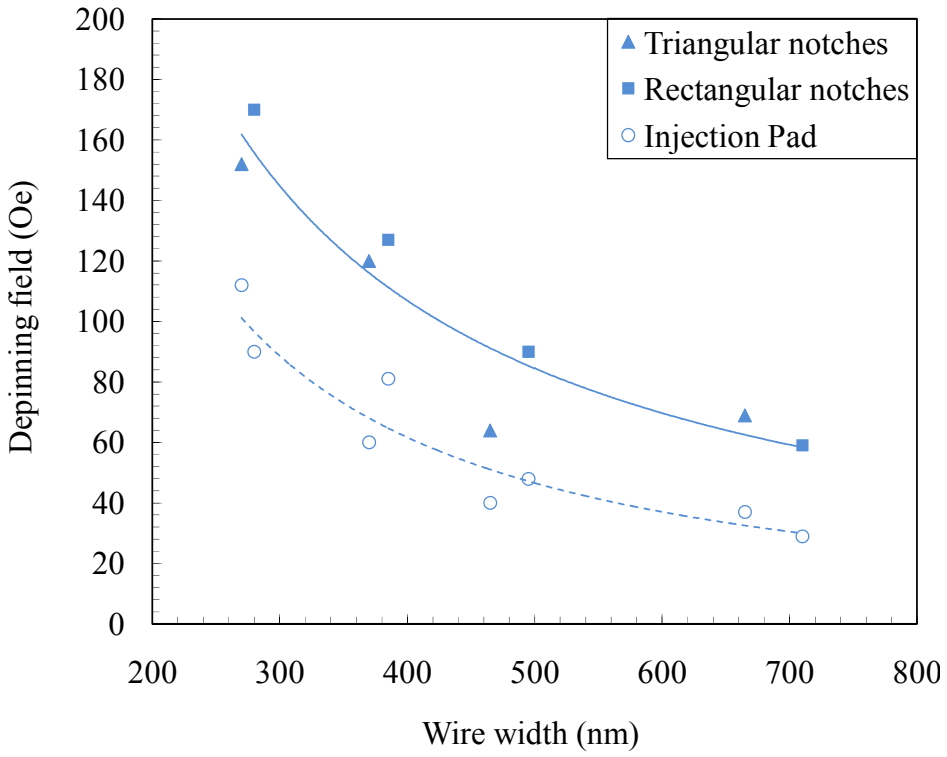

Figure 7:17. Injection field data (○) and notch depinning data as measured from MOKE hysteresis loops for triangular notches (▲) and rectangular notches (■), respectively. All notches have a nominal depth half that of the wire width. Lines are a guide to the eye only.

The measurements presented here are for notch structures with a nominal depth that was half the wire width. The corresponding injection field for each domain wall into the respective nanowire are also shown for comparison (○). As the switching field measured after the notch is larger than that of the injection field this suggests that a propagating domain wall is pinned by each notch structure.

As magnetostatic energy is dominant for materials with weak magnetocrystalline anisotropy and negligible magnetostriction, such as $Ni_{81}Fe_{19}$, it is reasonable to suppose that varying the notch geometry will allow for modification of the domain wall potential energy landscape. As such, it is expected that a given wall structure will experience different pinning interactions depending on the geometrical structure of the notch. However, this is not observed experimentally. It is observed that the specific geometry for single asymmetric notch structures is of secondary importance, and instead it is the wire width that is the dominant factor in determining the depinning field. Indeed, although the data may suggest an influence of shape at narrower wire widths this cannot be distinguished from sample to sample variation, as seen in Figure 7:8.

Figure 7:18 shows normalised MOKE hysteresis loops measured immediately after the notch, with the measured with the MOKE laser spot in position (*ii*) in Figure 7:16 (b). (a) a 385 nm wide wire containing a triangular notch 190 nm deep and also (b) a 390 nm wide wire containing a rectangular notch 220 nm deep. Each hysteresis loop contains two switching steps, which indicate that there are two principle depinning fields from each pinning structure. Domain wall injection into these nanowires occurred at (81 ± 2) Oe and (89 ± 2) Oe respectively, as measured from MOKE hysteresis loops taken at the nucleation pad-wire interface. The first step, H_1, occurs at (95 ± 2) Oe for the triangular notch and (115 ± 2) Oe for the rectangular notch, whilst the second step, H_2, occurs at (130 ± 2) Oe for both the triangular and rectangular notches.

It has been reported that different domain wall structures will experience different pinning interactions with a single triangular notch structure patterned on one side of the nanowire [64, 148, and 152]. This is because the spin configuration through a structurally asymmetric feature will present different energetic barriers to a propagating domain wall depending upon the micromagnetic spin structure and wall chirality of a given wall structure. Chirality is defined as the sense of magnetisation rotation, or the handedness of the magnetisation within the domain wall. For a given wall structure (transverse or vortex), the magnetisation within the wall can rotate in one of two directions, as shown in Figure 7:19.

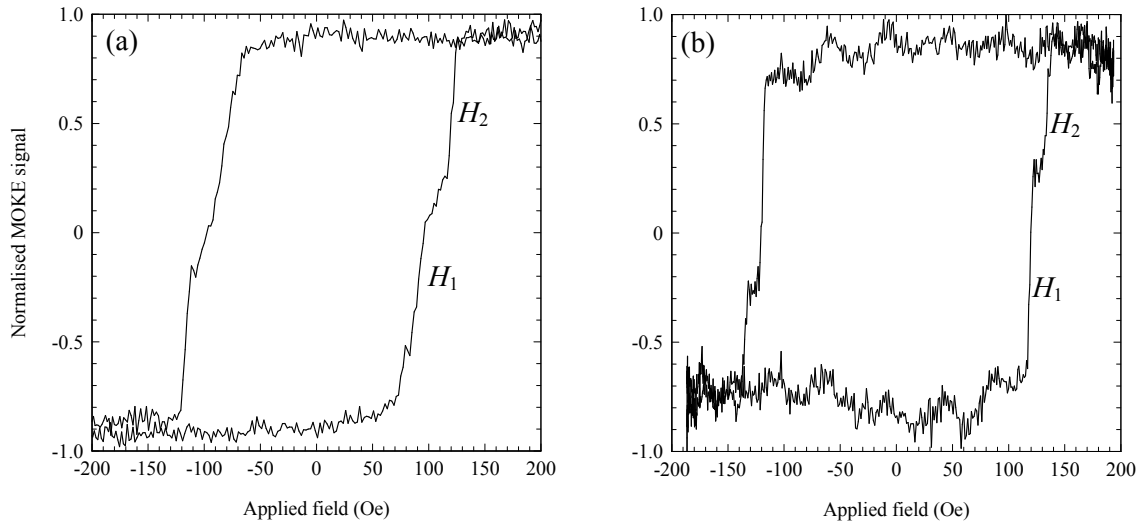

Figure 7:18. Normalised MOKE hysteresis loops illustrating domain wall depinning from (a) a 190 nm deep triangular notch in a 385 nm wide wire and (b) a 220 nm deep rectangular notch in a 390 nm wide wire, respectively.

When a domain wall is injected from a symmetrical pad-wire interface, these two chiralities are energetically degenerate: thus for a particular wall structure, there is an equal probability of it existing in either chirality.

As the spins in the nanowire follow the local edges of a notch structure, an asymmetric notch structure will lift this energetic degeneracy. The importance of the wall chirality in determining the pinning interaction with a notch structure is illustrated schematically in Figure 7:19. This energetic difference manifests itself as a difference in the magnetic field required to push the wall through a structural pinning feature. On the basis of micromagnetic energy considerations presented in section 7.2.5, the energetically favourable domain wall structure in a 300 nm wide, 10 nm thick nanowire is a vortex wall. It is suggested that these steps correspond to pinning interactions of the two vortex wall chiralities (clockwise and counter-clockwise, respectively). The pinning behaviour of each of these two wall structures is considered in turn in the following sections.

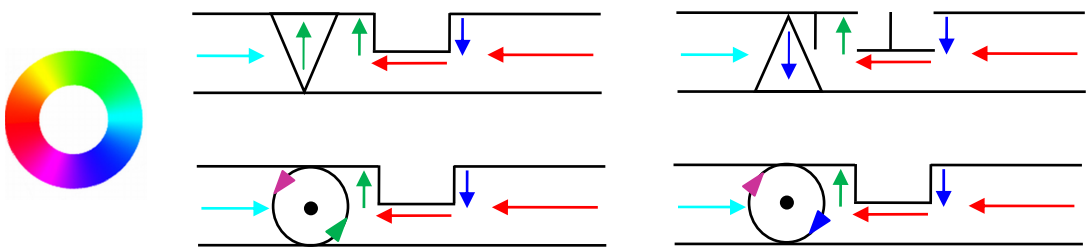

Figure 7:19. Schematic to show how an asymmetric pinning potential such as a rectangular notch patterned along one side of the nanowire, would split the degeneracy of the two wall chiralities of both transverse domain walls and vortex domain walls. The colour is used as a guide to show the direction of magnetisation rotation with the domain wall.

7.3.3 Analysis of vortex wall pinning behaviour of clockwise vortex domain walls using transmission electron microscopy

Figure 7:20 presents images of calculated vector induction distribution colour maps determined using the differential phase contrast (DPC) mode of Lorentz force TEM imaging to investigate the detailed domain wall pinning interactions of clockwise vortex walls with triangular and rectangular notches, respectively. DPC imaging was performed in the University of Glasgow by K. J. O'Shea [153]. A simplified schematic of the spin structure at each stage of the pinning process is also presented to aid interpretation.

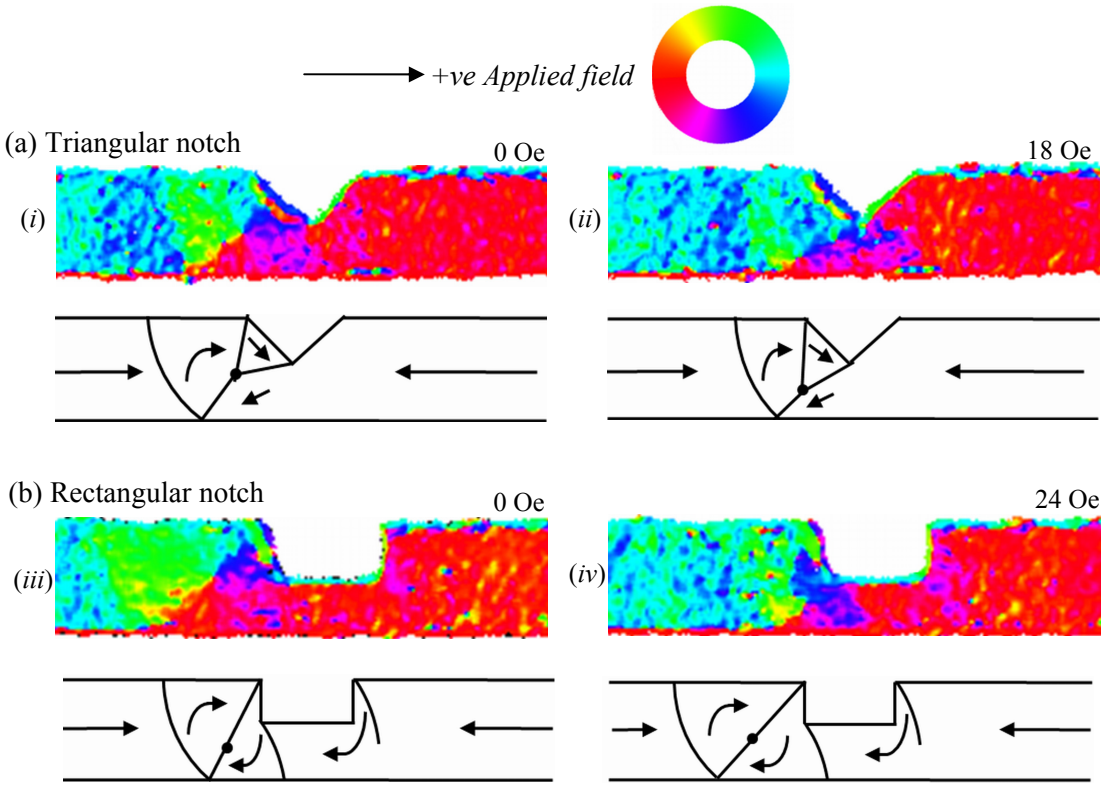

Figure 7:20. Colour induction maps measured using differential phase contrast transmission electron microscopy, comparing the pinning location for a clockwise vortex domain wall pinned in (a) a triangular and (b) a rectangular shaped notch in a 300 nm wide wire. The images on the left show the domain wall pinned at remanence, where the wall it remains pinned and becomes compressed ahead of the notch as the magnetic field is increased to give the images on the right. DPC imaging performed by K. J. O'Shea in the University of Glasgow [153].

In the differential phase contrast imaging, head-to-head domain walls were injected into the nanowires from a nucleation pad at approximately 12 Oe and were subsequently pinned at the notch. The applied field was then removed; the wall images shown in Figure 7:20 (*i*) and (*iii*) illustrate the form of the injected wall at remanence. In both the triangular and rectangular notches, the injected wall is pinned in front of the notch and resembles a vortex wall of clockwise chirality.

Figure 7:20 (a) shows DPC images of a clockwise vortex wall pinned in a triangular notch in a 300 nm wide wire. The geometry of the leading edge of each notch allows the wall to compress to some extent into the notch as the magnetisation in the wire directly below the notch is favorably aligned with the magnetisation in the leading part of the vortex. At remanence, (*i*), the central wall section of the vortex is aligned parallel with the edge of the notch and the leading edge of the wall is pinned at the apex of the triangular notch. As the applied magnetic field is increased along the positive *x* direction,

the vortex core of the wall moves down towards the lower edge of the wire, as shown in (*ii*).

At an applied field of (18 ± 2) Oe the wall depins abruptly. Figure 7:20 (b) shows DPC images of a clockwise vortex wall pinned in a rectangular notch structure. The abrupt edge of the rectangular notch prevents the wall from entering the narrow section of the notch, although the leading edge of the wall can be clearly seen to be pinned on the left hand side of the notch, as seen in (*iii*). As the applied field is increased, the wall remains pinned on the left hand side of the notch although it becomes significantly compressed in width. The geometry of the rectangular notch only allows for modest penetration of the leading edge of the wall into the notch, as shown in (*iv*). The wall was completely depinned from the rectangular notch at an applied field of (24 ± 2) Oe, which may suggest that rectangular notches may pin domain walls to a slightly higher fields than triangular notches.

Vector induction distribution colour maps were also used to investigate the detailed domain wall pinning interactions of counter-clockwise vortex walls with triangular and rectangular notches and are presented in Figure 7:21 (a) and (b). A simplified schematic of the spin structure at each stage of the pinning process is also presented to aid interpretation. The position of the pinned wall at remanence is shown in (*i*) and (*iii*); and it can be seen that both counter-clockwise vortex walls are pinned on the left-hand side of the notch. At remanence, it can be seen that counter-clockwise walls have a larger width than the corresponding clockwise vortex walls pinned in the same notches. Figure 7:21 (a) shows the pinning behaviour of a counter-clockwise vortex wall pinned in a triangular notch. At remanence, (*i*), it can be seen that the central wall section of the counter-clockwise vortex wall is aligned parallel with the edge of the notch as the leading edge of the wall is pinned at the notch apex. When the applied field is increased to 21 Oe, the vortex core is no longer distinguishable and the wall appears transverse-like. As the applied field is increased further, the central wall section moves closer to the edge of the notch, although the wall does not extend beyond the apex of the notch. A field of (31 ± 2) Oe is required to depin the counter-clockwise vortex from the triangular notch. The pinning behaviour of a counter-clockwise vortex wall in a rectangular notch is presented in Figure 7:21 (b).

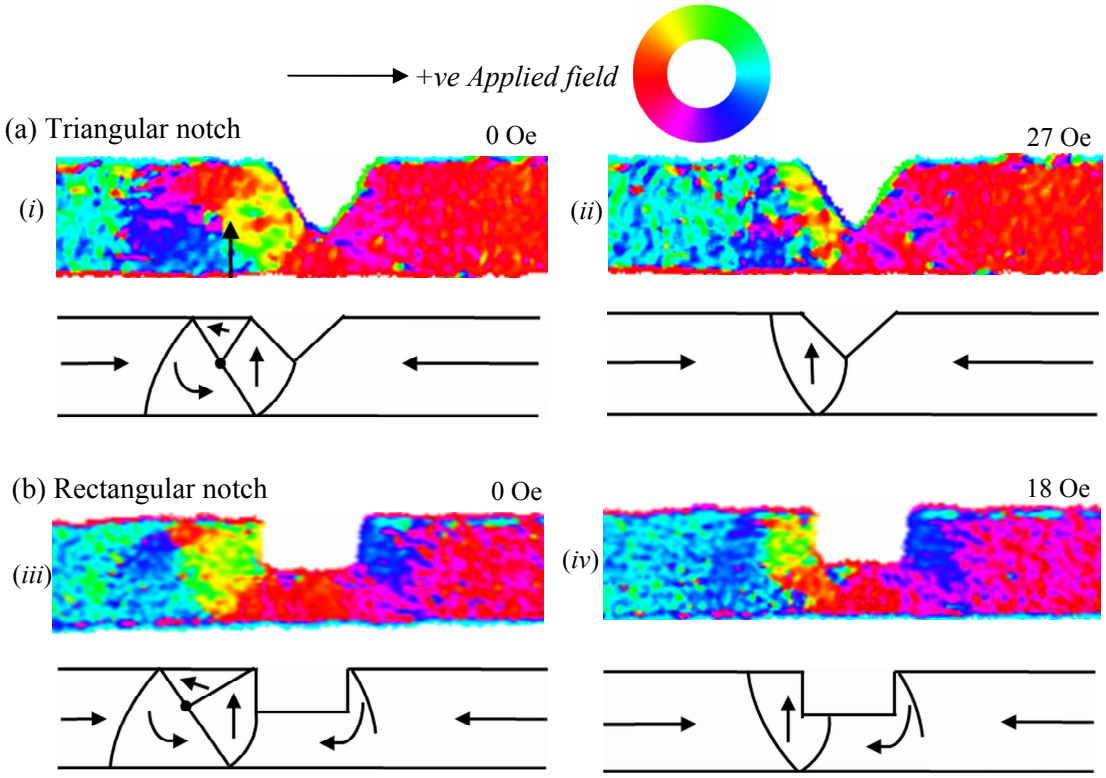

Figure 7:21. Colour induction maps measured using differential phase contrast transmission electron microscopy, comparing the pinning location for a counter-clockwise vortex domain wall pinned in (a) a triangular and (b) a rectangular shaped notch in a 300 nm wide wire. The images on the left show the domain wall pinned at remanence, where the wall remains pinned. As the magnetic field is increased it becomes compressed ahead of the notch to give the images on the right. DPC imaging performed by K. J. O'Shea in the University of Glasgow [153].

The abrupt edge of the rectangular notch prevents the wall from entering the pinning site, and the leading edge of the wall is pinned on the left hand side of the notch. At an applied field of 18 Oe, the wall compresses in width whilst simultaneously forcing the vortex core out of the wire until the wall appears transverse-like. The counter-clockwise vortex wall is depinned from the rectangular notch at an applied field of (22 ± 2) Oe.

The detailed DPC imaging suggests that both vortex wall chiralities display different pinning behaviour; although for a given domain wall chirality the behaviour in each pinning site is very similar. It is therefore suggested that the depinning events labelled H_1 and H_2 in Figure 7:18 correspond to depinning events of specific wall chirality, although further analysis is required to identify which depinning event corresponds to which wall structure.

7.3.4 Analysis of domain wall pinning behaviour at notch structures using micromagnetic simulations

Micromagnetic simulations were used to provide further insight into the pinning behaviour of clockwise and counter-clockwise vortex walls pinned in triangular and rectangular notch structures. Figure 7:22 presents images of clockwise vortex walls in triangular and rectangular notches calculated from OOMMF micromagnetic simulations. All of the simulations used the initial static wall structures as described for the data in Figure 7:15, with an applied field of 6 Oe that was used to propagate the domain wall toward the notch.

When the wall was located at the entrance of the notch, the magnetic field was reduced to zero to replicate the pinning behaviour observed at remanence in the same manner as the TEM imaging presented in Figure 7:20 and Figure 7:21. Following this, the magnetic field was then increased in steps of 2 Oe in the positive *x* direction until the wall was completely depinned from the notch. The images shown in Figure 7:22 (*i*) and (*iii*) correspond to the domain wall pinned in the notch at remanence whilst images (*ii*) and (*iv*) correspond to images of the pinned domain wall as it moves further into the notch on the application of an increased magnetic field. For the wall pinned in the triangular notch, the leading edge of the vortex is seen to 'anchor' itself to the apex of the triangular notch, with the core of the vortex approximately level with the depth of the notch. As the applied magnetic field increases further in (*ii*) the leading edge of the wall remains pinned in a similar location as shown in (*i*), although the wall width has narrowed appreciably. Furthermore, the vortex core has moved slightly further down toward the bottom edge of the nanowire. The wall completely depins at an applied magnetic field of 84 Oe, and retains both its structure and chirality as it moves through and out of the notch.

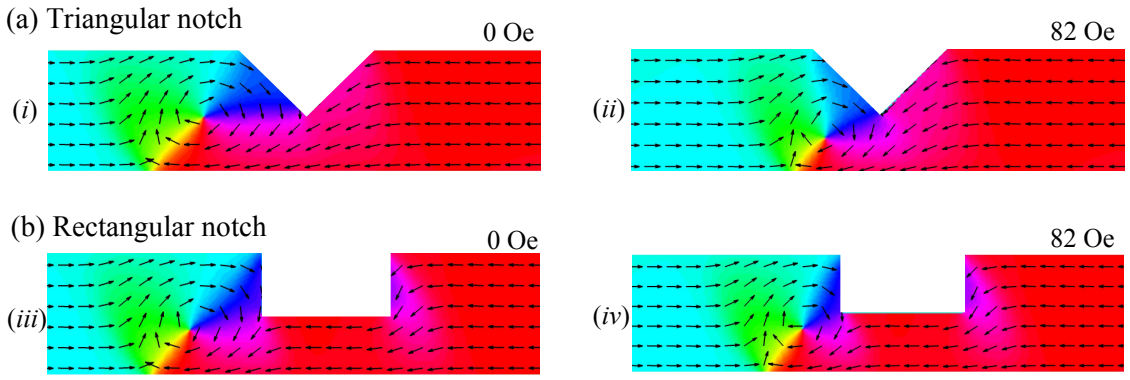

Figure 7:22. Micromagnetic simulations illustrating the pinning behaviour of clockwise vortex domain walls in (a) a triangular notch structure and (b) a rectangular notch structure below the depinning field at remanence (*left*) and just below the depinning field (*right*).

For the wall pinned in the rectangular notch, it can be seen that the leading edge of the vortex wall 'anchors' itself to the front of the rectangular notch. As the applied magnetic field increases further to (*iv*), the wall remains pinned in the same location and, as seen for pinning in the triangular notch, the wall width decreases significantly. In addition, the vortex core moves slightly further down toward the bottom edge of the nanowire. The clockwise vortex wall completely depins from the rectangular notch at an applied magnetic field of 84 Oe. Again, the wall retains its structure and chirality as it moves through and out of the pinning site.

Figure 7:23 presents OOMMF micromagnetic images of counter-clockwise vortex walls pinned in triangular and rectangular notches, and closely reproduce what is experimentally observed in Figure 7:21. As observed for the clockwise wall, this wall structure is also pinned at the left hand side of each notch structure although the domain wall is more asymmetric than the clockwise vortex wall at remanence. Indeed, the pinning behaviour of a clockwise vortex wall is noticeably different from that of the counter-clockwise wall, and, at remanence (shown in Figure 7:23(*i*) and (*iii*)) the wall is pinned at a location slightly further into the notch. This is because the spins in the wire that follow the notch geometry are parallel to the spins in the leading edge of the wall. In the case of the wall in the triangular notch, the vortex core of the wall is pushed from the middle of the wire and sits close to the top edge of the wire. Moreover, the domain wall appears quite asymmetric in character which is expected due to the local geometry of the spins in and around the notch. As the applied field is increased further in the positive *x* direction, the core of the counter-clockwise vortex wall is expelled out of the wire resulting in the transformation of the wall to a transverse wall.

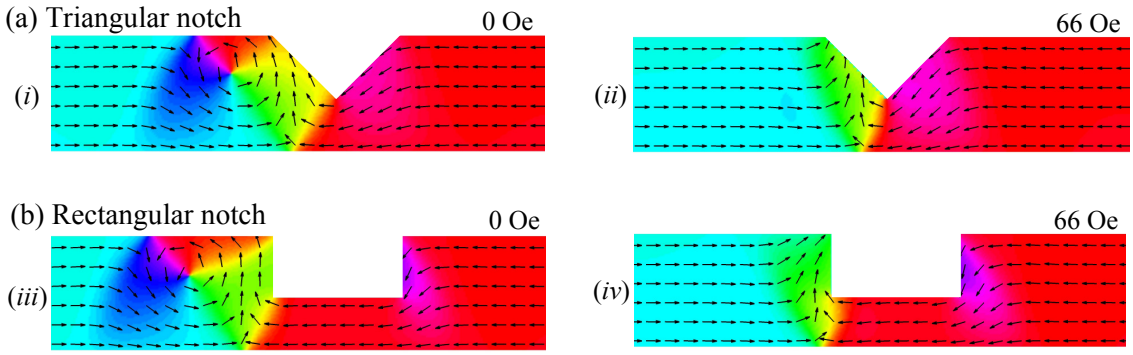

Figure 7:23. Micromagnetic simulations illustrating the pinning behaviour of counter-clockwise vortex domain walls in (a) a triangular notch structure and (b) a rectangular notch structure below the depinning field at remanence (*left*) and just below the depinning field (*right*).

This allows the wall to move further into the notch, and is in very good agreement with the DPC observations presented earlier. The pinning behaviour of the counter-clockwise vortex wall pinned in the rectangular notch is remarkably similar to that for the same wall structure pinning in the triangular counterpart, although it can be seen that the wall does not enter into the narrowest part of the notch due to the local spin geometry. The counter-clockwise wall structure is strongly pinned in both the triangular and rectangular notches, and is depinned at an applied magnetic field of 168 Oe and 170 Oe, respectively. Micromagnetic simulations show that the transformation to a transverse wall occurs at very similar fields for the counter-clockwise vortex in both pinning structures.

The pinning behaviour of clockwise and counter-clockwise vortex walls in triangular and rectangular notches observed by DPC imaging presented earlier in Figure 7:20 and Figure 7:21 are in good qualitative agreement with micromagnetic simulations presented here. It is thus suggested that the depinning events labelled H_1 in Figure 7:18 correspond to the depinning of clockwise vortex domain wall, whilst the depinning events labelled H_2 correspond to the depinning of counter-clockwise vortex domain wall.

The field values given by the DPC imaging are consistently smaller by a factor of ~ 5 than field values given by both the micromagnetic simulations and the MOKE measurements. The reason for this discrepancy is not clear, but it may be attributed to several factors. Such discrepancies may be related to material issues within the sample fabricated for the DPC imaging, or some perhaps unresolved discrepancy in the field calibration. In addition, it is possible that the heating of the silicon nitride membrane by the electron beam in the DPC imaging may have reduced the depinning fields of the domain walls. Further, all simulations were performed at zero temperature, and it is well known that the magnitude of the depinning field decreases as the temperature increase due to stochastic effects [154]. It is suggested the depinning fields measured in the MOKE may be influenced by thermal activation at room temperature in the measurements and/or perhaps by lithographic imperfections of the geometry of the real pinning structures. The field values measured in the DPC imaging are presented here for completeness.

7.3.5 Domain wall pinning potential landscapes

There is very good qualitative agreement between the micromagnetic simulations and the TEM observations, as well as the good quantitative agreement between field values obtained from micromagnetics and MOKE data. Indeed, this gives confidence to the

performance of further sophisticated analysis of micromagnetic simulations to provide details of the domain wall depinning energetics at these pinning site structures. The domain wall energy density, U_{DW}, is given by:

$$U_{DW} = \frac{E_{DW}}{V_{DW}} \tag{7:3}$$

Where E_{DW} is the total domain wall energy, defined in (7:1) and V_{DW} is the volume of the domain wall, which is given by δ_{DW} *w.t.* The energy density of the DW at each position is defined via:

$$U_{DW} = (U_{DW}^{Total} - U_{DW}^{Zeeman}) - (U_{No\ DW}^{Total} - U_{No\ DW}^{Zeeman}) \tag{7:4}$$

This is done to remove the Zeeman (field) energy and also to account for any energy associated with spin structure localised to the notch in the absence of a domain wall and also due to end effects.

Figure 7:24 presents pinning potential energy density landscapes derived from the micromagnetic simulations of clockwise vortex walls shown in Figure 7:22. In this figure, the domain wall energy per unit volume is presented as a function of distance from the geometrical centre of the notch, and accounts for changes in the domain wall energy as a result of compression in and around the notch. The domain wall position is defined as the distance of the vortex core to the centre of the pinning site structure. The constituent magnetostatic energy (*purple data points*) and exchange energy (*grey data points*) for each domain wall pinning interaction are also shown. It can be seen that the overall pinning behaviour of a clockwise vortex wall structure is largely determined by the magnetostatic energy. The domain wall is initially repelled from each notch structure, as seen by the small local potential barrier at approximately x = -400 nm. Using the images presented in Figure 7:25 (*i*) to (*iii*), it can be seen that this repulsion is due to the orientation of the spins in the leading edge of the wall and around the left hand side of the notch, which are approximately 180° out of phase from one another.

As a result of the large angles between adjacent spins in the leading part of wall and those in the wire around the entrance of the notch, the exchange energy is observed to increase. In addition, the wall becomes narrower in width and the core of the vortex wall is pushed toward the bottom edge of the nanowire. As a result, there is a corresponding increase in magnetostatic energy.

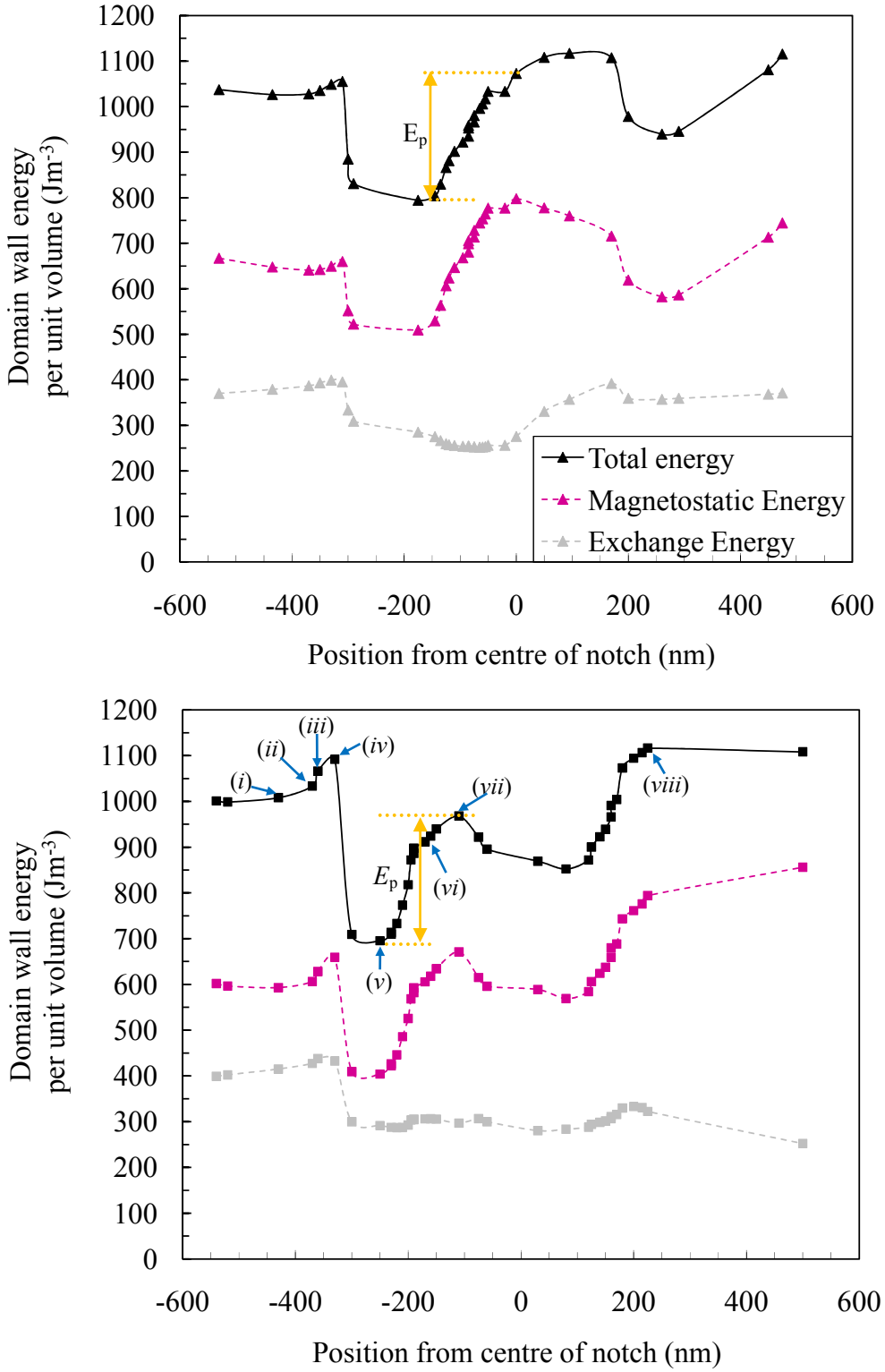

Figure 7:24. Total domain wall energy (*black data points*) as a function of position for clockwise vortex walls pinned in (a) a triangular notch (▲) and (b) a rectangular notch (■). The constituent magnetostatic energy (*purple data points*) and exchange energy (*grey data points*) of the domain wall are also shown. Images of the wall pinned in a rectangular notch at locations (*i*) to (*viii*) are shown in Figure 7:25.

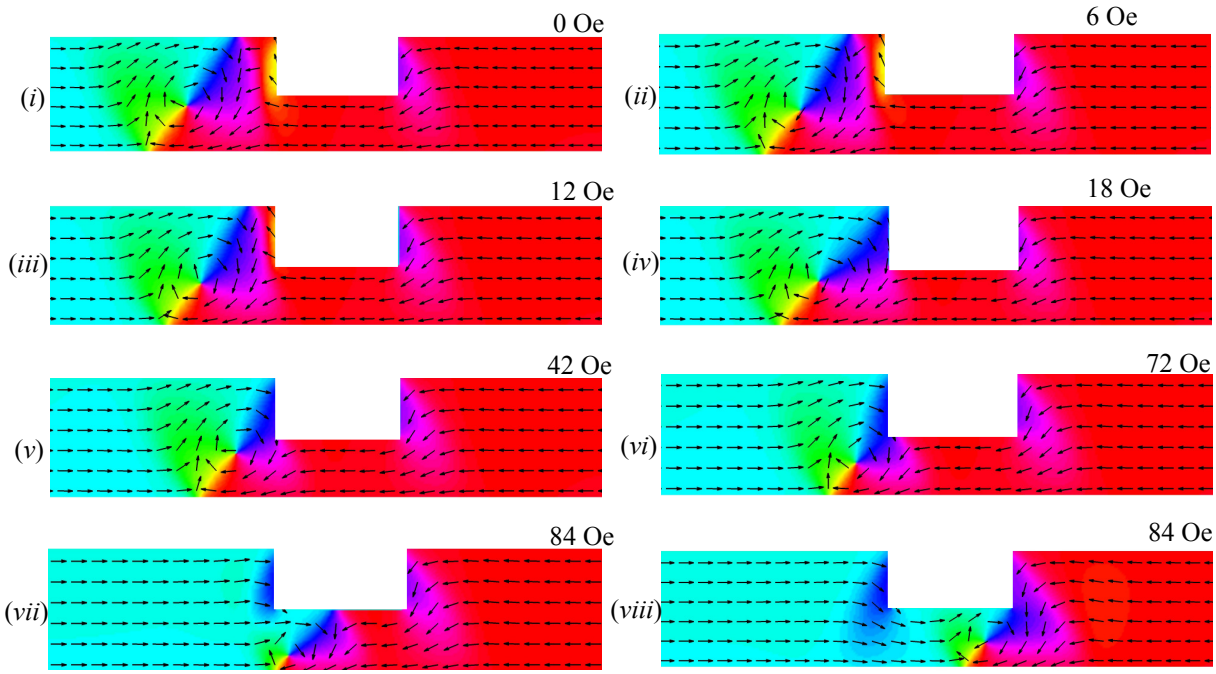

Figure 7:25. Micromagnetic simulation images to show the detailed pinning behaviour of a clockwise vortex wall in and around a rectangular notch structure. The corresponding energetics at locations (*i*) to (*viii*) are indicated in Figure 7:24 (b).

As the applied field is increased, the wall obtains enough energy to overcome this repulsion each notch then presents an attractive potential well to the domain wall. At point (*iv*), the wall 'anchors' itself to the leading edge of the notch. Energetically, this yields a large decrease in magnetostatic energy associated with such a pinning location as both the spins in the wall and around the notch rotate in the same direction. Due to flux closure considerations of the stray field from the wall, this is a very stable pinning location for a clockwise vortex wall. As the wall moves from position (*iii*) to (*iv*) there is a reduction in the angle between the spins within the wire following the notch and in the leading edge of the wall, which causes a reduction in the wall width and which yields a corresponding decrease in exchange energy. Thus, for a clockwise vortex wall in each notch structure, the wall becomes pinned in a potential well at the leading edge of the notch.

For the rectangular notch, the centre of this potential well is located approximately 200 nm from the geometrical centre of the notch. As the magnetic field is increased further, the wall remains pinned at the leading edge but the spin structure of the wall becomes very compressed. The clockwise vortex wall is depinned from each notch at a magnetic field of 84 Oe; the second dip observed in each pinning potential is simply due to

the spins within the domain wall re-arranging as it moves through and beyond the narrow part of the notch.

The depth of the well, E_p, is defined as the energy that the wall must acquire in order to completely depin from the notch. This is calculated by multiplying the energy density, $U_{DW,}$ by the volume of the wall (δ_{DW} .*w*.*t*) when it is at the bottom of the potential well, i.e. the final stable location before the wall depins from the notch. The potential well depth, E_p, is deduced to be 1.46 eV and 1.79 eV for a clockwise vortex wall pinned in a triangular and rectangular notch, respectively.

Figure 7:26 presents the equivalent domain wall pinning potential landscapes for counter-clockwise vortex walls. The constituent magnetostatic energy (*purple data points*) and exchange energy (*grey data points*) of the wall are also shown and in this case both energies are significant to the pinning behaviour. Detailed images from micromagnetic simulations of the pinning behaviour of a counter-clockwise vortex wall pinned in a rectangular notch are provided in Figure 7:27.

Each domain wall is initially attracted to each notch structure, as seen by the small potential well located between x = - 400 nm and x = -200 nm. Energetically, this is due to the parallel alignment of the spins in the leading edge of the wall and on the left hand side of the notch, as shown in Figure 7:27 (*i*) and (*ii*). Although the simulations show that the wall width increases in the initial pinning interaction, energetically this causes a large reduction in the magnetostatic energy. As the applied field increases, the wall falls into a local energy minimum and the wall becomes pinned at the leading edge of the notch since this causes a further considerable reduction in the magnetostatic energy, as can be seen in Figure 7:27 (*iii*) and (*iv*). The spin structure of the wall in (*iii*) and (*iv*) closely follows that of the spins around the edge of the notch and such a configuration results in large reduction in magnetostatic energy.

Further reduction in magnetostatic energy is achieved by forcing the wall to transform to a transverse wall, as indicated by the asterisk and shown in Figure 7:27 (*v)*. When this occurs, the apex of the transverse wall is used to define the central position of the wall. Further increase of the applied field, however, does not yield a further reduction in magnetostatic energy. Beyond the initial attraction, each notch presents a large potential barrier in which both exchange and magnetostatic energies make significant contributions in determining the depinning interaction of the wall with the notch.

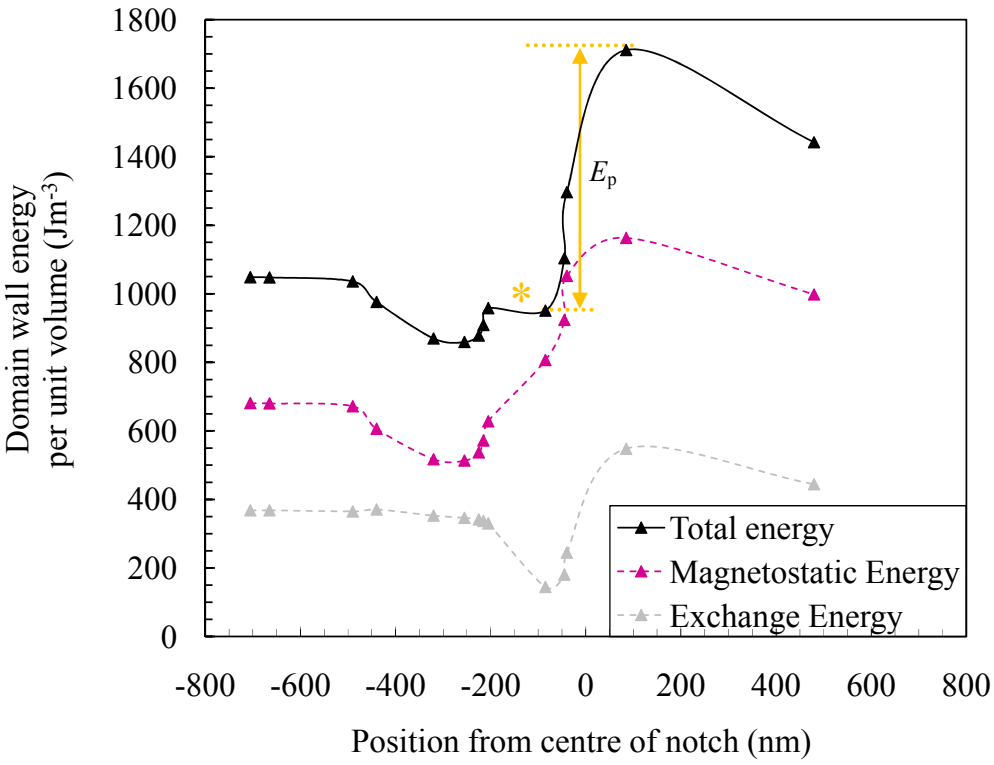

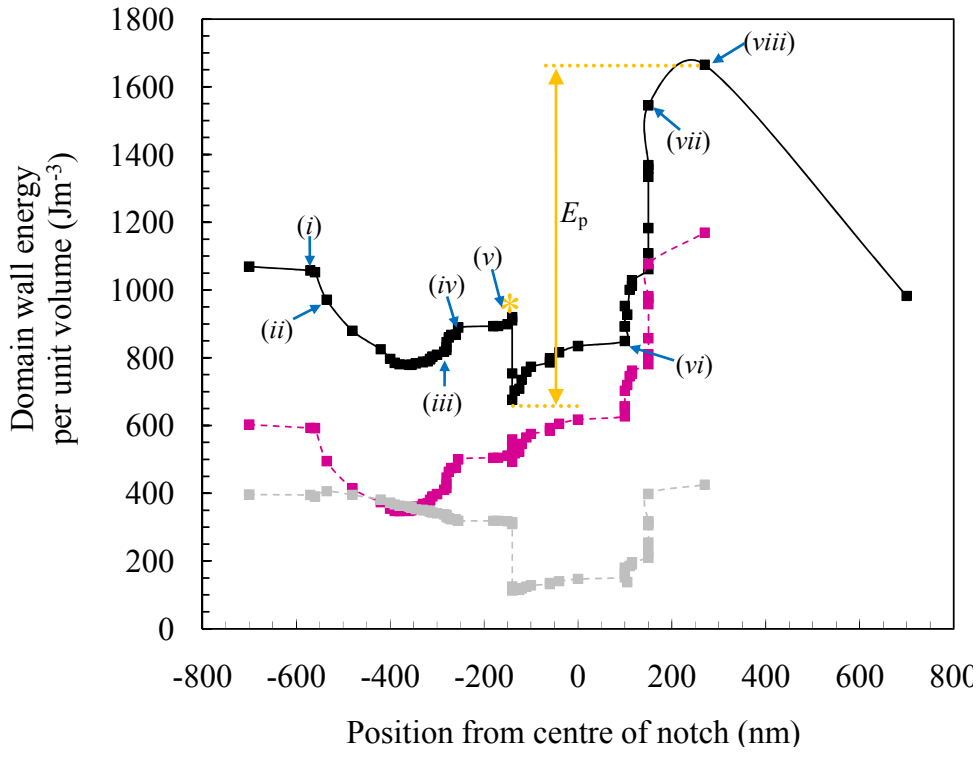

Figure 7:26. Domain wall energy as a function of position for counter-clockwise vortex walls pinned in (a) a triangular notch and (b) a rectangular notch. The constituent magnetostatic energy (*purple data points*) and exchange energy (*grey data points*) of the domain wall are also shown. Images of the wall at locations (*i*) to (*viii*) are shown in Figure 7:27. The asterisk corresponds to a transformation of the wall structure from a vortex wall to a transverse wall of up chirality.

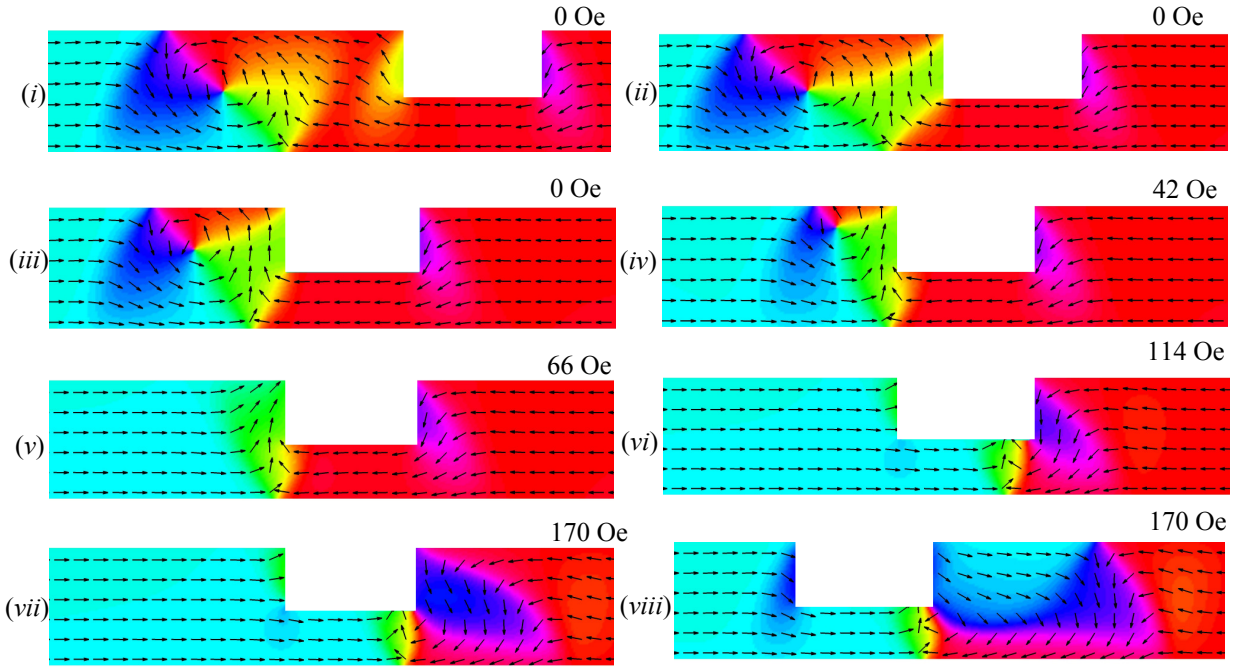

Figure 7:27. Micromagnetic simulation images to show the detailed pinning behaviour of a counter-clockwise vortex wall in and around a rectangular notch structure. The corresponding energetics at locations (*i*) to (*viii*) are indicated in Figure 7:26 (b).

The centre of this pinning potential is located approximately in the physical centre of the notch, and the wall is depinned from each notch structures at an applied magnetic field of 168 Oe and 170 Oe, respectively. The energy barrier, E_p, that counter-clockwise domain walls must overcome in order to completely depin from the notch is deduced as 2.30 eV and 2.63 eV for the triangular and rectangular notches respectively. This large potential barrier is mainly due to the fact that the spins within the wall are orientated antiparallel to those on the far side of the notch; thus there is a large exchange energy associated with this.

It can be seen that pinning potential profiles are primarily determined by the micromagnetic structure of the domain wall, with the specific geometry of the notch of secondary importance to the potential energy landscape. Both Figure 7:24 and Figure 7:26 show that the pinning potential experienced by each chirality of vortex wall as it propagates towards and depins from each notch structure is very similar, although the two wall chiralities experience very different landscapes to each other when pinned in the same notch geometry. Both triangular and rectangular notches may thus act as either a potential well or a potential barrier, with the exact nature of the pinning barrier determined by the micromagnetic spin structure of the propagating domain wall.

7.3.6 Quantification of pinning site stability

All magnetic data storage systems can be modelled to some extend by two magnetic potential wells separated by an energy barrier. The process of writing a data bit corresponds to forcing the system to occupy one of the potential wells. Domain wall based magnetic memory concept devices require the controlled pinning and depinning of domain walls at notches. An essential requirement for useful data storage is that thermally activated hopping from one well to another must be improbable over very long periods of time, as such hopping results in a loss of data. An acceptably long data lifetime is usually nominally taken as 10 years [155]. Thorough knowledge of the pinning potential profiles experienced by pinned domain walls, therefore, allows for the quantification of the pinning stability.

In the absence of an applied field or current, the probability for a domain wall to depin from a notch is known to depend upon the temperature [154, 156]. The probability of a domain wall hopping from one magnetic potential well to the other, τ_p, over a separating energy barrier, E_p, is described by the Arrhenius-Néel equation:

$$\tau_p = \frac{1}{\tau_0}\exp\left(\frac{E_p}{k_B T}\right) \tag{7:5}$$

Where T is the temperature of the system, k_B is the Boltzmann constant, τ_0 is a semi-phenomenological constant related to the gyromagnetic pression and is usually of the order of 10^{-10} s and E_p is the energy required to completely depin the wall from the notch (at the final stable pinning location). Values of E_p have been obtained from the domain wall pinning potential landscapes presented in Figure 7:24 and Figure 7:26 and are summarised in Table 7:1. Simple analysis of this equation shows that the stability criterion for an acceptably long data lifetime is deduced using:

$$E_p \geq 50 k_B T \tag{7:6}$$

In order to deduce a value for device stability, a temperature of 340 K was used so as to take any device heating into account. Stability values for clockwise and counter-clockwise vortex walls pinned in triangular and rectangular notches are provided in Table 7:2. All values presented in Table 7:2 are within this range, which suggests that such notch structures would be suitable in memory applications. It is worthwhile stating that only forward depinning of the domain wall has been considered here; for device applications the backward depinning of the wall (i.e., where it is depinned in a direction toward the

nucleation pad) must also be considered although this is beyond the scope of the investigation presented here.

Wall chirality	Notch structure	E_p (eV)
Clockwise vortex wall	Triangular	1.46
	Rectangular	1.79
Counter-clockwise vortex wall	Triangular	2.30
	Rectangular	2.63

Table 7:1. Comparison of energies required to completely depin a domain wall from triangular and rectangular notch structures as measured from OOMMF micromagnetic simulations presented in Figure 7:24 and Figure 7:26.

Wall chirality	Notch structure	Stability
Clockwise vortex wall	Triangular	49.83
	Rectangular	61.09
Counter-clockwise vortex wall	Triangular	78.51
	Rectangular	89.76

Table 7:2. Comparison of stability of pinned domain walls in triangular and rectangular notch deduced using equation (7:6) at 340 K.

7.3.7 Determination of pinning site saturation

Thus far, the discussion has focussed upon the pinning behaviour of domain walls in notch depths nominally half that of the wire width. The effect of an increasing notch depth on the magnitude of domain wall depinning field is presented Figure 7:28.

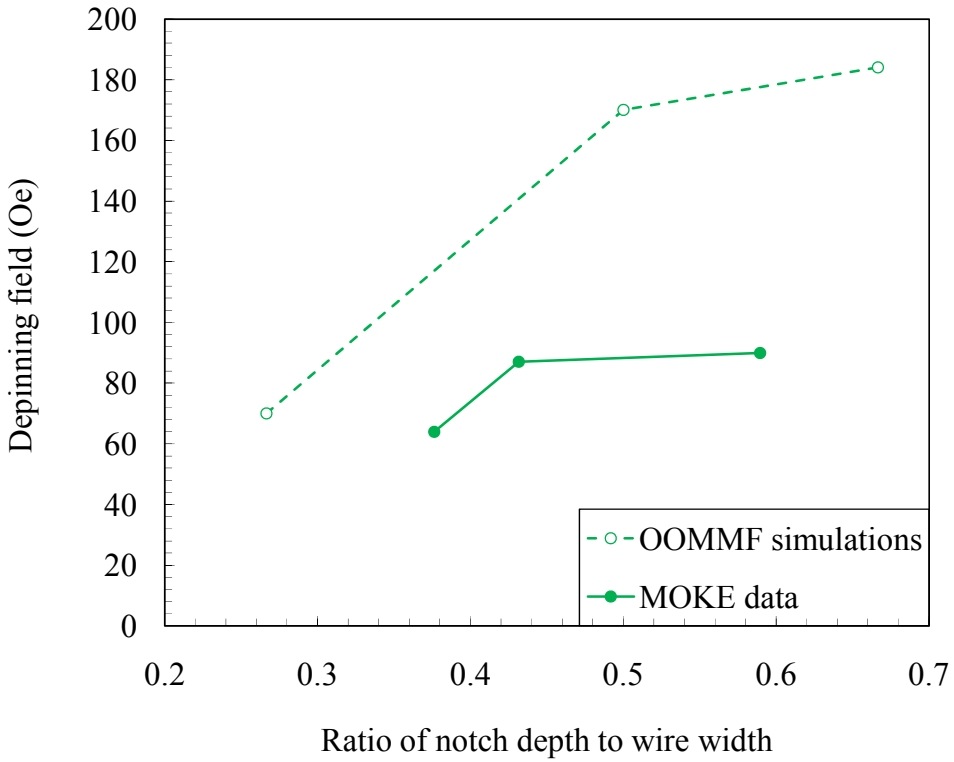

Figure 7:28. Domain wall depinning fields as a function of triangular notch depth as deduced from OOMMF micromagnetic simulations for a 300 nm wide wire, and for a 480 nm wide nanowire as measured from MOKE hysteresis loops.

In this figure, the magnitude of depinning fields from triangular notches of increasing depth in a 480 nm wide nanowire as measured by MOKE hysteresis loops, and a 300 nm wide nanowire wire as determined from micromagnetic simulations are compared. It can be seen that there is a strong dependence of the depinning field on the notch depth. When the notch depth increases from a notch depth 25% wire width, to 50% wire width both data plots show an initial increase in depinning field, which is in good agreement with data presented in [157, 158]. Both sets of data approach a plateau in the magnitude of depinning field, which suggests there is a limit to how much the pinning strength of a single notch structure can be increased by simply increasing its physical depth into the wire. For notches deeper than approximately 60% wire width, further increase in the notch depth does not yield a significantly deeper potential well.

Micromagnetic simulations suggest that for notch depths greater than 60% of the wire width the domain wall is strongly pinned by the notch. As the magnetic field increases there is enough energy associated with this applied field to reverse the remainder of the wire without actually depinning the original wall from the notch. Domain wall propagation along the remainder of the nanowire actually occurs by nucleation of a second

domain wall, a transverse wall of down chirality, from the right hand side of the notch. Examples of this behaviour can be seen in Figure 7:27 (*vii*) and (*viii*), and is also demonstrated for counter-clockwise walls pinned in notches of this depth. For notches of this depth (75% of the wire width), the domain wall chirality becomes less important, as both structures are strongly pinned in both triangular and rectangular notch geometries.

The results presented in Figure 7:17 suggest that the precise geometry of the notch structure is relatively unimportant; whilst Figure 7:28 suggests that increasing the notch depth does not necessarily yield a significantly greater pinning potential for the wall and can instead lead to further wall nucleation at the notch rather than the original wall simply depinning in its original format. Such results are important in optimisation of the design of notch structure for device applications that are based upon reliable and reproducible domain wall pinning interactions.

7.4 The effect of temperature and thermal activation on domain wall pinning behaviour predicted by micromagnetic simulations

Micromagnetic simulations have been used extensively within this chapter to provide insight into the relationship between domain wall energy and its sophisticated internal micromagnetic structure. In addition, micromagnetic modelling has provided important information on spin structure and pinning behaviour of domain walls in notch structures with a level of detail that cannot currently be accessed by experimental techniques due to limitations in both spatial and temporal resolution.

It is important to recognise that, as with other phenomenological approaches, micromagnetic modelling has significant limitations in terms of the physical phenomena that are included in the description of the modelled system. These limitations, such as limits on the structural definition imposed by the cellular basis of model, practical limitations imposed by the need for realisable computation times due to cell size and low spin damping and, importantly here, the use of zero temperature simulations, need to recognised. Nonetheless it is generally recognised that simplified models can give significant physical insight. Zero temperature micromagnetic simulations have been shown in many cases to reproduce domain structures observed experimentally ([146, 147, 148, 152 and 165]). By definition, such modelling of the magnetisation switching behaviour using zero temperature simulations does not incorporate the effect of thermal excitations and it is recognised that this is a limitation. However, the models provide

limiting case results (limited by all of the model assumptions, including temperature). Here modelling has been used for the comparison of spin structures in magnetic structures with different geometry and this work should be considered with these limitations in mind. Further developments of micromagnetic simulations to include spin torque terms and thermal fluctuation have been developed but it is not clear that such implementations provide physically robust representations of the real physics.

As previously discussed in section 4.5, micromagnetic calculations seek to find the lowest total energy of the system without making any initial assumptions as to what this distribution may be. To do this, the Landau-Lifshitz equation is solved for a given effective field that includes both an applied field as well as the ferromagnetic energy terms provided in Table 3:1. It is important to realise, however, that the magnetisation distributions provided by micromagnetic simulations are only fully valid for a perfect structure (with no defects such grain boundaries and crystal faults present within the material or any edge roughness) and at $T = 0$ K. In real structures, however, the magnetisation distributions - and therefore the structure and pinning behaviour of domain walls - are affected by both defects within the $Ni_{81}Fe_{19}$ alloy and the presence of edge roughness of the nanowires due to the lithography process. In addition, the presence of finite temperature will also provide the spin magnetic moments with thermal activation energy $k_B T$ which is equivalent to 26 meV for $T = 300$ K. Thus, micromagnetic simulations have been employed within this thesis to provide qualitative insight into the structure and pinning behaviour of domain walls in the first instance.

The pinning behaviour of domain walls in 150 nm deep notches (50% wire width in 300 nm wide, 10 nm thick nanowires) observed by DPC imaging showed that the pinning behaviour was reproducible in different nanowires of the same nominal dimensions despite variations in the sample-to-sample lithography. Furthermore, a strong qualitative agreement between both the domain wall spin structure and the domain wall behaviour was given by the zero temperature micromagnetic simulations and experimental observations of domain wall pinning by DPC imaging performed at finite temperature has been observed. Micromagnetic simulations have allowed for a detailed analysis of the energy barrier presented by the notch depths investigated suggest that the perturbations to the energy density landscape presented are significantly higher than the thermal energy $k_B T$ at room temperature. In contrast, DPC imaging of the domain wall pinning behaviour in 75 nm deep notches (25% wire width) was not reproducible with the domain wall

pinning at different locations within the notch and depinning at different fields on successive field reversal cycles of the same nanowire structure. Analysis of the energy barrier presented by shallower notches to a domain wall show that the perturbations to the energy density landscape presented are comparable to the thermal activation energy at room temperature. The variations in pinning behaviour observed experimentally cannot be reproduced with micromagnetic simulations, whilst the depinning field predicted by micromagnetic simulations is expected to decrease with an increase of temperature [154, 156] due to the effects of thermal activation.

7.5 Chapter conclusion

A combination of MOKE magnetometry, differential phase contrast Lorentz force transmission electron microscopy and OOMMF micromagnetic simulations has allowed for a systematic study into domain wall pinning behaviour as a function of geometrical confinement within planar nanowires. The parameter space has been explored for two different notch geometries with MOKE results suggesting that depinning fields are relatively insensitive to the detailed geometry of the notch. Instead the magnitude of depinning field of a wall from a notch structure appears to be strongly influenced by the wire width. The dependence of the domain wall pinning behaviour on the domain wall chirality at two different pinning site structures has been investigated. It has been observed that when pinning sites are comparable in size to the domain wall width then the detailed geometry of the notch is of secondary importance to the domain wall depinning field. A given domain wall structure and chirality will experience very similar depinning fields from both triangular and rectangular notches of the same depth and width. The spatial extent of the potential well is found to extend far beyond the physical size of the notch due to the comparable size of the domain wall. Micromagnetic simulations have shown that each notch structure may act as either a potential well or as a potential barrier, and this is determined by the micromagnetic structure and chirality of the propagating domain wall. Similar work has recently been reported for domain wall pinning in anti-notches [159]. A limit to the increase in pinning potential of notches that is achieved by increasing the depth of the notch has also been established. Indeed, pinning site saturation occurs when the notch depth to wire width ratio exceeds approximately 0.6 [158]. The results presented in this chapter are important in the optimisation of field driven domain wall propagation and pinning behaviour in nanowires.

Chapter 8. Domain wall anisotropic magnetoresistance in $Ni_{81}Fe_{19}$ planar nanowire structures

8.1 Introduction

Magnetic domains walls in nanowires are the subject of intensive research both in terms of improving the understanding of the basic physical processes [160] and also for developing potential applications [63, 64, 145, 147 and 161]. The resistivity of a ferromagnet typically exhibits anisotropic magnetoresistance (AMR), whereby it depends on the angle between the electric current and the magnetisation. In addition to the AMR contribution, further spintronic contributions to the electrical resistance of domain walls have been proposed [162, 163]. These effects are termed the *intrinsic* domain wall resistance and are usually much smaller than the AMR contribution in 3*d* transition metal nanowires. In the case of $Ni_{81}Fe_{19}$ nanowires, such contributions to domain wall resistance may be very small (typically contributing approximately 0.1% to 1% of the total resistivity). Indeed, it is found that the magnetoresistance of a domain wall in nanowires wider than 100 nm is dominated by the anisotropic magnetoresistance effect [105].

The presence of a domain wall in an axially magnetized nanowire changes the electrical resistance of the nanowire because the magnetisation within the wall deviates from the long axis of the wire, as shown in Figure 8:1. As discussed in section 6.3, in conventional anisotropic magnetoresistance the resistivity is high when the magnetisation and current path are parallel ($\rho_{\parallel}$) and is low when the magnetisation and current are perpendicular ($\rho_{\perp}$). In general, the resistivity of a ferromagnet is of the form:

$$\rho(\theta) = \rho_{\perp} + \delta\rho \cos^2(\theta) \qquad (8:1)$$

Where $\rho(\theta)$ is the resistivity of a spin magnetic moment orientated at an angle θ between the local magnetisation direction and the long axis of the nanowire. The magnitude of the change in resistance of the nanowire is determined by the anisotropic magnetoresistance, $\delta\rho$, given by $\rho_{\parallel} - \rho_{\perp}$. Where $\rho_{\parallel}$ and $\rho_{\perp}$ are the resistivities when the magnetisation and applied current are parallel and perpendicular, respectively [99].

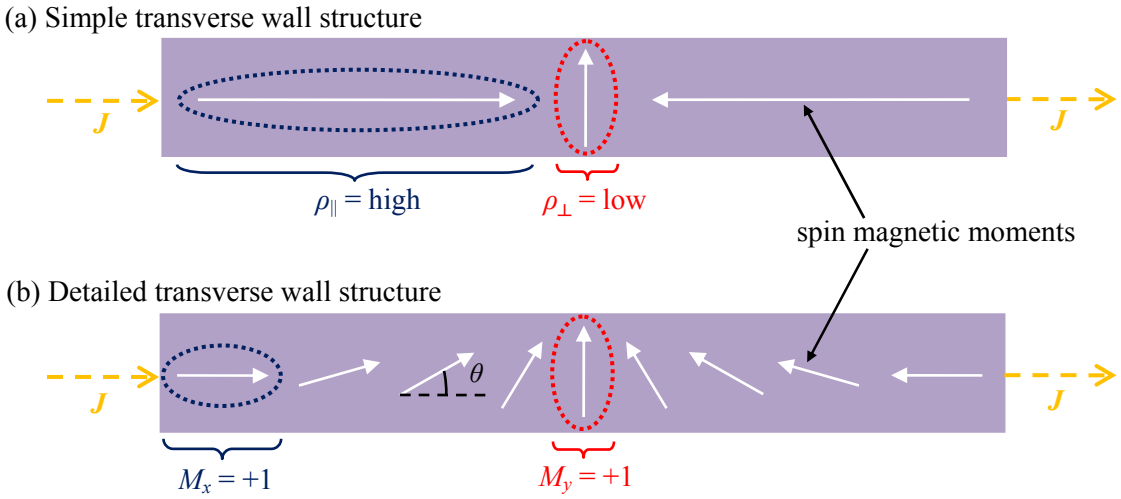

Figure 8:1. Schematic diagram to show the (a) simple and (b) detailed spin rotation within a head-to-head transverse domain wall. A domain wall causes a drop in electrical resistance of the nanowire because the spins within the wall are no longer orientated along the axial length of the nanowire.

The micromagnetic spin structures of transverse and vortex walls are very different, as discussed in section 7.2.4. It was reported in chapter 7 that the pinning interaction experienced by a domain wall with a notch is determined by both the structure and chirality (sense of magnetisation rotation) of the domain wall. There are many reports in the literature of structure dependant domain wall pinning behaviour including references [152, 159, 164, and 165]. It has also recently been reported that both the wall structure and the chirality (sense of magnetisation rotation) of domain wall pinned at a notch can be readily identified by subtly different magnetoresistance signatures [123, 148 and 166]. Anisotropic magnetoresistance is thus not only a powerful tool with the potential to establish the *presence* of a domain wall in a nanowire, but also the particular *structure* of the domain wall can be identified.

The ability to identify, with confidence, the micromagnetic structure of a domain wall is particularly important for nanowires of dimensions in which metastable wall configurations may exist as an alternative to the energetically favourable wall type, as discussed in section 7.2.4. In order to achieve this it is necessary to have a physically realistic model such that an accurate and reliable interpretation of the domain wall resistance can be obtained. In the literature, however, there is currently only a simple and somewhat crude model used to interpret the change in resistance of a $Ni_{81}Fe_{19}$ nanowire due to the presence of a domain wall [102] which is based upon a simplified representation of a domain wall described by the one dimensional wall width parameter δ_{DW} [61, 167].

This model overlooks the sophisticated micromagnetic spin structure present in walls which may be important for wires in which the difference in energy between a transverse wall and a vortex wall is small.

In this chapter, a detailed analysis of the change in resistance due to a single domain wall in $Ni_{81}Fe_{19}$ nanowire as a function of the wire width and thickness is presented. A method to predict the resistance of a domain wall has been developed in which the anisotropic magnetoresistance for individual simulation cells within micromagnetic simulations is calculated. The model developed here considers both the detailed micromagnetic structure of the wall and the thickness dependence of both the electrical resistivity, ρ_{ave}, and the magnetoresistance, $\delta\rho$. The parameter space has been mapped for domain walls nanowires with thicknesses from 3 to 20 nm and widths from 50 to 400 nm.

8.2 Detecting domain walls in planar nanowire structures using anisotropic magnetoresistance

8.2.1 Introduction

The presence of a domain wall within a nanowire can be detected by the resistance change:

$$\delta R = R_{DW} - R_{sat} \tag{8:2}$$

Where δR is the change in resistance of the nanowire, R_{DW} is the resistance of the nanowire containing a single domain wall, and R_{sat} is the resistance of the nanowire at saturation, which is stated in [101] as:

$$R_{sat} = \frac{\rho_{\|} L}{wt} \tag{8:3}$$

Where L is the length of the nanowire, w is the wire width and t is the wire thickness and $\rho_{\|}$ is the resistivity when the applied current is parallel to the magnetisation. In this expression, it is assumed that all the spins within the nanowire are parallel to the long axis of the nanowire; however, the spins at the end of the nanowire tend to be partly orientated across the wire width as shown Figure 7:1. Equation (8:3) is thus a simplified expression for the nanowire resistance at saturation. The resistance of the nanowire containing a domain wall, R_{DW}, is expressed as:

$$R_{\mathrm{DW}} = \int_{L/2}^{-L/2} \rho(\theta) \frac{dx}{wt} \tag{8:4}$$

Where $\rho(\theta)$ was provided in equation (8:1). In the limit that the domain wall width is proportional to the wire width, and assuming there is no resistance variation across the width of the wire, then the change in resistance in a nanowire due to the presence of a domain wall can be expressed as:

$$\delta R = -\frac{2 \cdot \delta\rho \cdot \delta_{\mathrm{DW}}}{wt} \tag{8:5}$$

Where δR is the change in electrical resistance, $\delta\rho$ is the anisotropic magnetoresistance, δ_{DW} is the domain wall width, w is the nanowire width and t is the nanowire thickness.

8.2.2 One dimensional domain wall width profiles

The model presented in the previous section requires suitable definitions of the domain wall width. The domain wall width is a critical parameter for both field and current driven domain wall motion although, as previously discussed in section 3.5.1, since a domain wall is a *continuous* rotation of the magnetisation, the wall width is a fairly difficult concept to define. As such, there is no unique definition of the domain wall width for a quasi-static domain wall in a nanowire structure.

Nakatani *et al.* [61] derive a simple expression for the domain wall width estimated by fitting the domain wall magnetisation profile to that of a one dimensional (1D) Bloch wall. As discussed in section 3.5.1, the angle between the local magnetisation direction and the long axis of the nanowire, $\theta(x)$, is given by:

$$\theta(x) = 2\arctan\left[\exp\left(\frac{\pi x}{\delta_{\mathrm{DW}}}\right)\right] \tag{8:6}$$

Which is the analytic solution used to describe the magnetisation rotation simple 1D Bloch wall. Thiaville *et al*. [168] previously used this expression to describe the two in-plane components of the magnetisation, M_x and M_y, for a Bloch domain wall in a narrow nanowire. These are expressed as:

$$M_x = \cos\left[\theta(x)\right] = \tanh\left(\frac{x}{\delta_{\mathrm{DW}}}\right) \tag{8:7}$$

And:

$$M_y = \sin\left[\theta(x)\right] = \operatorname{sech}\left(\frac{x}{\delta_{DW}}\right) \tag{8:8}$$

Nakatani *et al*. [61] extended the definitions provided in [168] to wider Néel walls in planar nanowire structures. These profiles are shown graphically in Figure 8:2 and these expressions allow approximate 1D wall width parameters to be extracted. These are given by:

$$\delta_{DW}^{TW} = \frac{w}{\pi}; \quad \delta_{DW}^{VW} = \frac{3w}{4} \tag{8:9}$$

Where w is the width of the nanowire, and δ_{DW}^{TW} and δ_{DW}^{VW} are the wall width parameters for transverse and vortex walls, respectively. It is important to note that the actual length scale over which most of the magnetisation changes is much larger, and is given by $\pi\delta_{DW}$ [168]. These definitions indicate that the wall width parameter scales linearly with wire width with only a weak dependence on the wire thickness. Furthermore, for a given wire width, a vortex wall is expected to be significantly wider than the corresponding transverse wall which is a reasonable approximation based on the micromagnetic simulations presented in Figure 7:11. Interestingly, there is no unique definition for the asymmetric transverse wall, although it was shown by Nakatani *et al*. [61] that its width increases with both increasing nanowire width and thickness. It is important to note that these wall width expressions are widely used in the literature as guidelines for the static domain wall width in planar nanowire structures for nanowire widths and thicknesses beyond which they are valid.

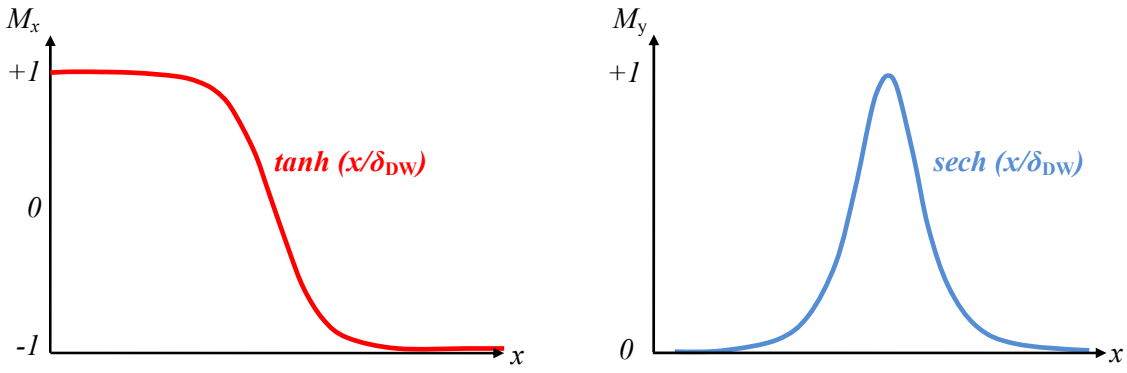

Figure 8:2. Graphical representations of the tanh and sech profiles based on the 1D Bloch wall profile given in [61 and 167] and commonly used to describe the M_x and M_y rotation profiles within Néel walls in planar nanowires.

8.2.3 Domain wall resistance using the one dimensional model

Knowledge of the one dimensional approximation for the transverse and vortex domain wall width allows expressions for the domain wall resistance to be developed. The change in resistance with a transverse domain wall present is thus given by:

$$\delta R_{\mathrm{TW}} = -\frac{2\cdot\delta\rho\cdot\left(w/\pi\right)}{wt} = -\frac{2\delta\rho}{\pi t} \tag{8:10}$$

And similarly for a vortex wall:

$$\delta R_{\mathrm{VW}} = -\frac{2\cdot\delta\rho\cdot\left(3w/4\right)}{wt} = -\frac{3\delta\rho}{2t} \tag{8:11}$$

Figure 8:3 presents values of the transverse and vortex wall resistance calculated using this model. Following the analysis presented in [101] a constant value of $\delta\rho$ equal to 0.3 μΩcm was used (assuming a constant resistivity of ρ_{ave} = 30 μΩcm and an AMR ratio of 1%). For all film thicknesses, it can be seen that the calculated values vary inversely with film thickness, as expected from both equations (8:10) and (8:11).

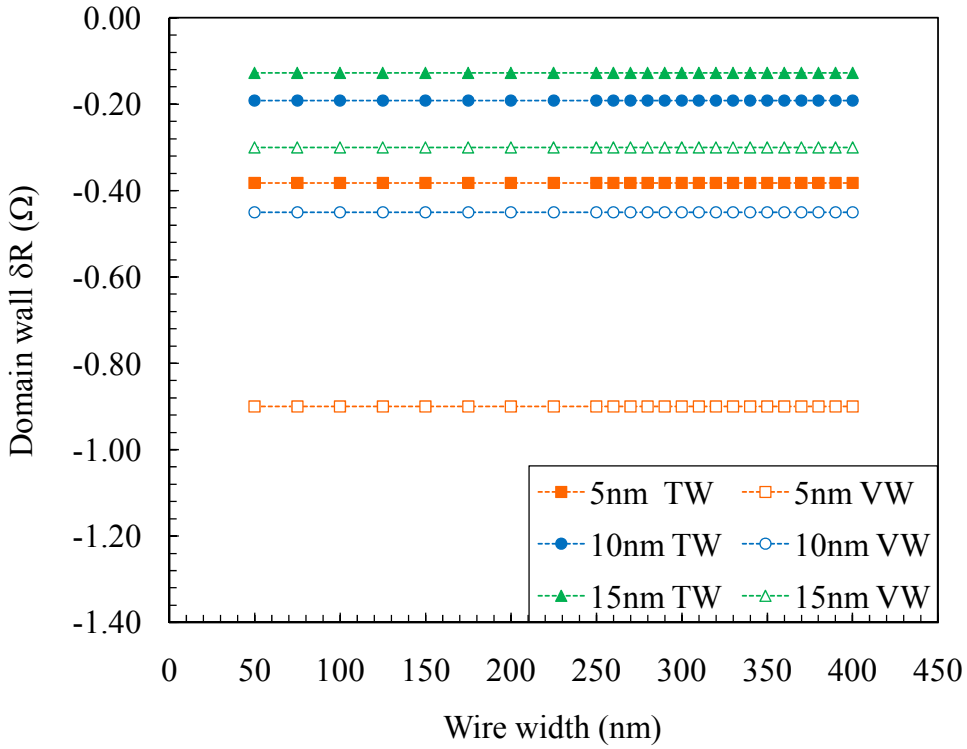

Figure 8:3. Calculated domain wall resistance as a function of wire width for 5, 10 and 15 nm thick nanowires using the domain wall resistance values given by equations (8:10) and (8:11), which are based upon 1D Blochwall width parameters given in [61]. Values of ρ_{ave} used = 30 μΩcm with $\delta\rho$ = 1%, as given in [102].

The calculated domain wall resistance is independent of nanowire width, and for a given nanowire thickness this model predicts constant values of resistance for each respective domain wall structure. It is suggested here that such an approach neglects the changes in micromagnetic spin structure that may occur as a function of changes in the nanowire width, and therefore such a model may not accurately represent the domain wall resistance.

The domain wall structure is the result of an energy minimisation process that is largely determined by the cross-sectional dimensions of the nanowire. In 10 nm thick nanowires, micromagnetic simulations presented in section 7.2.4 showed that the transverse wall is energetically favourable for $w < 150$ nm, above which the vortex wall becomes increasingly energetically favourable. Moreover, it was also shown that for nanowire widths between 150 nm and 400 nm both structures may co-exist due to the small differences in energy between each state, as shown in Figure 7:12. As the wire width increases toward that for which a vortex wall is stable the structure of the transverse wall changes drastically and becomes highly asymmetric with a large number of low angle spins, as shown in Figure 7:11 (c).

The 1D model does not account for such a transformation and instead predicts that the domain wall resistance of a symmetric transverse wall in a narrow nanowire will be identical to that of a highly asymmetric transverse wall in a wide nanowire of the same thickness. Furthermore, the 1D model neglects to provide any expressions for the structure of domain walls at geometrical features such as notches. As shown in sections 7.3.4 and 7.3.5, domain walls are not pinned in the narrowest section of the notch; instead, they tend to pin at the leading edge of the notch with the exact pinning location determined by the chirality of the wall and the precise geometry of the notch. Whilst it is possible to estimate the width of pinned walls, a solid and reproducible method that allows confident interpretation of the domain wall resistance needs to be developed so that an accurate interpretation of δR can be made. Accurate interpretation allows for accurate knowledge of the domain wall structure such that the observed behaviour may be fully and correctly understood.

8.2.4 An electrical conduction channel model for the anisotropic magnetoresistance of domain walls

Figure 8:3 shows how the one dimensional Bloch wall width parameter provides a poor description of the domain wall structures observed in planar nanowire structures since it

neglects a significant proportion of the sophisticated micromagnetic spin structure. In addition to this, the use of typical values which are independent of film thickness is also a poor approximation as the investigation presented in chapter 6 highlighted how both the resistivity and magnetoresistance of $Ni_{81}Fe_{19}$ thin films are both strongly thickness dependent parameters. Thus, any model of domain wall resistance must also include these important properties in order for it to provide accurate and physically meaningful results. In this chapter, an alternative model to calculate the domain wall resistance is developed. This model is based upon micromagnetic simulations and therefore by-passes the need for a definition of domain wall width.

Figure 8:4 presents a schematic of the electrical structure of the nanowire used within the model developed here. Each nanowire is represented as a network of conduction channels containing resistors in series along the axis of the nanowire. The number of channels is equal to the nanowire width divided by the cell size and is equal to 5 nm in this study; thus, a 600 nm wide wire would contain 120 conduction channels. As an individual cell within the micromagnetic simulation contains an individual spin, each cell corresponds to an individual resistor within the conduction network.

For each completed field step within the simulation, the OOMMF software saved an *.odt* file that contained M_x, M_y and M_z information within every cell within the modelled element. This meant that the magnetisation within each 6 μm long nanowire element could then be represented by three matrices of the form (*n* x 1200), where the *n* is the number of conduction channels.

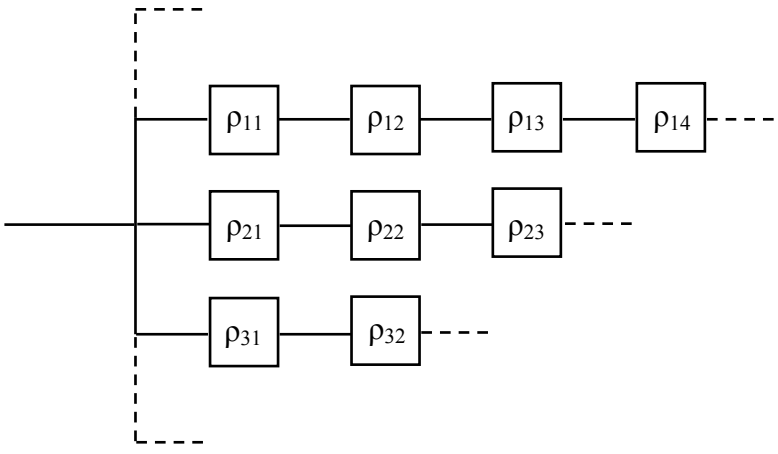

Figure 8:4. Schematic of the electrical network representing a nanowire used to calculate the resistance of a nanowire containing a domain wall. Each resistor represents a cell from the micromagnetic simulations and has an area equal to 5 nm^2.

This then allowed the angle of the spin between the local magnetisation and the current along the x axis, θ, to be deduced via:

$$\theta = \tan^{-1}\left(\frac{M_y}{M_x}\right) \tag{8:12}$$

Following this, it was possible to deduce the resistivity of each cell using equation 8.1. The total resistivity of each conduction channel was obtained by summing the resistivity of the cells as resistors in series and the total resistivity of the nanowire, ρ_{total}, was obtained from the summation of these conduction channels in parallel. This was then used to calculate the total resistance of the nanowire, R_{total}, which was obtained via:

$$R_{\text{total}} = \frac{\rho_{\text{total}} L}{A} \tag{8:13}$$

Where L and A correspond to the length and the cross-sectional area of an individual cell, respectively. Whilst this is a reasonable and practical approach, it is recognised that this model is simplified by the fact that the current cannot flow directly between adjacent diagonal or vertical cells.

The following sections discuss the sophisticated magnetisation rotation profiles that can exist within transverse and vortex domain wall structures, and thus emphasise the need for the domain wall resistance to be modelled with a two dimensional approach as described here. Following this, the best form for values of $\rho_{\parallel}$ and $\rho_{\perp}$ in $Ni_{81}Fe_{19}$ thin films is explored with a discussion of thickness dependent values of $\rho_{\parallel}$ and $\rho_{\perp}$ that are deduced from best fit lines to data reported in the literature and also measure in this study. Finally, the chapter concludes with comparison of δR for transverse and vortex domain walls as calculated using the one dimensional model described in the literature and the two dimensional model developed here for thickness dependent values of $\rho_{\parallel}$ and $\rho_{\perp}$ as reported both within the literature and also as presented in chapter 6.

8.3 A detailed analysis of magnetisation rotation profiles using micromagnetic simulations

8.3.1 Analysis of average magnetisation rotation profiles

Insight into the relationship between the micromagnetic spin structure of a transverse domain wall and the cross-sectional nanowire dimensions have been obtained using quasi-

static micromagnetic simulations. Micromagnetic simulations have been used to compare the magnetisation rotation profiles of each domain wall structure to that given by the 1D model. This section compares domain wall structures for nanowire widths in which micromagnetic simulations performed in section 7.2.4 suggest that both wall structures are able to co-exist with only small differences in energy. Using a combination of the results presented in 7.2.4 and the Nakatani phase diagram [61] as a guide, one of two basic domain wall structures - transverse and vortex - were investigated. The selected wall type was introduced into a 6000 nm long rectangular shaped structure with width w and thickness t, and allowed to relax to its equilibrium configuration at zero-applied field. Standard magnetic parameters for $Ni_{81}Fe_{19}$ were used, including saturation magnetisation M_s = 860 x 10^3 A/m and an exchange energy constant A = 13 x 10^{-12} J/m, and a cell size of 5 nm was used. All simulations were performed in a quasi-static regime with the damping parameter α set at 0.5 to speed up the convergence time.

The one dimensional model of the domain wall width parameter is based upon the average magnetisation rotation profile within the wall. Figure 8:5 presents average domain wall width rotation profiles (M_x, M_y and M_z) for transverse domain walls in 10 nm thick, 150 nm and 300 nm wide wires. Within the 1D model the transverse wall width can be approximated by w/π; for (a) a 150 nm and (b) a 300 nm wide this corresponds to transverse wall width of approximately 48 nm and 95 nm, respectively.

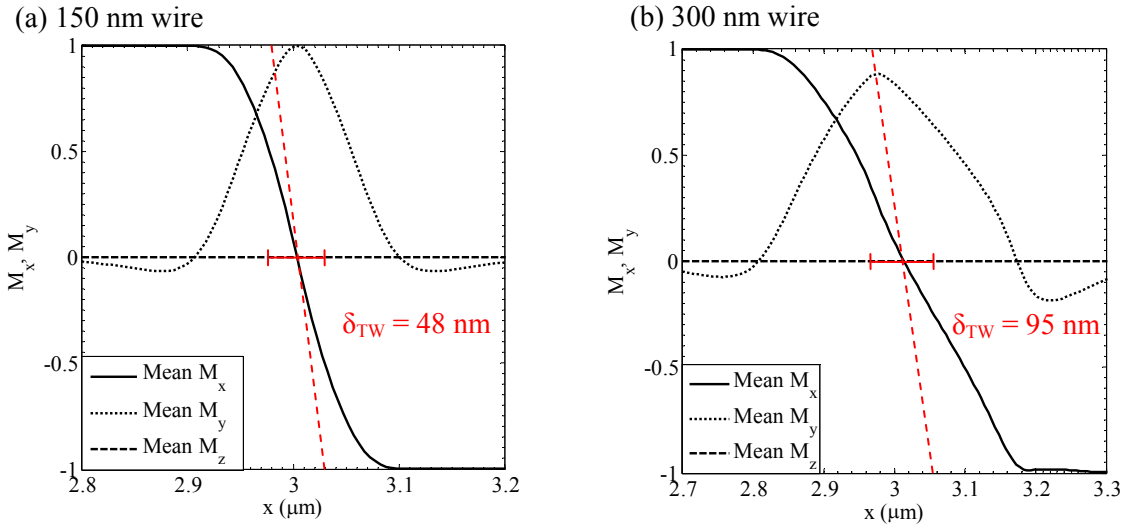

Figure 8:5. Average domain wall width profiles for magnetisation rotation in the x, y and z directions within a transverse wall in (a) a 150 nm wire and (b) a 300nm wire, as deduced from micromagnetic simulations. 1D Bloch wall parameters are highlighted by red lines; δ_{TW} = 48 nm and 95 nm, respectively.

For a transverse wall in a 150 nm wide nanowire, the average M_x and M_y profiles show reasonable resemblance to the 1D profiles presented in Figure 8:3. However, as the wire width increases to 300 nm this resemblance is less reasonable. This is because at this wire width, the transverse wall becomes highly asymmetric and contains a substantial number of spins orientated at low angles across the wire width. The values of the wall width given by the 1D Bloch wall model appear to underestimate the average domain wall width suggested here.

Figure 8:6 presents average M_x, M_y and M_z profiles for a vortex wall in 10 nm thick nanowires that are 150 nm and 300 nm wide, respectively. The vortex wall width is approximated by $3w/4$; for a 150 nm and 300 nm wide this corresponds to wall width of approximately 113 nm and 225 nm, respectively. Both M_x and M_y rotation profiles appear to resemble the combinations of two transverse walls of opposite chiralities, which are shown to be a reasonable approximation in Figure 8:7. In addition, for each vortex wall structure, there is a small peak in the M_z profile located at the centre of the wall: this corresponds to the spins at the centre of the wall pointing out of the *xy*-plane of the nanowire forming the vortex core. The flat, central portion that can be seen in Figure 8:7 (a) and (b) corresponds to the vortex core where the spins point out of the plane of the nanowire. The 1D Bloch wall is not a reasonable representation of the average magnetisation rotation profile within a vortex domain wall.

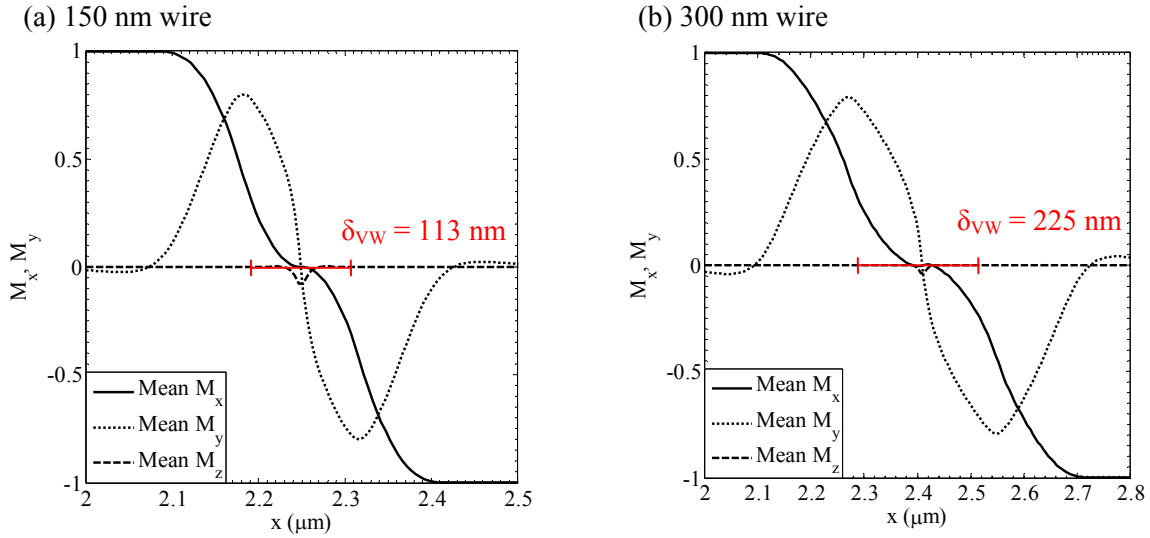

Figure 8:6. Average domain wall width profiles for magnetisation rotation in the *x*, *y* and *z* directions within a transverse wall in (a) a 150 nm wire and (b) a 300nm wire, as deduced from micromagnetic simulations. 1D Bloch wall widths are also indicated by the red lines, and correspond to a wall width of 113 nm and 225 nm in each wire width.

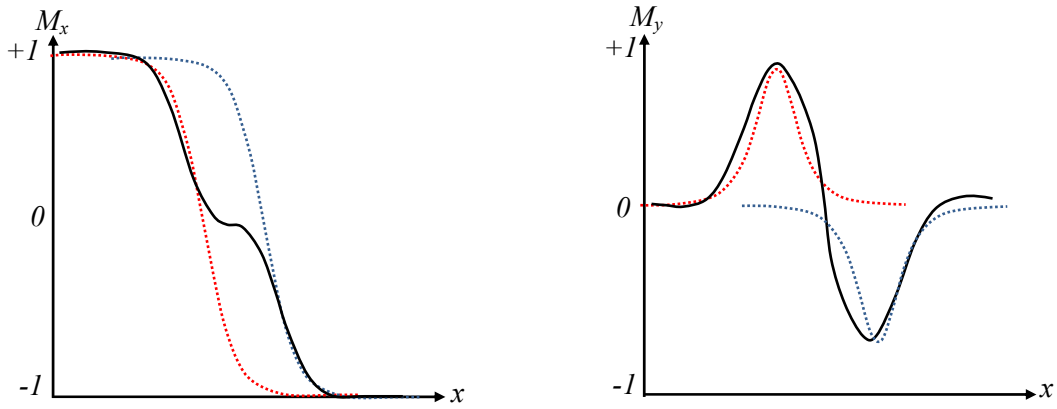

Figure 8:7. Schematic to show how the average M_x and M_y profiles within a vortex wall (shown by solid, black line) resemble a superposition of two tanh and sech profiles, as shown by the red and blue dashed lines.

8.3.2 Detailed magnetisation rotation profiles within transverse wall structures

Further insight into the deviation of the magnetisation reversal profile of both transverse and vortex wall structures from the 1D Bloch wall profiles can be gained by considering the magnetisation reversal profile at various locations across the width (different y locations) of the nanowire. Figure 8:8 presents detailed spin rotation profiles at various different locations across the nanowire for a transverse wall in a 150 nm wide, 10 nm thick nanowire.

As shown in section 7.2.4, a transverse wall is the energetically favourable wall structure in a nanowire of such dimensions; this is reflected in the symmetric spin structure within the wall. The domain wall is narrowest at the bottom of the structure, as shown by the purple line, and gets wider across the nanowire width. Each magnetisation reversal profile channel is 5 nm wide, which corresponds to the cell size used in the micromagnetic simulations. The wall is at its widest at approximately two-thirds across the wire width, after which the wall width begins to decrease. The green line corresponds to the magnetisation rotation profile at the top of the wall. The 1D Bloch wall parameter is a reasonable representation of the transverse wall width across the width of the nanowire in narrow wires, as all channels bear some resemblance to tanh profiles. The value of the 1D wall width parameter appears to underestimate the width of this wall structure.

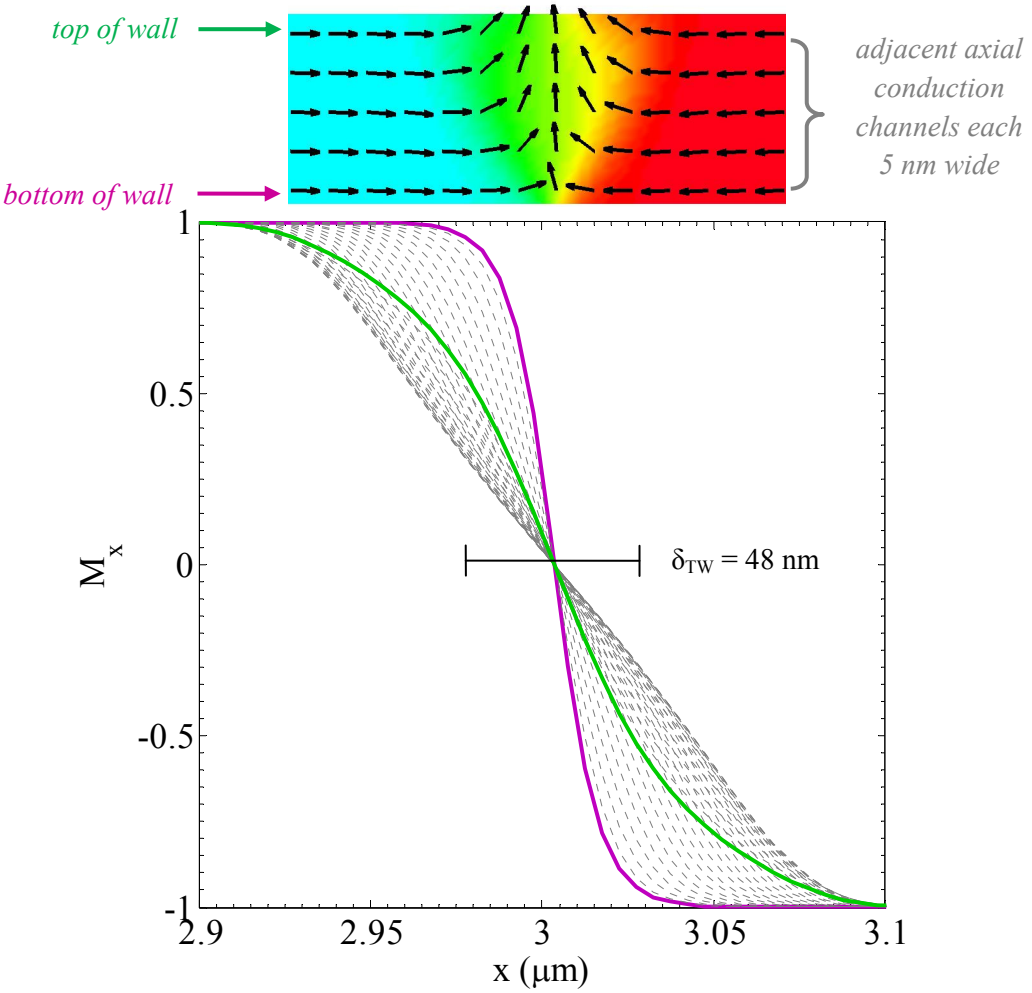

Figure 8:8. Variation of wall width at increasing y locations across the width of the nanowire for a head-to-head transverse wall in a nanowire 150 nm wide, 10 nm thick. The purple line corresponds to the spin rotation at the bottom of the wall, where y = 0, whilst the green line corresponds to the spin rotation at the top of the wall, where y = 150 nm. The grey lines correspond to adjacent channels of spin rotation 5 nm wide. The equivalent 1D wall width parameter, δ_{TW}, is shown for comparison.

Figure 8:9 presents detailed magnetisation rotation profiles at different locations across the wire for a transverse wall in a 300 nm wide, 10 nm thick nanowire. A transverse wall is not energetically favourable wall structure in a 10 nm thick nanowire of this wire width, although according to micromagnetic simulations such a wall structure is only 10% higher in energy than the vortex wall and so it may be attainable in real structures at finite temperatures. The energetic unfavourability of this wall structure is reflected in the highly asymmetric structure of the magnetisation rotation of the wall, which develops in an attempt to reduce the magnetostatic energy associated with the large number of magnetic moments orientated across the strip with within a transverse wall.

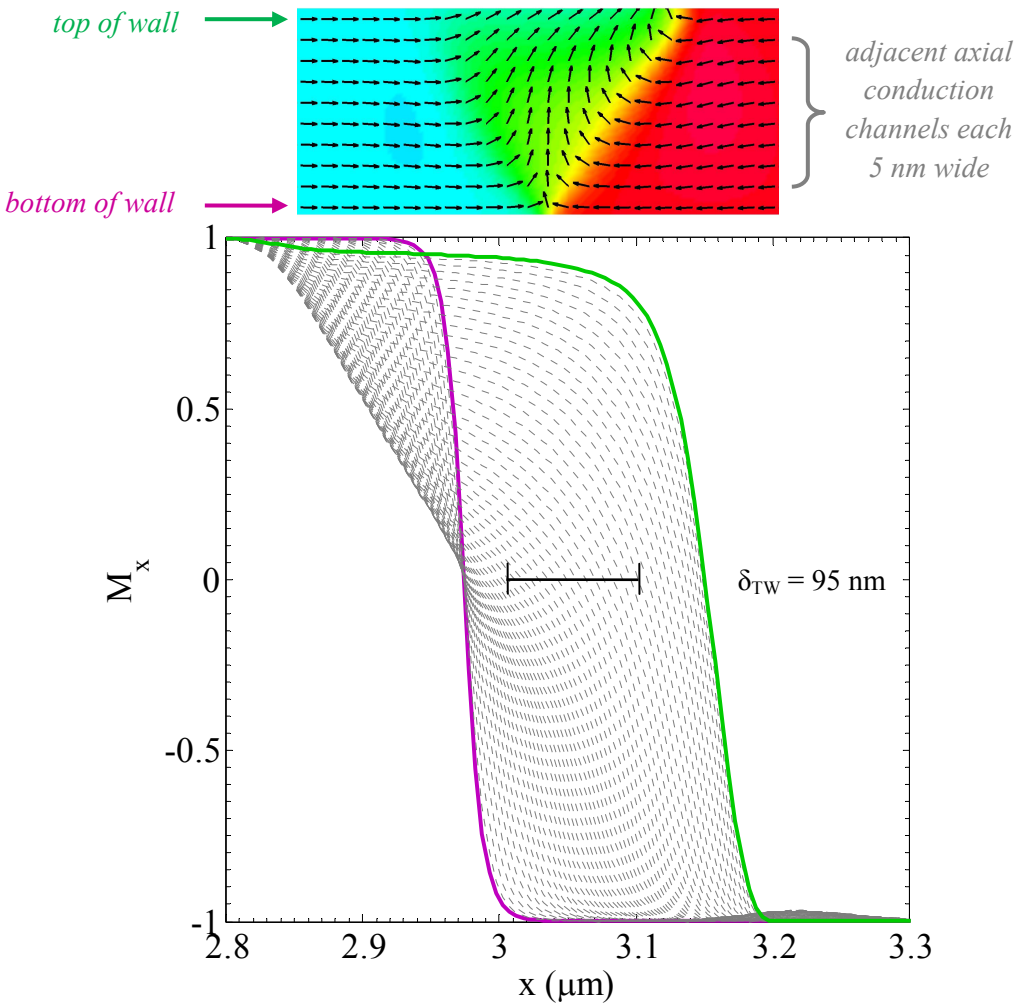

Figure 8:9. Variation of wall width at increasing y locations across the width of the nanowire for a head-to-head transverse wall in a 300 nm wide nanowire 10 nm thick. The purple line corresponds to the spin rotation at the bottom of the wall, where $y = 0$, whilst the green line corresponds to the spin rotation at the top of the wall, where $y = 300$ nm. The grey lines correspond to adjacent channels of spin rotation separated by 5 nm. The 1D Bloch wall width is also indicated.

The wall is narrowest and symmetrical at the bottom of the wire - indicated by the purple line - and gets increasingly wider across the nanowire width. The wall is widest and is also highly asymmetrical at the top of the nanowire, as shown by the green line.

It is clear that the average magnetisation rotation profile presented in Figure 8:5 (b) is not an accurate representation of the micromagnetic spin structure within an asymmetric transverse wall as very few channels resemble tanh-like profiles. Consequently, the 1D Bloch wall parameter significantly underestimates the width of an asymmetric transverse wall as it neglects the detailed micromagnetic spin structure (large number of low angle spins) within such a wall structure. Any model of the domain wall resistance should be more accurate when such a spin structure exists.

8.3.3 Detailed magnetisation rotation profiles within vortex wall structures

Figure 8:10 presents detailed spin profiles at various locations across the nanowire width for a vortex wall in a 150 nm wide, 10 nm thick nanowire. This wall structure is not energetically favourable in a 10 nm thick nanowire of this width, although micromagnetic simulations presented in section 7.4.2 show that such a structure is only 1.9% higher energy than the corresponding transverse wall structure. Thus, such a structure could be expected to occur at finite temperature. Detailed spin profiles for a vortex wall in a 300 nm wide, 10 nm thick nanowire are shown in Figure 8:11. The detailed magnetisation reversal profiles of a vortex wall exhibit large deviations from the average wall profiles as shown in Figure 8:6.

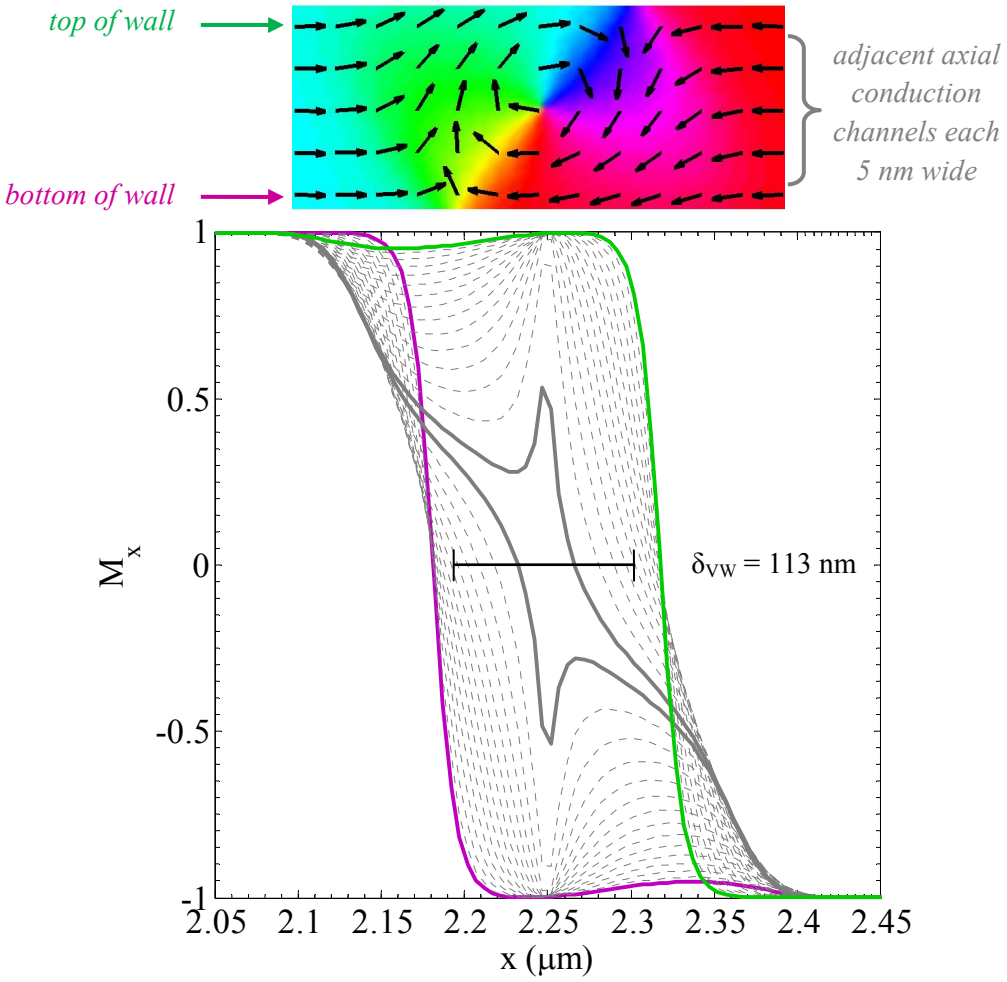

Figure 8:10. Variation of wall width at increasing y locations across the width of the nanowire for a head-to-head vortex wall in a 150 nm wide nanowire 10 nm thick. The purple line corresponds to the spin rotation at the bottom of the wall, where $y = 0$, whilst the green line corresponds to the spin rotation at the top of the wall, where $y = 150$ nm. The 1D Bloch wall width is shown for comparison.

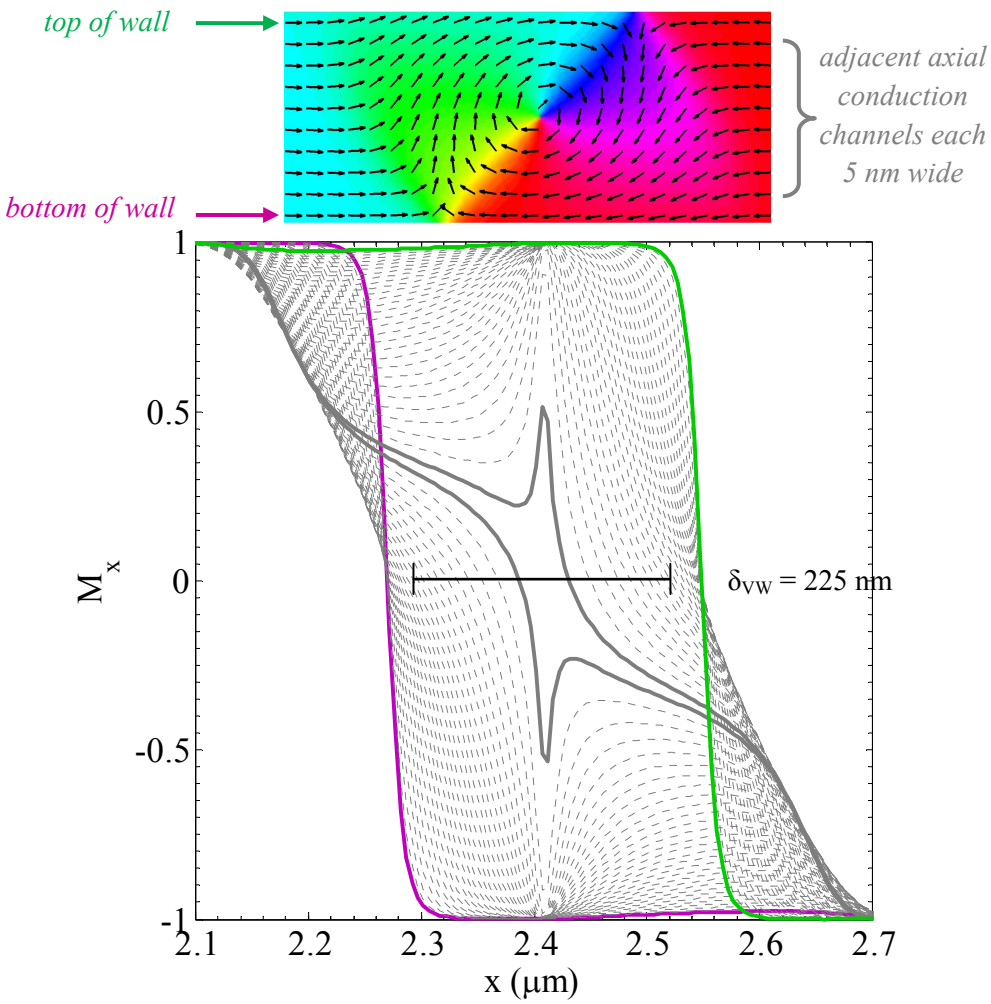

Figure 8:11. Variation of wall width at increasing y locations across the width of the nanowire for a head-to-head vortex wall in a 300 nm wide nanowire 10 nm thick. The purple line corresponds to the spin rotation at the bottom of the wall, where $y = 0$, whilst the green line corresponds to the spin rotation at the top of the wall, where $y = 300$ nm. The 1D Bloch wall width is shown for comparison.

Indeed, each wall structure only resembles that of the average wall width profile occur at the top and bottom of each vortex wall structure (green and purple lines, respectively), whilst the remainder of the spin profiles are more complicated. The solid grey lines correspond to the magnetic moments along the centre of the nanowire, where the spin magnetic moments are orientated out of plane. The 1D Bloch wall width does not account for the detailed nature of the spin rotation that occurs within a vortex wall, in which a significant number of spins are orientated at low angles.

8.4 Thickness dependence of resistivity and magnetoresistance parameters

In addition to using simplified expressions for domain wall width, the earlier domain wall resistance model presented in section 8.1 used values of resistivity, ρ_{ave}, and anisotropic magnetoresistance, $\delta\rho$, that were independent of the nanowire thickness. As described chapter 6, this is not physically realistic for $Ni_{81}Fe_{19}$ as both resistivity and anisotropic magnetoresistance were observed to display strong thickness dependence in the thin films investigated within this study.

It is widely reported in the literature that the resistivity of a thin film increases as the thin film thickness decreases, due to Fuchs scattering [136]. This was also observed for the films investigated within the study presented in chapter 6. The thickness dependence of the magnetoresistance is less well understood; whilst McGuire suggests that $\delta\rho$ is independent of film thickness [99], the results presented in chapter 6 show that $\delta\rho$ exhibits a strong thickness dependence for $t < 10$ nm. In order to be physically realistic, it is necessary that any model of the domain wall resistance should establish the nature of the thickness dependence of the resistivity parameters, and take them into account as appropriate. In this section, the nature of the thickness dependence of resistivity and magnetoresistance as reported in the literature and within this study will be compared.

8.4.1 Thickness dependent values of resistivity parameters as characterised in the literature

Figure 8:12 presents thickness dependent values of both the resistivity and anisotropic magnetoresistance ratio of thin films as a function of film thickness below 50 nm for $Ni_{82}Fe_{18}$ films measured by several workers [119, 120, 121 and 122] along with data measured by Atkinson [169] for nominally $Ni_{81}Fe_{19}$ films.

Each set of data shows that as film thickness decreases, the resistivity increases, as is expected since the resistivity increases noticeably when the mean free path, of the conduction electrons is comparable to film thickness due to diffuse scatter at the surfaces [136], as previously discussed in detail in section 6.3.2. This is attributed to the very high deposition rate of 1000 $Ås^{-1}$, compared to the data collected from films deposited by Atkinson (♦) [169] at a much lower rate of 0.5 $Ås^{-1}$. Indeed, the differences between all data sets are attributed to the differences in the substrates and the rate and temperature of

the thin film deposition; details of the preparation methods used for each data set are described in Table 6:4.

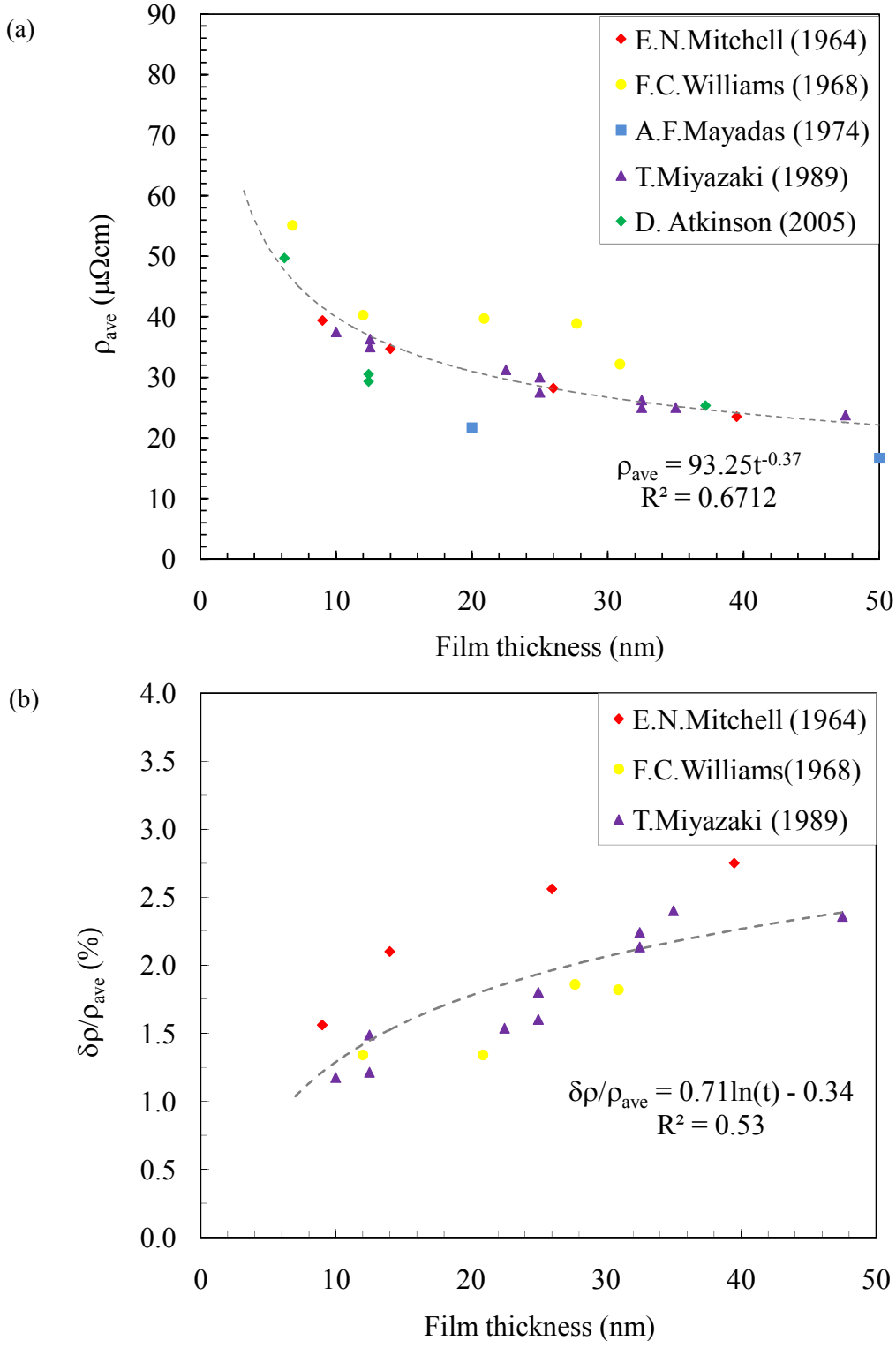

Figure 8:12. (a) Comparison of the thickness dependent resistivity of five data sets for $Ni_{81}Fe_{19}$ thin films. The line is the best fit to all of the data, and (b) Comparison of the thickness dependent anisotropic magnetoresistance ratio for three data sets for $Ni_{81}Fe_{19}$ thin films. The lines are the best fit to all of the data.

A line of best fit to the entire data set allows the thickness dependence of the resistivity to be represented as:

$$\rho_{\text{ave}} = 93.249 t^{-0.368} \tag{8:14}$$

Where t is measured in nm and ρ_{ave} is given in μΩcm. A power law was chosen due to the nature of Fuchs surface scattering [136]. In general, the resistivity data is fairly consistent across these studies, with the largest differences occurring between 20 and 30 nm for the Williams and Mitchell data (●) [120].

The available literature data for $\delta\rho$ is more limited [120, 121, 122], but shows that it is independent of film thickness for t > 50 nm and below that shows a weak logarithmic dependence of the AMR ratio upon thickness. The thickness trend of the data is similar between the studies but there is greater variation in magnitude compared to the resistivity alone, which again may be attributed to either the preparation method or to some variation in composition. In this instance, the best fit to the experimental data is given by:

$$\frac{\delta\rho}{\rho_{\text{ave}}} = 0.7057 \ln(t) - 0.3356 \tag{8:15}$$

In contrast to the thickness dependence, the wire width dependence of the resistivity can be ignored as the length scale at which such effects emerges is around 45 - 50 nm [170]. Values of $\rho_{\parallel}$ and $\rho_{\perp}$ as a function of thin film thickness have been deduced from the lines of best fit in equations (8:14) and (8:15) via the relations:

$$\delta\rho = \rho_{\parallel} - \rho_{\perp} \text{ and } \rho_{\text{ave}} = \frac{1}{3}\left(\rho_{\parallel} + 2\rho_{\perp}\right) \tag{8:16}$$

Values of $\rho_{\parallel}$ and $\rho_{\perp}$ are presented in Table 8:1.

Film thickness (nm)	$\rho_{\parallel}$ **(μΩcm)**	$\rho_{\perp}$ **(μΩcm)**	$\delta\rho$ **(μΩcm)**
3	62.42	62.15	0.27
4	56.23	55.87	0.36
5	51.85	51.44	0.41
6	48.52	48.05	0.45
7	45.88	45.41	0.47
10	40.31	39.79	0.52
12	37.72	37.19	0.53
15	34.78	34.24	0.54
20	31.33	30.78	0.55

Table 8:1. Values of $\rho_{\parallel}$ and $\rho_{\perp}$ for $Ni_{81}Fe_{19}$ deduced using the respective lines of best fit provided in Figure 8:12 used to deduce the change in resistance of a nanowire due to the presence of a domain wall.

8.4.2 Thickness dependent values of resistivity parameters as characterised in this study

The magnetoresistance behaviour of $Ni_{81}Fe_{19}$ thin films thermally evaporated on pre-oxidised silicon substrates was investigated in detail in chapter 6. Figure 8:13 presents thickness dependent values of both the resistivity and anisotropic magnetoresistance ratio of the thin films studied within this investigation and previously presented in chapter 6. All of the data was used to obtain a line of best fit to represent the thickness dependence of the resistivity when the magnetisation and current are parallel and perpendicular, respectively. The best fit to the experimental data for the resistivity is given by:

$$\rho_{\text{ave}} = 71.853t^{-0.221} \tag{8:17}$$

Whilst the best fit for the anisotropic magnetoresistance ratio as a function of film thickness is given by:

$$\frac{\delta\rho}{\rho_{\text{ave}}} = 0.5039\ln(t) - 0.5342 \tag{8:18}$$

In each case, t is measured in nm and ρ_{ave} is given in μΩcm.

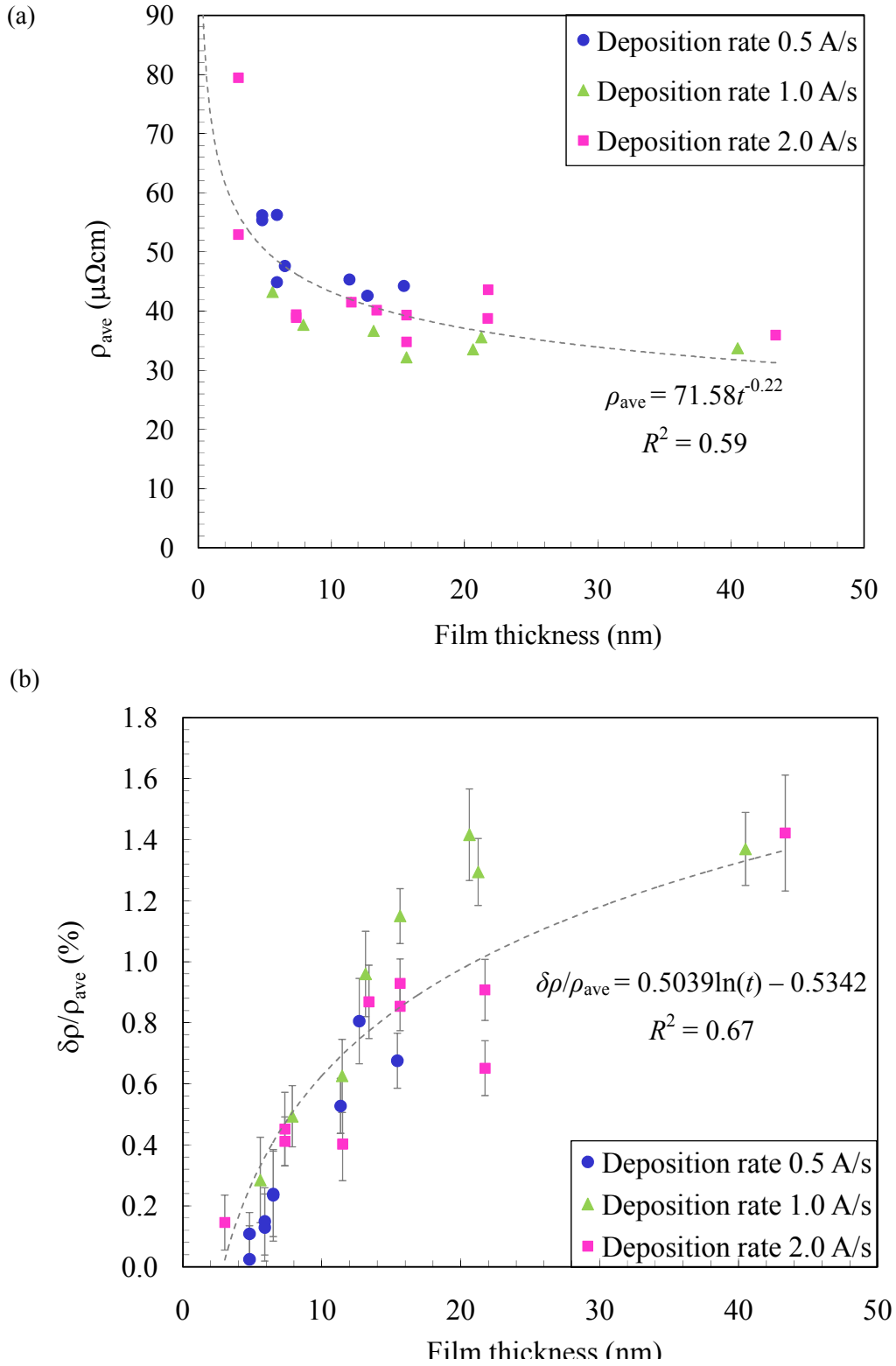

Figure 8:13. Experimentally measured values of (a) ρ_{ave} and (b) $\delta\rho/\rho_{ave}$ for $Ni_{81}Fe_{19}$ thin films thermally evaporated on pre-oxidised silicon substrates, taken from data presented in Table 6.1, 6.2 and 6.3, respectively. The lines are the best fit to all of the data. This data was previously presented in Chapter 6 but is reproduced here for convenience to the investigation presented within this chapter.

Table 8:2 presents average values of $\rho_{\parallel}$ and $\rho_{\perp}$ deduced using the equations given in (8:16). Although qualitatively the data presented in Figure 8:12 and Figure 8:13 show similar trends in the thickness dependence of both resistivity and magnetoresistance, quantitatively there are significant differences in the values of $\rho_{\parallel}$ and $\rho_{\perp}$. In the literature, the AMR ratio ($\delta\rho/\rho_{ave}$) exhibits a weak thickness dependence believed to be the result of a strong thickness dependence of the resistivity. The films investigated within this study exhibit a strong thickness dependence of $\delta\rho$, which means that the AMR ratio for the films investigated within this study tends to zero for $t < 10$ nm. It is the combination of the strong thickness dependence of $\delta\rho$ with the thickness dependence of ρ_{ave} gives a very small AMR ratio. Such differences are expected to have a considerable effect on the values of domain wall resistance. These differences are largely attributed to the differences in preparation of films, as explained in section 6.4 and were previously summarised in Table 6:4.

Film thickness (nm)	$\boldsymbol{\rho_{\parallel}}$ **(μΩcm)**	$\boldsymbol{\rho_{\perp}}$ **(μΩcm)**	$\boldsymbol{\delta\rho}$ **(μΩcm)**
3	73.16	73.14	0.02
4	68.72	68.60	0.12
5	65.46	65.28	0.18
6	62.91	62.68	0.23
7	60.84	60.57	0.27
10	56.29	55.95	0.35
12	54.10	53.72	0.39
15	51.54	51.11	0.43
20	48.41	47.94	0.47

Table 8:2. Values of $\rho_{\parallel}$ and $\rho_{\perp}$ for $Ni_{81}Fe_{19}$ deduced using the respective lines of best fit provided in Figure 8:13 used to deduce the change in resistance of a nanowire due to the presence of a domain wall.

8.5 Comparison of domain wall resistance values calculated using the 1D and 2D models

In this section, a detailed analysis of the change in resistance given by a domain wall in $Ni_{81}Fe_{19}$ nanowires as a function of the wire width and thickness is presented. Values of the change in resistance due to the presence of a domain wall have been deduced using the 1D method presented in the literature and are compared to those deduced using the 2D method described in section 8.2.4. For each model, average values of $\rho_{\|}$ and $\rho_{\perp}$ from data presented within the literature and measured within this study have been incorporated. This approach has been used this to map the parameter space for transverse and vortex domain walls in $Ni_{81}Fe_{19}$ nanowires with thickness from 3 nm to 20 nm and widths from 50 nm to 400 nm.

8.5.1 Domain wall resistance using thickness dependent resistivity parameters from the literature

Figure 8:14 compares values of domain wall resistance as a function of wire width and thickness calculated using both the 1D Bloch wall width model and conduction channel model. Thickness dependent resistivity parameters presented in Table 8:1 were used to deduce values of $\rho_{\|}$ and $\rho_{\perp}$ for each thickness investigated. The majority of domain walls shown are favourable (lowest energy) structures, however, unfavourable (higher energy) structures of up to 15% higher energy are also included to reflect the domain wall structures that may exist in real nanowire samples. Domain wall energies calculated using micromagnetics are all calculated for perfect structures at zero temperature and also due to variations in the wire width due to edge roughness; it is therefore not unreasonable to suggest that a 15% higher energy state may exist in a real nanowire structure at finite temperature. Domain wall AMR has the potential to be extremely useful for the correct identification of domain wall structures in which there is a small difference in the energy of favourable and unfavourable domain wall states. It is therefore important to consider values of δR for both types of domain wall structure.

There are significant differences between the domain wall resistance values given by the 1D model and those given by the conduction channel model developed within this study.

(a) Simple 1D Bloch wall width model

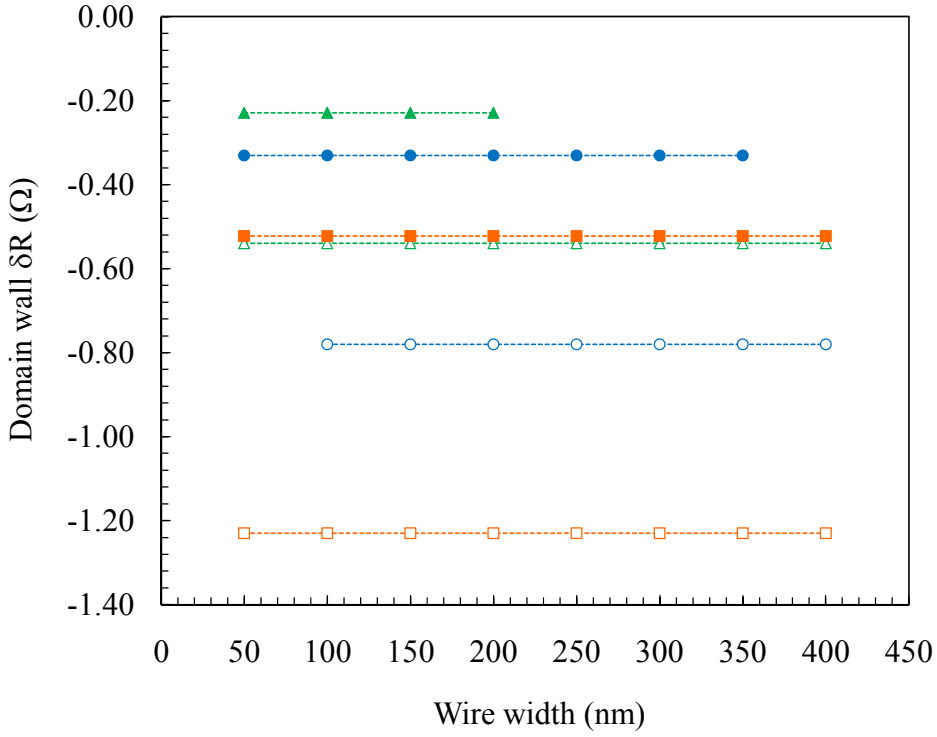

(b) Conduction channel model

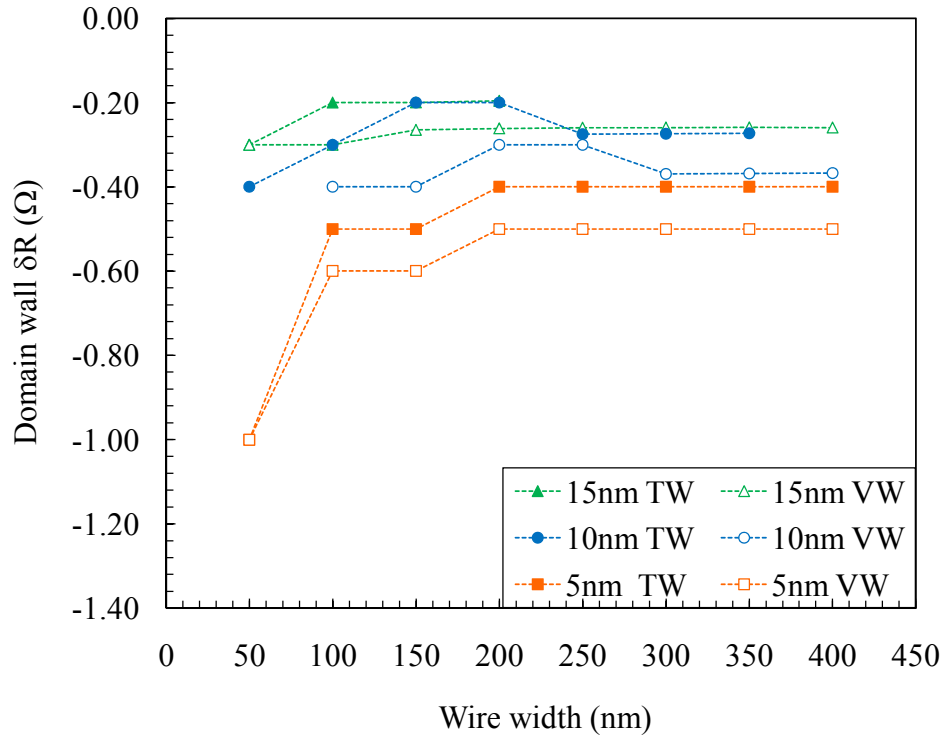

Figure 8:14. Domain wall resistance as a function of wire width for 5 nm, 10 nm and 15 nm thick nanowires deduced using (a) the simple model using the 1D Bloch wall width parameters and (b) the conduction channel model and thickness dependent resistivity parameters deduced from lines of best fit to data presented in Figure 8:12. In each graph the lines are guides to the eye only.

It can be seen that, for a given wire thickness, the 1D model predicts large differences in domain wall resistance for different domain wall structures, with the vortex wall producing a much larger (more negative) signal than the corresponding transverse wall. In the conduction model, however, it can be seen that the predicted values of vortex and transverse wall resistance are much closer in magnitude. The 1D model also suggests that for a given wall structure and nanowire thickness there is no dependence of the domain wall resistance upon the wire width. The data given by the more detailed model, however, shows a clear dependence of the domain wall resistance on the width of the nanowire.

These differences can be understood by considering the micromagnetic structure of the domain wall. In section 8.3, it was seen that the 1D model underestimates the domain wall width for both transverse and vortex wall structures as it neglects the contribution from a large number of low angle spins present within the walls. It is suggested that the large values of the vortex wall resistance are due to the oversimplification of the micromagnetic structure in the 1D model; such large values of δR for the vortex wall can only be obtained if there were a large number of high angle spins present within the wall. Whilst there are many high angle spins, as shown in Figure 8:9 and Figure 8:10, there are many low angle spins, which make a finite, although smaller, contribution to the total resistance of the vortex wall structure. For a 10 nm thick nanowire, each wall structure shows a strong wire width dependence of the domain wall resistance. It is suggested that the clear dependence of the value of domain wall resistance on nanowire width is due to the changes in domain wall structure that may occur. As discussed in section 7.2.4, micromagnetic simulations show that the wall structures exhibit subtle changes in micromagnetic spin structure as a function of nanowire width which is a direct result of the energetic cost associated with the formation of particular wall structure. The present analysis shows that dependence of the wall resistance on wall structure is significantly larger than previously predicted.

Figure 8:15 presents domain wall resistance values for transverse and vortex walls in a 300 nm wide wire as a function of film thickness calculated by both the simple 1D model (♦) and detailed modelling approach developed here (■).

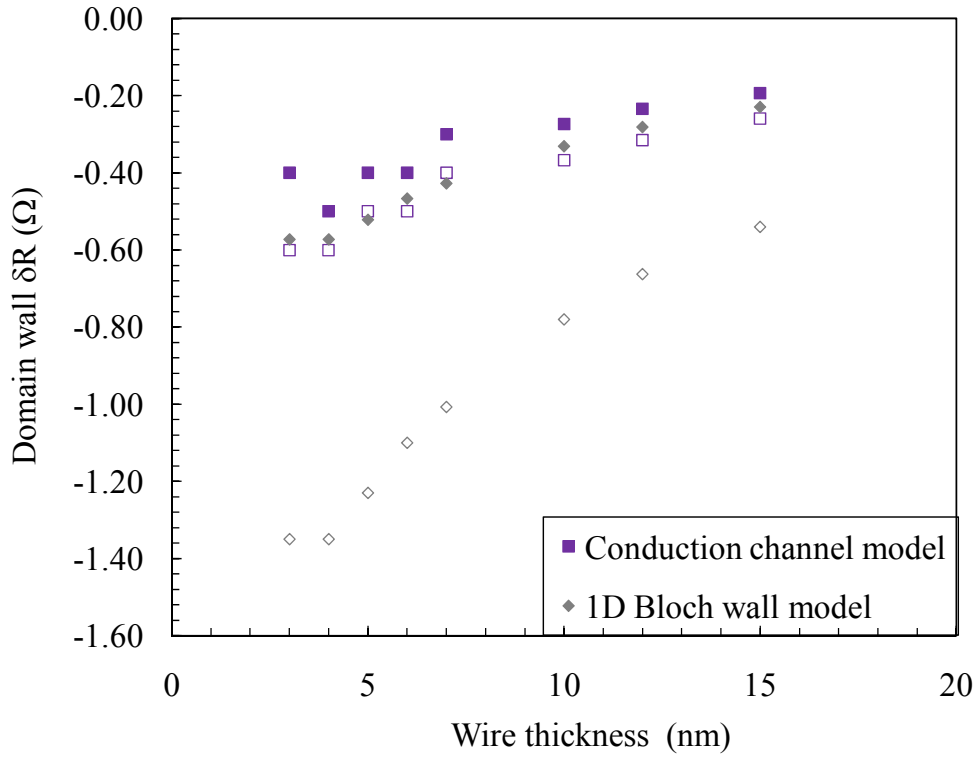

Figure 8:15. Comparison of the thickness dependence of the domain wall resistance in a 300 nm wide wire as deduced from the conduction channels model (■) and from the 1D model (♦), for transverse wall (*solid symbols*) and vortex walls (*open symbols*), respectively.

The large differences between the values vortex wall resistance predicted by the models are clearly visible. It is interesting to note that the values predicted by the 1D model for a transverse wall lie close to those given by this detailed modelling for that of a vortex wall. The proximity in δR for a transverse wall and vortex wall structure could potentially lead to misidentification of a wall structure in experimental measurements.

8.5.2 Domain wall resistance using resistivity parameters measured in this study

Figure 8:16 compares values of domain wall resistance as a function of wire width and thickness calculated using the 1D Bloch wall width model and conduction channel model calculated using thickness dependent resistivity parameters presented in Table 8:2. The overall changes in resistance given by these values are much smaller than those presented in Figure 8:14, which is the direct result of the much smaller values of $\delta\rho$ and consequently $\delta\rho/\rho_{ave}$.

(a) Simple 1D Bloch wall width model

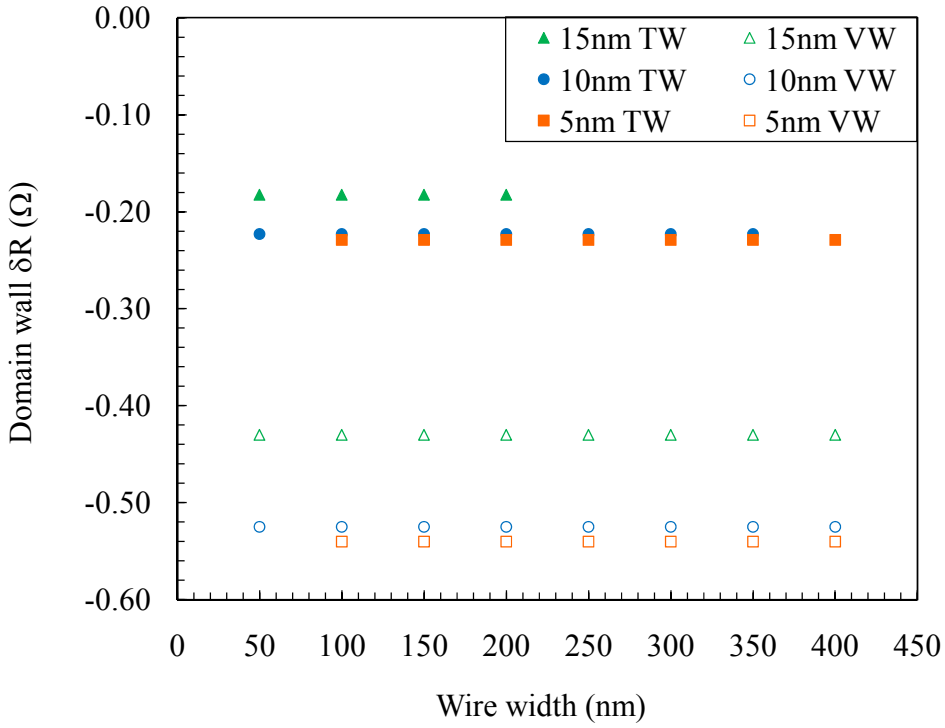

(b) Conduction channel model

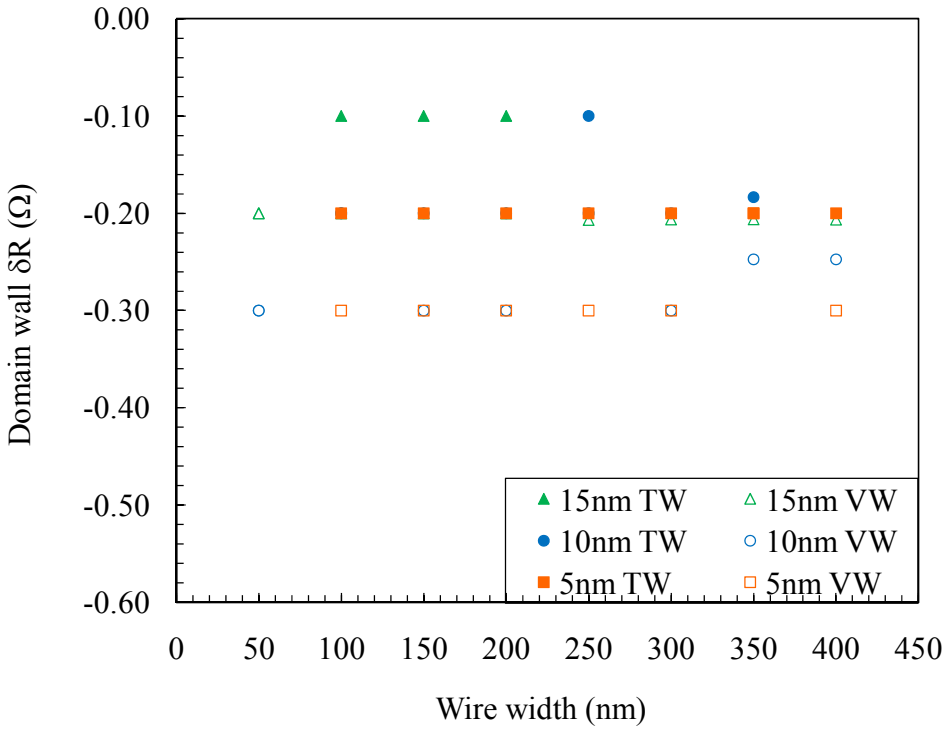

Figure 8:16. Domain wall resistance as a function of wire width for 5 nm, 10 nm and 15 nm thick nanowires deduced using (a) the simple model using the 1D Bloch wall width parameters and (b) the conduction channel model and thickness dependent resistivity parameters deduced from lines of best fit to data presented in Figure 8:13. In each graph the lines are guides to the eye only.

In the 1D model, the smaller values of $\delta\rho$ only affect the magnitude of the predicted δR values. The general trends observed in Figure 8:14 remain the same in that the resistance of a vortex wall is almost three times larger than that for the transverse wall structure in a wire of the same thickness. The greatest change in resistance occurs for a vortex domain wall in a 5 nm; as wire thickness increases the domain wall resistance decreases. Interestingly, there is no overlap in signals from transverse and vortex wall structures in wires of different thicknesses, as there was Figure 8:14 (a), and it is suggested that this is because of the smaller values of $\delta\rho$ measured within this study.

The incorporation of values of $\delta\rho$ measured from this study into the conduction channel model leads to very different values of domain wall resistance as shown in Figure 8:16 (b). Unlike for the data presented in Figure 8:14 (a), there is no coherent dependence of δR upon either wall structure or nanowire thickness. In general, the vortex domain walls cause a larger drop in the resistance of the nanowire than the transverse walls, although this is not as clear cut as the data presented in Figure 8:14 (b). It is clear from Figure 8:14 (a) and (b) that the magnitude of $\delta\rho$ significantly affects the predicted domain wall resistance, and therefore highlights the importance of reasonable values of $\delta\rho$ in addition to thorough knowledge of the domain wall spin structure.

Figure 8:17 presents domain wall resistance values for transverse and vortex walls in a 300 nm wide wire as a function of film thickness calculated by both the simple 1D model (♦) and detailed modelling approach using values of the AMR ratio obtained in this study (■). A similar trend is seen to that presented in Figure 8:15, and it is clear that the resistance of a transverse wall is smaller than that of a vortex wall. This is attributed to vortex walls being larger and hence containing more off-axis spins. Domain wall resistance values given by the 1D model are larger for both transverse and vortex domain walls, although the smaller $\delta\rho$ values leads to less overlap between values of the transverse wall resistance measured by the 1D model and the vortex walls given by the detailed modelling.

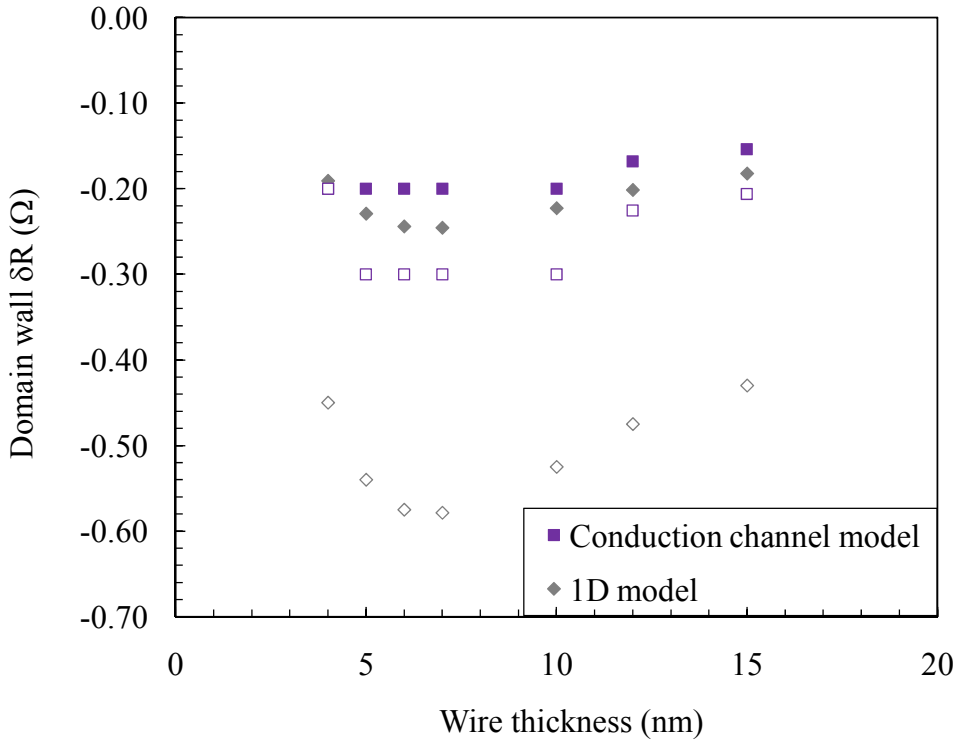

Figure 8:17. Comparison of the thickness dependence of the domain wall resistance in a 300 nm wide wire as deduced from the conduction channels model (■) and from the 1D model (♦), for transverse wall (*solid symbols*) and vortex walls (*open symbols*), respectively.

8.6 Further work and development of the electrical conduction channel model

High sensitivity anisotropic magnetoresistance measurements of carefully designed $Ni_{81}Fe_{19}$ nanowires could be used as a rigorous test of the validity of electrical conduction channel model developed within this thesis. Figure 8:18 presents a schematic diagram of an L-shaped nanowire which could be used to measure the change in resistance δR due to the presence of a domain wall. In this nanowire geometry, a domain wall will be nucleated and injected into the nanowire through the application of a magnetic field in the y direction. Once injected, the domain wall will propagate along the nanowire toward the curved region. The domain wall will remain pinned in the curved region of the nanowire until a suitable field in the x direction is applied, and so provided an electrical measurement is made before H_x is applied then a value of δR can be obtained. Only one domain wall is injected per field reversal cycle.

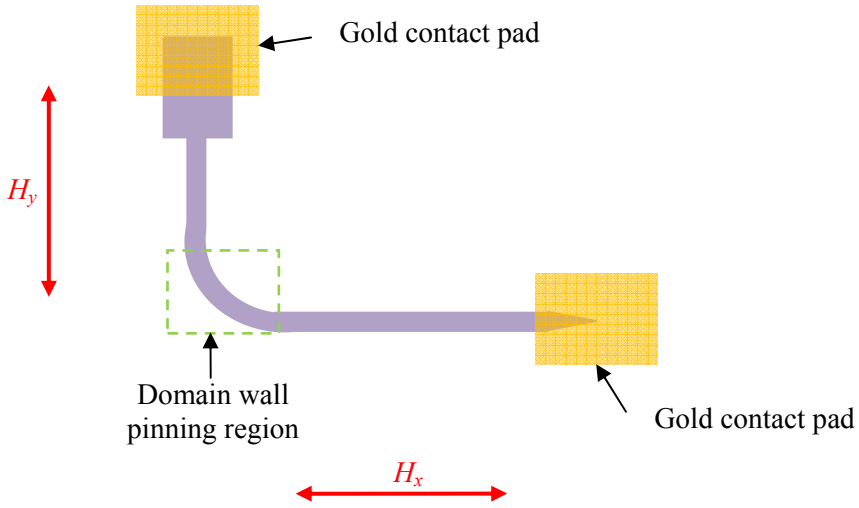

Figure 8:18. Schematic to show suggest design of an L-shaped nanowire structure that could be used to test the electrical conduction channel model developed within this chapter. A domain wall would be nucleated, and subsequently injected, into the nanowire through the application of a magnetic field in the *y* direction where it will pin in the curved region of the nanowire until a suitable field in the *x* direction is applied. In each field sequence only one domain wall would be injected into the nanowire allowing δR to be measured which can then be compared to the values predicted by both the 1D model and the electrical conduction channel model.

It is therefore suggested that δR measurements be taken over a large number of field reversal cycles (100 field sweeps would be sensible), as the domain wall may pin in slightly different locations due to the combination of edge roughness and the stochastic nature of pinning behaviour associated with temperature. A large set of resistance measurements for a given nanowire would allow for a mean δR (with an associated standard deviation) to be obtained which can then be compared to the values predicted by both the 1D model and the electrical conduction channel model.

In the first instance, it would be useful to fabricate 300 nm wide nanowires for a variety of nanowire thickness between 3 nm and 20 nm and compare the values of δR to those given in Figure 8:15 and Figure 8:17. Following this, it would be beneficial to measure δR for wires of a given thickness, starting with 5 nm, and investigate the effect of increasing wire width on the change in nanowire resistance. Such measurements should give domain wall resistance values for both transverse and vortex domain wall structures. As discussed in sections 7.2.3 and 7.2.4, micromagnetic simulations showed that for each nanowire thickness, both favourable and unfavourable domain wall structures are able to exist for a selection of nanowire widths. Thus, if this is the case, then values of δR for 100

field reversal cycles will exhibit two distinct populations of values with the higher frequency population corresponding to that of the energetically favourable structure. Such measurements would then also be useful in supporting the results obtained from micromagnetic simulations in section 7.2.

The exact nature of making good electrical contact to nanowire structures is beyond the scope of the work presented here; however, in reference [148], for example, electrical measurements of nanowire structures have been reported for $Ni_{81}Fe_{19}$ nanowires using gold contact pads with a chromium underlayer. Thus, it would also be necessary to measure values of $\rho_{\parallel}$ and $\rho_{\perp}$ for $Ni_{81}Fe_{19}$ thin films with Cr/Au underlayers so that any the effect of scattering at the SiO_2/Cr/Au/$Ni_{81}Fe_{19}$ interface may be accounted for.

8.7 Chapter conclusion

In this chapter the change in the electrical resistance of a nanowire due to the presence of a domain wall has been examined. The form of the 1D model commonly used to interpret values of domain wall resistance has been described, and the limitations of this model have been explored. This has included an analysis of the detailed magnetisation reversal profiles within both transverse and vortex wall structures, and a discussion of why the 1D Bloch wall profile does not provide an accurate description of the domain wall width in $Ni_{81}Fe_{19}$ nanowire structures. Thickness dependent resistivity parameters given in the literature and also measured here have been presented and compared.

A detailed model of domain wall resistance has been developed which is based upon the micromagnetic structure of vortex and transverse walls and which incorporates experimentally determined thickness dependence of the resistivity to map the width and thickness dependence of wall resistance in $Ni_{81}Fe_{19}$ nanowires. For a given nanowire structure the difference between the domain wall resistance of vortex and transverse walls is found to be significantly less than that predicted by the 1D model. Finally, although the detailed modelling takes individual spin magnetic moments into account, the sensitivity of the conduction channel model is ultimately limited by the value of $\delta\rho$ at each thickness. It is therefore imperative to characterise the magnetoresistance behaviour of thin films before using magnetoresistance as a tool to identify the presence of domain walls as the thin film resistivity and anisotropic magnetoresistance is extremely sensitive to the preparation conditions; it is not enough to rely on values of $\delta\rho$ provided in the literature.

Chapter 9. Conclusions

The study of the thickness dependence of the magnetic and magnetoresistance behaviour of $Ni_{81}Fe_{19}$ thin films and nanowire structures has allowed for a thorough understanding of the effect of geometrical confinement on domain wall structure and pinning behaviour to be developed. $Ni_{81}Fe_{19}$ thin films between 3 nm and 40 nm thick were fabricated using thermal evaporation at stable deposition rates of 0.5 Å/s, 1.0 Å/s and 2.0 Å/s on pre-oxidised silicon substrates.

In chapter 5 x-ray scattering measurements were used to characterise the out-of-plane structure of $Ni_{81}Fe_{19}$ thin films. X-ray reflectivity measurements were used to provide accurate measurements of $Ni_{81}Fe_{19}$ film thicknesses and to quantify the width of the $SiO_2/Ni_{81}Fe_{19}$ interface. Best fit simulations to the measured data suggest that all films are continuous in the out-of-plane direction, and are capped with 1 nm thick natural oxide layer, which was found to independent of both deposition rate and film thickness and perhaps also expands over time. Direct interpretation of x-ray diffraction data suggests that these films are largely (111) textured in the out-of-plane direction. For all film thicknesses investigated, the location of the Bragg angle for the (111) plane was shifted from that of the bulk and it is suggested that the growth of the initial few layers of nickel-iron upon the SiO_2 substrate are strained by up to 0.17% from the bulk value due to the shortening of bonds at the interface. The out-of-plane lattice parameter of subsequent $Ni_{81}Fe_{19}$ layers was 0.99% less than that of the bulk value. A combination of x-ray diffraction measurements and high resolution transmission electron microscopy reveal that the thin film microstructure was characterised by a small crystallite grain size, of typical size 6 nm, which displayed a weak dependence on film thickness and was independent of the deposition rate.

The magnetic and magnetoresistance behaviour of $Ni_{81}Fe_{19}$ thin films were investigated in chapter 6. The normalised MOKE signal was observed to be proportional to film thickness until the penetration depth of the incident laser light was reached (approximately 15 nm for incident light of wavelength 658 nm), beyond which the signal asymptotically reduced toward the maximum. Vibrating sample magnetometry (VSM) measurements revealed that the magnetic moment per cross-sectional area was linearly proportional to the film thickness which was in good agreement with the results obtained from MOKE. The shape of the MOKE hysteresis loops suggest that there was no

systematic anisotropy present, whilst coercivity measurements revealed that all films are very soft, as is expected for NiFe alloys of this composition. The lack of a systematic dependence of coercivity upon film thickness, down to the thinnest films, combined with the clear thickness dependence of both the MOKE signal and VSM measurements suggested that all films were ferromagnetic and continuous, with no magnetic dead layer present at the substrate interface.

Electrical resistance measurements showed that the thin film resistivity, ρ_{ave}, increases as film thickness decreases, which was consistent with the Fuchs-Sondheimer surface scattering model. In general, the thin film resistivity observed here was larger than reported previously in the literature, which was understood to be the result of the increased scattering associated with small crystallite grains. Moreover, the anisotropic magnetoresistance, $\delta\rho$, is observed to be strongly dependent upon on film thickness for $t < 10$ nm, and tends toward zero for $t < 7$ nm. This thickness dependence was larger than has previously reported in the literature, where it was suggested that $\delta\rho$ should be independent of film thickness for $Ni_{81}Fe_{19}$ films. It was suggested that the loss of AMR observed here was due to an increase in magnetostriction as film thickness decreases, which was caused by the change in the out of plane lattice parameter and the associated residual stress at the $SiO_2/Ni_{81}Fe_{19}$ interface. The anisotropic magnetoresistance ratio, $\delta\rho/\rho_{ave}$, measured in this study was significantly less than has previously been reported for bulk $Ni_{81}Fe_{19}$, and this has been attributed to the strong thickness dependence of the anisotropic magnetoresistance.

Chapter 7 presented a systematic study into domain wall structure and pinning as a function of geometrical confinement within planar nanowires. Magneto-optical Kerr effect magnetometry, differential phase contrast Lorentz transmission electron microscopy imaging and OOMMF micromagnetic simulations were used to provide detailed information into the nature of domain wall pinning behaviour as a function of nanowire width and notch geometry. It was observed that domain wall pinning is largely determined by the wire width and thickness. When the notch dimensions were comparable in size to the domain wall width, the detailed geometry of the notch was found to be of secondary importance to the domain wall depinning field. Indeed, it was also observed that for a given domain wall structure (transverse or vortex) experienced very similar depinning fields from both triangular and rectangular notches of the same depth and width.

Micromagnetic simulations have shown that a given notch structure may act as either a potential well or as a potential barrier, which is determined by the micromagnetic structure of the domain wall that is interacting with the notch. In addition, micromagnetic simulations also suggest that the spatial extent of the potential well extends far beyond the physical size of the notch due to the finite size of the domain wall. Moreover, pinning site saturation was observed to occur when the notch depth to wire width ratio exceeds approximately 0.6. These results are important in the optimisation of both field and current-driven domain wall propagation and pinning behaviour in nanowires.

In chapter 8, the change in the electrical resistance of a nanowire due to the presence of a domain wall was examined. A detailed model was developed to predict the change in resistance of a nanowire due to the presence of a domain wall and compared to a much simpler one dimensional model that is currently widely used in the literature. The approach developed here takes both thickness dependent resistivity parameters and the detailed micromagnetic structure of a domain wall into account, and the nanowire has been modelled as a network of electrical conduction channels. For a given nanowire thickness, the difference between the domain wall resistance of vortex and transverse walls was found to be significantly less than that predicted by the one dimensional model that is widely used in the literature. Finally, although the detailed modelling takes individual spin magnetic moments into account, the sensitivity of the conduction channel model was ultimately limited by the magnitude of the anisotropic magnetoresistance ratio. As both thin film resistivity and AMR ratio are extremely sensitive to the preparation conditions (including deposition method, substrate conditions, and the presence and type of under-and capping layers); it is not enough to rely on values provided in the literature. In order to take advantage of the potential sensitivity of anisotropic magnetoresistance to both the presence and structure of a domain wall, it is imperative to fully characterise the magnetoresistance behaviour of thin films before using magnetoresistance as a tool to identify domain walls in planar nanowire structures.

References

[1] Kittel, C., '*Introduction to Solid State Physics'* 7th edition, John Wiley & Sons, New York (1996)

[2] Uhlenbeck, G. E., and Goudsmit, S., *'Ersetzung der Hypothese vom unmechanischen Zwang durch eine Forderung bezgülich des inneren Verhaltens jedes einzelnen Elektrons' (Replacement of the hypothesis of the mechanical obligation by a demand concerning the internal behaviour of individual electrons)* Die Naturwissenschaften **13** (1925) 953-954

[3] Uhlenbeck, G. E., and Goudsmit, S., *'Die Kopplungsmöglichkeiten der Quantenvektoren im Atom' (The coupling possibilities of the quantum vectors in the atom)* Zeitschrift für Physik A **47** (1926) 618-625

[4] Uhlenbeck, G. E, and Goudsmit, S., *'Spinning electrons and the structure of spectra' Nature* **117** (1926) 264-265

[5] Gerlach, W., and Stern, O., *'Das magnetische moment des silberatoms' (Magnetic moments of silver atoms)* Zeitschrift für Physik A **9** (1922) 353-355

[6] Rosenberg, H. M., '*The Solid State'* 3rd edition, Oxford University Press, Bristol (2004)

[7] Cullity, B. D., '*Introduction to Magnetic Materials*', Addison-Wesley, Reading Massachusetts (1972)

[8]'http://physics.nist.gov/cgi-bin/cuu/Value?eqgammae|search_for=gyromagnetic' *accessed 10th May 2010.*

[9] O'Handley, R.C., '*Modern Magnetic Materials: Principles and Applications*' John Wiley & Sons, New York (2000)

[10] Langevin. P., *'Magnétisme et théorie des electrons' (Magnetism and the theory of electrons)* Annales de Chemie et de Physique **5** (1905) 70-127

[11] Morrish, A. H., '*The Physical Principles of Magnetism'* John Wiley & Sons, New York (1965)

[12] Néel, L., *'Influence des fluctuations du champ moléculaire sur les propeirties magnétiques des corps' (The influence of magnetic field fluctuations on the properties of a magnetic body)* Annales de Physique **18** (1932) 5-105

[13] Heisenberg, W., *'Zur theorie des ferromagnetismus' (On the theory of ferromagnetism)* Zeitschrift für Physik A **49** (1928) 619-636

[14] Slater, J.C., *'The ferromagnetism of nickel'* Physical Review **49** (1936) 537-545

[15] Slater, J.C., *'The ferromagnetism of nickel II: temperature effects'* Physical Review **49** (1936) 931-937

[16] Slater, J.C., *'The theory of ferromagnetism: lowest energy levels'* Physical Review **52** (1937) 198-214

[17] Stoner, E.C., *'Collective electron ferromagnetism'* Proceedings of the Royal Society London -Series A **165** (1938) 372-414

[18] Stoner, E.C., *'Collective electron ferromagnetism II: energy and specific heat'* Proceedings of the Royal Society London - Series A **169** (1939) 339-371

[19] Stoner, E.C., *'Collective electron energy and specific heat'* Philosophical Magazine **25** (171) (1938) 899-926

[20] Friedel, J., Leman, G., and Olszewski, S., *'Metals and alloys: on the nature of magnetic couplings in transitional metals'* Journal of Applied Physics **32** (1961) S325-S330

[21] Kittel. C., '*Introduction to Solid State Physics'* 2nd edition, John Wiley & Sons, New York (1956)

[22] Weiss, P., *'La variation du ferromagnétisme avec la temperature' (The variation of ferromagnetism with temperature)* Comptes Rendus **143** (1906) 1136-1139

[23] Weiss, P., *'L'Hypothèse du champ molèculaire et de la propriété ferromagnétique' (The hypothesis of the molecular field and the property of ferromagnetism)* Journal de Physique et le Radium **6** (1907) 661-690

[24] Landau, L.D., and Lifshitz, E., *'On the theory of the dispersion of magnetic permeability in ferromagnetic bodies'* Physikalische Zeitschrift der Sowjetunion **8** (1935) 153-169

[25] Hubert, A., and Schäfer, R., '*Magnetic domains: the analysis of magnetic microstructures'* Springer-Verlag, Berlin (2000)

[26] Aharoni, A., '*Introduction to the theory of ferromagnetism'* Clarendon Press, Oxford (1986)

[27] van Vleck, J. H., *'A survey of the theory of ferromagnetism'* Reviews of Modern Physics **17** (1945) 27-46

[28] Kronmüller H., and Fähnle M., '*Micromagnetisation and the microstructure of ferromagnetic solids'* Cambridge University Press, Cambridge (2003)

[29] Mader, S., and Nowick, A.S., *'Metastable Co-Au alloys; examples of an amorphous ferromagnet'* Applied Physics Letters **7** (1965) 57-59

[30] Barkhausen, H., *'Zwei mit Hilfe der neuen Verstärker entdeckte Erscheinungen' (Two phenomena, discovered with the help of the new amplifiers)* Zeitschrift für Physik **20** (1919) 401-403

[31] Sixtus, K. J., and Tonks, L., *'Propagation of large Barkhausen discontinuities'* Physical Review **37** (1931) 930-958

[32] Bloch, F., *'Zur theorie des austauschproblems und der remanenzerscheinung der ferromagnetika' (On the theory of the exchange problem and the remanence phenomenon of ferromagnets)* Zeitschrift für Physik **74** (1932) 295-335

[33] Honda, K., and Kaya, S., *'On the magnetisation of single crystals of iron'* Scientific Reports of Tohoku Imperial University **15** (1926) 721-754

[34] Becker, R., *'Zur theorie der magnetisierungskurve' (On the theory of the magnetisation curve)* Zeitschrift für Physik **62** (1930) 253-269

[35] Akulov, N. S., *'Zur theorie der magnetisierungskurve von einkristallen' (On the theory of the magnetisation curve of single crystals)* Zeitschrift für Physik **67** (1931) 794-807

[36] Becker, R., *'Elastische spannungen und magnetische eigenschaften' (Flexible tensions and magnetic characteristics)* Zeitschrift für Physik **33** (1932) 905-913

[37] Becker, R., and Döring, W., *'Ferromagnetismus'* Springer, Berlin (1939)

[38] Bitter, F., *'Experiments on the nature of ferromagnetism'* Physical Review **41** (1932) 507-515

[39] Frenkel, J., and Dorfman, J., *'Spontaneous and induced magnetisation in ferromagnetic bodies'* Nature **126** (1930) 274-275

[40] Heisenberg, W., *'Zur theorie der magnetostriktion und der magnetisierungskurve' (On the theory of magnetostriction and the magnetisation curve)* Zeitschrift für Physik **69** (1931) 287-297

[41] Stoner, E. C., and Wohlfarth, E. P., *'A mechanism of magnetic hysteresis in heterogeneous alloys'* Philosophical Transactions of the Royal Society London -Series A **240** (1948) 599-644

[42] Kittel, C., *'Physical theory of ferromagnetic domains'* Reviews of Modern Physics **21** (1949) 541-583

[43] Brown, W. F., Jr *'Micromagnetics'* Interscience Publishers, New York (1963)

[44] Brown, W. J., Jr. *'Ferromagnetic domains and the magnetisation curve'* Journal of Applied Physics **11** (1940) 160-172

[45] Brown, W. J., Jr *'Theory of the approach to magnetic saturation'* Physical Review **58** (1940) 736-743

[46] Brown, W. J., Jr '*The effect of dislocations on magnetisation near saturation'* Physical Review **60** (1941) 139-147

[47] Brown, W. J., Jr *'Virtues and weaknesses of the domain concept'* Reviews of Modern Physics **17** (1941) 15-19

[48] Kittel, C., *'Theory of the structure of ferromagnetic domains in films and small particles'* Physical Review **70** (1946) 965-971

[49] Honda, K., and Kaya, S., *'On the magnetisation of single crystals of iron'* Scientific Reports of Tohoku University **15** (1926) 721-753

[50] Kaya, S., *'On the magnetisation of single crystals of nickel*' Scientific Reports of Tohoku University **17** (1928) 639-663

[51] Kaya, S., *'On the magnetisation of single crystals of cobalt'* Scientific Reports of Tohoku University **17** (1928) 1157-1177

[52] Bozorth, R. M., *'Directional ferromagnetic properties of metals'* Journal of Applied Physics **8** (1937) 575-588

[53] Bozorth, R. M., *'Ferromagnetism'*, Van Nostrand, London (1951)

[54] van Vleck, J. H., *'Quelques aspects de la théorie du magnétisme' (Aspects on the theory of magnetism)* Annales de l'Institut Henri Poincaré **10** (1947) 27-47

[55] Bozorth, R. M., and Walker, J. G., *'Magnetic crystal anisotropy and magnetostriction of iron-nickel alloys'* Physical Review **89** (1953) 624-628

[56] Lilley, B. A., *'Energies and widths of domain boundaries in ferromagnetics'* Philosophical Magazine **41** (1950) 792-813

[57] Middelhoek, S., *'Domain walls in thin Ni-Fe films'* Journal of Applied Physics **34** (1963) 1054-1059

[58] Néel, L., *'Energie des parois de Bloch dans les couches minces' (Bloch wall energy in thin films)* Comptes Rendus de l'Académie des Sciences **241** (1955) 533-536

[59] Huber, E. E., Smith, D. O., and Goodenough, J. B., *'Domain wall structure in permalloy films'* Journal of Applied Physics **29** (1958) 294-295

[60] McMichael, R.D., and Donahue, M. J., *'Head to head domain wall structures in thin magnetic strips'* IEEE Transactions on Magnetics **33** (1997) 4167-4169

[61] Nakatani, Y., Thiaville, A., and Miltat, J., *'Head-to-head domain walls in soft nanostrips: a refined phase diagram'* Journal of Magnetism and Magnetic Materials **290** (2005) 750-753

[62] Allwood, D. A., Xiong, G., Faulkner, C. C., Atkinson, D., Petit, D., and Cowburn, R. P., *'Magnetic domain wall logic'* Science **309** (2005) 1688-1692

[63] Diegel, M., Mattheis, R., and Halder E., *'360° domain wall investigation for sensor applications'* IEEE Transactions of Magnetics **40** (2004) 2655-2657

[64] Atkinson, D., Eastwood, D.S., and Bogart, L. K., *'Controlling domain wall pinning in planar nanowires by selecting domain wall type and its application in a memory concept'* Applied Physics Letters **92** (2008) 022510

[65] Allwood, D. A., Xiong, G., Faulkner, C. C., Atkinson, D., Vernier, N., and Cowburn, R. P., '*Submicrometer ferromagnetic NOT gate and shift register'* Science **296** (2002) 2003-2006

[66] Broers, A. N., *'Resolution limits for electron-beam lithography'* IBM Journal of Research and Development **32** (1988) 502-513

[67] Atkinson, D., *'Patterning nanostructures to study magnetisation processes'* Journal of Physics: Conference Series **17** (2005) 33-39

[68] Röntgen, W. C., *'On a new kind of radiation'* Nature **53** (1896) 274-276

[69] Als-Nielsen, J., and McMorrow, D., '*Elements of modern X-ray physics'* Wiley, Chichester (2001)

[70] 'http://www.kayelaby.npl.co.uk/chemistry/3_1/3_1_2.html' *accessed on 26th January 2010*

[71] 'http://hence.lbl.gov/optical_constants/' *accessed 26th January 2010*

[72] Kiessig, H., *'Interferenz von Röntgenstrahlen an dünnen Schichten'* (Interference of x-rays in thin layers) Annalen der Physik **402** (1931) 715-725 & 769-788

[73] *Bede REFS (version 4.5): User Manual*, Bede plc, Durham (2007) available from Jordan Valley PLC

[74] Parratt, L. G., *'Surface studies of solids by total reflection of x-rays'* Physical Review **95** (1954) 359-369

[75] Wormington, M., Panaccione, C., Matney, K.M., and Bowen, D.K., *'Characterization of structures from X-ray scattering data using genetic algorithms'* Philosophical Transactions of the Royal Society of London - Series A **357** (1999) 2827-2848

[76] Bragg, W. L., *'The structure of some crystals as indicated by their diffraction of x-rays'* Proceedings of the Royal Society of London - Series A **89** (1913) 248-277

[77] Laue, M., *'Eine quantitative Prüfung der Theorie für die Interferenzerscheinungen bei Röntgenstrahlen' (A quantitative examination of the theory for interference features with x-rays)* Proceedings of the Bavarian Academy of Sciences (1912) 363-373

[78] 'http://webelements.com/silicon/crystal_structure.html' *accessed on 3rd March 2010*

[79] Faraday, M., *'On the magnetisation of light and the illumination of magnetic lines of force'* Philosophical Transactions of the Royal Society (London) **136** (1846) 1-20

[80] Kerr, J., *'On rotation of the plane of polarisation by reflection from the pole of a magnet'* Philosophical Magazine **3** (1877) 321-343

[81] Kerr, J., *'On reflection of polarised light from the equatorial surface of a magnet'* Philosophical Magazine **5** (1877) 161-177

[82] Allwood, D.A., Xiong, G., Cooke, M. D., and Cowburn, R. P, *'Magneto-optical Kerr effect analysis of magnetic nanostructures'* Journal of Physics D: Applied Physics **36** (2003) 2175-2182

[83] Fowler, Jr., C. A., and Fryer, E. M., *'Magnetic domains on silicon iron by the longitudinal Kerr effect'* Physical Review **86** (1953) 426

[84] Qiu, Z. Q., and Bader, S. D., *'Surface magneto-optical Kerr effect'* Review of Scientific Instruments **71** (2000) 1243-1255

[85] Miyahara, T., and Takahashi, M., *'The dependence of the longitudinal Kerr magneto-optic effect on saturation magnetisation in NiFe films'* Japanese Journal of Applied Physics **15** (1976) 291-298

[86] Lide, D. R., *'CRC Handbook of Chemistry and Physics'* 73rd Edition, CRC Press, Boca Raton (1992)

[87] Gilbert, T.L., *'A Lagrangian formulation of the gyromagnetic equation of the magnetisation field'* Physical Review **100** (1955) 1243

[88] Donahue, M. J., and Porter, D. G., *'OOMMF user's guide, version 1.0'* Technical Report No. NISTIR 6376, National Institute of Standards and Technology, Gaithersburg (1999)

[89] 'http://math.nist.gov/oommf'

[90] Nibarger, J. P., Lopusnik, R., Celinski, Z., and Silva, T. J., *'Variation of magnetisation and the Landé g factor with thickness in NiFe films'* Applied Physics Letters **83** (2003) 93-95

[91] Schryer, N. L., and Walker, L. R., *'The motion of 180° domain walls in uniform dc magnetic fields'* Journal of Applied Physics **45** (1974) 5406-5421

[92] Nakatani, Y., Thiaville, A., and Miltat, J., *'Faster magnetic walls in rough wires'* Nature Materials **2** (2003) 521-523

[93] Donahue, M. J., and McMichael, R. D., *'Exchange energy representations in computational micromagnetics'* Physica B **233** (1997) 272-278

[94] Newell, A.J., Williams, W., and Dunlop, D. J., *'A generalization of the demagnetizing tensor for non uniform magnetisation'* Journal of Geophysical Research - Solid Earth **98** (1993) 9551-9555

[95] Aharoni, A., *'Demagnetizing factors for rectangular ferromagnetic prisms'* Journal of Applied Physics **83** (1999) 3432-3434

[96] Mott, N. F., *'The electrical conductivity of transition metals'* Proceedings of the Royal Society **153** (1936) 699-717

[97] Campbell, I. A., and Fert, A., *'Transport properties of ferromagnets'* in *'Ferromagnetic materials'* Vol. 3., Edited by Wohlfarth, E. P., North Holland Publishing Company, Amsterdam (1982)

[98] Thomson, W., *'On the electro-dynamic qualities of metals: effects of magnetisation on the electric conductivity of nickel and iron'* Proceedings of the Royal Society **8** (1857) 546-550

[99] McGuire, T.R., and Potter, R. I., *'Anisotropic magnetoresistance in ferromagnetic 3d alloys'* IEEE Transactions on Magnetics **11** (1975) 1018-1040

[100] Smit, J., *'Magnetoresistance of ferromagnetic metals and alloys at low temperatures'* Physica **16** (1951) 612-627

[101] Armstrong, H., *'Magnetoresistance measurement system instruction manual v1.0'* ChiralMEM Technical Note HA3, Durham University (2010)

[102] Parkin, S., and Thomas, L., *'Current induced domain wall motion in magnetic nanowires'* Handbook of Magnetism and Magnetic Materials Vol. 2, Edited by Kronmüller, H., and Parkin, S., Eds, Wiley, Barcelona (2007)

[103] '*Two-piece spring probe P25-XX22*' Customer Information Sheet, Harwin U.K PLC

[104] *'Low level measurements handbook: precision DC current, voltage, and resistance measurements'* 6th edition, Keithley Instruments, Inc., Cleveland Ohio, (2004)

[105] Parkin, S. S. P., Kaiser, C., Panchula, A., Rice, P. M., Hughes, B., Samant, M., and Yang, S-H., *'Giant tunnelling magnetoresistance at room temperature with MgO (100) tunnel barriers'* Nature Materials **3** (2004) 862-867

[106] Yuasa, S., Nagahama, T., Fukushima, A., Suzuki, Y., and Ando, K., *'Giant room-temperature magnetoresistance in single-crystal Fe/MgO/Fe magnetic tunnel junctions'* Nature Materials **3** (2004) 868-871

[107] Gallagher, W. J., and Parkin, S. S. P., *'Dependence of the magnetic tunnel junction MRAM at IBM: from first junctions to a 16-Mb MRAM demonstrator chip'* IBM Journal of Research and Development **50** (2006) 333-333

[108] Bland, J. A. C., Johnson, A. D., Norris, C., and Lauter, H. J., *'Absolute value of the magnetic moment per atom in Ag/Fe/Ag (001) and Ag/Co/Ag(001) epitaxial sandwich structures'* Journal of Applied Physics **67** (1990) 5397-5399

[109] Song, O., Ballentine, C. A., and O'Handley, R. C., *'Giant surface magnetostriction in polycrystalline Ni and NiFe films'* Applied Physics Letters **64** (1994) 2593-2595

[110] Atkinson, D., *in private communication* (2010)

[111] Hollingworth, M. P., Gibbs, M. R. J., and Murdoch, S. J., *'Magnetostriction and surface roughness of ultrathin NiFe films deposited on SiO_2'* Journal of Applied Physics **94** (2003) 7235-7239

[112] Kim, Y.K., and Silva, T. J., *'Magnetostriction characteristics of ultrathin permalloy films'* Applied Physics Letters **68** (1996) 2885-2886

[113] Hatton, H.J., and Gibbs, M. R. J., *'Interface contributions to magnetostriction in transition metal based soft magnetic multilayers'* Journal of Magnetism and Magnetic Materials **156** (1996) 67-68

[114] Birkholz, M., '*Thin film analysis by X-ray scattering*' Wiley-VCH, Weinheim (2006)

[115] Bowen, D. K., and Tanner, B. K., *'X-ray metrology in semiconductor manufacturing'* Taylor and Francis, London (2006)

[116] Bevington, P. R., Robinson, D. K., '*Data reduction and error analysis for the physical sciences*' 2nd edition, McGraw-Hill, New York (1992)

[117] Cullity, B.D., '*Elements of x-ray diffraction'* 2nd Edition, Addison-Wesley, Reading Massachusetts (1978)

[118] Mendis, B. G., *in private communication* (2010)

[119] Mitchell, E.N., Haukaas, H.B., Bale, H. D., and Streeper, J. B., *'Compositional and thickness dependence of ferromagnetic anisotropy in resistance of iron-nickel films'* Journal of Applied Physics **35** (1964) 2604-2608

[120] Williams, F.C., and Mitchell, E. N., '*A study of resistance and magnetoresistance in nickel-iron thin films'* Japanese Journal of Applied Physics **7** (1968) 739-742

[121] Mayadas, A. F., Janak, J.F., and Gangulee A., *'Resistivity of permalloy thin films'* Journal of Applied Physics **45** (1974) 2780-2781

[122] Miyazaki, T., Ajima, T., and Sato, F., *'Dependence of magnetoresistance on thickness and substrate temperature for 82Ni-Fe alloy film'* Journal of Magnetism and Magnetic Materials **81** (1989) 86-90

[123] Bogart, L. K., and Atkinson, D., *'Domain wall anisotropic magnetoresistance in planar nanowires'* Applied Physics Letters **94** (2009) 042511

[124] Krzyk, S., Schmidsfeld, A., Klaui, M., and Rudiger, U., *'Magnetotransport effects of ultrathin $Ni_{80}Fe_{20}$ films probed in situ'* New Journal of Physics **12** (2010) 013001

[125] Funaki, H., Okamoto, S., Kitakami, O., and Shimada, Y., *'Improvement in magnetoresistance of very thin permalloy films by post-annealing'* Japanese Journal of Applied Physics part 2 **33** (1994) L1304

[126] Lee, W. Y., Toney, M. F., Tameerug, P., Allen, E., and Mauri, D., *'High magnetoresistance permalloy films deposited on a thin NiFeCr or NiCr underlayer'* Journal of Applied Physics **87** (2000) 6992-6994

[127] Fassbender, J., von Borany, J., Mücklich, A., Potzger, K., and Möller, *'Structural and magnetic modifications of Cr-implanted Permalloy'* Physical Review B **73** (2006) 184410

[128] Ding, L., Teng, J., Zhan, Q., Feng, C., Li, M.-H., Han, G., Wang, L-J., Yu, G-H., and Wang, S-Y., *'Enhancement of the magnetic field sensitivity in Al_2O_3 encapsulated NiFe films with anisotropic magnetoresistance'* Applied Physics Letters **94** (2009) 162506

[129] Snoek, J. L., *'The Weiss-Heisenberg theory of ferromagnetism and a new rule concerning magnetostriction and magnetoresistance'* Nature **163** (1949) 837-838

[130] Moog, E. R., Zak, J., Huberman, M. L., and Bader S. D., *'Magneto-optic rotation and ellipticity of ultrathin ferromagnetic films'* Physical Review B **39** (1989) 9496 - 9499

[131] Moog, E.R., Liu, C., Bader, S.D., and Zak, J., *'Thickness and polarisation dependence of the magneto-optic signal from ultrathin ferromagnetic films'* Physical Review B **39** (1989) 6949-6956

[132] Hayashi, K., Sawada, M., Yamagami, H., Kimura, A., and Kakizaki, A., *'Magnetic dead layers in Fe films induced by a lattice mismatch at an interface'* Physica B: Condensed Matter **351** (2004) 324-327

[133] Yu, G. H., Zhao, H. C., Li, M. H., Zhu F. W., and Lai, W. Y., *'Interface reaction of Ta/$Ni_{81}Fe_{19}$ or $Ni_{81}Fe_{19}$/Ta and its suppression'* Applied Physics Letters **80** (2002) 455-457

[134] Ridler, A., *in private communication* (2007)

[135] Akhter, M.A., Mapps, D. J., and Ma Tan, Y. Q., '*Thickness and grain size dependence of the coercivity in permalloy thin films'* Journal of Applied Physics **81** (1997) 4122 - 4124

[136] Fuchs, K., *'Conductivity of thin metallic films'* Proceedings of the Cambridge Philosophical Society **34** (1938) 100-108

[137] Lovell, A. C. B., *'The electrical conductivity of thin metallic films. I. rubidium on pyrex glass surfaces'* Proceedings of the Royal Society **157** (1936) 311-330

[138] Appleyard, E. T. S., and Lovell, A.C.B., *'The electrical conductivity of thin metallic films II: Caesium and potassium on pyrex glass surfaces'* Proceedings of the Royal Society **158** (1937) 718-728

[139] Sondheimer, E.H., *'The mean free path of electrons in metals'* Advances in Physics **1** (1952) 1-42.

[140] Kaya, S., *'Die überstrukturbildung in den nickel-eisen legierungen und das permalloy problem' (The superstructure formation into nickel-iron alloys and the permalloy problem)* Journal of the Faculty of Science Hokkaido Universtiy 2 (1938) 29-53

[141] Mayadas, A. F., and Shatzkes, M., *'Electrical-resistivity model for polycrystalline film: the case of arbitrary reflection at external surfaces'* Physical Review B **1** (1970) 1382-1388

[142] Dieny, B., Li, M., Liao, S. H., Horng, C., and Ju, K., *'Effect of interfacial specular electron reflection on the anisotropic magnetoresistance of magnetic thin films'* Journal of Applied Physics **88** (2000) 4140-4145

[143] Ounadjela, K., Lefakis, H., Speriosu, V. S., Hwang, C., and Alexopoulos, P. S., *'Thickness dependence of magnetisation and magnetostriction of NiFe and NiFeRh films'* Journal de Physique **12** (1988) 1709-1710

[144] Néel, L, *'Anisotropie magnetique superficielle et surstructures dorientation' (Surface magnetic anisotropy and the orientation of superstructures)* Journal de Physique et la Radium **15** (1954) 225-239

[145] Parkin, S. S. P., U. S. Patents 6,834,005, 6,898,132, 6,920,062, 7,031,178 and 7, 236,386 (2004 to 2007)

[146] Klaui, M., *'Head to head domain walls in magnetic nanostructures'* Journal of Physics: Condensed Matter **20** (2008) 313001

[147] Parkin, S, S, P., Hayashi, M., and Thomas, L., *'Magnetic domain-wall racetrack memory'* Science **320** (2008) 190-194

[148] Hayashi, M., Thomas, L., Rettner, C., Moriya, R., Jiang, X., and Parkin, S. S. P., *'Dependence of current and field driven depinning of domain walls on their structure and chirality in permalloy nanowires'* Physical Review Letters **97** (2006) 207205

[149] Cowburn, R. P., Allwood, D. A., Xiong, G., and Cooke, M. D., *'Domain wall injection and propagation in planar permalloy nanowires'* Journal of Applied Physics **91** (2002) 6949-6951

[150] Kirk, K. J., Chapman, J. N., McVitie, S., Aitchison, P. R., and Wilkinson, C. D. W., *'Switching of nanoscale magnetic elements'* Applied Physics Letters **75** (1999) 3683-3685

[151] McVitie, S., *in private communication* (2008)

[152] Petit, D., Jausovec, A. V., Read, D., and Cowburn, R. P., *'Domain wall pinning and potential landscapes created by constrictions and protrusions in ferromagnetic nanowires'* Journal of Applied Physics **103** (2008) 114307

[153] O'Shea, K. J., *in private communication* (2008)

[154] Himeno, A., Okuno, T., Ono, T., Mibu, K., Nasu, S., and Shinjo, T., *'Temperature dependence of depinning fields in submicron magnetic nanowires with an artificial neck'* Journal of Magnetism and Magnetic Materials **286** (2005) 167-170

[155] Cowburn, R. P., *'Superparagmagnetism and the future of magnetic random access memory'* Journal of Applied Physics **93** (2003) 9310-9315

[156] Lendecke, P., Eiselt, R., Meier, G., and Merkt, U., *'Temperature dependence of domain wall depinning fields in constricted permalloy nanowires'* Journal of Applied Physics **103** (2008) 073909

[157] Klaui, M., Ehrke, H., Rüdiger, U., Kasama, T., Dunin-Borkowski, R. E., Backes, D., Heyderman, L. J., Vaz, C. A. F., Bland, J. A. C., Faini, G., Cambril, E., and Wernsdorfer, W., *'Direct observation of domain wall pinning at nanoscale constrictions'* Applied Physics Letters **87** (2005) 102509

[158] Faulkner, C. C., Cooke, M. D., Allwood, D. A., Petit, D., and Atkinson, D., *'Artificial domain wall nanotraps in $Ni_{81}Fe_{19}$ wires'* Journal of Applied Physics **95** (2004) 6717- 6719

[159] O'Shea, K. J., McVitie, S., Chapman, J. N., and Weaver, J. M. R., *'Direct observation of changes to domain wall structures in magnetic nanowires of varying width'* Applied Physics Letters **93** (2008) 202505

[160] Marrows, C. H., *'Spin-polarised currents and magnetic domain walls'* Advances in Physics **54** (2005) 585-713

[161] King, J. A., Eastwood, D. S., Bogart, L. K., Armstrong, H., and Atkinson, D., '*ChiralMEM: A novel concept for high density magnetic memory technology'* Nanotech Conference and Exposition Vol. 1: Technical Proceedings (2009) 623-635

[162] Tatara, G., and Fukuyama, H., *'Resistivity due to a domain wall in a ferromagnetic metal'* Physical Review Letters **78** (1997) 3773-3776

[163] Levy, P. M., and Zhang, S. F., *'Resistivity due to domain wall scattering'* Physical Review Letters **79** (1997) 5110-5113

[164] Bogart, L. K., Eastwood, D. S., and Atkinson D., *'The effect of geometrical confinenment on domain wall pinning in planar nanowires'* Journal of Applied Physics **104** (2008) 033904

[165] Bogart, L. K., Atkinson, D., O'Shea, K. J., McGrouther, D., and McVitie, S., *'Dependence of domain wall pinning potential landscapes on domain wall chirality and pinning site geometry in planar nanowires'* Physical Review B **79** (2009) 054414

[166] Hayashi, M., Thomas, L., Rettner, C., Moriya, R., and Parkin, S. S. P., *'Direct observation of the coherent precession of magnetic domain walls propagating along permalloy nanowires'* Nature Physics **3** (2007) 21-25

[167] Thiaville, A., Garcia, J. M., and Miltat, J., '*Domain wall dynamics in nanowires'* Journal of Magnetism and Magnetic Materials **242** (2002) 1061-1063

[168] Malozemoff, A. P., and Slonczewski, J. C., '*Magnetic domain walls in bubble memory'* Academic Press, New York (1979)

[169] Atkinson, D., *in private communication* (2008)

[170] Durkan, C. E., and Welland, M. E., *'Size effect in the electrical resistivity of polycrystalline nanowires'* Physical Review B **61** (2000) 14215-14218